THESIS FOR THE DEGREE OF DOCTOR OF PHILOSOPHY

ACTIVE MATTER IN A CRITICAL STATE
FROM PASSIVE BUILDING BLOCKS TO
ACTIVE MOLECULES, ENGINES AND ACTIVE DROPLETS

Falko Schmidt

Department of Physics
University of Gothenburg

Gothenburg, Sweden 2020

UNIVERSITY OF GOTHENBURG

Trycksak
3041 0234

Active Matter in a Critical State
From passive building blocks to
active molecules, engines and active droplets

Falko Schmidt
Department of Physics
University of Gothenburg

Abstract

The motion of microscopic objects is strongly affected by their surrounding environment. In quiescent liquids, motion is reduced to random fluctuations known as Brownian motion. Nevertheless, microorganisms have been able to develop mechanisms to generate active motion. This has inspired researchers to understand and artificially replicate active motion. Now, the field of active matter has developed into a multi-disciplinary field, with researchers developing artificial microswimmers, producing miniaturized versions of heat engines and showing that individual colloids self-assemble into larger microstructures.

This thesis taps into the development of artificial microscopic and nanoscopic systems and demonstrates that passive building blocks such as colloids are transformed into active molecules, engines and active droplets that display a rich set of motions. This is achieved by combining optical manipulation with a phase-separating environment consisting of a critical binary mixture. I first show how simple absorbing particles are transformed into fast rotating microengines using optical tweezers, and how this principle can be scaled down to nanoscopic particles. Transitioning then from single particles to self-assembled modular swimmers, such colloidal molecules exhibit diverse behaviour such as propulsion, orbital rotation and spinning, and whose formation process I can control with periodic illumination. To characterize the molecules dynamics better, I introduce a machine-learning algorithm to determine the anomalous exponent of trajectories and to identify changes in a trajectory's behaviour. Towards understanding the behaviour of larger microstructures, I then investigate the interaction of colloidal molecules with their phase-separating environment and observe a two-fold coupling between the induced liquid droplets and their immersed colloids. With the help of simulations I gain a better physical picture and can further analyse the molecules' and droplets' emergence and growth dynamics. At last, I show that fluctuation-induced forces can solve current limitations in microfabrication due to stiction, enabling a further development of the field towards smaller and more stable nanostructures required for nowadays adaptive functional materials. The insights gained from this research mark the path towards a new generation of design principles, e.g., for the construction of flexible micromotors, tunable micromembranes and drug delivery in health care applications.

Keywords: active matter, nonequilibrium, self-assembly, microswimmers, nanomotors, optical tweezers, colloidal molecules, active droplets, critical Casimir forces

This thesis is based on the work contained in the following scientific papers:

Paper I: **Microscopic engine powered by critical demixing**
Falko Schmidt, Alessandro Magazzú, Agnese Callegari, Luca Biancofiore, Frank Cichos, and Giovanni Volpe
Phys. Rev. Lett. **120**, 068004 (2018)

Paper II: **Non-Equilibrium Properties of an Active Nanoparticle in a Harmonic Potential**
Falko Schmidt, Hana Šípovà-Jungová, Mikael Käll, Alois Würger, and Giovanni Volpe
arXiv preprint arXiv:2009.08393 (2020)

Paper III: **Light-controlled assembly of active colloidal molecules**
Falko Schmidt, Benno Liebchen, Hartmut Löwen, and Giovanni Volpe
J. Chem. Phys. **150**, 094905 (2019)

Paper IV: **Measurement of anomalous diffusion using recurrent neural networks**
Stefano Bo, **Falko Schmidt**, Ralf Eichhorn, and Giovanni Volpe
Phys. Rev. E, **100**:010102 (2019)

Paper V: **Responsive Environments Induce Hierarchical Self-Organization in Active Particles**
preliminary list of authors in alphabetical order: Jens Grauer, Benno Liebchen, Hartmut Löwen, **Falko Schmidt**, and Giovanni Volpe
manuscript in preparation (2020)

Paper VI: **QED Casimir forces vs. Critical Casimir forces: Trapping and releasing of flat metallic particles**
preliminary list of authors in alphabetical order: Agnese Callegari, Abdallah Daddi-Moussa-Ider, Mikael Käll, Hartmut Löwen, Battulga Munkhbat, **Falko Schmidt**, Timur Shegai, Ruggero Verre, and Giovanni Volpe
manuscript in preparation (2020)

Reprints were made with permission from the publishers.

IN MEMORY OF

AARON SWARTZ
(1986-2013)

and the world of freely accessible knowledge he might have created.

"Once I realized that there were real serious problems, fundamental problems,
that I could do something to address, I didn't see a way to forget that;
I didn't see a way not to."

Contents

Contents

CHAPTER 1

Introduction

Since I was a little boy, building things became one of my passions. Starting with simple building blocks made of wood I created structures, typically wobbly towers that occasionally fell on top of me. Later on, I used smaller blocks as wooden blocks got replaced by Lego bricks, enabling me to build more complex structures. Instead of wobbly towers, creative concept cars were now speeding over the floor. Over 10 years later, I started my PhD using even smaller building blocks. In fact, I would have to use a microscope instead of my naked eyes to see them and use light tweezers instead of my fingers to assemble them into something, that is now as equivalently exciting as building towers and cars was in my childhood. Understanding the connection between the movement of objects and their building blocks became the topic of my research in active matter.

Let us disassemble the term "active matter" and start with "matter". Matter is what physics is concerned about, from the tiniest elements that build up our atoms, to single cells, to complex living organisms as ourselves, to planets and entire galaxies. Physics investigates the interaction of different types of matter on all length scales. But not every type of matter is considered active (just imagine a stone in your front yard). So what actually is active? You would consider running a marathon as being active, such as you would describe birds flying across the sky and an engine propelling a car as being active. What these three systems have in common is that they require energy, indicated by us sweating or running out of fuel, and that some type of energy source produces this motion like muscles and the car's engine. We humans are of course not the only ones able to be active or produce machines for it, but animals and other living organisms have developed similar mechanisms long ago.

Let us start with a familiar example, the flight of birds. Over millions of years in evolution, birds have developed wings in order to, for example, access food that was previously inaccessible to their competitors. These wings enable them to lift off the ground, manoeuvre through the air and eventually land safely. How are they able to produce these types of motion? While birds move their wings up and down they create a pressure on the air, enabling them to lift off. This is a direct consequence of Newton's third law stating that an action equals a reaction. Leonardo da Vinci, 200 years earlier than Newton, recognised this principle and writes in his notes that birds were able to fly because: "The body applies a force on the air that is as big as the force from the air on the body" [1].

However, if birds would move their wings in the same way up as they move them down, they would create the exact counter pressure that pushes them back down. This illustrates that symmetric or reciprocal motion can result in a zero net movement. But birds do not perform the exact same motion, in fact, it is non-reciprocal as they bend and spread their wings during take off. After more careful observations, Leonardo DaVinci further recognized that the asymmetric shape of a bird's wing enables them to glide through the sky. After drawing the cross-section of a wing, which is stronger bend on the top than on the bottom, he concluded that the larger distance air is flowing across the top of the wing creates the necessary lower pressure that keeps the bird in the air [2]. This principle became only later known as Bernoulli's principle [3]. Therefore, asymmetry, whether it is found in the non-reciprocal motion of the object or in its shape, plays a significant role for generating active motion.

While the movement of birds is not significantly obstructed by their environment due to the low viscosity of air, the motion of bacteria, amoebas and other single-celled organisms only few micrometres in size (corresponding to about 1/100 of a human hair) is strongly impeded by their aqueous environment, where the viscosity of water is about 50 times higher. Imagine standing in between countless bumper cars at a funfair on a busy Sunday afternoon, and as you start loosing track of the individual cars, their bumping into you makes you move in zig-zags. Similarly, on the microscopic scale, the surrounding water molecules randomly push the cells around, causing an erratic motion, which is called Brownian motion (after the botanist Robert Brown who looked at the motion of individual pollen under a microscope [4]). Cells or similarly small objects that lack any form of motility or active motion are therefore referred to as immotile or passive particles. How are they then able to locate food, shelter and each other? In order to overcome this problem, nature has utilised a rich variety of methods for their non-reciprocal motion. Some bacteria have developed flagella, which are long helical filaments, whose rotation allows them to move forward, similar to the motion of a propeller (see example image in Fig. 2.1a, Ref. [5]). Algae, on the other hand, developed a different swimming technique using their flagella that resembles breaststrokes [6]. Researchers started investigating different types of propulsion mechanism by the microorganisms themselves. Since then, they efficiently replicated those under laboratory conditions, in order to build their own artificial systems, which I will describe in further detail in section 2.1. Although the specific mechanisms for the self-propulsion of microorganisms differ from those of large animals, the principle of non-reciprocality in space (flagella bundle together at one end of the bacterium to propel in the opposite direction) or time (algae's breaststrokes) appears strikingly similar.

One type of such an artificial system has been envisioned in the science-fiction movie *Fantastic Voyage*, in which a shrunken submarine is injected into a human body and starts its mission to clear a blood vessel from a life threatening clot. This was back in 1966. Nowadays, researchers have already shown that such small robots can be realized to, for instance, release drugs at specific locations inside the body [7–11]. To this end, light has become a very versatile manipulation tool that allows researchers to precisely manipulate artificial active matter systems. An example is the invention of optical tweezers that allowed for capturing and holding microscopic objects in place and moving them at will [12, 13]. Furthermore, through light-matter interaction such
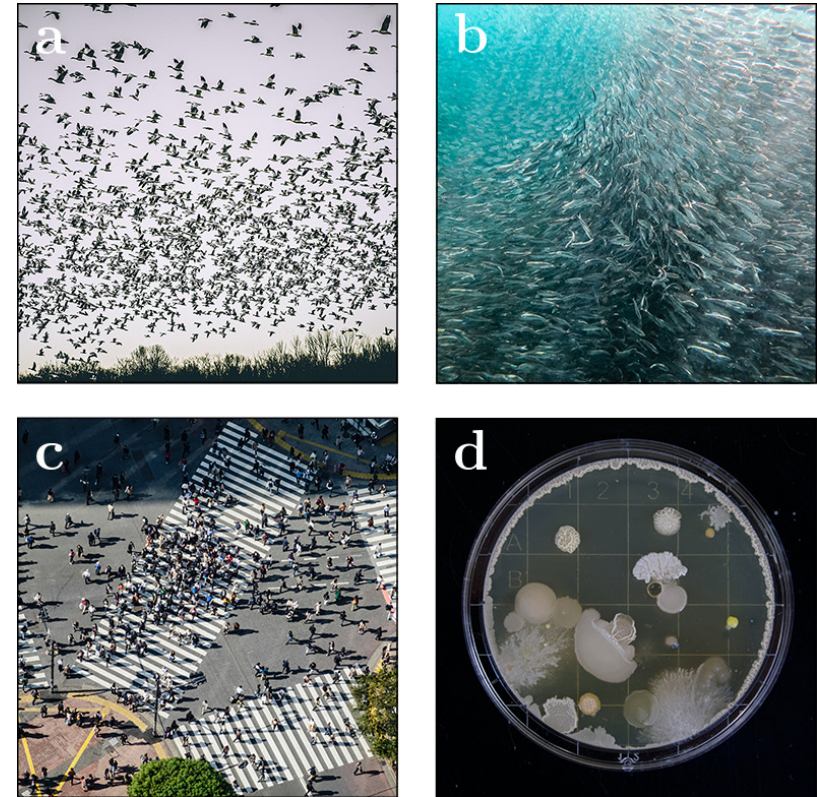

Figure 1.1: **Examples of natural active matter systems: a** flock of birds, **b** school of fish, **c** crowds crossing Shibuya square in Tokyo, and **d** cultures of cells.

as absorption, otherwise passive objects could be set into translational and rotational motion [14–16], as I will explain in more depth in section 2.2.

In active matter systems interesting behaviour occurs when single individuals organize and coordinate in hundreds to tens of thousands such as seen in flocks of birds, schools of fish, human crowds and cultures of cells (see Fig. 1.1). Regardless of the kind of individual (whether it is a bird, fish, human or cell), there are basic physical principles that govern active matter systems and therefore the formation of matter into larger hierarchical structures. Even passive matter is built out of simple building blocks such as atoms (which in turn consist of even more basic elements) that self-assemble into larger structures starting from simple dimer molecules such as hydrogen gas, to benzene rings with more than 12 atoms, to proteins, to cells and in turn living beings. In a similar way, active matter systems can build up into large organized structures from already active building blocks [17].

A simpler way of studying self-assembly processes under laboratory conditions is by using an artificially produced building block, called colloid. Colloids are typically spherical particles that can come in different sizes from tenths of micrometers (on the size of cells) down to a few nanometers (on the size of a virus). They can be fabricated with different properties such as adding magnetic

susceptibility, fluorescent tags for microscopy or antibodies for biomedical applications [18–21]. Since their motion can easily be manipulated and observed, they have been thoroughly used in scientific studies [22–25]. How colloids have been employed to study self-assembly processes and build complex artificial structures is further described in section 2.3.

In order for any building block to interact with each other their "interaction space" must be limited to increase such probability. This often occurs in phase-separating systems such as vesicles, tiny liquids droplets surrounded by a fatty ring and used by cells for cargo transport in and out. These systems increase the concentration of carried materials such as proteins and are therefore argued to be one of the possible origins of life [26–28], as further explained in section 2.4. Phase separation characterizes systems in which transitions between different states, referred to as phases of the system, occur. An example for this is the cooking of water, which changes its phase from liquid to gas. What makes such systems especially suitable for active matter applications is the existence of critical points at which phase transitions occur on very short time scales [29, 30], and which has been utilized for the self-propulsion of active matter [31, 32]. The phenomena of criticality is common across all natural sciences [33–37] and describes the point between order and disorder [38]. In fact, self-organized criticality is a phenomena where the system tunes itself towards criticality [39] and of which evidence has been found in neural networks (such as our brain [35, 38, 40], but which is still highly debated [41, 42]), forest fires [43] and power grids [44]. Very close to such a critical point, fluctuations between the two states of the system can generate forces that are large enough to induce self-assembly between microscopic particles [45, 46]. I will explain the nature of such forces and their applications in more detail in section 2.5.

After this brief introduction into the research topics of active matter concerning this thesis, I will present the challenges that arise when trying to mimic natural systems in order to design, fabricate and control artificial active matter systems and how I solved them in my research. This is especially important when considering applications such as drug delivery systems, autonomous search-and-rescue, bioremediation and more, where each application field has its own kind of requirements such as size, speed, biocompatibility, and steerability. I found that most interesting phenomena occur far away from equilibrium, that is when a suspension of colloids performing Brownian motion becomes active as they start to self-propel and self-assemble. In fact, I show that using two main tools, optical manipulation and a critical phase-separating liquid, I can precisely steer the system's behaviour in and out of equilibrium. I demonstrated new types of active matter systems and also provided insights into the underlying physical mechanisms with the help of simulations and theory. In the following, for each study performed during my PhD, I will present: a short *motivation*, the current *state-of-the-art*, the *aim* of the study, and at last the *main results* found.

1. Microscopic engines under light

Engines have undergone huge transformations and continuously shrunken in size since the invention of the steam engine. However, scaling down engines to the microscale is challenging due to the large thermal fluctuations present in the environment. Thus, new mechanisms for microscopic engines had to be developed, such as by setting colloids into continuous orbital rotations.
Until 2016, light became the state-of-the-art tool to manipulate microscopic objects; thanks to the possibility of transferring angular momentum, a rotational component of the beam, to the particle [14, 47, 48], while it could be held in a fixed location using a strongly focused laser beam, whose gradient forces trap the particle in the focal spot [13]. By developing sophisticated protocols that control the intensity and strength of the laser trap as well as the temperature of its environment, researchers were able to create miniaturized versions of heat engines, such as the Stirling, Carnot, and steam engine [49–51]. These systems utilized external light fields to drive a passive particle out of equilibrium.
My aim was to study a microscopic system, which is already intrinsically out-of-equilibrium and can be precisely controlled by either the intensity of the laser beam or the temperature of the environment.
I report on a light-absorbing particle immersed in a critical phase-separating mixture rotating around the focus of a laser beam with about 1200 rpm (comparable to a car engine at cruising speed). I adjust the performance of this critical engine with intensity and temperature, and show that by tuning these parameters alone the optically trapped particle transitions from Brownian motion inside the focus to fast orbital rotations around the focus of the beam. By taking images of the particles through a SEM (Scanning Electron Microscope) I identify clusters of highly absorbing iron oxide on the particle's surface. Through simulations I confirm that these clusters create hot spots that eventually lead to a local phase separation of the critical mixture and thus continuously drive the particle around the focus. These results are presented in section 3.1 and in **Paper I**.

2. Non-equilibrium properties at the nanoscale

Further miniaturizing our microscopic engines down to the nanoscale would increase their potential application range enormously, as nanoparticles are small enough to be taken up by single cells and are able to cross the blood-brain barrier, among many other possibilities [10, 52, 53]. However, the smaller our Brownian particles become, they get pushed around more in random directions, and also get reoriented more often. Referred to as Brownian rotation, this greatly hinders any directed motion on this scale. Thus, the question arises: how can researchers design and control a system of nanoscopic swimmers and engines?
Until the writing of this thesis in 2020, researchers have demonstrated that a large number of nanoscopic particles can self-propel, self-assemble, and show various other types of activity such as clustering, healing, spinning, although with limited degree of control (typically by switching their activity on and off) [54–59]. On single nanoparticles, however, there have been very few theoretical studies and even fewer experiments [16, 60, 61].

I propose to investigate the behaviour of a nanoscopic particle in a similar setting as for the microscopic engine in **Paper I**, that is inside a critical mixture and under the influence of a focused laser beam, whose confinement allows for better characterization of the particle's non-equilibrium properties. I find that the nanoparticle's rotational motion is less continuous as that of a microparticle. Nevertheless, I can see a clear transition from a solely optically trapped particle at low laser powers to a clear out-of-equilibrium signature at higher powers. Here, the particle shifts radially away from the center of the trap and instead rotates around it. As the particle is made of metal and therefore strongly light-absorbing I can tune its behaviour with laser power only. Furthermore, in order to gain higher control of its preferred direction of rotation I use polarized light causing the particle to spin around its own axis, which then couples back to its orbital rotation. I provide a theory for the particle's complex motion and conclude that its major contribution stems from its own asymmetric shape which I confirm with SEM images. These results are also presented in section 3.1 and in **Paper II**.

3. Self-assembly from passive building blocks to active swimmers

Although single colloids display various interesting behaviour by themselves [14, 51, 62, 63], most physical systems are made out of large numbers of individuals that create more complex matter with increasing functionality [59, 64]. When assembling larger structures from individual building blocks such as colloids, a few challenges need to be addressed: how can researchers arrange matter in custom-designed shapes despite the entropy maximization principle that dictates their arrangement at equilibrium (typically symmetric structures such as the tetrahedral structure of a four-colloid pyramid, more examples in Fig. 2.5a) [65–67], and how can they acquire activity after such a self-assembly process?
Starting from colloidal particles, 3D shapes have been created using either external triggers such as electric or magnetic fields [68], or through functionalized surface patches, e.g., as sticky DNA bonds such that these shapes resemble the molecular structure of molecules such as that of methane [69–71]. However, due to their passive nature, external fields are required to drive these colloidal structures out of equilibrium. Instead, they can be substituted by active particles such as Janus particles (after the Roman god of two faces), which due to their asymmetric shape and surface properties self-propel [31, 54, 72, 73]. By replacing passive colloidal building blocks with Janus particles, the so-formed molecules acquire motility as they spin around a center colloid [17]. Meanwhile, it has been proposed theoretically that activity can also be generated from passive building blocks of two different species, catalytically active and non-active colloids [74]. When colloids of both species come together, the non-reciprocal interaction between them produces motile molecules that depending on the internal configuration of colloids either self-propel, spin around their own axis or are non-motile. When I started my research on this topic in 2017 only one other experimental realization existed that showed the self-assembly from passive particles using ion-exchange raisin particles [75].
I propose to study an experimental system, which shows the self-assembly process of passive colloidal particles of two species into active colloidal molecules, and whose process can be easily controlled.

I demonstrate such self-assembly process using light-absorbing and non-absorbing particles, that self-assemble into active colloidal molecules under homogeneous light illumination. I explore a rich set of motion from migrators, rotators, spinners and inert molecules, whose self-assembly process I can initiate and stop using light illumination only. Furthermore, by using periodic illumination I can statistically control the size and types of molecules being formed. These results are presented in section 3.2 and in **Paper III**.

4. Characterization of anomalous diffusion using machine learning

The dynamical behaviour of colloids changes when subjected to nonequilibrium environments, in which they do not perform Brownian motion anymore. Researchers found that when tracing the motion of a protein inside a cell [76] or a colloid under the influence of a random optical potential [77], their motion is instead characterized by anomalous diffusion. This is in contrast to normal diffusion, which refers here, in the absence of concentration gradients, to the thermal motion of a particle. Depending on whether the particle's motion is constrained by boundaries or being accelerated, it becomes then subdiffusive or superdiffusive, respectively. Their dynamics can be identified using the mean-square-displacement (MSD) method, whose growth with time has an exponent α that is $\alpha \neq 1$ ($\alpha < 1$ subdiffusion, $\alpha = 1$ normal diffusion, $\alpha > 1$ superdiffusion). However, in cases where data is intermittent, data points are missing, or the amount of available data is limited, standard methods fail as they work best, when the amount of available data is large [78, 79].
For specific applications, alternative techniques have been developed [80–82]. Most of these techniques, however, are used under the assumption that the sample rate during data acquisition is regular, and the anomalous diffusion exponent does not change abruptly. Recently, data-driven approaches such as machine-learning have been applied to problems in physics as they can work with input data without given explicit rules, but only few of such works have been applied to the problem of anomalous diffusion [83–85].
I propose a new algorithm based on a recurrent neural network (RNN), which is able to perform well with difficult data sets under the constraints given above. I demonstrate that our neural network performs equally well to standard methods in cases where the trajectories of particles are sufficiently long. In cases, where trajectories are too short for standard methods to work I show that this algorithm is still able to correctly determine the anomalous diffusion coefficient. This allows me to further expand the capabilities of the algorithm to cases where particle dynamics are rapidly changing, e.g., when the activity of a self-propelling particle is being switched on and off. To confirm this I use the same experimental setup as in **Paper III**, where I employ periodic light illumination to assemble and disassemble active colloidal molecules, and show that the algorithm predicted such transitions correctly. This analysis tool therefore proves useful in complex systems, where standard approaches are unsuccessful. These results are presented in section 3.3 and in **Paper IV**.

5. Interaction between active particles and their local environment

A rich pallet of phenomena occur when passive systems such as a Brownian particle are driven out of equilibrium. There are two main principles to realize that: Either the environment itself is out of equilibrium and provides the required energy, such as found in many ratchet-like setups from AC-driven light fields to living organisms in 3D printed superstructures [86, 87], or the particle itself generates a local environment out-of-equilibrium in which it then self-propels [31, 54, 72, 73]. Nevertheless, whether the energy originates from a source outside or is induced by the particles themselves, the environment and the system of particles communicate only unidirectional with each other. This is, however, not always the case, as counter examples can be found in the macroscopic world, such as the dramatic feedback loop of global warming due to the melting of icebergs [88], or the intimate coupling between an unborn child and its mother during birth [89], which shows that there are responsive environments that influence and are influenced by the system.

For microscopic systems, a variety of methods have been proposed to generate nonequilibrium environments such as by structured light [90], or by random optical fields [77], among others [91–93]. On the other hand, particles themselves can be active due to an intrinsic conversion of energy thereby generating a local nonequilibrium environment [94], which I have also previously shown for the self-propulsion and self-assembly of light-absorbing particles in a critical binary mixture in **Paper III**.

I propose to study a comparable two-fold coupling of a microscopic nonequilibrium system and its environment in an easily controllable and simple setup.

I report on a set of experiments and simulations (based on the same experimental setup as in **Paper III**) that show that microscopic particles can interact in a feedback loop with their local environment through phase separation. I find a rich phenomenology from passive building blocks to active molecules, and passive to active "droploids", where particles and molecules are immersed inside a single droplet. I can tune their behaviour by shifting the criticality of the liquid and via illumination strength. I also observe interesting dynamically behaviour between molecules and droplets and characterize with the help of simulations how fast droplets emerge and fuse together. These results are presented in section 3.3 and in **Paper V**.

6. Fluctuation-induced forces

Over the last decade, microfabrication has produced increasingly smaller and more powerful devices such as electronic chips, now commonly found in our handheld devices. Such MEMS (microelectromechanical systems) now possess features that are so small and closely packed that they are only separated by tens of nanometers [95–97]. At this scale, surface forces such as the quantum electrodynamic (QED) Casimir force [98], which is attractive by nature, are strong enough to cause stiction. This unintentional adherence of two surfaces can even cause the total collapse of such microstructures leading to the failure of the whole device [99, 100].

Current methods either solve the problem during the manufacturing process such as by using super-critical fluids [101], freeze sublimation drying [102], vapour phase etching of sacrificial layers [103, 104] and others [105], or during

the device operation by changing the surface roughness [106], or by applying self-assembled monolayers (SAM) [107–109] to reduce adhesion and therefore stiction.

I propose a solution to the stiction problem by using a force of similar nature as the Casimir force, but whose strength and direction I can precisely tune, i.e. the critical Casimir force.

I provide experimental evidence that the critical Casimir force, which is based on the critical density fluctuations of a phase-separating liquid, can counterbalance and even overcome the QED Casimir force. I show that in the presence of such force the diffusion of a metal flake-like particle is drastically reduced when floating on top of a metal substrate. By tuning the temperature and changing the wetting properties (between water-adsorbing and non-adsorbing) of the substrate using SAM, the critical Casimir force is large enough to lift the particle further away from its surface and therefore drastically reduce the Casimir attraction. I demonstrate this principle in a simple proof-of-concept device where I observe the transition of a previously trapped flake from a metal to dielectric surface. These results are presented in section 3.4 and in **Paper VI**.

Outline

This thesis is structured as followed:

Chapter 2 gives a broader background into active matter and presents its various research fields in more depth as well as their current limitations.

Chapter 3 gives an overview and a summary of the research conducted during this PhD and specifies my contributions to each work.

Chapter 4 gives a general conclusion and an outlook into the future of this area of research.

Chapter 5 lists all published articles and manuscripts and their supplementary information, providing explicit details on research results, methods and experimental setups as well as their respective theoretical models.

Background

2.1 Strategies for self-propulsion of microswimmers

When observing small non-motile particles under the microscope it becomes evident that their motion is erratic [4]. Whether they are dust particles floating in a ray of sun light coming through your window or whether they are colloidal particles suspended in water, the collisions with the surrounding air or water molecules randomly push the particles around. This random movement, known as Brownian motion, depends directly on the environment the particle is suspended in such as the viscosity of the medium (the higher the viscosity the smaller the collisions) and temperature (the higher the temperature the larger the collisions). Generally, this motion can be described by a single constant, the diffusion constant D, describing how much a particle moves over time. Its SI units are therefore given in m^2/s. Thus, it provides crucial information about its local environment, which, for example, has been used in the context of single cells where injected particles uncovered the biological state of the cell and revealed the presence of diseases [76]. I will show later how the increased diffusion of a heated particle is a consequence of the particle's higher effective temperature. On a molecular level, the equipartition theorem states that the thermal energy of a system of particles is evenly divided among all degrees of freedom and are equal to $1/2\,k_\mathrm{B}T$. Therefore, a measurement of temperature is a measure of the thermal energy of the system. This thermal energy can be then translated into kinetic energy due to the molecules degrees of freedom for each translational direction, each rotational axis, one vibrational degree of freedom for every bond, and one angular degree of freedom for every pair of bonds. So far, these particles lack any form of self-generated motion or activity and are therefore referred to as passive particles.

In order for microorganisms or colloidal particles to overcome their environments random fluctuations (often referred to as thermal noise in this context), some energy source is required to induce active motion. Here, I discuss two main kinds of active motion in colloidal systems: motion along the gradient of an external field (e.g. electric, magnetic, concentration field), and motion due to intrinsic conversion of energy (that in turn can induce local field gradients) in form of self-propulsion [94, 110, 111]. External fields such as magnetic fields can be used for instance to induce rotational motion of artificial flagella attached to immobile red blood cells, which then self-propel [62, 112]. Particles might also be dragged along the field gradients or set into rotational motion

under a circulating field [18, 19]. Although the required technology is readily available (such as electromagnets and capacitors for magnetic and electric fields, respectively) their implementation into microscale applications requires complex experimental designs and can limit their application range (e.g. low penetration depths in biological tissue due to scattering [113]). Thus, intrinsic mechanisms that convert energy directly from the environment, such as through chemical reactions, are easier to implement and mimic natural systems better. However, care has to be taken when designing microswimmers intended for biological applications as many of the driving mechanisms presented in the literature involve harmful reagents such as hydrogen peroxide or employ high-energy UV light [16, 54, 55, 60, 61, 111, 114–117]. Investigating self-propulsion mechanisms has become a rapidly developing field in active matter research and will be explained in more detail here.
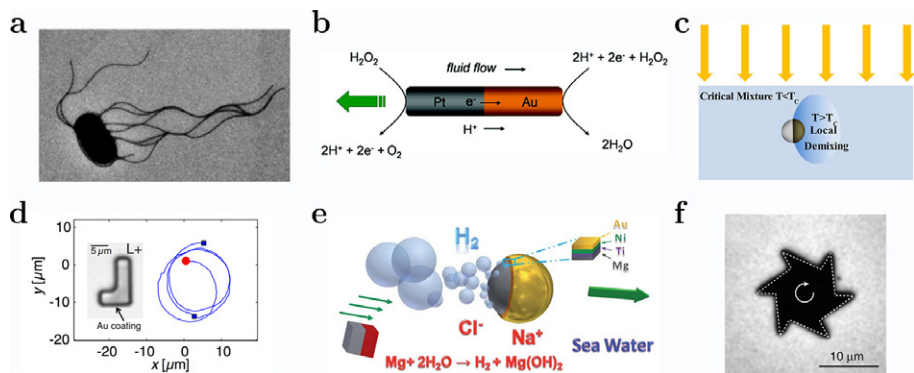

Figure 2.1: **Examples of microswimmers based on different propulsion mechanisms.** **a** Electron migrograph of a *Salmonella* cell with its flagella [5]. **b** A Janus rod propels in a hydrogen peroxide solution due to electrophoresis [118]. **c** Upon illumination, a Janus particle produces local demixing inside a critical mixture [31]. **d** Exposed under the same conditions as for **c**, an asymmetric particle in the shape of the letter "L" rotates in orbits [32]. **e** Chemical reactions on one hemisphere of a Janus particle produces bubbles inducing a recoil force on the particle [119]. **f** Thermocapillary forces can induce rotation of gear-shaped particles [120]. Images **(a-f)** are reproduced with permissions from Refs. [5, 31, 32, 118–120].

Since most biological entities on the microscale self-propel in aqueous solutions they are referred to as microswimmers. Examples of biological microswimmers are plentiful: algae, bacteria such as *Salmonella* (Fig. 2.1a), amoeboids, human sperm cells [5, 6, 121–123]. Despite the presence of thermal noise, sperm cells, for example, reach impressive speeds of up to $100\,\mu$m/s (30 times their own body size in a second). Investigating the underlying mechanisms will allow researchers to understand what happens when their movement is impaired causing lower conception rates [123].

Taking inspiration from nature, researchers went on a quest to explore methods for self-propulsion that will produce fast, efficient and biocompatible microswimmers, and whose motion can be externally controlled at will. Insights from this field will greatly improve researchers understanding of basic

physical principles governing small-scale systems and will lead to technological improvements in many areas besides physics. In medicine for instance, microswimmers could provide a new efficient way of delivering drugs directly to the treatment side, reducing the amount of drugs and side effects and avoiding unnecessary contamination of drinking waters [124, 125]. In first trials, drugs have already been attached to microswimmers, which were then externally guided by magnetic and electric fields [7, 9], or were using active microswimmers thereby increasing the amount of contacts the drug had with, e.g., the inner lining of the stomach wall [8]. Applications are not only restricted to biomedicine but are also found in the remediation of contaminated soil and ground water [126, 127] and for autonomous search and rescue missions [128].
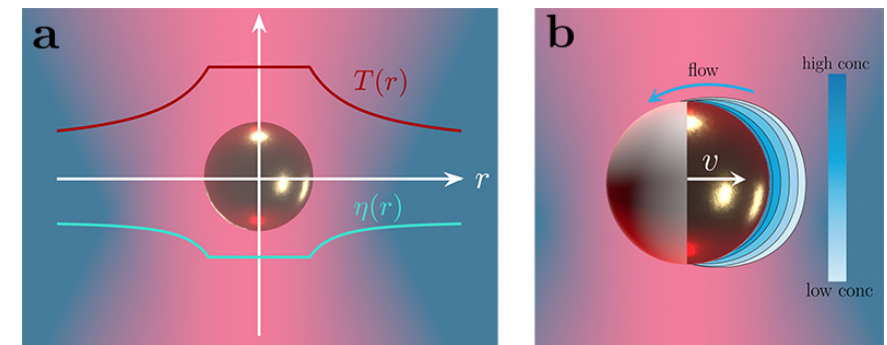

Figure 2.2: **Importance of shape asymmetry for self-propulsion. a** A spherical particle under illumination of a laser beam creates a temperature profile $T(r)$ that is constant at the particle's surface and decreases with $1/r$ radially outwards. Similarly, the viscosity $\eta(r)$ of the surrounding fluid changes. As the temperature profile is radially symmetric, the particle's effective temperature is increased leading to hot Brownian motion but no net movement. For a Janus particle in **b**, where only one hemisphere is coated with an absorbing material, a local concentration gradient can be induced through phase separation of a critical mixture. The resulting creep flow on the particle's surface produces linear motion of the particle with velocity v in the opposite direction.

Self-propulsion is based on the particle generating a local gradient in its vicinity, such as through temperature and chemical concentration gradients (and exploited in the work presented in **Papers I-V**). A full list of the types of motion due to gradients is provided in Ref. [129]. Establishing a gradient alone does not produce directed motion as asymmetry in the system is required either in form of non-reciprocal motion or due to spatial variations [130]. As I will show now, the latter one is commonly employed for the self-propulsion of artificial active matter. In Fig. 2.2 the differences between a completely spherical particle (Fig. 2.2a) and an asymmetric particle (Fig. 2.2b) are shown. Let us first consider the case of spherical particles, e.g. gold nanospheres under light illumination (typically lasers of high intensities), which absorb part of the light and consequently convert it into heat. This heat is radiated into its environment thereby increasing the temperature of the surrounding environment. Closest to the particle's surface the temperature T is highest and decreases with its radial distance as $1/r$ (as shown in red in Fig. 2.2a).

The environment reacts to that temperature difference, which can be seen in a decrease of viscosity η closest to the particle (as shown in blue in Fig. 2.2a). Although a gradient along the tangential direction of the particle is induced, this only leads to a larger diffusion of the particle, whose motion is therefore referred to as hot Brownian motion [131, 132]. As the thermal gradient is still radially symmetric across the whole particle surface it does not induce directed motion (as left and right side experience the same local changes).

Consequently, a gradient parallel to the particle's surface is required, which can be achieved through spatial variations, either by shape such as through intrinsic defects or deformities of the particle (as I will show in section 3.1 for the particles studied in **Paper I & II**) or through a change in composition such as coating one half of a dielectric sphere with a metal (as shown in Fig. 2.2b). This creates a Janus particle (named after the Roman god with two faces) of which only one half will heat under illumination, whereas its other side remains unaffected by light and therefore cold. The difference between hot and cold side induces a gradient across the particle's surface that causes a flow of water molecules from one to the other side (referred to as positive thermophoresis from hot to cold and negative for opposite flow direction). The resulting flow will induce a slip velocity on the particle in the opposite direction giving rise to self-propulsion [73, 133]. Similarly, self-propulsion is induced when a concentration gradient is induced. Analogously to hot and cold sides, sides of low and high concentration can be created through chemical reactions. In a study by Paxton and coworkers in 2004 [54], directed motion of a Janus rod, one half made of platinum the other of gold, was observed when immersed in a hydrogen peroxide solution (see Fig. 2.1b) [118]. Here, the dissociation of hydrogen peroxide on platinum creates free hydrogen ions which flow towards gold and recombine there with the surrounding hydrogen peroxide into water. Thereby, the ion flow towards gold induces a motion of the rod in the opposite direction, which is why this process is also referred to as self-electrophoresis. Diffusiophoresis can not only be induced by catalysis as described above but by light-induced phase separations as well, creating a water-rich phase on one and a water-depleted phase on the other side (see Fig. 2.1c) [31, 134]. The resulting flow of water creates a slip velocity on the particle's surface that propels it in the opposite direction (see schematic in Fig. 2.2b) [135]. More details on the topic of phase separations for propulsion are discussed in section 2.3. Janus particles due to their simplicity in design are commonly used as microswimmers [117, 136, 137] and in fact display a rich set of motion from simple migration, spinning, to orbital rotations of individual particles [72, 73, 138] and collective behaviours of clustering, swarming, and crystallization [64, 115, 139, 140].

Other studies have investigated 2D-chiral particles, whose mirror image is not superimposable (like your left and right hand), e.g. in the form of the letter "L" (see Fig. 2.1d) [32], asymmetric particles such as gears (see Fig. 2.1f) [120] or using vesicles (cellular organelles composed of lipid bilayers) [141]. Although phoretic motion is one of the most common driving mechanisms for active matter systems, other types exist, such as bubble propulsion, where the resulting gases from a chemical reaction induce a recoil force on the particle (see Fig. 2.1e) [119].

2.2 Optical manipulation of miniaturized machines

As evident from the examples of the previous section, external stimuli such as electro-magnetic fields are ideal to induce translational motion and therefore self-propulsion. Moreover, by tuning the properties of the applied field, particles can be set into continuous motion that is steerable in all directions. Magnetic fields are commonly employed for the rotation of microparticles with rotation rates up to $100\,\text{Hz}$ [142] (limited by the viscosity of the liquid [63]), but their practicality outside the laboratory is questionable due to the large equipment required [19]. Instead, light is a much more accessible manipulation tool as the size and costs of lasers and LEDs has come down immensely in the last two decades. Moreover, light provides a better means of control as wavelength, intensity and phase of the beam can be manipulated independently. By choosing an appropriate wavelength specific materials can be targeted, while leaving others unaffected. Near-infrared light, for example, can penetrate biological tissue undisturbed but strongly heats absorbing nanoparticles taken up by cancer cells for photothermal treatment [11]. For the manipulation of microparticles the phase component of a beam of light is most effectively. Similarly to a rotating magnetic field, the electromagnetic field of a beam can carry orbital angular momentum, which can be directly transferred to the particle. This induces a torque on the particle causing it to spin around its own axis and/or move on circular orbits. By shaping the beam of a light source, Gaussian beams (with a centred peak of highest intensity, see Fig. 2.3b) can be transformed into Laguerre-Gaussian (LG) beams. LG beams possess a helical wavefront for which they are also known as doughnut beams or optical vortices (see Fig. 2.3c). This enabled a new field of micro- and nanorotors of various shapes from simple nanorods with frequencies up to $1\,\text{kHz}$ [56], to gear-like shapes [15], and spherical but birefringent microparticles (the refractive index depends on the propagation direction and polarisation of the light beam, thus its optical properties vary across different axes of the particle) with hundreds of Hz rotation rates [14]. Microrotors have found various applications across many disciplines such as probing local fluid properties [48, 143], for micromixing [47], and hydrodynamic manipulation [144].

Light can not only induce rotation of particles but trap them at fixed locations and against gravity, too (see Fig. 2.3a). When light is being focused (as through the objective of a microscope) strong gradient forces are generated that attract nearby particles towards the maximum of intensity at the focal point of the beam (see Fig. 2.3b). This enables trapping and dragging of particles with a moving beam of light. In this way, light becomes the optical equivalent of a mechanical tweezer, thus its name optical tweezers. In 2018, Arthur Ashkin has received half of the Nobel prize in physics for the invention of optical tweezers in 1986 [13]. Since then, this tool has found many applications in, for instance, biology and statistical physics where it enabled new types of experiments as particles could be studied over prolonged periods of time and thus provide critical insight into their local environments [145–148]. In fact, I have used optical tweezers to keep rotating microparticles at fixed position and therefore preventing their diffusion out of the laser beam (which I employ in the work presented in section 3.1 and in **Papers I & II**). Since optical tweezers and their working principles have been extensively described in literature [149], I
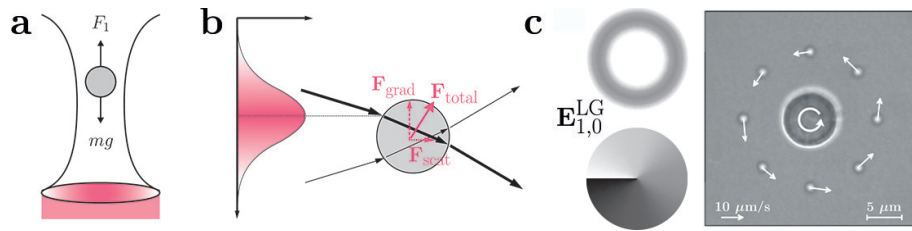
Figure 2.3: **Optical manipulation methods. a** An optical tweezers holds a particle inside a focused Gaussian beam of light. **b** Inside the focus of a Gaussian beam, the particle is attracted towards the high-intensity centre by gradient forces $\mathbf{F}_{\text{grad}}$ and pushed along the beam's direction by scattering forces $\mathbf{F}_{\text{scat}}$. Arrows indicate the refraction of a ray of light inside a sphere and their thickness represents the number of rays passing through. **c** In a Laguerre-Gaussian beam (modes $l = 1$, $m = 0$) with doughnut shaped intensity and a circular phase, microparticles can be set into rotation. Image reproduced with permission from Ref. [14].

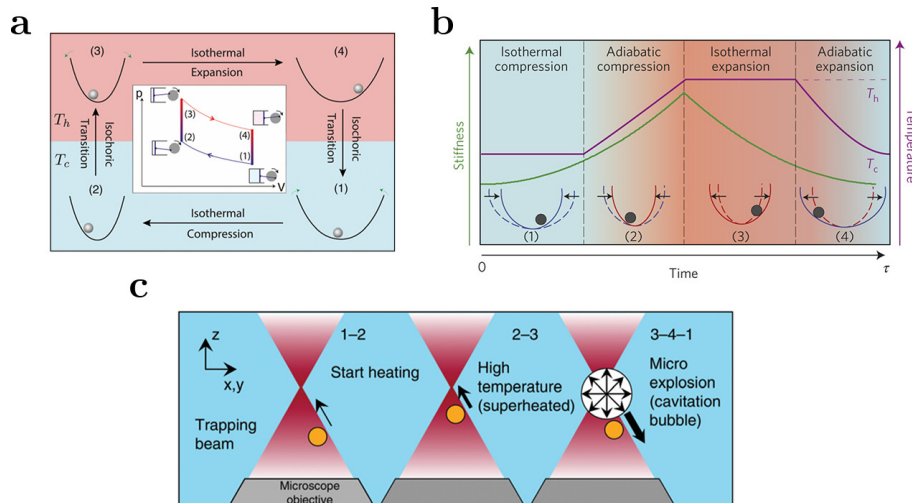will keep the focus their applications for miniaturized machines.

Figure 2.4: **Experimental realizations of microscopic engines based on optical tweezers. a** A microscopic particle inside the potential of an optical tweezers can mimic the working principle of a Carnot engine [50] and **b** of a Sterling engine [49]. An absorbing microparticle causes microexplosions when being trapped close the focal point where intensities are highest and induce a recoil force on the particle. Consequently, the particle performs an oscillatory motion inside the beam [51]. Images **(a-c)** are reproduced with permissions from Refs. [49–51].

An interesting example of employing optical tweezers to the rotational motion of microparticles are miniaturized heat engines. Classical heat engines are characterised by their work cycle where, for example, a petrol engine follows the Otto cycle (consisting of two adiabatic processes for compression and power

stroke and two constant volume processes for the heat rejection and combustion process), whereas the theoretical Carnot cycle (consisting of two adiabatic and two isothermal processes) is difficult to realize experimentally as all processes need to be reversible and are thus limited in practise by friction. However, physics on the microscopic scale can change and thus creates opportunities for the realisation of miniaturised heat engines such as the Brownian Carnot engine by Martìnez and coworkers (see Fig. 2.4a) [50]. A Brownian particle is trapped inside an optical tweezers, whose trapping stiffness k (the strength of confinement in the trap) can be adjusted with light intensity and the particle's temperature T through an external electric field. With these two parameters, the isothermal processes of the Carnot cycle can be replicated by adjusting the trapping stiffness, and the adiabatic processes by modifying temperature and trapping stiffness keeping T^2/k and therefore entropy constant. This shows that a microscopic particle as the working substance can transform thermal fluctuations into mechanical work. The Brownian Carnot engine is not the only example, as a micrometer-sized Stirling engine (see Fig. 2.4b) [49], a micrometre-sized steam engine (see Fig. 2.4c) [51], and my version of a miniaturized engine inside a critical binary mixture (see section 3.1 and **Paper I**) have been realised in the confinement of an optical tweezers.

Moreover, the area of nanoscopic engines has been widely unexplored with only few examples so far as thermal fluctuations typically prevail over any directed motion on such scale [16]. However, under the right conditions and employing external fields, impressive rotation frequencies for nanoscopic particles such as nanorods on the order of several kHz have been achieved [56]. This showcases that there is great potential for developing nanoscopic engines, such as my own realization presented in section 3.1 and in **Paper II**, which will open up new application areas that were previously unreachable for their microscopic equivalent [10].

2.3 Self-assembly of colloidal building blocks

Atoms are one of the most commonly known building blocks that self-assemble into hierarchical complex matter. Starting with atoms combining into molecules, more complexity and functionality is being added as building blocks are increasing in size, with molecules then assembling into larger proteins, which in turn are building blocks of cells and therefore the basis of life. Understanding how each element assembles from smaller building blocks is one of the core questions in physics [150].

In the laboratory, researchers have substituted these atomic building blocks by microscopic and nanoscopic colloids. Colloids are a type of particle that are typically spherical in shape, can be fabricated reproducibly in large quantities using standard methods and are observable under commercially available light microscopes from which large datasets can be acquired [22–24]. They are typically made out of inert materials such as gold or glass and are therefore suitable for biological and medical applications [25, 151]. Moreover, they can be modified for specific purposes adding, e.g., magnetic susceptibility, absorption properties, polarizability or fluorescent dyes, such that their motion can be easily tracked and steered by magnetic, AC electric or acoustic fields [18–20, 152].

Self-assembly processes in passive colloids are driven by the interaction-energy minimisation principle (reducing the free energy of the system) limiting the degree of control over their formation. Isotropic colloids therefore self-assemble into simple, closely packed structures such as large 2D colloidal crystals and 3D clusters that are radially symmetric in shape (see examples in Fig. 2.5a middle row) [150]. More specific structures can be designed by breaking the surface symmetry using, for example, surface patches made of DNA on which other colloids can attach to. These so formed shapes can replicate several molecular structures, such as the tetrahedral structure of a methane molecule in Fig. 2.5a [69, 153]. Nevertheless, these structures are inherently passive and require external fields to acquire motility.

When exchanging passive with active particles, locally created flows around such active particles [75, 114, 154, 155] (induced by temperature or concentration gradients) can not only drive their self-propulsion, but can lead in the presence of other nearby colloids to self-assembly [17, 156, 157]. More recent research investigates active particles, such as Janus particles, in combination with AC electric fields that self-assemble into microrotors around a passive particle in their center (see Fig. 2.5b) [17], and form large colloidal crystals under UV light illumination [64, 115]. Even in the absence of external fields Janus particles immersed in water and whose hemisphere is hydrophobic self-assemble into highly hierarchical structures such as long helices resembling DNA [156].

An alternative approach has been theoretically proposed in 2014 by Soto and Golestanian in which simple isotropic colloids self-assemble and acquire motility [74]. In their work, two species, chemically active and non-active colloids, do not self-propel in isolation. However, when in close proximity to another phoretic interactions induce attractions between active and non-active colloids and colloidal molecules form. In their simplest configuration a Janus dimer (made of one active and one non-active colloid) is formed thus breaking the action-reaction symmetry and subsequently to net motion of the dimer [158]. Depending on the internal arrangement of active and non-active colloids the
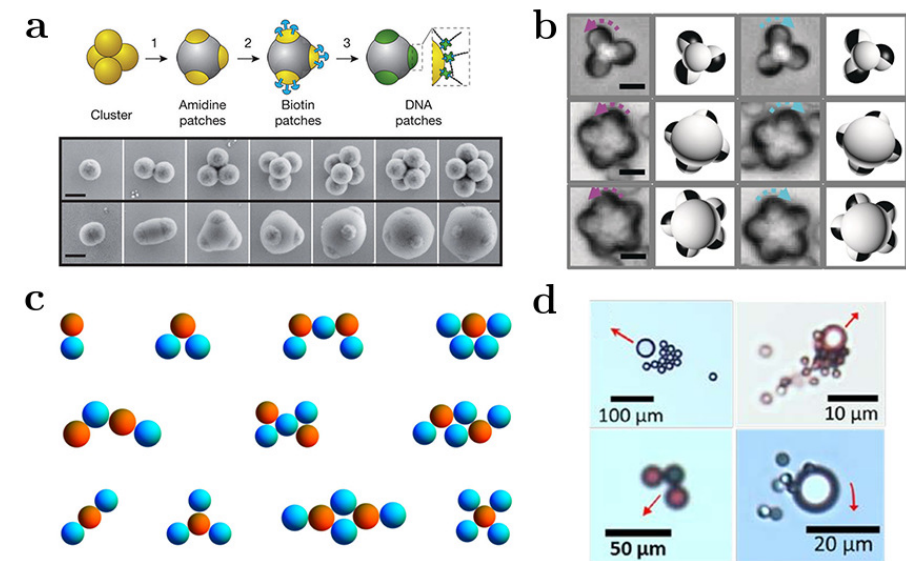

Figure 2.5: **Self-assembly into colloidal molecules. a** A cluster of passive particles is held together by DNA patches and can replicate several molecular structures but are non-motile [69]. **b** Active building blocks, here Janus particles, form colloidal molecules exhibiting active motion by spinning around a center colloid [17]. **c** Active colloidal molecules can self-assemble from immotile heterogeneous building blocks ("catalytically active" in red and "catalytically passive" in blue) and display various types of motion (migrating on top, rotating in middle, immotile on the bottom) depending on their internal configuration [74]. **d** Experimental realization of a self-assembling molecule from passive particles based on ion-exchange [75]. Images **(a-d)** are reproduced with permissions from Refs. [17, 69, 74, 75].

newly formed molecules can be classified into three categories that either self-propel, self-rotate or are inert (see Fig. 2.5c) and which I explore further in section 3.2 and in **Paper III**. In a similar way, early experiments have shown that two species of particles can attract each other via ion exchange forming motile colloidal molecules (see Fig. 2.5d) [75, 159].

2.4 Liquid-liquid phase separations

All micro- and nanomachines whether they are swimmers, rotators or motors require a constant flow of energy. This energy is either provided by the environment such as through external fields or by internal energy conversion such as through catalysis on the particle's surface.

An example are Janus particles whose hemisphere is coated with platinum and which are immersed inside a hydrogen peroxide solution. Their cap acts a catalyst to degrade the surrounding hydrogen peroxide into water and oxygen. The induced concentration gradient across the two hemispheres self-propels the particle until all of hydrogen peroxide is transformed and the Janus particle becomes immotile. Without "refueling" the system with its reagents or by providing an additional energy input this process is irreversible. Similarly, additional energy is required in form of latent heat between the liquid-solid boundary of water (remember the additional heat necessary to melt ice into water at 0°C). This is a characteristic of first order phase transitions where the first derivative of the free energy with respect to temperature at fixed volume, i.e. the entropy of the system, is discontinuous. Practically this implies that transitioning in between such phases of the system requires not only additional energy but time as well and is therefore impractical for the continuous propulsion of particles. Instead, second order phase transitions posses critical points at which the free energy's first derivative is continuous and such energetic boundary is absent. These principles are commonly found in natural systems for the self-organization of matter [39]:

"Self-organized criticality describes complex systems that are situated at the delicately balanced edge between order and disorder in a self-organized critical state. Only at the critical state, does the compromise between order and fluctuations exist [...]".
- Didier Sornette in Critical Phenomena in Natural Sciences,
2006, Springer 2$^{\text{nd}}$ Edition

In nature, such critical system are abundant on all length scales from, the gravitational clustering of the expanding universe [33], to earthquakes whose rupture is seen as a critical point [34], to the (still debated) critical state of the human brain [35, 38, 40–42], down to intracellular organisation [26, 36, 37, 160]. In physics, examples can be found for instance in magnets at their Curie temperature T_c [161] or in mixtures of liquids at their critical composition c_c and critical temperature T_c [30, 162]. The latter is commonly used for active matter purposes [31, 32], which I will further discuss here.

A solution of two liquids does not always mix homogeneously (such as for water and ethanol) but can remain demixed (such as for water and oil). Liquids mix because the system's mixed state has higher entropy, which is the thermodynamically favourable condition. In contrast, demixed states oppose entropy-driven mixing as the system's energy is lower when similar molecules, such as oil molecules, are close to each other [26].

In critical systems, a binary mixture of liquids (such as that of water and 2,6-lutidine) is found in both states, mixed and demixed, depending on the system's temperature and the composition ratio of the mixture. The phase
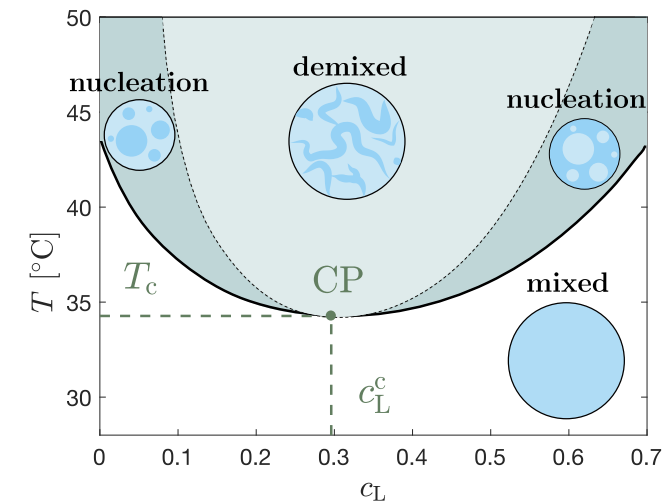

Figure 2.6: **Phase diagram of a water–2,6-lutidine mixture.** Given by its temperature T and the mass fraction of lutidine inside the total solution c_L the system is found in different phases: mixed (white background) where the solution acts as a normal fluid, and demixed (light grey background) separated by the spinoidal curve (black dotted line) where water and 2,6-lutidine completely phase separate from each other. In between the two states nucleation (dark grey background) in either one of two phases occurs beyond the binodal curve (black solid line) and eventually turns into complete demixing. Only at the critical point CP with T_c and c_L^c does the transition between mixing and demixing occur immediately. Data taken from Ref. [30].

diagram in Fig. 2.6 shows distinct regions of mixed state (white background) and demixed state (light gray background). Both states are separated by two lines. Following a transition from mixed to demixed state, i.e. by increasing the temperature, the binodal curve (black solid line) is crossed first and marks the transition into a region (dark gray) in which both states can coexist, therefore also called coexistence curve. Characteristic features of this phase are nucleations in form of droplets rich in either one of the phases in minority (a larger 2,6-lutidine concentration leads to the formation of water-rich droplets and vice versa). These droplets grow in size over time, which I will further investigate in the presence of particles in **Paper V**. Upon further increase in temperature a second line, the spinoidal curve (black dotted line), is crossed into a region where complete spinoidal decomposition occurs. Here, the two phases, water and 2,6-lutidine, completely separate from each other, which results into characteristic worm-like structures. In mathematical terms, the spinodal curves satisfies the conditions at which the second derivative of the Gibbs free energy is zero. Therefore, crossing over from mixed to demixed state requires to overcome an energy barrier (here a large increase in temperature) indicated by the gap between binodal and spinodal line, everywhere except at the critical point CP where both lines coincide. The critical point is given by a critical temperature T_c and a critical composition of 2,6-lutidine c_L^c inside

the mixture ($T_c = 34.1$°C, $c_L^c = 0.286$). Although this example represents a phase diagram with a lower critical solution temperature, upper critical solution temperature, both upper and lower critical solution temperature, or even ternary mixtures with multiple critical points exist as well [29, 163, 164]. Since crossings between the two states close to the critical point are possible with minimal energy changes, critical binary mixtures have gained increasing interest in the active matter community. By illuminating a Janus particle immersed in such a critical mixture, its light-absorbing cap radiates heat into the surrounding solution [31]. With sufficient absorption the critical temperature is exceeded and thus causes local demixing of the solution surrounding its cap. As its opposite side remains cold and the solution therefore mixed, a concentration gradient establishes across the particle's surface leading to diffusiophoretic motion [135, 165]. I exploit the phenomena of criticality in all experimental systems presented in **Papers I-V** to drive colloidal systems out of equilibrium and to induce active motion.

The critical binary mixture of water–2,6-lutidine is commonly used in experiments due to its lower critical solution temperature close to room temperature. However, 2,6-lutidine is toxic and is therefore not applicable in biological environments. Readily available alternatives exist such as a critical mixture of water, AOT and decane with similar characteristics [166] as well as other types of liquid-liquid mixtures, e.g. aniline/cyclohexane [162] and Pluronic F127, which instead of a mixed-demixed transition exhibit a liquid-gel transition depending on temperature and critical composition [167]. It is important to note that critical systems are universal in the sense that parameters of the phase diagram, here temperature and concentration, can be replaced by others commonly found in nature such as pH value, activity, and polymer concentration [168, 169].

In fact, liquid-liquid phase transition are a common principle for intracellular organisation and played an important role in the formation of life [27]. As droplets start to nucleate in polymer solutions, the polymer concentration inside the droplet drastically increases and with it the probability for reactions to occur. It is argued that this is the mechanism exploited by protocells at the early stages of life, which used liquid droplets as reaction centres [26]. More and more evidence is found that this provides the basis for the formation of more complex compartments such as the nucleolus of a cell [36, 37, 169, 170]. Active matter research in such critical systems could provide a deeper understanding into their underlying mechanisms by gaining better control such as through light-activation in biological systems [171], or by designing artificial cells and active droplet systems in the laboratory [28, 160], which I also investigate in **Paper V**.

2.5 Fluctuation-induced forces

Interesting phenomena occur close to the critical point of our system which is an important characteristic of all critical systems. While approaching the critical point, local density fluctuations emerge that gradually increase in strength, in terms of their correlation length and relaxation time, and which diverge at the critical point [172]. In other words, the binary solution constantly demixes and remixes at times and length scales that depend on the temperature difference $\Delta T = T - T_c$. Those fluctuations start at a molecular level and quickly grow into the microregime, thereby becoming relevant for microparticles and microdevices.

When such fluctuations are spatially confined in between two surfaces, such as in between two plates, the difference in modes of fluctuations inside and outside results into an attraction of the two plates (see Fig. 2.7a). This effect was first predicted by Hendrik Casimir in 1948, who studied the quantum electrodynamic vacuum fluctuations in between two uncharged conductor plates [98]. The resulting attractive force was named after him as Casimir force. The force decays with the inverse distance to fourth power $\sim L^{-4}$, is therefore only predominant in the sub-micron regime and highly sensitive to changes in surface height. This has been exploited for the development of new techniques for probing surface properties with nanometer precision using small tips [173, 174]. As the Casimir force scales linearly with area, large conducting surfaces such as those found in micro- and nanofabrication become considerably affected where it can cause undesired stiction and therefore failure in microelectromechanical systems (MEMS) [99, 100].
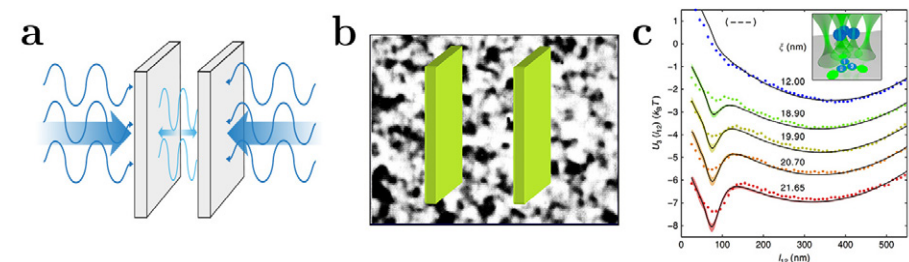

Figure 2.7: **Fluctuation-induced forces. a** Due to electrodynamic quantum fluctuations in vacuum, two conducting plates experience an attractive Casimir force (blue arrows) as fluctuations are bound in between the plates compared to free space. **b** Analogously, two objects inside a critical mixture experience a critical Casimir force due to the density fluctuations close to the critical point. **c** Critical Casimir forces are exploited to investigate the non-additivity in a multiple particle setup as shown by the inter-particle potential U_3 when approaching the critical point (here indicated by the correlation length ξ) [175]. Images **b, c** are reproduced with permissions from Refs. [175, 176].

Analogously, density fluctuations in critical binary liquids confined between two surfaces (such as two plates, two spheres, or a sphere and a wall) induce an equivalent force, which in reference to the previous is called critical Casimir force (CCF) (see Fig. 2.7b). Depending on the boundary conditions the

critical Casimir force can be either attractive for symmetric or repulsive for asymmetric boundary conditions. The boundary conditions are given by the surface affinity for either one of the components of the binary liquid. Thus, symmetric (asymmetric) boundary conditions refer to a preferable affinity of the same (opposite) component. This can be achieved for example by modifying the surface wetting properties using self-assembled monolayers [176–178] such that they either repel or attract water (hydrophobic and hydrophilic, respectively). As for the Casimir force, the CCF is only predominant at short distances and scales linearly with area. Since their theoretical prediction by Fisher and de Gennes in 1978 [172], CCF have been experimentally measured with microscopic particles close to a surface. It has been theoretically and experimentally demonstrated that their strength can be tuned by adjusting the temperature close to the critical temperature and through surface patches [45, 176, 179, 180]. Furthermore, CCF have been used to study the non-additivity of forces between multiple colloids, showing the universality of this technique (see Fig. 2.7c) [175]. As CCF can be precisely tuned in strength and direction they become an ideal candidate for self-assembled active matter systems [181], such as shown for quantum dots and patchy colloids assembling into predefined colloidal molecules [46, 182–184]. In section 3.4 and in **Paper VI**, I will explain how CCF can be tuned with temperature to reverse the effect of the reduced diffusion of metal particles due to Casimir attraction.

Critical solutions provide a novel route for active matter systems that enable constant, fuel-less propulsion, the self-assembly of colloids into hierarchical structures, mimic the mechanisms of protocells, and whose strength can be precisely controlled using temperature. It forms the basis upon which I have built our own realizations of a microscopic and a nanoscopic engine (section 3.1 and **Papers I & II**), which initiate the self-assembly of immotile colloids into active molecules and droplets (section 3.2 & 3.3 and **Papers III & V**), and which is a sensitive tool for manipulating MEMS devices(section 3.4 and **Paper VI**).

Research results

3.1 From optically trapped microparticles and nanoparticles to engines powered by critical demixing

Researchers and laypersons alike have a fascination with building machines that allow us to precisely control our surrounding environment and to find new ways for us to move, work and interact with each other. We largely understand how engines work in our everyday life, but researchers still investigate how complex machines can operate and be realized on the microscopic scale. Inspired by the study of natural propulsion mechanisms of single-cellular organisms [5, 6, 123], researchers have developed new methods to produce artificial microswimmers that could mimic their biological counterpart [62, 90, 112]. By attaching reactive centres to their body, cargo transports for drug delivery [10, 185] as well as the chemical degradation of pollutants in the environment [126, 127] became possible. This enabled whole new application fields across multiple disciplines with benefits for the personal and public health [8, 21, 119, 128]. However, microswimmers are still subjected to their environment, which causes random reorientations due to Brownian rotation. To achieve a higher degree of control over their motion, external fields have been employed, which allowed to steer microswimmers in all directions [92, 110, 112]. Using these types of fields, nonmotile particles can be set into rotational motion too, which led to the development of micromixers and micropumps [14, 47, 63, 118, 142]. The rotational component of motion is an important aspect for the development of machines as it allows their continuous operation, which is of course most evident for engines. In the last decade, a great variety of micron-sized engines have been proposed, from miniaturised steam engines to the microscopic equivalents of heat engines such as the Sterling or Carnot engine [49–51]. I have described their working processes in more detail in section 2.2. It becomes apparent that in order to recreate the thermodynamic processes of a Sterling or Carnot cycle for colloidal particles, complex dynamic protocols are in place that require the adjustment of multiple system parameters at once [49, 50]. In contrast, the proposed microscopic steam engine is an intrinsically simpler system that requires no external guidance, as its principle is based on the interaction of an absorbing particle and a light beam, resulting into microexplosions that propel the particle radially outwards. However, the control over the strength of such explosions and therefore the amplitude and frequency of such motion is limited. Moreover, temperatures far over 300°C are required to induce evaporation of water, thus

rendering this system unsuitable for biological applications.

Consequently, solutions are sought for that allow the continuous rotation of a particle, whose motion can be precisely controlled with few experimental parameters, and which is realizable in biological environments.

In **Paper I**, I have proposed and realized a new type of microscopic engine driven by the reversible demixing of a critical mixture at the particle's surface. As in the works presented above, I use optical tweezers to keep the particle in place. However, in stark contrast to the microscopic steam engine, I show that steady orbital rotations centred around such focus occur when placing an absorbing particle inside a focused laser beam. I study the motion of a particle made of porous silica, in which iron oxide nanoparticles are encapsulated. As part of the light is absorbed locally on its surface, phase separation of the surrounding critical mixture are induced leading to self-diffusiophoresis. Trapped by the optical potential of the laser beam the particle moves along stable orbits at about 1200 rpm.

It is important to mention that such phase separations are already induced at temperatures close to $T_c \approx 34.1°C$, therefore remaining within the acceptable biological window of temperature. Moreover, such phase separation are completely reversible, which means that areas demixed by the absorbing particle's presence are remixing as soon as the particle moves on and temperatures drop below T_c. In this way, the particle's motion continues as long as a light source is present and does not require any type of fuel as used in more "conventional" systems [54, 55]. Although our engine is realised in a mixture of water and 2,6-lutidine, a toxic solution for biological matter, readily available alternatives exist at similar critical temperatures (see section 2.4). I have tested several phase separating solutions such as the surfactant pentaethylene glycol monododecyl ether (C12E5) and the hydrogel Pluronic F127 in combination with *Bacillus subtilis* and *Escherichia coli* bacteria, and found them to thrive in such solutions (this work is yet to be published).

Through simulations of our microparticle inside a critical binary mixture, I concluded that its motion is a result of local accumulations of iron oxide nanoparticles on its surface, at which stronger demixing occurs (similar to the hot and cold side of a Janus particle). I confirm this through SEM images of our particles, which reveal the presence of such large clusters (see Fig. 3.2a). Furthermore, I show that I can tune the behaviour of our engine via the ambient temperature of the solution and the applied laser power from a solely optically trapped particle to performing orbital rotations. Since this systems only needs to be tuned close to the critical temperature T_c, changing either parameter while keeping the other one fixed, is sufficient to tune the particle's behaviour and therefore allows for a simpler manipulation of such systems. Consequently, I use the light source as a multi-purpose tool, that serves as a switch to turn activity on and off and tune its behaviour continuously in between both states, and which serves as the anchor around which the particle is rotating.

At last, I study the work output of our microscopic engine at different temperatures and powers and determine its efficiency. I find that its efficiency is comparable with those of similarly sized engines [14, 120].

With that in mind, this proposed engine design leads the way towards continuously driven, easily controllable and high work output machines that potentially enables new levels of precision for medical tools in microsurgeries

and treatments. In the future, the need for invasive methods will decrease, as ingested microparticles are non-toxic, biodegradable and can be externally guided to the treatment side via light, penetrating through the skin and thus minimizing side effects [186]. Naturally occurring phase separations inside the human body have already been discovered and could in principle be utilized to drive such miniaturised machines [26, 37, 170].

Towards the goal of complex micromachines, the output of a single engines requires further amplification, and more research on the synchronization and coupling of such engines, which is yet not fully understood [140, 187, 188].

Since our publication in 2018, more types of engines have been proposed and experimentally realized, such as a spin quantum heat engine [189], photothermocapillary oscillators [190] and an optofluidic microengine [191], showing the rapid development of the field.
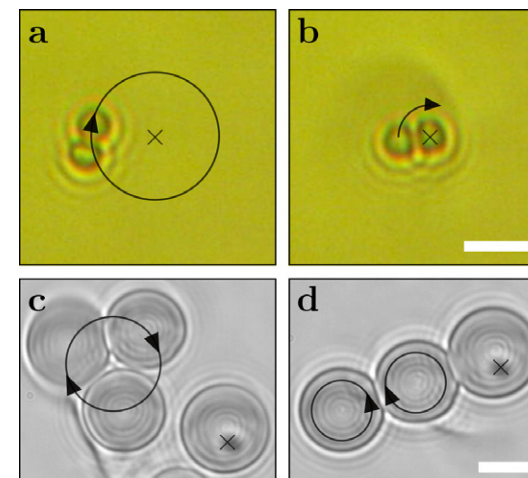

Figure 3.1: **Early experimental tests on self-assembled microengines.**
a A dimer particle moves on constant orbits around the center of an optical tweezers, whereas, in **b**, a dimer particle spins around its trapped absorbing particle due to local demixing (visible as a darker background). In **c**, three colloids cluster and rotate at high rates next to a pinned absorbing particle. In **d**, the pinned absorbing particle on the right first attracts two other colloids, forming a colloidal chain. The induced clockwise rotation of the center particle, causes a counter-clockwise rotation of the left particle, resembling a gear-like system. The $\times$ marks the location of the focused laser beam. Scale bar for **a,b** represents $2\,\mu$m, for **c,d** $5\,\mu$m.

In early experiments, I have tested the behaviour of dimers, made out of one absorbing and one non-absorbing particle, and produced by collaborator Lucio Isa at ETH Zürich using their capillary method [192]. Immersed inside the critical mixture and under the influence of an optical tweezers, the dimer either self-propels on stable orbits around the trap center (see Fig. 3.1a), or is spinning around its own axis while the absorbing particle is trapped in the center (see Fig. 3.1b). This shows that interesting types of motion occur when different particle geometries are combined and can provide an additional way of tuning an engine's behaviour. However, the dimer's particles had been melted together

during fabrication. Ideally, microengines self-assemble from simple colloidal building blocks such as presented for molecules in **Paper III**. In a first trial to realize this, I have placed colloids close to the strong demixing of an absorbing particle, which has been fixed to the surface. The induced flows by this particle lead to the self-assembly of a cluster of colloids, which performs fast rotations (see Fig. 3.1c). I also observe the formation of a colloidal chain where a transfer of angular momentum occurs, resembling a gear-like mechanism (see Fig. 3.1d). The cause of this motion and transfer of momentum is not fully understood yet, as the role of hydrodynamics, temperature and concentration fields, as well as the critical Casimir force has not been investigated, but where simulations could greatly improve our knowledge of such critical active matter systems.

Although microscopic particles are small enough to be ingested and guided through e.g. the vascular system, most parts of the body such as the brain, as well as individual cells remain inaccessible. Nanoscopic particles, however, are able to pass through the blood-brain barrier [10] and can be absorbed by single cells through e.g. endocytosis [52]. Further minimizing microscopic engines down to the nanoscale is challenging, as rotational diffusion plays a significantly larger role and greatly hinders any directed motion of the particle. Because of the difference in scaling between translational diffusion, which scales with the linear dimension of the particle, and rotational diffusion, which scales with the volume, active directed motion is strongly inhibited as the particle reorients at short timescales. Although experiments have shown that nanomotors can be realised, their motion typically translates to a hot Brownian motion with an effective higher temperature [16, 58, 60, 61, 116].

On the other hand, studying active particles inside the confinement of a potential, such as the widely employed harmonic potential, can provide important physical insights into active matter systems [193]. Experimentally, this has been studied for toy robots in a parabolic potential landscape [194], as well as for microparticles in an acoustic [195] and an optical trap, as presented above in **Paper I**. Nevertheless, these systems are comparatively large such that their motion is predominantly driven by their self-propulsion and where Brownian rotation occurs at much larger time scales.

In **Paper II**, I show that the active directed motion of a nanoparticle can be achieved in a critical binary mixture and a harmonic optical potential generated by a Gaussian focused beam of light. I study the motion of a gold nanoparticle in an optical tweezers setup and observe orbital rotations far away from the trapping centre. Surprisingly, I find that the particle exhibits behaviour far from equilibrium, and which does not resemble a hot Brownian motion. I observe a clear shift of behaviour from an optically trapped particle at low laser powers with a Gaussian probability distribution to a strong out-of-equilibrium signature at high laser powers, where its non-Gaussian distribution is shifted away from the centre of the focused beam and towards its edge. With the help of theoretical models, I conclude that the main contribution to the particle's motion stems from self-diffusiophoresis as a result of its non-spherical shape. I confirm this through SEM images in which their crystalline facets become visible (see Fig. 3.2e). Furthermore, we show that we can statistically control the direction of orbital rotation by adjusting the circular polarisation of the beam. In fact, I find that circular polarization induces a torque on the particle, whose spinning rotation couples back to its orbital rotation such that the

direction of polarization and its orbital rotation are aligned.
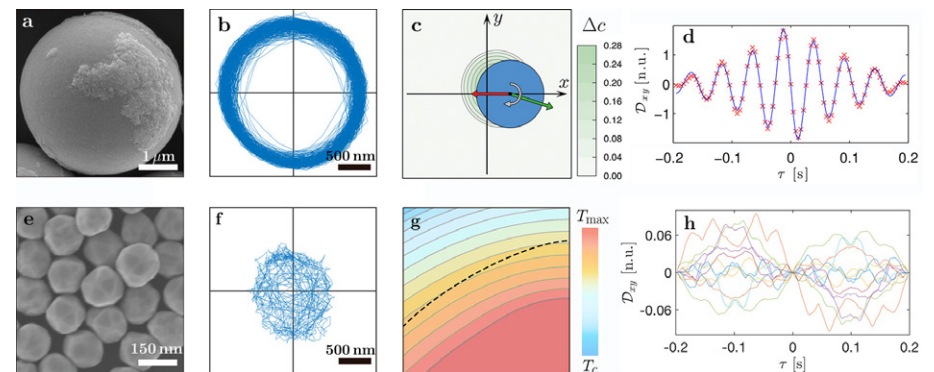
Figure 3.2: **Driving mechanism of a microscopic engine (a-d) vs. a nanoscopic engine (e-h). a** The SEM image of the microparticle reveals large clusters of iron oxide nanoparticles on its surface. **b** Constant orbital rotations of the particle around the center of the beam are observed in experiments as seen in this $6.4\,\mathrm{s}$-long trajectory in the x–y plane. Higher local absorptions lead to an increase in temperature that, when $T > T_c$, **c** cause demixing of the surrounding solution and a concentration gradient that is responsible for the orbital rotation of the particle. **d** This is characterized by its differential cross-correlation function $\mathcal{D}_{xy}$ at single frequency $f = 20\,\mathrm{Hz}$ and at almost maximal amplitude of $\mathcal{D}_{\max} = \pm 2$ (experimental values red crosses, theoretical fit blue line). In contrast, a nanoscopic particle as shown in the SEM image **e** possesses clear crystalline facets and therefore slightly non-spherical. In experiments **f**, the particle $1\,\mathrm{s}$-long trajectory shows a clear shift away from its trapping center and rapid transitions through the same. **g** The particle's shape asymmetry leads to a creep flow close to the facet's edges, as the equidistant line (black dotted line) to the particle's surface crosses its isothermal lines (in color). **h** The differential cross-correlation of its motion reveals only weak orbital motion ($\mathcal{D}_{xy} \ll 0.1$) at different frequencies. Images and data for **(a-d)** taken from **Paper I**, reproduced with permission from Ref. [196], and for **(e-h)** from **Paper II**.

Differently from **Paper I**, in **Paper II** I find that motion is not driven by the generation of hot spots on the particle's surface, as the surface temperature of our metallic nanoparticle is constant, but because of its shape asymmetry. This in turn causes temperature gradients (and subsequently chemical concentration gradients when $T > T_c$) parallel to its surface and subsequently induces creep flows. I illustrate these differences in Fig. 3.2. From experimental observations alone, it becomes clear that the engine's motion on both scales is strikingly different; the particle on the microscale performs constant orbital rotations at $1200\,\mathrm{rpm}$ (see Fig. 3.2b) whereas the particle on the nanoscale performs orbital rotations at varying rotation rates and radii and changes its direction of rotation frequently (see Fig. 3.2f). For that reason, I could not employ the same methods for data analysis as differential cross correlations of the translational components work best for motions at fixed frequency and radius, but fail when the rotations are discontinuous (compare Fig. 3.2d vs. Fig. 3.2h).

I have found that in the case of nanoparticles, the probability distributions and velocities (i.e. total, radial and azimuthal velocities) illustrate best their out-of-equilibrium behaviour. This shows once more that thermal fluctuations on the nanoscale are non-negligible and different mechanisms are required to generate active motion. I therefore propose to design future systems with nanoparticles, whose shape possess strong asymmetry as found for instance in nanorods with large aspect ratios. This could potentially increase the efficiency of its propulsion mechanism and result into higher velocities and more linear motion. I have tested two types of asymmetric particles, a nanorod and a chiral particle, produced by collaborators at Mikael Käll's lab [56, 197], under the same experimental conditions as in **Paper II** and found their trajectories to be strikingly different. In a comparison in Fig. 3.3 it can be seen that the shape strongly influences the particle's motion. However, more experiments accompanied with theory and simulations are required to understand their exact interaction.

Because of their size, nanoparticles open up a new regime for manipulation that was previously inaccessible by microparticles. First studies show that nanoparticles can be used inside single cells such as cancer cells for treatment [11], can cross the blood-brain barrier [10] and find many more application in the treatment of water and soil [119, 126]. Nevertheless, more basic studies, such as ours, are needed to gain further insights into the underlying non-equilibrium physics for the development of future nanorobotics.
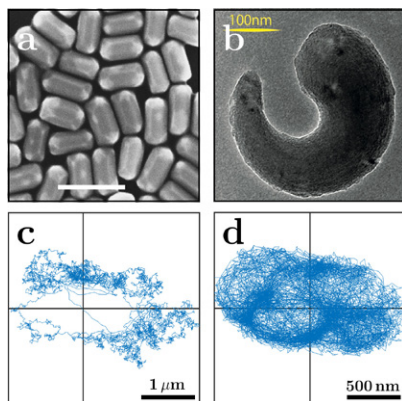

Figure 3.3: **Preliminary results on the motion of a nanoscopic particle depending on its shape.** **a** SEM image of nanorod and **b** of a chiral nanoparticle, and their corresponding trajectories in **c** and **d**, respectively. Scale bar in **a** represents 200 nm. Images in **a,b** are adapted and reproduced with permission from Refs. [56, 197].

Contributions to the work:

In **Paper I** I have been designing, implementing and conducting the experiments for which I have built a homemade optical tweezers setup including a bright field microscope. At first, I have acquired data using a quadrant photodiode but found that the strong demixing around the particle interfered with the particle's signal such that I switched to digital video microscopy. I have analysed the experimental data, contributed to the particle dynamics simulations and

prepared figures and manuscript for publishing.

Paper II has been a result of a collaboration between our group and Mikael Käll's group of nanophotonics at Chalmers University of Technology. For all experiments I have used their group's dark field microscope setup in combination with an optical tweezers and polarisation control of the beam described in the supplementary information and in further detail in Ref. [56]. I have conducted the experiments, analysed the experimental data and prepared figures and manuscript for publication. The theoretical model has been developed by our collaborator Alois Würger at the University of Bordeaux.

3.2 Light-activated self-assembly and disassembly of colloidal building blocks

Assembling large machineries (e.g. for car manufacture) requires putting together hundreds if not thousands of parts and involves a lot of labour. Similarly, assembling microscopic systems from colloidal building blocks (e.g. by using optical tweezers) would be a tedious task. In nature, however, structures self-assemble from their building blocks as a result of entropy maximisation [150]. Researchers found that using microscopic building blocks such as colloids, large crystalline structures are formed [66, 67]. In order to gain a higher degree of control over their formation process, surface patches have been used to recreate the geometric structures of molecules [69, 184]. Such colloidal molecules are nevertheless inherently passive and thus require external fields to be driven out of equilibrium. By replacing passive building blocks with self-propelling particles, e.g. Janus particles, such colloidal molecules acquire motility, too [17, 115]. An alternative approach has been theoretically proposed based on the self-assembly from a heterogeneous suspension of immotile building blocks [74]. Here, catalytically active colloids can attract non-active colloids forming colloidal molecules, which in their simplest configuration are Janus dimers, which break their internal symmetry and consequently self-propel. This shows that self-propelling building blocks are unnecessary to display a rich set of motion [198]. This principle has been shown experimentally using ion exchange resin particles, whose self-assembly starts immediately upon immersion of the particles and which self-propel until the ion exchange subsides and molecules disassemble [75]. Under these conditions the self-assembly process is not reversible. Hence, a better control over the molecule formation process is required, where activity can be switched on and off, and the molecule's speed can be tuned.

In **Paper III**, I propose an alternative mechanism for the reversible self-assembly of active colloidal molecules. Using two different species of homogeneous particles, light absorbing and non-absorbing, and suspended inside a critical binary mixture, I can precisely control the self-assembly process by light illumination. I employ the same type of absorbing particle as for **Paper I**, containing iron oxide nanoparticles, whereas non-absorbing particles are made of plain silica. Both particle types possess the same size and are prepared in a sample cell whose walls are only slightly further separated than their diameter. In a dilute suspension, both species behave as passive particles performing Brownian motion. Upon illuminating the sample with a defocused laser (here optical forces are negligible compared to **Paper I & II**), absorbing particles create local flow fields in their vicinity through demixing of the solution. Enhanced by the presence of the sample cell's boundaries, these flows attract nearby non-absorbing particles, and molecules start forming. In their simplest form, one absorbing and one non-absorbing particle form a dimer molecule that resembles a Janus particle. The presence of the non-absorbing particle breaks the radial flow symmetry surrounding the absorbing particle, and thus the whole dimer acquires motility and self-propels. Results in **Paper I** suggested that hot-spots created by local clusters of nanoparticles on its surface could in principle induce active motion without the presence of other particles. Here, however, illumination strengths are comparatively low and only induce temperatures large enough for phase separation to occur ($T \approx T_c$), but not self-propulsion.

Under continuous light illumination, molecules grow in size over time and depending on their internal configuration of absorbing and non-absorbing particles exhibit either migration, spinning, orbital rotation or are static (in agreement with the proposed structures in Ref. [74]). I find that molecules will continue to grow under illumination, either until a large ring of non-absorbing particles has formed around the molecule, or all suspended particles have been engulfed by molecules.

Upon switching the illumination off, flows recede, molecules disassemble, and their particles diffuse away. In this way, I can control the molecule formation using light only, assembling and disassembling them as desired. I have effectively demonstrated this by limiting the molecules' size through periodic illumination. At short periods of illumination, small molecules typically of type migrator form, whereas under long periods of illumination, molecules have saturated with non-absorbing particles and therefore become static. Together with setting the ratio of absorbing vs. non-absorbing particles in suspension, I can statistically control the types and sizes of molecules being formed.

I have shown that our self-assembly process is reversible, self-limiting and does not require any "fuel" compared to conventional systems [54, 55], and where molecules remain active as long as an external source of energy is provided. I have replicated our experimental findings through simulations that permitted me to go beyond experimental limitations and explore the full parameter space of the self-assembly process.

In addition to what has been published in **Paper III**, I find that molecule growth can be inhibited not only by switching the illumination off, but by decreasing the interaction strength between the two species, too (Fig. 3.4a). By reducing the illumination to a minimum, only Janus dimers will form in solution, whereas larger molecules exist only transiently. To characterise their interaction strength better, I have also investigated the distance between an absorbing and non-absorbing particles just before assembling into a Janus dimer. I find that with increasing illumination strength the separation distance, at which attraction started to occur, increased (Fig. 3.4b). At last, I study the growth dynamics of clusters up to their saturation point, at which growth stopped depending on the fraction of absorbing vs. non-absorbing particles (Fig. 3.4c,d).

These additional experiments and simulations give further insights into the self-assembly process and provide a proof-of-principle system for the assembly of modular swimmers. Studying self-assembly processes is an important step for building more complex micro- and nanomachines. In cells for instance, the uptake of foreign material is strongly limited by size [52] such that individual building blocks need to be reassembled at the target location, similar to the fitting of a ship inside a bottle. This novel route, presented in **Paper III**, should proof useful as a design principle for the development of a new generation of active materials. In particular, it allows to design functionality in highly-controllable synthetic systems, which is a most often uncontrollable defining feature of biological systems.

Since our initial submission to the preprint server arXiv in the beginning of 2018, other types of experimental systems for the self-assembly of colloidal molecules have been presented and more theoretical work on the self-assembly of such systems has be done [158, 159, 199–202], which shows that the field is rapidly developing. However, the studies presented
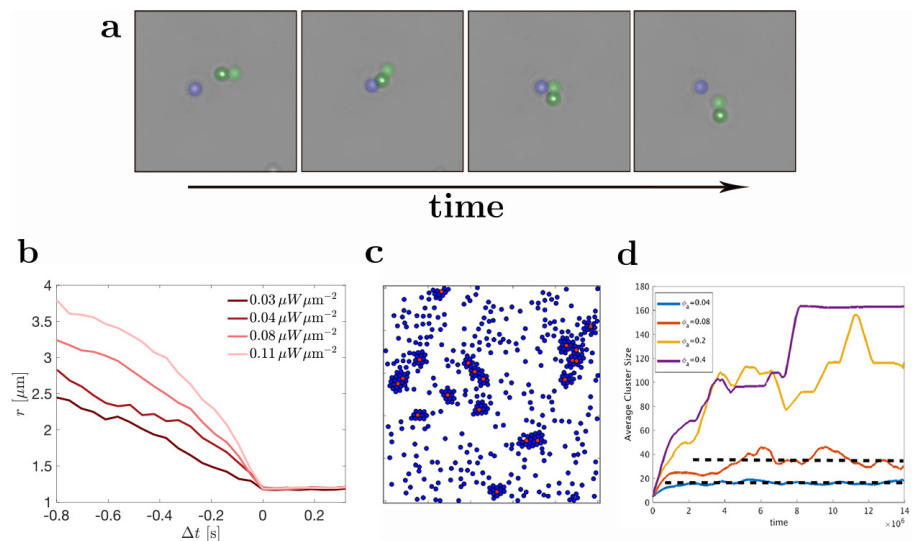
Figure 3.4: **Further insights into the self-assembly process of colloidal molecules. a** Snapshots of a Janus dimer molecule (in green). At minimum intensity the dimer passes by a non-absorbing particle (in blue) without interacting with it. **b** Experimental measurement of the inter-particle attraction, when a Janus dimer is formed, depending on intensity where r is the distance between the particles' centre and Δt the time difference to the moment the molecule has formed ($\Delta t = 0$). **c** Snapshot of simulations of saturated growth where absorbing particles are completely surrounded by a ring of non-absorbing ones. **d** Dependence of the average cluster size on the ratio of absorbing to non-absorbing particles ϕ_{a}.

demonstrate a new powerful machine learning algorithm for analyzing complex systems. Nevertheless, much work is still required to expand the capabilities of the network to other cases such as that of fractional Brownian motion. Since our publication of this work in the middle of 2019, more algorithms have been proposed to the anomalous diffusion problem which is exemplified by the ongoing "Anomalous Diffusion Challenge" [203], showing the current trend of applying machine learning for active matter systems [204–207].

Contributions to the work:
In **Paper III**, I have designed and built the experimental setup based upon the setup used for **Paper I**, but where the optical tweezers has been replaced by a defocused laser source illuminating the particles from the top. I have acquired and analysed the experimental data and prepared the figures and manuscript for publication. The theoretical model and simulations of our particles have been done in collaboration with Benno Liebchen and Hartmut Löwen from Heinrich-Heine Universität in Düsseldorf.

In **Paper IV**, I have conducted the experiments and provided two sets of experimental data, one already presented in **Paper III**, another one based on speckle light field experiments, where the subdiffusion of particles has been observed. I have contributed in the writing of the manuscript for publication and the preparation of figures. The algorithm was developed by Stefano Bo from the Royal Institute of Technology and Stockholm University.

here are far from extensive; future simulations and experiments could investigate the molecular details of phoretic and hydrodynamic interactions, how individual molecules interact with each other and how this principle could be applied to microscopic engines that self-assemble and synchronize [140].

In **Paper IV**, because of the interesting dynamics involved in **Paper III**, I have used these experimental data to test a deep learning based algorithm for studying the anomalous diffusion exponent of particles. Due to the experimental conditions, in which trajectories are short and the system dynamically switches between different states of activity under periodic light illumination, standard methods such as the empirical mean squared displacement (MSD) are unsuitable. For this reason, together with Stefano Bo from Stockholm University, we have developed a recurrent neural network (RNN, similar algorithms are used in Google's translational services) that is able to determine an exact anomalous diffusion coefficient and at which point in time such transitions occur. RNN do not only perform equally well as the MSD method in cases with many data points but outperforms it when data points are limited. Moreover, I confirm with our experimental data gathered in **Paper III** that transitions between states with illumination on and off and their anomalous diffusion exponent can be predicted correctly. I therefore

3.3 Coupled interactions of active colloidal molecules with their environment

Feedback loops shape the way humans are interacting with their environment, e.g. through climate cycles, but are in fact also essential regulatory mechanisms inside the human body and on a cellular level. Recently, it has been established beyond unreasonable doubt that the melting of ice sheets in Greenland lead to an accelerated warming as darker surfaces are uncovered, which increases global heating and causes more ice to melt [88]. In living beings, such processes are referred to as homeostasis [208]. They ensure for instance that blood sugar levels are kept stable, where an increase in glucose levels in the blood is detected by the pancreas, resulting into insulin secretion until normal blood glucose levels are reached (negative feedback loop), or maintain uterine contractions during child birth, when stimulated receptor cells send signals to the brain, which releases oxytocin into the bloodstream, stimulating further contractions, and thus more oxytocin is released (positive feedback loop) [89]. In cells, feedback mechanisms generate both simple and complex spatiotemporal signaling responses in order to communicate between each other [209]. The interactions between systems and their environment are bidirectional and operate in a feedback loop. For microscopic systems, I have shown in previous results (**Papers I - III**) how a microparticle shapes its environment through phoretic interactions. On the other hand, microparticles are also subjected to and influenced by their environment especially under nonequilibrium conditions [77, 90–93]. While in these examples, the particle-environment interaction is only unidirectionally, it is also important to understand how the feedback of an environment can couple back to a system of microparticles, which could greatly improve how researchers design artificial microscopic systems.

I find that our experimental system in **Paper III** is also an example of a bidirectional coupling of a system of light-absorbing colloids and their local critical environment. In conditions with a large density of absorbing particles, the stronger local demixing creates a response of the environment, as large droplets start forming around absorbing particles and active colloidal molecules. The droplet's internal composition gradient and its interface generate a feedback on the molecules that can lead to their disassembly.

In **Paper V**, I show that such coupling creates a new type of active matter systems, which I call *active droploids*, as their embedded colloids induce active motion of the droplet itself. Such droploids form as a result of the interaction between particles and environment, where absorbing particles create local chemical concentration gradients that induce the assembly of colloidal molecules through phoretic attractions as in **Paper III**. However, when temperatures exceed the critical temperature $T > T_c$, local phase separations expand to large water-rich droplets engulfing active molecules. As the molecules are still migrating, they continuously shape their environment, causing the droplet to follow their motion.

I systematically explore the full phase diagram where I find four different states, depending on the amount of energy feeding into the system of particles (i.e. through light intensity and the amount of absorbing particles), and depending on the composition ratio of the binary mixture. At low energy inputs $T < T_c$, I identify a disorder phase of immotile dispersed particles, at medium inputs

$T \approx T_c$ active colloidal molecules, and two new phases i.e. active droploids at high inputs $T > T_c$, and immotile droploids at inputs greatly exceeding the critical temperature of the system $T \gg T_c$.
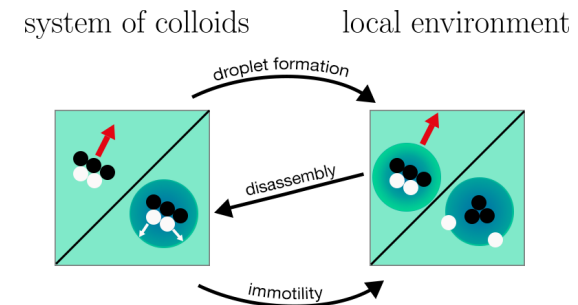

Figure 3.5: **Schematic of the feedback loop between a system of colloids and its local environment.** The absorbing particles of an active colloidal molecule affect their local environment by inducing strong demixing that leads to droplet formation. Since the colloidal molecule is active, their feedback generates active motion of the droploid, too (direction of motion indicated by red arrows). Eventually, due to further demixing the concentration gradient inside the droplet vanishes and a pure water-rich phase is established. This causes a feedback on the colloidal molecules as weakly hydrophilic non-absorbing particles are pushed towards the droplets interface and molecules subsequently disassemble. Consequently, also the droplet environment becomes immotile.

The latter is another good example of the bidirectional coupling. Strong demixing surrounding the absorbing particles at high temperatures creates an almost pure water-rich phase inside the droplet and therefore pushes the less-hydrophilic non-absorbing particles to the droplet's interface. Consequently, molecules disassemble leaving the absorbing particles in the center of the droplet such that the whole droploid becomes immotile. Theoretical modelling of the particle and droplet dynamics reproduced these experimental findings and allowed me to visualize the differences in the droplet's internal composition gradient between active and immotile droploids (see schematic in Fig. 3.5). Moreover, the simulations provide better statistics to quantify at which input energy such transition occurs, while the droplet speed gradually decreases with the amount of non-absorbing particles on its interface increasing.

Over time, droplets will continue to grow in size as more particles and molecules are being absorbed and fuse together with other droplets. From measuring the droplet size over time, I find that the growth process is faster for active droploids than for immotile droploids. Furthermore, I demonstrate that the droplet formation process can be guided and arrested with light through periodic illumination of the sample.

This approach provides a novel route for generating droplets in a liquid-liquid mixture that exhibit motility and can be easily controlled externally. It also provides a minimal model of protocells for understanding intrinsic and extrinsic forces driving compartmentalization as an important step towards understanding biological regulation associated with diseases such as Alzheimers and Parkinson [210, 211].

Contributions to the work:

In **Paper V**, I have performed the experiments and analysed the experimental data as well as prepared the figures and manuscript for publication. The theoretical model and simulations of our active matter system have been done in collaboration with Jens Grauer from Heinrich-Heine Universität in Düsseldorf.

3.4 QED Casimir forces vs. critical Casimir forces: Towards solving the stiction problem

There has been immense progress in the field of microfabrication over the last couple decades producing ever decreasing feature sizes while overall increasing the output power of microelectromechanical system (MEMS) and nanoelectromechanical system (NEMS) devices. This is evident by the capabilities of our mobile devices where, for example, commercial CPU chips now possess transistors that are less than 10 nm in size. Early on, during the development of microstructures, researchers discovered that at submicron scales, surfaces can unintentionally adhere together and therefore lead to leaking currents, the collapse of structures, and to device failure [95]. This phenomena, known as stiction, is a common problem during device manufacturing and is caused by surface forces such as capillary, hydrogen bonding, van der Waals, and electrostatic forces. By using different processing techniques, liquid-vapour interfaces could be avoided [101–105] and surface roughening reduced the contact area [106]. Even after fabrication, devices remain prone to stiction and thus anti-stiction surfaces were developed, where the chemical composition of a surface is altered using hydrocarbon or fluorocarbon-based self-assembled monolayers (SAMs) [107–109].

Another source of stiction, the quantum electrodynamic (QED) Casimir force [98], plays an important role for parallel plate geometries as often found in MEMS and NEMS devices. As a result of QED vacuum fluctuations in between two conducting parallel plates, an attractive Casimir force arises, which scales with the inverse of the fourth power of the separation distance and thus becomes relevant in cases where device features are separated by only tens of nanometers [99]. A few theoretical approaches have been proposed to show that Casimir reduction is possible under certain conditions [212–214], but which are difficult to realize in practise and require complex materials [215–218]. Recently, stable Casimir equilibrium of a single and stacked metal particles has been demonstrated experimentally by coating one surface with a low-refractive index thin film [219] or by tuning the concentration of ligands in solution [220]. However, such approaches require a specific choice of permittivity relations between the materials in use and cannot be adjusted dynamically while the system is in operation, thus limiting their application range.

In **Paper VI**, I propose an alternative approach for reversing QED Casimir stiction using a force of similar nature, but based on the density fluctuations of a near-critical binary mixture. I can tune the strength and direction of the induced critical Casimir force (CCF) with temperature and carefully chosen SAMs, respectively.

To proof this, I originally designed a MEMS made of thin metal bridge hanging over a trench (see Fig. 3.6a,b) together with collaborator Ruggero Verre from Chalmers University of Technology. Using holographic interferometry, I would have been able to measure the changes in height of the bridge, if a CCF had been applied. Ideally, I would have been able to demonstrate that I can reverse the bending of a bridge due to gravity and the Casimir attraction. However, due to technical difficulties in the fabrication process, where structures already collapsed, detached or did not bend at all, I decided to switch to a much simpler system, where I would study the effect of both forces on the diffusion
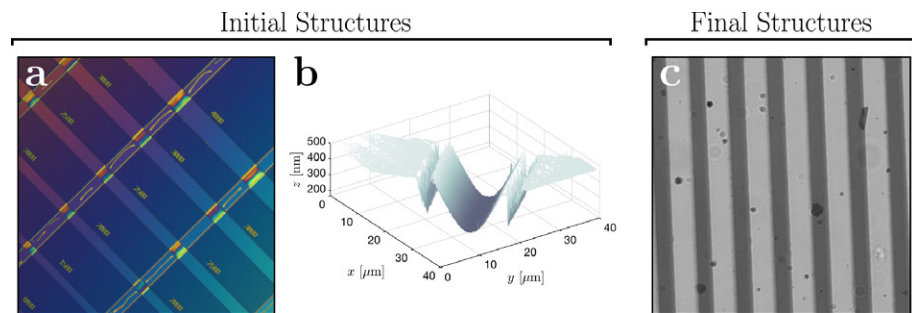
Initial Structures | Final Structures

Figure 3.6: **Comparison of initially produced microstructures vs. final simplified structure. a** Differential interference contrast microscope image of multiple metal microstructures forming bridges over trenches. The bending of each bridge can be seen by the change in contrast and in **b** where an atomic force microscope (AFM) measurement revealed its 3D structure and the quality of the fabrication process. However, due to complications during fabrication such as collapses, or the absence of any bending, I switched to much simpler microstructures in **c**, where Au stripes have been sputtered across a glass surface and where the diffusion of metal flakes reveals more precise information.

of a suspended flake-like particle.

I find that the diffusion constant of a flat metal particle on top of a metal substrate reduces as the Casimir attraction decreases the particle's height above surface. Close to the surface, stronger hydrodynamic interactions hinder its diffusion thus decrease the diffusion constant. When immersed inside a critical binary mixture, tuning the temperature of the system close to its critical point is sufficient to induce CCFs that are strong enough to affect the particle's height above surface. By choosing appropriate wetting properties of the surface using functionalized SAMs, the resulting CCF is either attractive or repulsive, depending on whether particle and surface possess equal or opposite preferences for one of the mixture's phases, respectively. I observe this in a change of the particle's diffusion constant, that decreases when the CCF is attractive and increases when being repulsive.

I use digital video microscopy to track the particle's motion and calculate from the mean squared displacement its diffusion constant. Using hydrodynamic simulations I can reconstruct its height above surface from its diffusion constant alone, and show that I was able to measure changes in height with nanometer precision using this simple indirect method, compared to the more complex analysis involved in holographic interferometry. From the information on the particle's height, I can then calculate the QED Casimir force as well as the CCF and show that close to the critical temperature T_c, the repulsive CCF dominates the particle's motion.

At last, I demonstrate that this principle can be applied to release a trapped particle, whose free diffusion was previously impeded due to Casimir attraction. I have therefore used a simple microstructure consisting of parallel metal stripes sputtered across a glass surface (see Fig. 3.6c). At temperatures below the critical point ($T < T_c$), large metal flakes are trapped on top of the stripes, whereas close to the critical point ($T \approx T_c$), flakes are lifted far enough from its surface such that the attractive QED Casimir force diminishes and flakes freely

diffuse to the glass surfaces. By reversing temperatures ($T \ll T_c$), the particles are eventually trapped again on top of the stripes, and the process can be repeated from the beginning. This simple proof-of-principle device shows that the QED Casimir effect can be compensated for by CCF.

Since critical binary mixtures possess universal quantities, the application range of our proposed solution can be expanded to other sources of stiction too, and might prove valuable as a dynamic method for tuning the thickness of flexible membranes, which are ubiquitous building blocks in MEMS and NEMS.

Contributions to the work:

In **Paper VI**, I have designed and performed the experiments, analyzed the data and prepared manuscript and figures for publication. I have fabricated the microstructures in collaboration with Ruggero Verre at Chalmers University of Technology. The hydrodynamic simulations have been performed in collaboration with Abdallah Daddi-Moussa-Ider from Heinrich-Heine Universität in Düsseldorf.

Conclusions and Future Prospects

After decades of active matter research investigating logical microswimmers and designing artificial active particles, research in this field has produced complex micromachines that self-assemble, perform work, and are able to synchronize with others [139, 221].

In my research, I started with simple microswimmers turning them into powerful microengines using optical tweezers (**Paper I**), and continued investigating their nanoscopic equivalent, whose increased thermal motion I steered with polarized light (**Paper II**). Transitioning from single microswimmers to self-assembled modular molecules, I have shown a rich diversity of motion and how I gained control over their formation using periodic illumination (**Paper III**). I have characterized the molecules' dynamics using a deep-learning algorithm that outperforms standard methods (**Paper IV**). I have then carefully investigated the interactions that occur between such molecules and their nonequilibrium environment, gaining detailed insights into their bidirectional coupling that will help shape new artificial active matter systems (**Paper V**). At last, I studied larger microfabricated structures, in which I have demonstrated that critical fluctuations of a binary mixture can induce forces on microparticles that are strong enough to overcome QED Casimir attraction, and thereby providing an alternative method to avoid stiction in future MEMS and NEMS devices (**Paper VI**).

I have shown that a rich set of motions for self-assembled colloidal systems is achieved by a combination of optical manipulation and a critical phase-separating mixture, in which the colloids are immersed. The critical binary mixture of water–2,6-lutidine has proven valuable; due to the close proximity of its critical point to room temperature, local phase-separations are induced with minimal temperature changes causing concentration gradients that lead to the self-propulsion and self-assembly of particles (**Papers I-IV**). Locally induced phase-separations then provide the nonequilibrium conditions required to study the non-reciprocal interactions between colloids and their local environment (**Paper V**). Moreover, fast demixing and remixing of the binary mixture close to the critical point induces forces, whose strength and sign of direction can be adjusted by temperature and surface modifications (**Paper VI**). Importantly, phase separations are completely reversible and thus can be induced repeatedly,
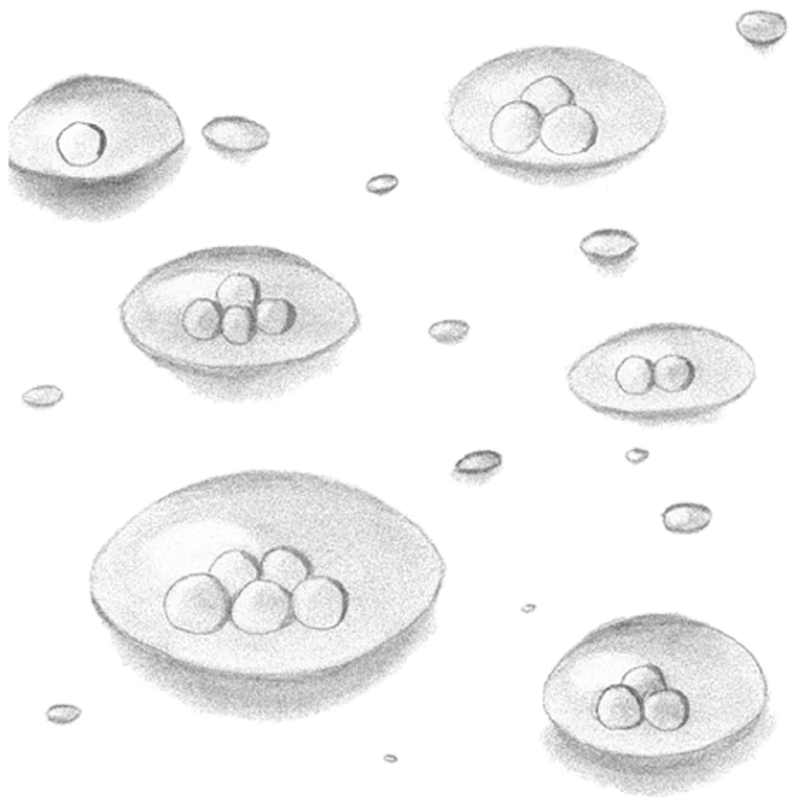
without changing the solution's composition as required, e.g., in systems based on catalytic reactions.

Light, on the other hand, fulfils two purposes in my active matter systems: as a switch for activating and deactivating self-propulsion and self-assembly, and to guide particles through optical manipulation. When light is being strongly focused, or carries angular momentum, optical forces are used to manipulate and control the particle's motion. I have used optical tweezers to trap the particle at fixed location while it performs orbital rotations around the trap center (**Papers I & II**), or to steer the particle's direction of rotation with circular polarized light (**Paper II**). Exploiting the light absorption properties of particles, phase separation is selectively induced by illumination of absorbing particles only, whereas non-absorbing particles remain unaffected (**Papers III-V**). By turning the light source on and off, and precisely tuning its value of intensity, active motion can be initiated, arrested, or adjusted such that for instance the work output of a microengine is maximized (**Paper I**), or only Janus dimers are emerging when the illumination strength is minimal (**Paper III**). Thus, light enables quick heating and cooling of a system of particles, compared to raising or lowering the sample's temperature, allowing for dynamic particle manipulation.

The future of micromachines depends on the development and improvement in the field of microscopic and nanoscopic engines, the self-assembly of individual building blocks to larger structural components, and the minute forces that govern microfabrication processes. But most importantly, it depends on how the insights from each part can be combined and integrated into powerful machines, whose capabilities will expand beyond current technical limitations in surgeries, medical treatments, remediation of the environment and others. This requires researchers to investigate the interplay of multiple active systems in more detail, such as the synchronization of microengines, the molecular details of phoretic interactions driving self-assembly processes, and how surface forces shape the operation of larger microstructures. I will give a more detailed outlook of each field in the following sections.

4.1 Outlook on microengines and nanoengines driven by critical demixing

In **Paper I**, I have presented a self-propelling absorbing microparticle, immersed inside a critical binary mixture, and performing orbital rotations around the focus of a laser beam.

Simulations have shown that the randomly distributed hot spots on the particle's surface induce the local demixing responsible for its motion. While measuring multiple particles in suspension I have seen that not every particle performs equally well under the same experimental conditions, whereas some do not self-propel at all and others escape the optical trap due to strong demixing. This depends on their individual surface distribution of absorbing nanoparticles. Thus, designing specific absorption properties would allow for more controlled rotation rates, which could be fine tuned in such a way that faster and more efficient microengines are produced. This similarly applies to the proposed nanoscopic engine in **Paper II**, where I have found that the random orbital rotations of the nanoparticle are caused by deformities in the particle's shape.

Based on this principle, particles with higher asymmetry such as nanorods or even chiral particles could provide more directed motion as well as perform higher spin rates under circularly polarized light [56, 197]. For the fabrication of such predesigned structures, 3D printing techniques such as two-photon polymerization could be used [222].

Furthermore, I have shown that the microengine's work output depends on laser power and temperature. This work output, however, is only potentially accessible, as the produced work here is immediately dissipated as heat into the environment. Thus, the engine stops operating as soon as the light source is switched off. For future practical applications where engines are part of larger complex micromachines, it remains to be demonstrated that their work can be transformed, for instance by dragging a load attached to the particle, which is especially important for drug delivery applications. More theoretical papers on the work output of engines have been published, but which are far from extensive and still lack experimental realizations [223–225].

Although the work output of a microscopic engine can be improved, it remains small and thus requires further amplification using either lever-like microstructures [226], or by synchronizing and connecting multiple engines in parallel. This has been shown using self-assembled microgears made of catalytic particles or driven by bacteria [139, 221], but not in combination with critical mixtures, where the presence of an attractive or repulsive critical Casimir force can influence the self-assembly of colloids [181]. Future studies could further investigate the influence of potentials on the self-assembly process of colloidal microengines and how it affects their rotational motion and therefore work output.

4.2 Outlook on the self-assembly of colloidal building blocks

In **Paper III**, I have presented an experimental system in which small non-motile building blocks self-assemble into motile colloidal molecules. In **Paper V** I have studied the feedback loop between colloids and their local environment creating active droploids.

The simulation models I have used to reproduce the experimental results allowed me to quantify the molecules' motion and droplet growth in more detail. Nevertheless, they do not provide a microscopic picture and are not based on first-principle, but are rather phenomenological. Molecular dynamics simulations, for instance, could provide more details on the phoretic interactions between absorbing and non-absorbing particles and could be tested experimentally using tracer particles [154, 181].

I have shown in section 3.1 that the principle of self-assembly can be applied to microengines as well, where multiple colloids perform synchronized rotational motion. This is, however, not the only way to organize matter as active colloidal molecules "surfing" on top of a dense layer of non-absorbing colloids could in principle induce crystallization [64], and are therefore a promising tool to manipulate large microsystems beyond individual colloids.

Light, on the other hand, has been an important tool to activate and deactivate the self-assembly of colloidal molecules and droplet formation, and periodic lighting enabled me to control their size. In these experiments, the whole

sample area had been illuminated, while by creating a spatiotemporal pattern of light instead, such as through a spatial light modulator, colloids and their colloidal molecules could be controlled more selectively and dynamically. In combination with hydrogels such as Pluronic F127, the particle's motion could be arrested where light illumination causes gelation of the sample. This could provide an alternative route towards switchable microfluidic devices composed of gates and reversible boundaries. Moreover, this method could be used to fix small organisms such as bacteria in place while keeping their flagella unaffected, permitting new types of studies for investigating their propulsion mechanisms only.

In **Paper IV**, I have proposed a machine-learning algorithm for characterizing the anomalous diffusion coefficient that outperforms standard methods when the amount of available data is restricted and is able to determine when changes of that coefficient occur. Although the algorithm performed well and was able to characterize transitions of passive colloids into active molecules and vice versa, more testing and development is required such that it can be applied to other cases, e.g. for fractional Brownian motion, too. Machine learning algorithms have shown their enormous potential in various active matter applications such as for particle tracking and force field calibration [227, 228], and could be used for instance for the identification of particle motion, or to design more efficient microswimmers and MEMS devices, composed of synchronized and self-assembled microengines.

4.3 Outlook on critical Casimir force in microstructures

Paper VI provides an example of how stiction in MEMS and NEMS devices due to the attractive QED Casimir force can be reversed using the critical Casimir force (CCF), and how this enables a previously trapped metal particle to freely diffuse again. This proof-of-principle system can not only be applied to reverse Casimir attraction, but generally applies to cases of stiction where the distance between surfaces is in the submicron regime.

Since the CCF is tunable by temperature and the surface's wetting properties, it can be used to adjust the cavity size of flexible membranes, which are commonly used as building blocks in MEMS, and thus provide an alternative method for their operation. By using light again instead of adjusting the sample's temperature, even faster changes could be achieved.

CCF have been used to assemble colloidal structures [181], but which remain of passive nature, and more experimental studies are needed to explore the possibilities of using CCF for self-assembled active matter systems such as for colloidal microengines and more. Towards that end, the interplay with other forces such as electrostatic, van der Waals forces requires further theoretical analysis to understand the observed aggregation behaviour.

CHAPTER 5

Compilation of papers

5.1 Paper I: Microscopic engine powered by critical demixing

Attached below is the full paper as published in Physical Review Letters as well as its accompanying Supplementary Information, providing more details on diffusiophoretic motion, the experimental setup and the numerical simulations. In addition we provide experimental results of the temperature dependence on engine operation, as well as control experiments employing smaller particles as well as non-absorbing particles.
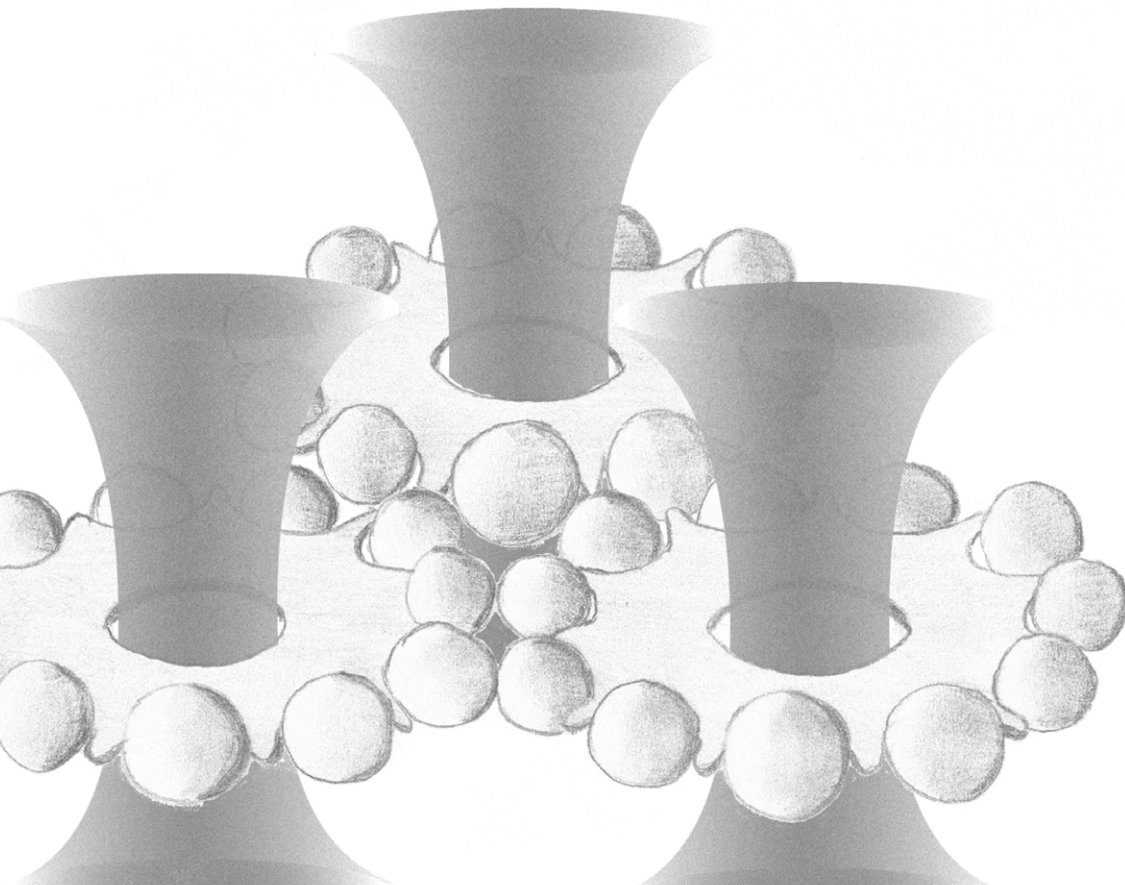
Microscopic Engine Powered by Critical Demixing

Falko Schmidt,[1,2,3] Alessandro Magazzù,[1,2] Agnese Callegari,[2] Luca Biancofiore,[4] Frank Cichos,[3] and Giovanni Volpe[1,2,*]

[1]*Department of Physics, University of Gothenburg, 41296 Gothenburg, Sweden*
[2]*Soft Matter Lab, Department of Physics and UNAM—National Nanotechnology Research Center, Bilkent University,
Ankara 06800, Turkey*
[3]*Peter Debye Institute for Soft Matter Physics, Faculty of Physics and Earth Sciences,
Leipzig University, 04103 Leipzig, Germany*
[4]*Department of Mechanical Engineering, Bilkent University, Ankara 06800, Turkey*

We experimentally demonstrate a microscopic engine powered by the local reversible demixing of a critical mixture. We show that, when an absorbing microsphere is optically trapped by a focused laser beam in a subcritical mixture, it is set into rotation around the optical axis of the beam because of the emergence of diffusiophoretic propulsion. This behavior can be controlled by adjusting the optical power, the temperature, and the criticality of the mixture.

Introduction.—Engines are central to many natural and technological systems as devices capable of converting energy into mechanical work. During the last few decades, a lot of effort has gone into miniaturizing engines for applications in nanoscience and nanotechnology [1,2]. Differently from their macroscopic counterparts, microscopic engines are not completely deterministic, because they operate on energy scales where thermal fluctuations become relevant, and, therefore, need to be treated within stochastic thermodynamics [3,4].

Several approaches have been proposed to realize microscopic engines. Microrotators have been realized by transferring light's orbital and spin momentum to microparticles [5,6] or by employing rotating magnetic fields [7–9]. Prototypes of microscopic heat engines have been realized exploiting the nucleation of vapor bubbles inside silicon microcavities, some with a working volume of only 0.6 mm^3 [10–12]. More recently, optically trapped particles have been employed to reproduce microscopic versions of the Stirling and Carnot cycles, and to study their stochastic thermodynamic properties [13,14]. Also, a microscopic steam engine has been developed based on the periodic generation of cavitation bubbles by an optically trapped particle [15].

Here, we introduce a new mechanism to power a microscopic engine that relies on the local and reversible demixing of a critical mixture surrounding a microparticle. In particular, we show that an absorbing microsphere, suspended in a critical binary mixture and optically trapped, is able to perform rotational motion around the beam waist and to produce work thanks to the local demixing generated by the (slight) increase of the temperature of the solution when the particle approaches the focal point. The properties of this microscopic engine can be controlled by adjusting optical power, ambient temperature,

and mixture criticality. Differently from the artificial microscopic engines mentioned above, the type of microscopic engine we propose here does not rely on the transfer of (angular) momentum from an external source (from circularly polarized light fields [5,6], high-order laser beams [16], or magnetic fields [8]) or on a flow of energy from a hot reservoir to a cold reservoir (microscopic Stirling [13], Carnot [14], and steam engines [15]). On the latter point, while in our realization of this type of engine a small temperature gradient is present to locally induce critical demixing, the presence of such temperature gradient is not generally required by the driving mechanism of this kind of engine, as it can be powered by other sources of critical demixing like pH or concentration gradients.

Results.—We consider an absorbing microsphere (silica with iron-oxide inclusions, $R = 1.24 \pm 0.04$ μm, Supplemental Material Sec. I and SEM image in Supplemental Fig. S1 [17]) optically trapped in a binary water–2,6-lutidine mixture at the critical lutidine mass fraction $c_c = 0.286$ with a lower critical point at $T_c \approx 34\,°C$ [phase diagram in Fig. 1(a)] [18]. When $T < T_c$, the mixture is homogeneous and behaves like a normal fluid. As T approaches T_c [arrow in Fig. 1(a)], density fluctuations emerge. Finally, as T exceeds T_c, the mixture demixes into water-rich and lutidine-rich phases.

The setup consists of an optical tweezers with a near-infrared laser beam ($\lambda = 976$ nm) built on a homemade inverted microscope; the sample-stage temperature (T_0) is measured and stabilized with a feedback controller to ± 3 mK (Supplemental Fig. S2 and Supplemental Sec. II [17]). The particle position is tracked by digital video microscopy at 296 fps. Rhodamine B, which is water soluble and fluoresces around the wavelength of 600 nm, is added to the solution as an indicator of the phase separation
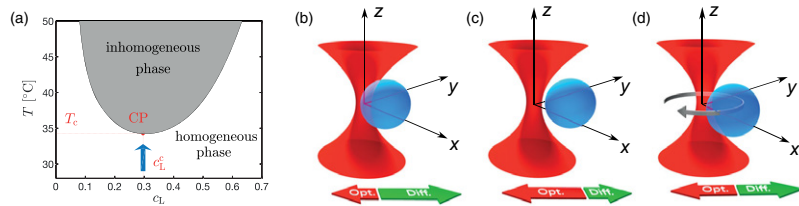
FIG. 1.   Critical engine working principle. (a) Phase diagram of the water–2,6-lutidine mixture featuring a lower critical point (*CP*) at the bottom of the coexistence line (black solid line). The system is prepared at the critical lutidine mass fraction $c_c = 0.286$ and at a temperature T_0 significantly (some degrees) below the critical temperature $T_c \approx 34\,°C$ (arrow). (b)–(d) An optically trapped microsphere experiences a harmonic restoring optical force that attracts it towards the center of the optical trap near the focal spot (red arrows). If the particle absorbs the illumination light, the temperature of the surrounding fluid increases generating an asymmetric temperature profile, which is hotter on the side of the particle closer to the focal spot. Because of the criticality of the mixture, the temperature gradient, in turn, generates a concentration gradient surrounding the particle and, eventually, a diffusiophoretic drift (green arrows). (b) When the particle is close to the focal spot, the diffusiophoretic drift dominates. (c) Instead, when the particle is far from the focal spot, the optical-force-induced drift dominates. (d) The equilibrium position along the radial direction lies where the optical and diffusiophoretic drifts balance each other and depends on the value of T_0 and on the light intensity; here the presence of small asymmetries in the temperature and demixing profile around the particle make the particle rotate around the optical axis (gray arrow).

of water and lutidine: the detected intensity increases with the local relative water content so that a higher intensity close to the particle's hydrophilic surface marks the region where the critical temperature T_c has been exceeded.

The microsphere is attracted by optical forces (red arrows in Figs. 1(b)–1(d) and Supplemental Figs. S3(a)–S3(c) [17]) towards the optical trap center, near the focal spot. Because of the presence of iron-oxide inclusions, the microsphere partly absorbs the trapping light and converts it into heat, producing a local temperature increase (Supplemental Figs. S3(d)–S3(f) [17]). Since the particle side closer to the focal spot is hotter, an asymmetric temperature profile arises in the liquid surrounding the particle. Because of the mixture criticality, this temperature profile induces a concentration profile around the particle (Supplemental Figs. S3(g)–S3(i) [17]). Finally, the presence of this concentration profile generates a diffusiophoretic motion [19] of the particle away from the focal spot (green arrows in Figs. 1(b)–1(d) and Supplemental Figs. S3(a)–S3(c) [17]). Since the heating produced by the particle depends on the light intensity, it decreases as the particle moves radially away from the focal spot and, therefore, also the associated chemical gradient and diffusiophoretic motion decrease. Consequently, the particle settles off-axis, where the optical-force-induced drift is balanced by the diffusiophoretic drift, i.e., where the total radial force acting on the particle is zero (Fig. 1(d) and Supplemental Fig. S3(b) [17]). Importantly, there are small asymmetries in the composition of the particle (Supplemental Fig. S1 [17]) that induce asymmetries in the temperature and demixing profiles and, consequently, make the particle rotate around the optical axis (gray arrow in Fig. 1(d) and Supplemental Fig. S3(b) [17]). Several parameters play a role in the workings of this engine, in particular the trapping beam power P and the ambient temperature T_0. While the critical engine presented here is powered by the

localized critical demixing induced by a small temperature gradient, critical engines can be powered by other sources of critical demixing, e.g., localized pH or concentration gradients, that do not require temperature differences (Supplemental Fig. S5 [17]).

Laser power dependence.—We start by setting the ambient temperature to $T_0 = 26\,°C$. At low laser power ($P = 0.6$ mW at the trap), the particle lingers around the optical trap center [solid line in Fig. 2(a)]. From the trajectory we calculate the velocity drift field, which indicates the direction and magnitude of the particle's velocity as a function of its position, and the differential cross-correlation function $\mathcal{D}_{xy}$, whose value indicates the magnitude of the rotational component of the force fields [20,21] (Supplemental Sec. VI [17]). The resulting drift field [white arrows in Fig. 2(b)] points towards the optical trap center and $\mathcal{D}_{xy}$ [Fig. 2(b)] is negligible, showing that there is no cross-correlation between the movement along the x and y directions, which means that nonconservative forces and therefore rotation are absent (i.e., the rotation rate $\Omega_{xy} \approx 0$ rpm). All these results are consistent with the behavior of an optically trapped particle in a noncritical medium [22]; this is expected because at low power the heating is not enough to approach T_c and, thus, to produce a demixing profile around the particle.

Even increasing the power up to $P = 1.5$ mW, the particle is still constrained around the optical trap center [Fig. 2(d)], the drift field points towards the center of the trap [Fig. 2(e)], and nonconservative forces are negligible [Fig. 2(f)]. Also in this case, $\Omega_{xy} \approx 0$ rpm. This is because the temperature increase due to light absorption is still insufficient to reach T_c.

Increasing the optical power to $P = 2.1$ mW, the temperature of the solution surrounding the particle reaches T_c leading to a local demixing [Fig. 2(g)].
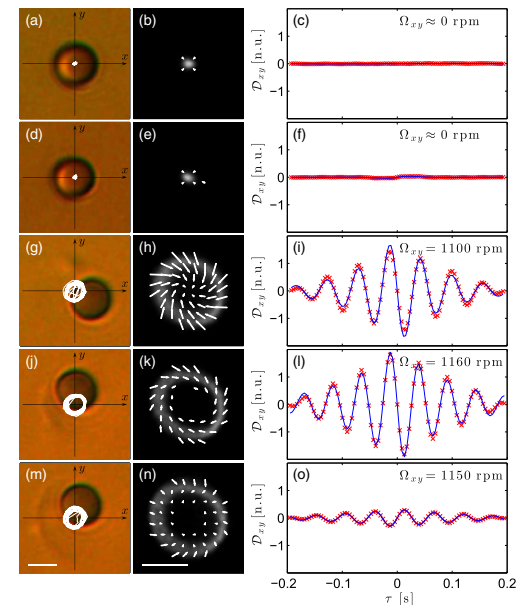
FIG. 2.   Engine performance as a function of laser power. The ambient temperature of the sample is fixed at $T_0 = 26\,°C$, while the laser power at the optical trap is (a)–(c) $P = 0.6$, (d)–(f) 1.5, (g)–(i) 2.1, (j)–(l) 2.7, and (m)–(o) 3.2 mW. [(a),(d),(g),(j),(m)] Bright-field images of the particle with 0.6 s trajectories represented by white solid lines. [(b),(e),(h),(k),(n)] Velocity drift fields (white arrows) and particle position probability distributions (background color, brighter colors represent higher probability density). [(c),(f),(i),(l),(o)] Experimental (red symbols) and fitted (blue solid lines) differential cross-correlation functions $\mathcal{D}_{xy}$ in the xy plane, from which the rotation rate of the particle Ω_{xy} can be obtained as fit parameter (reported in the right column). The white bars in (m) and (n) correspond to 1 μm. See also Supplemental Video 1 [17].

The brighter regions surrounding the particle in Fig. 2(g) correspond to water-rich regions, where the fluorescence of the Rhodamine B dye added to the solution is enhanced. The resulting concentration gradient induces a diffusiophoretic drift that pushes the particle radially outwards from the center, where it reaches a radial equilibrium position and starts rotating inside a toroidal region around the optical axis [Figs. 1(b)–1(d)]. This rotational motion can be seen from the particle trajectory [solid line in Fig. 2(g)] and, more quantitatively, from the drift field [white arrows in Fig. 2(h)], the particle probability distribution [background shading in Fig. 2(h)], and $\mathcal{D}_{xy}$ [Fig. 2(i)], which shows the sinusoidal behavior characteristic of rotational force fields. The resulting rotation of the particle is $\Omega_{xy} = 1100$ rpm. The rotational motion of the particle is due to structural asymmetries in the particle itself

(e.g., in the distribution of the iron oxide and in its surface properties, Supplemental Fig. S1 [17]) and in the ensuing temperature gradient profile. Sometimes it can be observed that the rotation stops, the particle moves towards the center, and subsequently restarts rotating in the opposite direction; this behavior occurs whenever the Brownian fluctuations overcome the diffusiophoretic drift acting on the particles and orient the particle towards the optical trap center.

Increasing the power even further to $P = 2.7$ mW, the particle performs constant revolutions around the optical trap center at $\Omega_{xy} = 1160$ rpm without changing its direction during the measurement. Its radial equilibrium position reaches about 1 μm [Fig. 2(j)]. The resulting drift field shows clearly a steady clockwise rotation [Fig. 2(k)] and $\mathcal{D}_{xy}$ increases its amplitude [Fig. 2(l)]. This rotation rate is comparable with those reached by micropumps and microrotors driven by optical vortices [23] while using only milliwatts (in contrast to several watts) of laser power.

As the power is further increased to $P = 3.2$ mW, the particle not only rotates around but passes occasionally through the optical trap center and changes randomly its direction of rotation [Fig. 2(m)]. We determine $\Omega_{xy} = 1120$ rpm. The higher laser power makes the temperature of the critical mixture surrounding the particle significantly exceed T_c, leading to a disruption of the balance between optical and diffusiophoretic drifts. Consequently, the particle is attracted towards the optical trap center before being pushed radially outwards by diffusiophoresis and returning to rotational motion. This leads to a partial disruption of the rotational component of the drift field [Fig. 2(n)] and to a decrease of $\mathcal{D}_{xy}$ [Fig. 2(o)].

When the power is further increased, the diffusiophoretic motion exceeds the optical trapping potential and therefore the particle escapes from the optical trap.

Ambient temperature dependence.—Fixing $P = 2.7$ mW, the critical engine operation as a function of T_0 is optimal at $T_0 = 26\,°C$, where the particle steadily rotates around the optical trap center at $\Omega_{xy} = 1160$ rpm (Supplemental Sec. IV and Supplemental Fig. S4 [17]).

Mixture criticality dependence.—To explore the dependence on the mixture criticality, we repeated the measurements at an off-critical lutidine mass fraction of 0.236 as a function of P and T_0. We did not observe any rotational behavior even at high power ($P > 6$ mW) and therefore concluded that the mixture criticality is an essential ingredient for the engine to work. Indeed, when the mixture is off-critical, water and lutidine undergo a more complex cooling and remixing process than when it is critical [24]; in particular, the presence of latent heat introduces a hysteresis cycle that slows down the remixing process when the temperature of the mixture drops below the binodal line (Supplemental Fig. S5(a) [17]). This prevents the engine from working because it is eventually obstructed by a bubble rich in one of the two phases created and stabilized around the particle so that the particle is
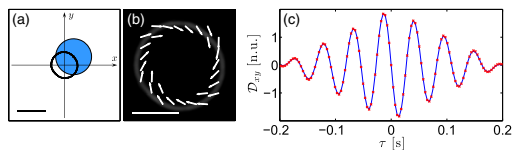
FIG. 3. Simulation of a critical engine. (a) Particle (blue circle) with corresponding 0.6 s trajectory (black line). The black bar corresponds to 1 μm. (b) Drift field (white arrows) and particle position distribution (background color, brighter colors represent higher probability density). The white bar corresponds to 1 μm. (c) Differential cross-correlation function $\mathcal{D}_{xy}$ in the xy plane, from which the rotation rate is estimated to be $\Omega_{xy} = 1200$ rpm.

symmetrically surrounded by a single-phase liquid that inhibits diffusiophoretic propulsion so that the particle is optically trapped as usual in a homogenous fluid.

Particle size dependence.—The critical engine works also for smaller particles ($R = 0.49 \pm 0.03$ μm, Supplemental Figs. S6 and S7 [17]). The behavior is similar and the rotational rate higher ($\Omega_{xy} = 4600$ rpm at $P = 1.5$ mW and $T_0 = 23\,°\text{C}$, Supplemental Sec. V [17]). Furthermore, the critical engine working principle can be scaled down to the nanoscale as long as the slip velocity on the particle surface scales $\propto R^{-1}$; however, we expect the smooth rotational behavior to be disrupted by the increase of translational and rotational Brownian diffusion (Supplemental Secs. III and V [17]).

Simulations.—To gain a deeper understanding of the mechanism responsible for the behavior observed experimentally, we also investigate the dynamics of the system numerically (Supplemental Sec. VII [17]). We consider an absorbing hydrophilic particle held by an optical trap. We assume that the particle is slightly asymmetric in its shape and material properties (nonuniform absorption and surface roughness). The optical forces are calculated using generalized Mie theory [22]. The temperature increase in the surroundings of the particle is calculated by determining the absorption of the laser light by the iron-oxide inclusions [25] and using the stationary heat equation to estimate the ensuing heat conduction [26]. This temperature increase causes a local demixing of the binary solution near the particle, resulting in an increase of the local concentration of water, because of the hydrophilicity of the particle's surface. The diffusiophoretic drift and torque acting on the particle are then calculated from the slip velocity field generated around the particle [19]; we remark that an alternative model that takes into account additionally advection has been proposed [27] and has been found to be in agreement with experiments in viscoelastic critical media [28]. Figure 3(a) shows a typical trajectory obtained from simulations, which features the rotational motion at a rotational rate $\Omega_{xy} = 1200$ rpm, in quantitative agreement with the experiments [compare with Figs. 2(j) and S4(g)]; the corresponding drift field [Fig. 3(b)] and $\mathcal{D}_{xy}$ [Fig. 3(c)]
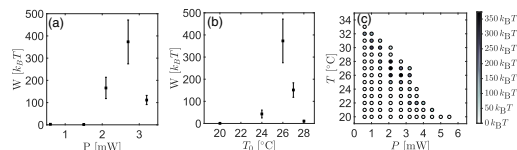

FIG. 4. Work dependence on laser power and ambient temperature. Work W as a function of (a) laser power P ($T_0 = 26\,°\text{C}$) and (b) ambient temperature T_0 ($P = 2.7$ mW). (c) Work as a function of P and T_0. The circles represent the performed measurements. W features a maximum for $P = 2.7$ mW and $T_0 = 26\,°\text{C}$.

are also in quantitative agreement with the experiments [compare with Figs. 2(k) and S4(h), and with Figs. 2(l) and S4(i), respectively].

Performance.—The rotational motion of the particle around the beam waist is intrinsically nonconservative and corresponds to a rotational force field. Through the analysis of $\mathcal{D}_{xy}$ (Supplemental Sec. VI [17]), we evaluate the work performed by the particle during a single rotation about the z axis as [29]

$$W = 2\pi \frac{\Omega_{xy}}{\omega_\rho} k_B T, \qquad (1)$$

where W is directly proportional to the rotation rate Ω_{xy} associated with the nonconservative force field and inversely proportional to the transverse relaxation frequency ω_ρ of the optical trap. The efficiency of the engine is given by $\eta_{\text{eff}} = [(\Omega_{xy}W)/P]$. The value of W is plotted as a function of P and T_0 in Fig. 4. The maximum of $W = 373k_BT$ and $\eta_{\text{eff}} = 1.16 \times 10^{-14}$ is reached for $P = 2.7$ mW and $T_0 = 26\,°\text{C}$ at $\Omega_{xy} = 1160$ rpm. The amount of work performed by this critical engine exceeds that of colloidal heat engines such as the Brownian Carnot engine ($W_{\text{max}} = 5k_BT$) [14] and the micrometer-sized heat engine ($W_{\text{max}} = 0.3k_BT$) [13]. Its efficiency is comparable to the efficiency of a rotating object driven by the transfer of the angular momentum from a circularly polarized beam ($\eta_{\text{eff}} \sim 10^{-14}$) [6]. Even though in our case the work done by the particle is immediately dissipated as heat into the fluid, it remains in principle accessible, e.g., by attaching a load to the particle.

Discussion.—We have realized a micron-sized critical engine that can extract work from the criticality of a system. In our realization, the efficiency of the critical engine can be tuned by adjusting the laser power, the ambient temperature, or the mixture criticality. Compared to other micron-sized engines developed in the last years [13–15], this critical engine has the advantages of not relying on the transfer of external angular momentum and of working at temperatures close to room temperature. It is in principle possible to control the sense of rotation of the critical engine by designing chiral particles with a controllable absorption profile. The work performed per cycle exceeds

that of other microscopic heat engines by orders of magnitude [13,14]; its efficiency is comparable to micron-sized engines driven by transfer of optical (angular) momentum [16], while much higher efficiencies can be achieved with alternative mechanisms such as the thermocapillary effect [30]. Moreover, with only a few milliwatts of laser power the engine reaches rotation rates of 1200 rpm for 1.24 μm-radius particles and of 4600 rpm for 0.49 μm-radius particles; these values are much larger than those of micron-sized heat engines, which reach rates of about 10 rpm [13]. Furthermore, in experiments with optical vortices similar rotation rates can only be achieved at powers on the order of watts [23,31,32].

Importantly, since many natural and artificial systems are tuned near criticality, the critical engine working principle can be exploited in diverse applications and used to explain how natural phenomena work (e.g., molecular motors acting within a cellular membrane). In fact, it can exploit any order parameter tuned near criticality in a given system, e.g., pH-value or particle concentration [33]. This also means that the critical engine operation can arise also in the absence of temperature gradients, as long as other gradients capable of tuning the system criticality are present. Since phase separations have been already widely found inside the human body [34,35] and some of them are known to be sources of diseases such as protein condensation [36], new biocompatible engines can be designed based on our critical engine that could be able to perform medical surgeries noninvasively such as the treatment of arteriosclerosis.

---

*giovanni.volpe@physics.gu.se

[1] W. R. Browne and B. L. Feringa, Nat. Nanotechnol. **1**, 25 (2006).
[2] L. K. E. A. Abdelmohsen, F. Peng, Y. Tu, and D. A. Wilson, J. Mater. Chem. B **2**, 2395 (2014).
[3] U. Seifert, Rep. Prog. Phys. **75**, 126001 (2012).
[4] I. A. Martínez, É. Roldán, L. Dinis, and R. A. Rica, Soft Matter **13**, 22 (2017).
[5] N. B. Simpson, K. Dholakia, L. Allen, and M. J. Padgett, Opt. Lett. **22**, 52 (1997).
[6] M. E. J. Friese, T. A. Nieminen, N. R. Heckenberg, and H. Rubinsztein-Dunlop, Nature (London) **394**, 348 (1998).
[7] S. L. Biswal and A. P. Gast, Anal. Chem. **76**, 6448 (2004).
[8] A. Ghosh and P. Fischer, Nano Lett. **9**, 2243 (2009).
[9] B. Eickenberg, F. Wittbracht, P. Stohmann, J.-R. Schubert, C. Brill, A. Weddemann, and A. Hutten, Lab Chip **13**, 920 (2013).
[10] J. Kao, X. Wang, J. Warren, J. Xu, and D. Attinger, J. Micromech. Microeng. **17**, 2454 (2007).
[11] C. Lee, M. Liamini, and L. G. Frechette, J. Microelectromech. Syst. **20**, 326 (2011).
[12] S. Percy, C. Knight, S. McGarry, A. Post, T. Moore, and K. Cavanagh, *Thermal Energy Harvesting for Application at MEMS Scale*, Springer Briefs in Electrical and Computer Engineering, 1st ed. (Springer-Verlag New York, 2014).
[13] V. Blickle and C. Bechinger, Nat. Phys. **8**, 143 (2012).
[14] I. A. Martinez, E. Roldan, L. Dinis, D. Petrov, J. M. R. Parrondo, and R. A. Rica, Nat. Phys. **12**, 67 (2016).
[15] P. A. Quinto-Su, Nat. Commun. **5**, 5889 (2014).
[16] H. He, N. R. Heckenberg, and H. Rubinsztein-Dunlop, J. Mod. Opt. **42**, 217 (1995).
[17] See Supplemental Material at http://link.aps.org/supplemental/10.1103/PhysRevLett.120.068004 for recorded brightfield images of the engine as a function of laser power.
[18] C. A. Grattoni, R. A. Dawe, C. Y. Seah, and J. D. Gray, J. Chem. Eng. Data **38**, 516 (1993).
[19] A. Würger, Phys. Rev. Lett. **115**, 188304 (2015).
[20] G. Volpe and D. Petrov, Phys. Rev. Lett. **97**, 210603 (2006).
[21] G. Volpe, G. Volpe, and D. Petrov, Phys. Rev. E **76**, 061118 (2007).
[22] P. H. Jones, O. M. Maragò, and G. Volpe, *Optical Tweezers: Principles and Applications* (Cambridge University Press, Cambridge, England, 2015).
[23] K. Ladavac and D. G. Grier, Opt. Express **12**, 1144 (2004).
[24] E. D. Siggia, Phys. Rev. A **20**, 595 (1979).
[25] E. J. G. Peterman, F. Gittes, and C. F. Schmidt, Biophys. J. **84**, 1308 (2003).
[26] D. Rings, R. Schachoff, M. Selmke, F. Cichos, and K. Kroy, Phys. Rev. Lett. **105**, 090604 (2010).
[27] S. Samin and R. van Roij, Phys. Rev. Lett. **115**, 188305 (2015).
[28] J. R. Gomez-Solano, A. Blokhuis, and C. Bechinger, Phys. Rev. Lett. **116**, 138301 (2016).
[29] G. Pesce, G. Volpe, A. Imparato, G. Rusciano, and A. Sasso, J. Opt. **13**, 044006 (2011).
[30] C. Maggi, F. Saglimbeni, M. Dipalo, F. De Angelis, and F. Di Leonardo, Nat. Commun. **6**, 7855 (2015).
[31] S. H. Tao, X. C. Yuan, J. Lin, X. Peng, and H. B. Niu, Opt. Express **13**, 7726 (2005).
[32] D. G. Grier, Nature (London) **424**, 810 (2003).
[33] E. Tagliazucchi, D. R. Chialvo, M. Siniatchkin, E. Amico, J.-F. Brichant, V. Bonhomme, Q. Noirhomme, H. Laufs, and S. Laureys, J. R. Soc. Interface **13**, 20151027 (2016).
[34] I. Digel, C. Maggakis-Kelemen, K. F. Zerlin, P. Linder, N. Kasischke, P. Kayser, and G. M. Artmann, Biophys. J. **91**, 3014 (2006).
[35] X. M. Liu, L. S. Wang, L. Wang, J. Huang, and C. He, Biomaterials **25**, 5659 (2004).
[36] W. M. Jacobs and D. Frenkel, Biophys. J. **112**, 683 (2017).

Microscopic Engine Powered by Critical Demixing

Supplementary Information

Falko Schmidt,[1,2,3] Alessandro Magazzù,[1,2] Agnese Callegari,[2]

Luca Biancofiore,[4] Frank Cichos,[3] and Giovanni Volpe[1,2,*]

[1]*Department of Physics, University of Gothenburg, 41296 Gothenburg, Sweden*

[2]*Soft Matter Lab, Department of Physics and*

UNAM – National Nanotechnology Research Center,

Bilkent University, Ankara 06800, Turkey

[3]*Peter-Debye-Institute for Soft Matter Physics,*

Faculty of Physics and Earth Science,

University of Leipzig, 04103 Leipzig, Germany

[4]*Department of Mechanical Engineering,*

Bilkent University, Ankara 06800, Turkey

_____

* giovanni.volpe@physics.gu.se

I. ABSORBING PARTICLES

The particles used in our experiments are magnetic silica particles (radius $R = 1.24 \pm 0.04\,\mu$m, produced by Microparticles GmbH). These particles are made of porous silica into which iron oxide nanoparticles are let to diffuse, and they are coated with an external layer of silica. A typical SEM image of such a particle can be seen in supplementary Fig. S1. During production, clusters of iron oxide occur at the surface changing the particle's absorption properties locally. Every single particle possesses a unique distribution of iron oxide, which is typically asymmetric and gives rise to the asymmetric diffusiophoretic drift responsible for the particle's orbital motion.

II. SETUP

The schematic of the setup is shown in supplementary Fig. S2. The optical tweezers is built on a homemade inverted microscope. The trapping laser beam ($\lambda = 976\,$nm) is focused through an oil-immersion objective (100×, NA = 1.30).

The sample chamber is prepared using a microscopic slide with a cavity (liquid volume $V = 30\,\mu$l) and sealed using a coverslip. The whole sample is temperature-stabilized using a copper-plate heat exchanger coupled to a water circulating bath (T100, Grant Instruments) with $\pm 50\,$mK temperature stability. Two Peltier elements (TEC3-6, Thorlabs) placed on the trapping objective permit us to fine-tune ($\pm 3\,$mK) the temperature using a feedback controller (TED4015, Thorlabs).

A second laser ($\lambda = 532\,$nm) is used to illuminate the sample through a 20× objective (NA = 0.45) and excites the fluorescent dye Rhodamine B (C.I. 45170, Merck) dissolved in the solution. The emission peak of this dye is at $\lambda \approx 600\,$nm. A CMOS camera (DCC1645C, Thorlabs) records the light emitted by the sample at a frame rate of 296 fps. We have verified that the addition of Rhodamine B does not alter the critical properties of the solution.

The recorded videos are analyzed using standard digital video microscopy algorithms to obtain the three-dimensional position of the particle. We have found that the particle predominantly moves in the xy-plane. We have therefore neglected the information about the z-position in our analysis.

III. DIFFUSIOPHORESIS

Diffusiophoresis is the self-propulsion of particles along a concentration gradient. In our case, this concentration gradient is triggered by a local increase in temperature ΔT that leads to a local demixing of the binary solution and hence to a concentration gradient $\Delta \phi$ (as depicted in Fig. S3). The boundary between mixed and demixed regions experiences a nonuniform pressure as well as a steady current flow, which results into a slip velocity $\mathbf{v}_s(\mathbf{r}) \propto \Delta \phi$. Depending on the particle's wetting properties (hydrophilic or hydrophobic) the sign of the resulting net motion of the particle changes (more details can be found in Ref. [1]). This behavior can be in principle scaled down to the nanoscale as long as $\mathbf{v}_s(\mathbf{r}) \propto R^{-1}$.

IV. AMBIENT TEMPERATURE DEPENDENCE OF CRITICAL ENGINE OPERATION

We fix the laser power at $P = 2.7\,\mathrm{mW}$ and study the behavior of the critical engine as a function of the ambient temperature T_0.

At $T_0 = 20°\mathrm{C}$, the system behaves as a standard optical trap: the particle trajectory lingers near the center of the optical trap (solid line in Suppl. Fig. S4a); the drift field points towards the optical trap center (white arrows in Suppl. Fig. S4b); $\mathcal{D}_{xy}$ is negligible (Suppl. Fig. S4c); and $\Omega \approx 0\,\mathrm{rpm}$.

As T_0 is increased to 24°C, the particle explores a larger area around the center of the optical trap (Suppl. Fig. S4d) and rotational forces start emerging as shown by the drift field (Suppl. Fig. S4e) and by $\mathcal{D}_{xy}$ (Suppl. Fig. S4f). The corresponding average rotation of the particle is $\Omega_{xy} = 1060\,\mathrm{rpm}$. The diffusiophoretic drift generated by the particle is however not large enough to set the particle into constant rotation around the optical axis, as can be seen from the fact that the particle trajectory occasionally crosses the center of the trap (solid line in Suppl. Fig. S4d).

At $T_0 = 26°\mathrm{C}$, the particle steadily rotates around the optical trap center (Suppl. Fig. S4g), leading to a well-defined rotational drift field (Suppl. Fig. S4h) and to an increase of $\mathcal{D}_{xy}$ (Suppl. Fig. S4i). The corresponding rotation rate is $\Omega_{xy} = 1160\,\mathrm{rpm}$.

At even higher temperatures (i.e. $T_0 = 27°\mathrm{C}$ and $T_0 = 28°\mathrm{C}$), the particle starts to occasionally change its orientation passing through the optical trap center before returning to its revolutionary motion (Suppl. Figs. S4j,m). With increasing T_0, the drift field looses the rotational component (Suppl. Figs. S4k,n) and $\mathcal{D}_{xy}$ decreases (Suppl. Figs. S4l,o), which are clear signatures of decreasing rotational forces. The corresponding average rotation rates are significantly affected by the frequent changes of direction leading to $\Omega_{xy} \approx 0\,\mathrm{rpm}$.

A further increase in temperature leads to the particle being pushed away from the optical trap by the presence of overwhelming diffusiophoretic drifts.

V. PARTICLE SIZE DEPENDENCE OF CRITICAL ENGINE OPERATION

We have also demonstrated experimentally that the critical engine works for particles of different sizes. In particular, we reproduced the critical engine operation as function of laser power and ambient temperature using a smaller particle of radius $R = 0.49 \pm 0.03\,\mu\mathrm{m}$.

In Fig. S6, the engine performance is studied for a particle of radius $R = 0.49\,\mu\mathrm{m}$ at a fixed ambient temperature of $T_0 = 21°\mathrm{C}$ as a function of the laser power P (compare with Fig. 2 for $R = 1.24\,\mu\mathrm{m}$). When $P = 0.6\,\mathrm{mW}$, the particle is just optically trapped (Fig. S6a-c), and its rotation rate is $\Omega_{xy} = 0\,\mathrm{rpm}$. When the power is increased to $P = 1.5\,\mathrm{mW}$, the particle performs rotations around the trapping laser beam (Fig. S6d-f) with a rotation rate $\Omega_{xy} = 4020\,\mathrm{rpm}$. At even higher power ($P = 2.7\,\mathrm{mW}$), the particle is randomly passing through the center of the laser beam (Fig. S6g-i), leading to a decrease of its rotation rate ($\Omega_{xy} = 2860\,\mathrm{rpm}$).

In Fig. S7, the engine performance is studied for a particle of radius $R = 0.49\,\mu\mathrm{m}$ at fixed power $P = 1.5\,\mathrm{mW}$ as a function of the ambient temperature T_0 (compare with Fig. S4 for $R = 1.24\,\mu\mathrm{m}$). At $T_0 = 19.5°\mathrm{C}$, the particle is just optically trapped and features a small rotation with $\Omega_{xy} = 1200\,\mathrm{rpm}$ (Fig. S7a-c). At $T_0 = 23°\mathrm{C}$ (Fig. S6d-f), it performs continuous rotations at similar rates as in Fig. S5f ($\Omega_{xy} = 4600\,\mathrm{rpm}$). At an even higher temperature ($T_0 = 27°\mathrm{C}$), the particle stops rotating due to larger demixing on the particles surface and its motion outside the optical trap becomes completely uncorrelated (Fig. S6g-i).

Comparing the behavior of the particles with $R = 0.49\,\mu\mathrm{m}$ (Figs. S6 and S7) and $R = 1.24\,\mu\mathrm{m}$ (Figs. 2 and S4), the smaller particle reaches a higher rotation rate of 4600 rpm, but its differential cross correlation function decays faster, since for smaller particles thermal fluctuations become more dominant. Moving towards the nanoscale, for even smaller

particles we expect the smooth rotational behavior of the critical engine to be disrupted by the increase of translational and rotational Brownian diffusion.

VI. DATA ANALYSIS

Each trajectory is analyzed by calculating the corresponding drift field, differential cross-correlation function $\mathcal{D}_{xy}$, rotation rate Ω_{xy}, and work W.

The velocity drift fields are derived from the measured trajectory as

$$\mathbf{v}(\mathbf{r}) = \frac{1}{\Delta t} \langle \mathbf{r}_{n+1} - \mathbf{r}_n | \mathbf{r}_n \approx \mathbf{r} \rangle, \tag{1}$$

where $\mathbf{r}_n$ is the position of the particle in the xy-plane and Δt is the time interval between subsequent positions of the particle. The calculated magnitude and direction of the local velocity is indicated by white arrows in Figs. 2, S4, S6 and S7.

The differential cross-correlation function $\mathcal{D}_{xy}(\tau)$ of the particle motion is calculated as [2, 3]:

$$\mathcal{D}_{xy}(\tau) = C_{xy}(\tau) - C_{yx}(\tau), \tag{2}$$

where $C_{xy}(\tau) = \frac{\langle x(t)\, y(t+\tau) \rangle}{\sqrt{\langle x(t)^2 \rangle \langle y(t)^2 \rangle}}$ and $C_{yx}(\tau) = \frac{\langle y(t)\, x(t+\tau) \rangle}{\sqrt{\langle x(t)^2 \rangle \langle y(t)^2 \rangle}}$. The theoretical expression of $\mathcal{D}_{xy}(\tau)$ for a trapped spherical particle rotating in a plane can be obtained from the Langevin equation in a non-homogeneous force field [3] as

$$\mathcal{D}_{xy}(\tau) = 2D\, \frac{e^{-\omega_\rho |\tau|}}{\omega_\rho} \sin\left(\Omega_{xy} \tau \right), \tag{3}$$

where D is the diffusion coefficient, ω_ρ is the radial relaxation frequency of the particle in the optical trap (obtained from the autocorrelation function [4]), and Ω_{xy} is the rotational frequency of the particle in the xy-plane. The value of Ω_{xy} is obtained by fitting the experimental $\mathcal{D}_{xy}(\tau)$ (Eq. (2)) to the theoretical expression in Eq. (3). The resulting hydrodynamic viscous torque is then:

$$\overline{\mathbf{\Gamma}}_{xy} = \overline{\mathbf{r} \times \mathbf{F}_{\mathrm{drag}}} = \gamma\, \overline{\mathbf{r} \times \mathbf{r} \times \Omega_{xy}} = \gamma\, \Omega_{xy}\, \sigma_{xy}^2\, \hat{\mathbf{z}}, \tag{4}$$

where $\mathbf{r}$ is the position of the particle, $\gamma = 6\pi\eta R$ is the friction coefficient, defined by Stokes law and related to the medium viscosity η and to the particle's radius R, and σ_{xy}^2 is the variance of the particle's position in the plane orthogonal to the torque.

The work performed during a single rotation about the z-axis can be expressed as [5]:

$$W = \int_0^{2\pi} \overline{\Gamma}_{xy}\, d\theta = 2\pi\, \frac{\Omega_{xy}}{\omega_\rho}\, k_{\mathrm{B}} T. \tag{5}$$

VII. NUMERICAL SIMULATIONS

The motion of the particle is simulated using a standard finite-difference algorithm based on a three-dimensional Langevin equation describing the motion of the particle under the action of Brownian motion, optical forces, and diffusiophoretic drifts and torques [4]. The particle is modeled as a silica microsphere (radius $R = 1.24\ \mu$m) with iron-oxide inclusions (25% of total weight) distributed inhomogeneously near the surface of the particle. The optical force on the particle is calculated using generalized Mie theory (particle refractive index $n_{\mathrm{p}} = 1.46$, medium refractive index $n_{\mathrm{m}} = 1.38$ [6]) and assuming a linearly polarized Gaussian beam (wavelength $\lambda_0 = 976$ nm) focused through a high-NA objective (NA = 1.30) [4]. The temperature increase as a function of position, $\Delta T(\mathbf{r})$, is obtained using Fourier's law of heat conduction [7]:

$$\nabla^2 (\Delta T(\mathbf{r})) = -\frac{\alpha}{C} I(\mathbf{r}), \tag{6}$$

where $I(\mathbf{r})$ is the light intensity, α is the absorption coefficient of iron (for iron $\alpha = 2.43 \cdot 10^7\ \mathrm{m}^{-1}$, we assume no absorption in silica and water–2,6-lutidine), and C is the thermal conductivity (for iron $C = 73\ \mathrm{W m^{-1} K^{-1}}$, for silica $C = 1.4\ \mathrm{W m^{-1} K^{-1}}$, for water–2,6-lutidine $C = 0.39\ \mathrm{W m^{-1} K^{-1}}$). Where $T_0 + \Delta T(\mathbf{r}) > T_{\mathrm{c}}$, a concentration gradient $\Delta\phi(\mathbf{r})$ is induced, which, in proximity of the critical temperature T_{c}, is [1]

$$\Delta\phi(\mathbf{r}) = \sqrt{\frac{T_0 + \Delta T(\mathbf{r}) - T_{\mathrm{c}}}{K}}, \tag{7}$$

where K is a constant. The concentration gradient $\Delta\phi(\mathbf{r})$ generates a slip velocity field $\mathbf{v}_{\mathrm{s}}(\mathbf{r})$ in the layer around the particle. The diffusiophoretic drift is then $\mathbf{v}_{\mathrm{p}} = -\langle \mathbf{v}_{\mathrm{s}}(\mathbf{r}) \rangle$ [1], while the diffusiophoretic torque is $\mathbf{T}_{\mathrm{ph}} = \langle \mathbf{r}_{\mathrm{s}} \times (-\gamma \mathbf{v}_{\mathrm{s}}) \rangle$, where $\mathbf{r}_{\mathrm{s}}$ is the vector connecting the center of mass of the particle to the particle's surface. We remark that Ref. [8] suggests that at a high velocity of the particle ($> 10\ \mu\mathrm{m\,s^{-1}}$) the effect of advection around the particle plays a significant role and alters the motion of the particle compared to the model in Ref. [1]; nevertheless we have found quantitative agreement between our simulations based on Ref. [1] without advection and our experiments, suggesting that advection can be neglected in this case.

A. Supplementary Video 1

Engine performance as a function of laser power. Recorded brightfield images of the particle at a frame rate of 296 Hz. The ambient temperature of the sample is fixed at $T_0 = 26°C$, while the laser power at the optical trap is increased stepwise. See also Fig. 2.

B. Supplementary Video 2

Engine performance as a function of ambient temperature. Recorded brightfield images of the particle at a frame rate of 296 Hz. The laser power at the optical trap is fixed at $P = 2.7$ mW, while the ambient temperature of the sample is increased stepwise. See also supplementary Fig. S4.

C. Supplementary Video 3

Simulation of a critical engine. (left) An absorbing particle in a critical mixture rotating around the center of an optical trap, (middle) corresponding temperature profiles (the isotemperature lines are spaced by 5 K), and (right) concentrations profiles (the iso-concentration lines are spaced by 0.04) in the xy-plane ($z = 0$). See also supplementary Fig. S3.
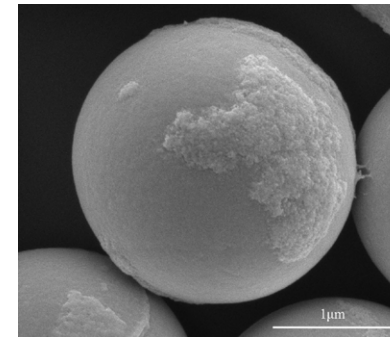
FIG. S1: Image of an absorbing microsphere acquired by scanning electron microscopy (SEM). The particle is a silica microsphere with radius $R = 1.24 \pm 0.04 \,\mu$m and iron oxide inclusions. The rough regions on the surface of the microsphere correspond to iron oxide clusters.
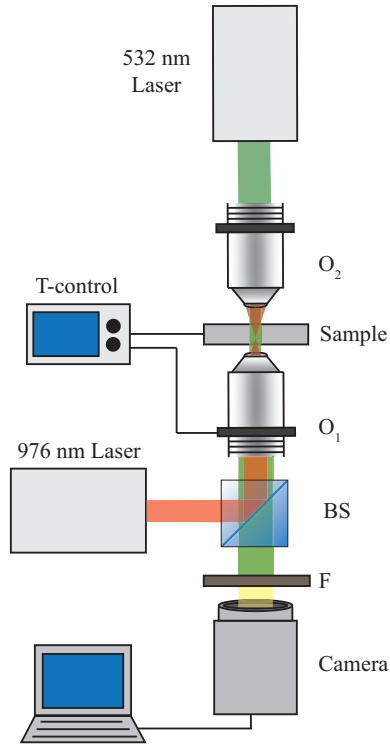
FIG. S2: Schematic of the experimental setup. The trapping laser ($\lambda = 976\,\text{nm}$) is reflected by the dichroic beam splitter (BS) onto objective O_1 ($100\times$, NA $= 1.30$), which focuses the light inside the temperature-stabilized sample. The whole sample is illuminated by a defocused green laser through objective O_2 ($20\times$, NA $= 0.45$); the forward-scattered light is filtered (filter F) to eliminate the excitation laser light and projected onto a camera.
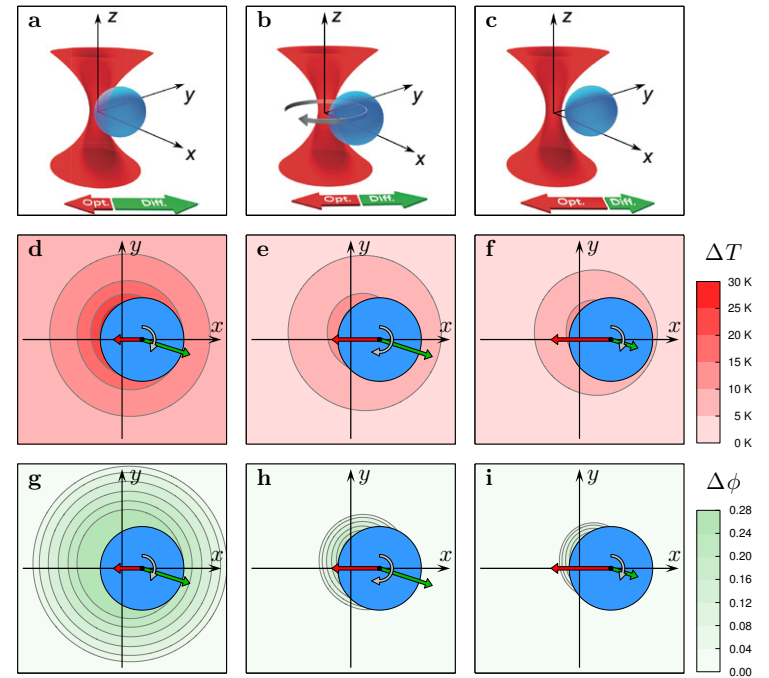

FIG. S3: Simulation of a critical engine. (a-c) Absorbing particle in a critical mixture held at various radial distances from the center of an optical trap, and corresponding (d-f) temperature profiles (the isotemperature lines are spaced by $5\,\text{K}$) and (g-i) concentrations profiles (the isoconcentration lines are spaced by 0.04) in the xy-plane ($z = 0$). As the distance from the center of the trap increases, the drift due to the optical forces (red arrows) increases and the diffusiophoretic drift (green arrows) decreases. The presence of small asymmetries in the temperature and demixing profile around the particle make it rotate around the optical axis; the corresponding tangential force (gray arrow) is maximized at the equilibrium configuration where the optical-force-induced drift balances the diffusiophoretic drift. (a), (b), and (c) correspond to Fig. 1(a), 1(c), and 1(b) respectively. See also the corresponding supplementary Video 3.
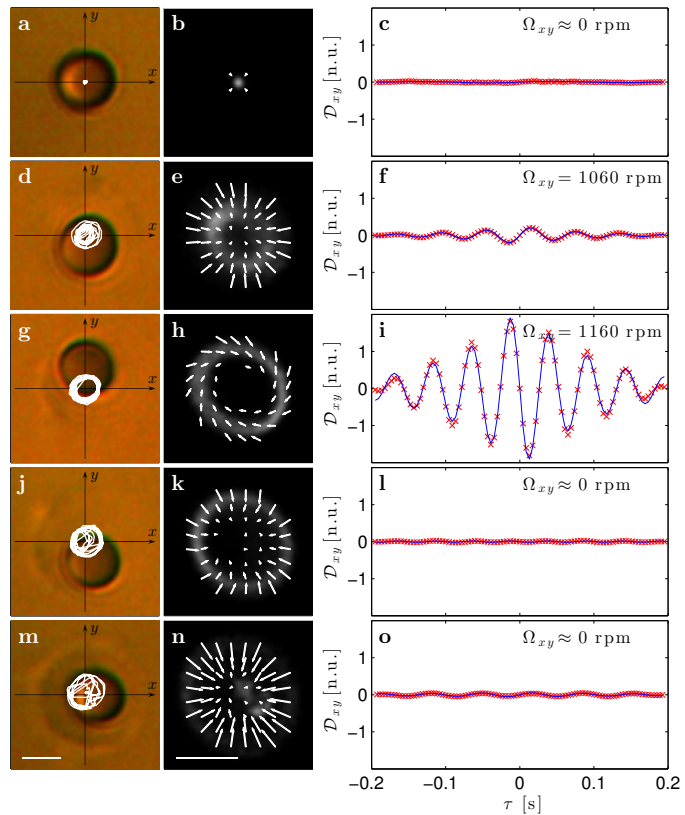
FIG. S4: Engine performance as a function of ambient temperature for a particle with $R = 1.24\,\mu$m. The laser power at the optical trap is fixed at $P = 2.7\,$mW, while the ambient temperature of the sample is (a-c) $T_0 = 20$, (d-f) 24, (g-i) 26, (j-l) 27, and (m-o) 28°C. (a,d,g,j,m) Bright-field images of the particle with $0.6\,$s trajectories represented by white solid lines. (b,e,h,k,n) Velocity drift fields (white arrows) and particle position probability distributions (background color, brighter colors represent higher probability density). (c,f,i,l,o) Experimental (red symbols) and fitted (blue solid lines) differential cross-correlation functions $\mathcal{D}_{xy}$ in the xy-plane, from which the rotation rate of the particle Ω_{xy} can be obtained as fit parameter (reported in the right column). The white bars in (m) and (n) correspond to $1\,\mu$m. (g-i) are the same data as Fig. 2j-l. See also supplementary Video 2.
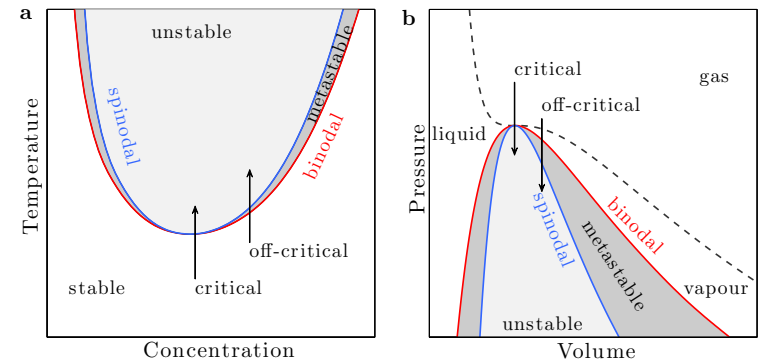
FIG. S5: Schematic phase diagram of a mixture showing the spinodal and binodal lines. The distance between the two lines is related to the latent energy required for the phase separation to occur. Only at the critical point the two lines coincide and, therefore, there is no latent energy and hysteresis. (a) Phase diagram depending on temperature and concentration corresponding to our realization of the critical engine. (b) Phase diagram depending on pressure and volume as an alternative system in which the proposed critical engine can operate (note the upper critical point).
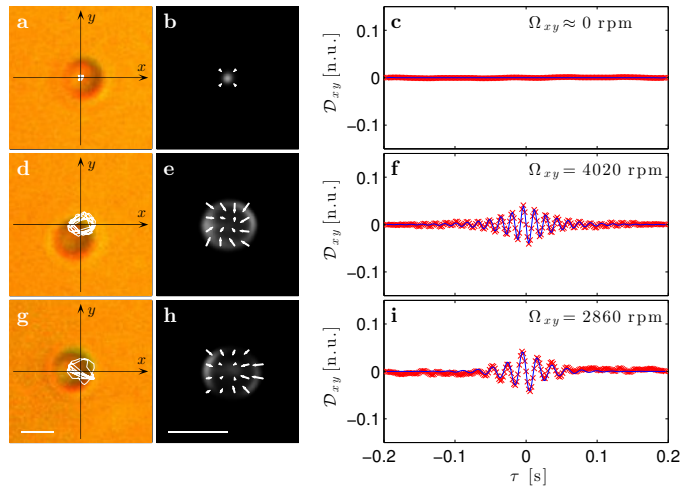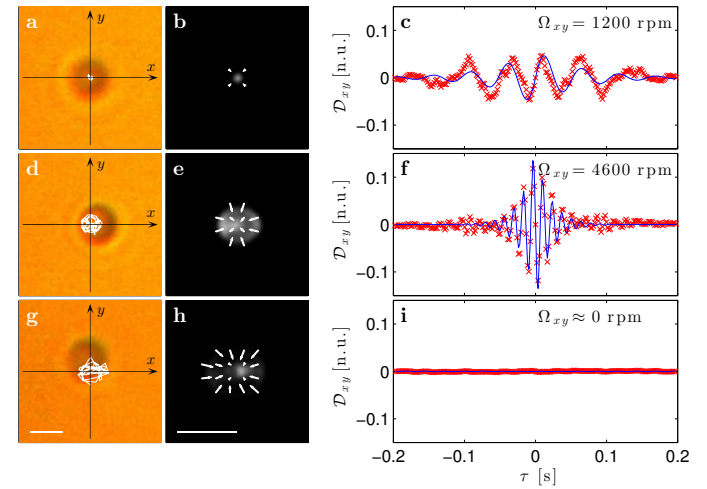
FIG. S6: Engine performance as a function of laser power for a particle with $R = 0.49\,\mu$m. The ambient temperature of the sample is fixed at $T_0 = 21$°C, while the laser power at the optical trap is (a-c) $P = 0.6$, (d-f) 1.5, and (g-i) 2.7 mW. (a,d,g) Bright-field images of the particle with 0.1 s trajectories represented by white solid lines. (b,e,h) Velocity drift fields (white arrows) and particle position probability distributions (background color, brighter colors represent higher probability density). (c,f,i) Experimental (red symbols) and fitted (blue solid lines) differential cross-correlation functions $\mathcal{D}_{xy}$ in the xy-plane, from which the rotation rate of the particle Ω_{xy} can be obtained as fit parameter (reported in the right column). The white bars in (g) and (h) correspond to $1\,\mu$m.

FIG. S7: Engine performance as a function of ambient temperature for a particle with $R = 0.49\,\mu$m. The laser power at the optical trap is fixed at $P = 1.5$ mW, while the ambient temperature of the sample is (a-c) $T_0 = 19.5$, (d-f) 23, and (g-i) 27°C. (a,d,g) Bright-field images of the particle with 0.1 s trajectories represented by white solid lines. (b,e,h) Velocity drift fields (white arrows) and particle position probability distributions (background color, brighter colors represent higher probability density). (c,f,i) Experimental (red symbols) and fitted (blue solid lines) differential cross-correlation functions $\mathcal{D}_{xy}$ in the xy-plane, from which the rotation rate of the particle Ω_{xy} can be obtained as fit parameter (reported in the right column). The white bars in (g) and (h) correspond to $1\,\mu$m.

5.2 Paper II: Non-equilibrium properties of an active nanoparticle in a harmonic potential

Attached below is the preprint version of our paper as found on arXiv and its accompanying Supplementary Information, providing more details on the self-propulsion mechanism, with figures on the experimental setup and a phase diagram on the critical binary mixture of water and 2,6-lutidine.

[1] A. Würger. Self-diffusiophoresis of Janus particles in near-critical mixtures. *Phys. Rev. Lett.*, 115:188304, 2015.

[2] G. Volpe and D. Petrov. Torque detection using Brownian fluctuations. *Phys. Rev. Lett.*, 97:210603, 2006.

[3] G. Volpe, G. Volpe, and D. Petrov. Brownian motion in a nonhomogeneous force field and photonic force microscope. *Phys. Rev. E*, 76:061118, 2007.

[4] P. H. Jones, O. M. Maragò, and G. Volpe. *Optical tweezers: Principles and applications.* Cambridge University Press, Cambridge, UK, 2015.

[5] G. Pesce, G. Volpe, A. Imparato, G. Rusciano, and A. Sasso. Influence of rotational force fields on the determination of the work done on a driven brownian particle. *J. Opt.*, 13(4):044006, 2011.

[6] C. A. Grattoni, R. A. Dawe, C. Y. Seah, and J. D. Gray. Lower critical solution coexistence curve and physical properties (density, viscosity, surface tensio, and interfacial tension) of 2,6-lutidine + water. *J. Chem. Eng. Data*, 38:516–519, 1993.

[7] E. J. G. Peterman, F. Gittes, and C. F. Schmidt. Laser-induced heating in optical traps. *Biophys. J.*, 84(2):1308–1316, 2003.

[8] S. Samin and R. van Roij. Self-propulsion mechanism of active Janus particles in near-critical binary mixtures. *Phys. Rev. Lett.*, 115:188305, 2015.

15

Non-equilibrium Properties of an Active Nanoparticle in a Harmonic Potential

Falko Schmidt,[1, *] Hana Šípovà-Jungová,[2] Mikael Käll,[2] Alois Würger,[3, †] and Giovanni Volpe[1]

[1] *Department of Physics, University of Gothenburg, SE-41296 Gothenburg, Sweden*
[2] *Department of Physics, Chalmers University of Technology, SE-41296 Gothenburg, Sweden*
[3] *Laboratoire Ondes et Matière d'Aquitaine, Université de Bordeaux & CNRS, F-33405 Talence, France*
(Dated: September 17, 2020)

Active particles break out of thermodynamic equilibrium thanks to their directed motion, which leads to complex and interesting behaviors in the presence of confining potentials. When dealing with active nanoparticles, however, the overwhelming presence of rotational diffusion hinders directed motion, leading to an increase of their effective temperature, but otherwise masking the effects of self-propulsion. Here, we demonstrate an experimental system where an active nanoparticle immersed in a critical solution and held in an optical harmonic potential features far-from-equilibrium behavior beyond an increase of its effective temperature. When increasing the laser power, we observe a cross-over from a Boltzmann distribution to a non-equilibrium state, where the particle performs fast orbital rotations about the beam axis. These findings are rationalized by solving the Fokker-Planck equation for the particle's position and orientation in terms of a moment expansion. The proposed self-propulsion mechanism results from the particle's non-sphericity and the lower critical point of the solute.

INTRODUCTION

Active matter is constituted by particles that can self-propel and, therefore, feature properties and behaviors characteristic of systems that are out of thermodynamic equilibrium [1]. Active-matter systems range across scales going from large robots and animals, down to single-celled organisms and artificial active particles [2–5]. They have found a broad range of applications, *e.g.*, enhancing self-assembly, bioremediation, and drug-delivery [6, 7].

The presence of confinement, boundaries and obstacles has an important influence on the behavior of active particles. For example, motile bacteria form spiral patterns when confined in circular wells [8] and Janus particles reorient at walls [9]. Confinement can be provided also by the presence of external potentials, *e.g.*, electric, magnetic, or chemical potentials. A paradigmatic example of a confining potential is provided by the harmonic potential, which is widely employed to study physics, in general, and thermodynamics, in particular. It can also provide important insight into active-matter systems [10]. Experimentally, the motion of active particles in harmonic potentials has already been studied using macroscopic toy robots walking in a parabolic potential landscape [11], as well as microscopic active colloidal particles in an acoustic trap [12], in an active bath [13–15], and in an optical trap [16]. All these experiments have been performed with relatively large particles, where, in particular, active motion is mainly determined by the particle's self-propulsion, while the particle's rotational diffusion occurs on much longer time scales.

Moving down to the nanoscale, rotational diffusion acquires a much more important role, hindering directed motion [17]. This is because of the different scaling of translational and rotational diffusion: considering a spherical particle of radius a, its translational diffusion scales with its linear dimension (*i.e.*, proportional to a^{-1}), while its rotational diffusion scales with its volume (*i.e.*, proportional to a^{-3}). This limits the possibility of achieving and studying directed active motion on the nanoscale. In fact, while several nanomotors have been proposed and experimentally realized [4, 18–21], their activity translates into a hot Brownian motion, *i.e.*, into a higher effective temperature when exploring a potential well [22].

Here, we demonstrate an experimental system where an active nanoparticle held in a potential well features far-from-equilibrium behavior beyond hot Brownian motion. Specifically, we consider a nanoparticle immersed inside a critical binary mixture and confined by the optical potential created by an optical tweezers. At low laser power, the nanoparticle explores the optical tweezers potential as a hot Brownian particle, which is characterized by a Gaussian position distribution given by the Boltzmann factor of the potential. Increasing the laser power, we observe a transition towards a state with a clear out-of-equilibrium signature, where the nanoparticle moves away from the trap center acquiring a non-Gaussian position distribution. Furthermore, the nanoparticle performs orbital rotations around the trapping beam, whose direction we can statistically control by adjusting the polarization of the beam. We provide a theoretical model based on the solution of a Fokker-Planck equation in terms of a moment expansion, which provides strong evidence that the behavior of the nanoparticle in the optical trap is a result of its non-spherical shape. These results demonstrate the importance of asymmetry in nanoscale active systems as a determinant of their behavior in confinement. This insight provides a crucial stepping stone towards the next generation of fast and efficient nanomotors.

----

* falko.schmidt@physics.gu.se
† alois.wurger@u-bordeaux.fr
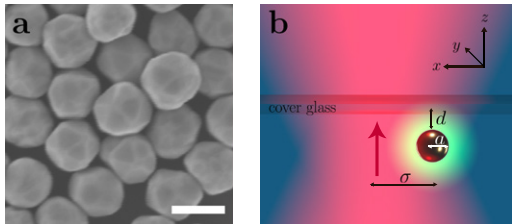
Figure 1. **Nanoparticles and their driving mechanism.** **a**: SEM image of the gold nanoparticles employed in this work. From this image, it can be appreciated how they are approximately spherical, but also feature characteristic crystalline facets. The scale bar is 150 nm. **b**: A nanoparticle (radius a) is trapped in a harmonic potential by a focused laser beam (magenta shading, propagating upwards in the direction of the red arrow, beam width σ). The particle is confined in a quasi-two-dimensional space in the xy-plane near the sample upper cover glass at distance d by the competing effects of the optical scattering force and the electrostatic repulsion by the glass. Depending on its distance from the trap center, the nanoparticle is irradiated by different intensities and, therefore, reaches different temperatures T. If T exceeds the critical temperature T_c, a concentration gradient is locally induced around the nanoparticle (green ring surrounding the particle), thereby leading to a drift velocity away from the trap's center.

RESULTS

We investigate the dynamics and probability distribution of gold nanoparticles trapped in a focused laser beam ($\lambda = 785$ nm). We employ commercially available monodisperse nanoparticles with radius $a = 75$ nm (Sigma Aldrich, $< 12\%$ variability in size). Although often referred to as "nanospheres", these nanoparticles feature a crystalline structure that distinguishes them from an ideal sphere, as can be seen in the SEM image in Fig. 1a.

As schematically shown in Fig. 1b, the trapping beam propagates upwards and is focused near the top cover glass surface of the sample cell. The nanoparticle is confined along the vertical z-direction at distance d from the cover glass by counteracting actions of the radiation pressure pushing it towards the cover glass and of the short-range electrostatic repulsion pushing it away from the glass surface [23]. Therefore, the nanoparticle is effectively confined in a quasi-two-dimensional space in the xy-plane parallel to the cover glass, where it is trapped by an optical tweezers in a harmonic optical potential, *i.e.*, $V(r) = -V_0 e^{-\frac{1}{2} r^2/\sigma^2}$, where $r = \sqrt{x^2 + y^2}$, σ is the beam waist and where the prefactor $V_0 = KP$ is proportional to the power P by the proportionality constant K.

A schematic of the experimental setup is shown in Suppl. Fig. 1. The nanoparticle motion is captured *via* digital video microscopy at 719 frames per second.

Non-equilibrium state

We start by trapping the particle in water to establish a baseline in a standard medium. [24] The trajectories and the resulting probability density histograms at laser power $P = 4.4$ and 7.3 mW are shown in Fig. 2a. The data are fitted with the Boltzmann probability density $\rho_{eq} \propto \exp\left(-\frac{V}{k_B T}\right)$. The particle is confined at the center of the beam, where the potential may be replaced by its harmonic approximation $V_h = V_0 r^2/\sigma^2$. Indeed, the data in Fig. 2a are very well described by a Gaussian profile. Since the stiffness of the potential increases with laser power, the distribution function is narrower at larger P.

We then study a nanoparticle in a near-critical mixture of water and 2,6-lutidine at a critical lutidine mass fraction $c_c = 0.286$ with a lower critical point at the temperature $T_c \approx 34°C$ (see phase diagram in Suppl. Fig 2) [25]. At a temperature T below T_c the mixture is homogeneous and behaves as a standard viscous fluid (just like water). When T approaches T_c density fluctuations emerge, leading to water-rich and lutidin-rich regions. Finally, when T exceeds T_c the solution demixes into water-rich and lutidin-rich phases.

The nanoparticle absorbs part of the laser light of the trapping beam. Its excess temperature with respect to the critical point of water–2,6-lutidine is explicitly

$$T(r) - T_c = \frac{a^2 \beta}{3\kappa} \left(P g(r) - P_c\right), \qquad (1)$$

with the beam profile $g(r) = e^{-\frac{r^2}{2\sigma^2}}$, the absorption coefficient β, the heat conductivity of the liquid κ, the laser power P, and the critical value P_c corresponding to the laser power at which T_c is attained. For a nanoparticle of $a = 75$ nm, the increase in surface temperature is about 6 K mW^{-1}, when the particle is in the highest-intensity region.

In Fig. 2b, we show the probability densities for a nanoparticle trapped in a near-critical mixture kept at $T_0 = 3°C$ *via* a heat exchanger coupled to a water bath (*i.e.*, about 30 K below T_c). At low laser power ($P = 4.36$ mW, $T = 31°C < T_c$), the nanoparticle position distribution is qualitatively similar to that of the nanoparticle in water (Fig. 2a) and features only very small deviations from a Gaussian profile. As we raise the laser power ($P = 7.25$ mW, $T = 45°C > T_c$), the nanoparticle position distribution acquires a distinctively non-Gaussian shape. Finally, as we raise the laser power even further ($P = 10.16$ mW, $T = 63°C > T_c$), the nanoparticle position distribution develops a peak at a finite radial distance r from the trap center, which is also observed in the form of a ring in the histogram of the trajectories. These non-Gaussian distributions cannot be ascribed to a harmonic potential at higher effective distribution and are clear signatures of the out-of-equilibrium nature of this system.
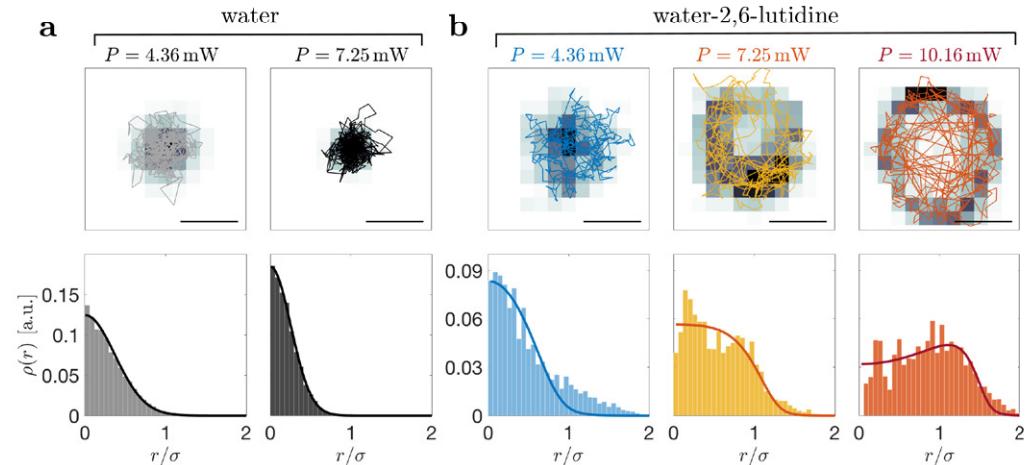
Figure 2. **Nanoparticle trajectories and probability density distributions.** Trajectories (top) and probability density $\rho(r)$ (bottom) for a nanoparticle with radius $a = 75$ nm held by an optical tweezers, **a**, in water at powers $P = 4.36$ and 7.25 mW, and, **b**, in a critical mixture of water–2,6-lutidine at $P = 4.36$, 7.25, and 10.16 mW. Sample trajectories in the xy-plane are shown for 200 ms, while the background shading indicates the counts (darker colors indicate higher counts); the scalebar is 1 µm. The probability densities $\rho(r)$ are calculated from data acquired for 1 s. **a**: In water, the data are well described by the Boltzmann distribution $\rho_{eq}(r) \propto \exp\left(-\frac{V}{k_B T}\right)$ (solid lines), which becomes narrower as the laser power P and, therefore, the optical trap potential depth increase. **b**: In water–2,6-lutidine, the particle features an out-of-equilibrium distribution, which broadens with increasing laser power. Here, the solid lines are given by Eq. (5). All data are taken at $T_0 = 3°C$, *i.e.*, ≈ 30 K below T_c. Due to absorption the particle's surface temperature increases by 6 K mW^{-1}. The radial distance has been normalized by the beam waist $\sigma = 340$ nm.

Self-propulsion of near-spherical particles

Fig. 3 shows the velocity profile $v(r)$ as a function of the distance from the beam axis, as well as its radial and azimuthal components v_r and v_θ. We have determined the local average velocity of the particle by dividing the distance between two subsequent positions by the time separation $\Delta t = 1.39$ ms. This local average velocity consists of an active contribution $u(r)$ depending on the beam intensity and thus on position, and a diffusive contribution v_D that accounts for Brownian motion as well as other random motion components,

$$v(r) = \sqrt{u(r)^2 + v_D^2}. \qquad (2)$$

With increasing power, the particle's surface temperature exceeds the lower critical point of water–2,6-lutidine (see SI [26]), causing a local modification of the composition according to the spinodal line of the phase diagram. Indeed, active motion above T_c has been reported for both Janus particles [27, 28] and silica colloids with iron-oxide inclusions [16]. The precise mechanism of thermally driven diffusiophoresis has been elucidated by both analytical theory and simulations [29, 30].

Yet, the usual mechanism of self-diffusiophoresis does not apply to homogeneous colloidal spheres, since their symmetry does not allow for a composition gradient along the surface. Therefore, we propose self-propulsion that arises from the non-spherical shape of our nanoparticles, visible in Fig. 1a. Although the large thermal conductivity of gold still imposes an isothermal surface, the temperature and composition gradients at finite distance induce active motion. This is schematically shown in Fig. 4, which shows the isothermals (grey lines) surrounding an asymmetric nanoparticle. Moving at a finite distance aways from the surface close to an edge (black dashed line, Fig. 4c), multiple isothermals are crossed, indicating a tangential concentration gradient responsible for the nanoparticle motion. For a spherical particle (black dashed line, Fig. 4c) isolines follow the shape of the particle and no tangential concentration gradient is produced. Similar observations have been made for a Leidenfrost ratchet [31].

Starting from an axisymmetric profile $R(\theta) = a(1 + \chi(\theta))$ with $\chi = \sum_n \alpha_n P_n(\cos\theta)$, with the polar angle θ and Legendre polynomials P_n, and evaluating the temperature profile in the vicinity of the *isothermal* surface of a gold particle, we obtain self-diffusiophoresis at a velocity $u \propto \alpha^2$. For later convenience, we rewrite the
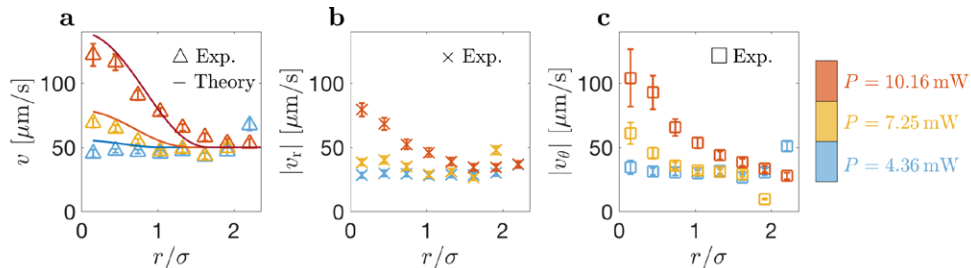
Figure 3. **Particle velocity dependence on radial position and laser power. a**: The particle's total velocity v follows the intensity profile of the laser beam indicated by solid lines given by Eq. (2), where $u_0 = 23.7$, 60.5 and $131.6\,\mu\mathrm{m\,s^{-1}}$ for $P = 4.36$, 7.25 and $10.16\,\mathrm{mW}$, respectively, taken from fits of $\rho(r)$ in Fig. 2. Similarly, **b**, the absolute radial velocity $|v_\mathrm{r}|$ and, **c**, the absolute azimuthal velocity $|v_\theta|$ follow the intensity profile of the beam. Data is taken from a single 1-s trajectory sampled at 719 Hz. Each data point is an average over the times the particle passes through that value of r/σ. Error bars are the standard error of the mean.
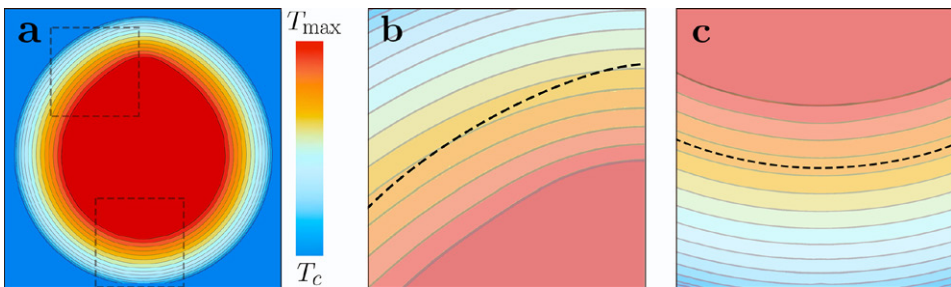
Figure 4. **Isothermals around a non-spherical particle. a** Composition profile $\phi(\mathbf{r})$ in the vicinity of a non-spherical particle at a temperature above the critical value T_C of water-2,6-lutidine. ϕ is constant at the isothermal surface and decreases with distance; the dark blue area indicates the range where $T \leq T_C$ and where the composition takes the bulk value ϕ_C. The grey lines in the critical droplet ($T \geq T_C$) indicate iso-compositon surfaces. **b** The curvature of the top of the particle is larger than of its bottom; as a consequence, ϕ varies more rapidly close to the top and the iso-composition lines are denser. The dashed line, at constant distance from the particle surface, crosses iso-composition lines; thus there is a composition gradient $\nabla_\parallel \phi$ parallel to the surface, which induces a diffusio-osmotic creep velocity and results in self-propulsion of the particle. [26] Our detailed analysis relates the particle velocity to the Fourier series of the particle shape $R(\theta)$. **c** Instead, the bottom of the particle is almost spherical with roughly constant curvature and zero creep velocity.

self-propulsion velocity as

$$u(r) = \begin{cases} u_0 \dfrac{Pg(r) - P_c}{P - P_c} & \text{for } r < r_c, \\ 0 & \text{for } r > r_c, \end{cases} \quad (3)$$

with $u_0 = C(P - P_c)$. Note that the velocity depends on the particle position with respect to the beam axis. At a critical distance $r_c = \sigma\sqrt{2\ln P/P_c}$ ($r_c = 570\,\mathrm{nm}$ with $P = 10.16\,\mathrm{mW}$ and $P_c = 2.5\,\mathrm{mW}$), the local beam intensity is identical to the critical value P_c, and the velocity vanishes. For $r > r_c$, the particle is passive. With $C = 12.7\,\mu\mathrm{m\,s^{-1}mW^{-1}}$ (in qualitative accord with system parameters, see SI [26]), this expression agrees rather well with the observed dependencies on position r and laser power P (solid lines in Fig. 3a).

As alternative mechanisms, we have also evaluated

(and excluded) diffusiophoresis due to the intensity gradient of the laser beam, and spontaneous symmetry breaking due to a small molecular Péclet number. Spontaneous symmetry breaking is excluded since it works only if "activity" and "mobility", as defined in Ref. [32] carry opposite signs. This condition can be met by chemically active particles producing a solute that is repelled from the surface, but not by phase separation above a lower critical point because the particle motion tends to diminish the composition gradient along its surface, independently of the wetting properties, while the spontaneous symmetry breaking would require that the moving particle enhances the gradient in the interaction layer. As to motion driven by the intensity gradient, it is not compatible with the fast orbital motion shown by the trajectories in Fig. 2, nor with the fast motion at the beam center where the

gradient vanishes. Details are given in the SI. [26]

Finally, we briefly discuss the anisotropy of the velocity data shown in Figs. 3b and 3c ($|v_\theta| > v_r$), which is also visible in the trajectories in Fig. 2b. Qualitatively, this is accounted for by the quadrupolar order parameter $\mathbf{Q}$ (see methods, Eq. (23)). Retaining only the dominant term results in the estimate

$$v_r^2 - v_\theta^2 \sim \frac{u^4}{\sigma^2 D_r^2}\frac{V}{k_\mathrm{B}T}. \quad (4)$$

Because $V < 0$, we find that the mean square of the tangential velocity component exceeds that of the radial one, in agreement with experiment. Such a velocity anisotropy has been observed previously for a walking robot in a parabolic dish. [11] This effect is readily understood by noting that the radial velocity scale is given by the slow uphill motion, whereas in tangential direction the particle moves at its full speed.

Probability density and polarization

The observed probability densities in water–2,6-lutidine shown in Fig. 2b cannot be described by the Boltzmann distribution. In order to relate these deviations to the particle's activity, we have investigated the dynamical behavior in terms of the steady-state distribution $\Psi(\mathbf{r},\mathbf{n})$, accounting for the gradient diffusion $-D\nabla\Psi$ with Einstein coefficient D, the optical tweezers force $\mathbf{F} = -\nabla V$, and the self-propulsion velocity $\mathbf{u} = u\mathbf{n}$. Since the direction of the latter is given by the nanoparticle axis $\mathbf{n}$, the distribution function $\Psi(\mathbf{r},\mathbf{n})$ depends both on the nanoparticle position $\mathbf{r}$ and on its orientation $\mathbf{n}$, and the Fokker-Planck equation (see methods, Eq. (13)) accounts for rotational diffusion, with coefficient D_r, and eventually for spinning motion due to an external torque.

Following previous work on the dynamics of Janus particles [33, 34], we resort to a moment expansion $\Psi = \rho + \mathbf{n} \cdot \mathbf{p} + ...$, where the probability density $\rho(\mathbf{r}) = \langle\Psi\rangle_\mathbf{n}$ and the polarization density $\mathbf{p}(\mathbf{r}) = \langle\mathbf{n}\Psi\rangle_\mathbf{n}$ are orientational averages with respect to $\mathbf{n}$. When truncating higher-order terms, one readily integrates the steady state

$$\rho(r) \propto \frac{1}{\sqrt{\mathscr{D}^2 + u(r)^2}}\exp\left(-\frac{V}{k_\mathrm{B}T}\Phi(r)\right), \quad (5)$$

where we have defined $\mathscr{D} = \sqrt{6D_r D}$ and

$$\Phi(r) = \frac{\mathscr{D}}{u_c + u}\arctan\frac{\mathscr{D}^2 - u_c u}{\mathscr{D}(u_c + u)}, \quad (6)$$

with the shorthand notation $u_c = CP_c$. At the critical radius r_c, the velocity u vanishes, and the probability density $\rho(r)$ smoothly reduces to the Boltzmann distribution $\rho_{eq} \propto e^{-V/k_\mathrm{B}T}$. With the relation for the bulk diffusion coefficients, $D_r = \frac{3}{4}D/a^2$, the ratio $u/\mathscr{D}$ reduces to the Péclet number Pe $= \sqrt{2}/3\,ua/D$, which still
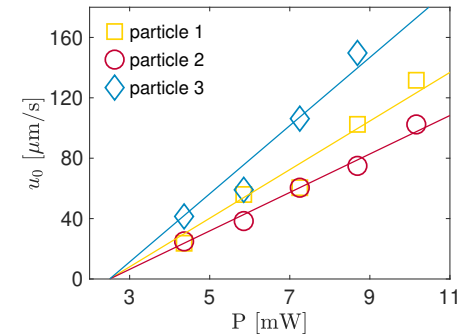

Figure 5. **Propulsion velocity as a function of the laser power.** The values of the propulsion velocity u_0 as a function of the laser power P are obtained from fits like those shown in Fig. 2b, using Eq. (5). The solid line is given by $u_0 = C(P - P_c)$, with $P_c = 2.5\,\mathrm{mW}$ and $C = 16.1$, 12.7 and $22.6\,\mathrm{ms^{-1}mW^{-1}}$ for particles 1, 2 and 3, respectively. The data of Figs. 2 and 3 are for particle 1.

depends on position and vanishes at $r = r_c$. The solid curves in Fig. 2b are calculated using Eq. (5), where the optical tweezers potential $V_0 = KP$ is parameterized by $K = 2.97 \times 10^{-17}\,\mathrm{J\,W^{-1}}$ (corresponding to about $7\,k_\mathrm{B}T_c$ per $1\,\mathrm{mW}$), whereas the solid curves in Fig. 3a are calculated using Eq. (2) where the velocity is parameterized by C and P_c. The fit curves describe the non-equilibrium behavior rather well, and account for the broadening of the distribution and for the bump emerging at $r \approx \sigma$.

Such fits have been done for three different particles at five values of the laser power P. Their propulsion speed u_0, plotted in Fig. 5, agrees well with Eq. (3). The three particles have the same radius a and absorption coefficient β; accordingly, they experience the same optical tweezers potential and reach the critical point at the same laser power P_c. Not surprisingly, the values of the slope C differ significantly, which can be related to the fact that C is proportional to the nonspericity parameter α^2, which varies from one particle to another (see Fig. 1a).

The quantity $\mathscr{D}$ has been calculated with a diffusion coefficient D fitted from the trajectory mean-squared displacement at short times. Its value ($D = 0.33\,\mu\mathrm{m^2s^{-1}}$ for the highest power and $0.45\,\mu\mathrm{m^2s^{-1}}$ for the others) is significantly smaller than the bulk value in water–2,6-lutidine above the critical point ($D_0 = 1.2$ and $2.3\,\mu\mathrm{m^2s^{-1}}$ in the lutidine-rich and water-rich phases, respectively, with viscosities taken from Ref. [25]). Similarly, the rotational diffusion coefficient used for the fitted curves of Figs. 2 and 5 is smaller than the theoretical value. There are two physical mechanism which are probably at the origin of this discrepancy: hydrodynamic coupling close to a solid boundary and the confining effect of the critical droplet surrounding an active particle

heated above T_c. The former reduces the drag coefficient of a sphere moving parallel to a wall. [35] For the latter, the critical droplet formed locally around the particle does not follow its motion but lags behind thus slowing down the particle's diffusion. A more detailed discussion is found below.

Controlling the direction of orbital rotation

Transfer of angular momentum from circularly polarized laser light to plasmonic nanoparticles is an efficient means for fuelling nanoscopic rotary motors at high-spin rates [36]. It has already been shown theoretically and experimentally verified that, even in a tightly focused Gaussian beam with circular polarization, spin-to-orbital light momentum conversion occurs and can lead to effects such as orbit splitting [37–39]. Here, we show that the spinning motion of an active particle results in orbital trajectories whose preferred handedness is imposed by the polarization of the beam. These measurements are taken with gold nanoparticles of $a = 100$ nm, at $P = 1$ mW, and at room temperature, thus leading to an increase in surface temperature of about 40 K, corresponding to 30 K above T_c.

We have investigated the azimuthal component of the velocity depending on the polarization of the beam (Figs. 6a-c). For linearly polarized light, v_θ is approximately zero, as expected (Fig. 6b). For circularly polarized light, however, we find v_θ to be different from zero: left-handed polarization results in a positive azimuthal velocity, corresponding to anti-clockwise rotation (Fig. 6a); and right-handed polarization, to negative v_θ corresponding to clockwise rotation (Fig. 6c).

This effect can be explained as follows: Due to spin angular momentum transfer from the laser light, the particle spins about its axis at frequency Ω (Figs. 6d-f). The particle's spinning motion under circular polarization is recorded via a photomultiplier. By placing a linear polarizer in front of the photomultiplier, the intensity of the scattered light changes with its orientation due to its non-sphericity. An active particle in a trap self-propels most of the time in outward direction, as rationalized by the finite polarization density $\mathbf{p} = -\nabla(u\rho)/D_r$ (Eq. (22)); the spinning motion then turns the particle axis in the azimuthal direction, $\dot{\mathbf{p}} = \Omega \times \mathbf{p}$. Solving the corresponding Fokker-Planck equation (see methods, Eq. (13)) with a finite spinning frequency, we find the azimuthal polarization p_θ given in Eq. (22) and the velocity

$$v_\theta = -\frac{\Omega u^2}{6D_r\sqrt{D_r^2 + \Omega^2}}\frac{F}{k_B T}. \tag{7}$$

Because of the inward optical tweezers force, $F < 0$, the orbital trajectory has the same handedness as the polarized light. The azimuthal velocity is expected to vary with the third power of the beam intensity, $v_\theta \propto P(P - P_c)^2$, to vanish in the center, and to reach its

maximum value at $r \approx \sigma$. Qualitatively, this expression reproduces the data of Fig. 6 with parameters corresponding to those used in Figs. 2-5. Although spin-to-orbital light momentum conversion can in principle induce similar results, we expect this effect to be comparably small. The spinning frequency Ω was obtained from fitting the scattering autocorrelation function in Figs. 6d-f with $C(\tau) = I_0^2 + 0.5I_1^2 \exp(-\tau/\tau_0)\cos(4\pi\Omega\tau)$, where I_0 is the average intensity, I_1 the intensity fluctuation amplitude, and τ_0 the decay time. [36] Surprisingly, we find that the particle is spinning under circular polarization at a frequency of about 3 Hz with a decay time of about $\tau_0 = 0.4$ s and therefore differs by 3 orders of magnitude compared to standard experiments in water [40]. Similarly as for its reduced diffusion constant mentioned above, we expect that hydrodynamic and boundary interactions are possible causes for its much reduced spinning motion (more details in the discussion). Regarding the much lower values of the laser power P and its critical value P_c, note that the nanoparticles with $a = 100$ nm absorb light about ten times more than those with $a = 75$ nm, thus leading to comparable effects at a ten times weaker power. The optical tweezers potential parameter K is proportional to both absorbed power and particle volume.

DISCUSSION

Swimming pressure

The probability density $\rho(r)$ is obtained from the stationary Fokker-Planck equation (see methods, Eq. (13)). It turns out instructive to rewrite the intermediate expression (see methods, Eq. (24)) as

$$\nabla \ln \rho = -\frac{\nabla\left(V + \frac{1}{2}H\right)}{k_B T + H}, \tag{8}$$

with $H = k_B T u^2/\mathscr{D}^2$. For passive particles one has $H = 0$, and readily recovers the Boltzmann distribution $e^{-V/k_B T}$. The denominator of Eq. (8) may be viewed as an effective temperature. It also appears in the effective diffusion coefficient of active particles, $D_{\text{eff}} = (k_B T + H)/\gamma$ [41], and the quantity ρH corresponds to the swimming pressure of active particles [42]. Assuming a constant self-propulsion velocity and discarding $k_B T$, one readily recovers the probability density $\rho \propto e^{-V/H}$ obtained previously for particles in an acoustic-wave trap [12]. From our moment expansion, however, we obtain an additional term $\frac{1}{2}H$ in the denominator of Eq. (8), which upon integration results in the intricate stationary state in Eq. (5). Since the velocity profile $u(r)$ roughly follows the laser intensity, $V + \frac{1}{2}H$ forms a "Mexican hat potential" which is less attractive than the bare optical tweezers potential and takes its minimum not at the beam axis but at a finite distance of the order r_c.
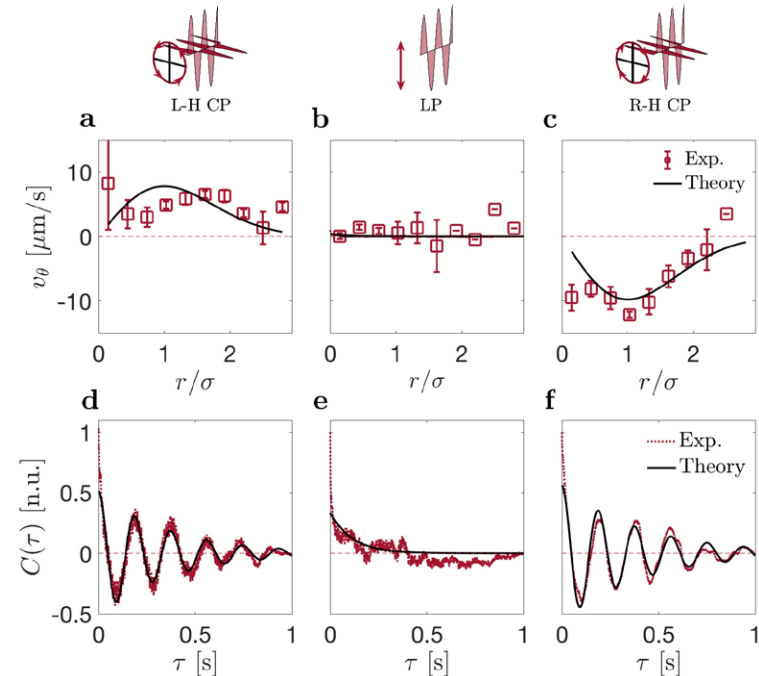
Figure 6. **Controlling the direction of orbital rotation through light polarization.** The particle orbital rotation is biased toward the direction of the polarization of the trapping beam (laser power $P = 1$ mW, nanoparticle radius $a = 100$ nm). **a-c:** Experimental values (red symbols) and theoretical fits (black lines) of the azimuthal velocity v_θ: **a**, for left-handed circular polarization, $v_\theta > 0$ showing counter-clockwise orbital rotation of the particle; **b**, for linear polarization (see also Figs. 1 and 2), $v_\theta \approx 0$ showing no preferred direction of rotation; and, **c**, for right-handed circular polarization, $v_\theta < 0$ showing clockwise orbital rotation. Error bars are the standard error of the mean. The solid line is calculated from Eq. (7) with Ω the same as in **a-c**, and taking $D_r = 70\,\text{s}^{-1}$, $K = 1.27 \times 10^{-16}\,\text{J W}^{-1}$ (corresponding to about $30\,k_B T_c$ per 1 mW), $u_0 = 120\,\mu\text{m s}^{-1}$, and $P_c = 0.2$ mW. **d-f:** Experimental (red lines) and theoretical fits (black lines) of the scattering autocorrelation $C(\tau)$ as a function of lag time τ. The absolute value of the spinning frequency Ω is **d** $|\Omega| = 2.7$ Hz for left-handed circular polarization, **e** $|\Omega| = 0$ Hz for linear polarization, and **f** $|\Omega| = 2.7$ Hz for right-handed circular polarization. The absolute value of the decay constant is **d** $\tau_0 = 0.37$ s for left-handed circular polarization, **e** $\tau_0 = 0.11$ s for linear polarization, and **f** $\tau_0 = 0.41$ s for right-handed circular polarization.

Diffusion coefficients

Using the experimental mean-square displacement at short times and the measured average velocity (Fig. 3), we obtain a value for the diffusion coefficient $D = 0.45\,\mu\text{m}^2\text{s}^{-1}$ for all laser powers except for the highest power where $D = 0.33\,\mu\text{m}^2\text{s}^{-1}$. These numbers are significantly smaller than the theoretical bulk Stokes-Einstein coefficient in water–2,6-lutidine above the critical point, which is $D_0 = 1.2$ and $2.3\,\mu\text{m}^2\text{s}^{-1}$ in the lutidine-rich and water-rich phases, respectively, with viscosities taken from Ref. [25]. Similarly, the rotational diffusion coefficient used for the fit curves of Figs. 2 and 5 is smaller than the theoretical value $D_r = k_B T/(8\pi\eta a^3)$.

Likewise, we would expect a spinning frequency Ω on the order of kHz and a decay constant τ_0 on the order of ms for particles of similar size in water [40].

Two physical mechanism could be at the origin of this discrepancy: hydrodynamic coupling close to a solid boundary, and the confining effect of the critical droplet surrounding an active particle. First, hydrodynamic interactions increase the drag coefficient of a sphere moving parallel to a wall [35], and similarly for rotational diffusion. In our experiment, the radiation pressure of the laser beam pushes the particle towards the glass boundary (Fig. 1), where the balance with electrostatic repulsion results in a stable vertical position close to the cover glass. Second, with velocities $u \sim 100\,\mu\text{m s}^{-1}$ and a

molecular diffusion coefficient of $D_m \sim 10\,\mu m^2 s^{-1}$, the molecular Péclet number ua/D_m is of the order of unity. This means that the local composition of the critical cloud, corresponding to the spinodal line of water–2,6-lutidine, does not follow the particle instantaneously but lags behind. This non-linear coupling may accelerate or slow down the particle [32]; for diffusiophoresis due to spinodal demixing, the velocity is always reduced. By the same token, the critical droplet does not follow instantaneously the particle's Brownian motion; the resulting composition gradient along the particle surface induces an opposite flow that drives the particle back and slows down diffusion.

Self-propulsion mechanism

For laser-heated gold nanoparticles in a near-critical mixture, there are two mechanisms for self-generated motion: At temperatures below the lower critical solution point (*i.e.*, $T < T_c$), we consider thermophoresis, whereas in the opposite case (*i.e.*, $T > T_c$), we expect diffusiophoresis to be dominant [29] (close to the lower critical point, a small change in temperature results in a large change of the spinodal composition; as a consequence, the composition gradient along the particle surface exceeds the underlying temperature gradient, thus giving rise to the surprisingly fast diffusiophoresis observed in various experiments [27].)

For *spherical* particles in a *uniform* laser field, the temperature $T(\mathbf{r})$ and the composition $\phi(\mathbf{r})$ are radially symmetric. However, active motion requires some symmetry breaking, which can in principle happen as a consequence of several possible mechanisms. First, spontaneous symmetry breaking due to a large molecular Péclet number [32] does not apply to the case of self-generated composition gradients, because Péclet numbers are too small and because composition fluctuations are not enhanced but reduced by the particle's motion. Second, the non-uniform intensity of the laser beam has little effect on gold nanparticles, since their high thermal conductivity results in an almost isothermal surface; also, the observed velocity profile (Fig. 3) is not compatible with this mechanism because the gradient of u vanishes at the center of the beam where in experiments we observe the highest value of v; moreover, the gradient of u is only along the radial direction, but equally fast motion is observed along the tangential component. Third, the non-spherical particle shape [43], on the contrary, turns out to be the mechanism driving our nanoparticles, as the SEM image of Fig. 1 shows a strong asphericity, and an estimate of the underlying parameters provides velocities that correspond to our experimental observations. [26]

CONCLUSION

We have demonstrated that a nanoparticle in an optical potential in a near-critical mixture provides a model for a nanoscopic active matter system under confinement. Our system shows a strong dependence on the external confinement allowing us to control the transition from passive to active motion by tuning laser power as well as to change the orbital motion *via* light polarization. Our theoretical framework in comparison with our experimental observations, provides strong arguments for a propulsion mechanism grounded on the nanoparticle non-sphericity mechanism: The numerical estimate for u is of the right order and magnitude, and u accounts for the three observations: (i) rapid motion in the center of the trap, (ii) rapid motion in both inward and outward direction, and (iii) rapid motion in azimuthal direction. The importance of systematic asymmetry provides insight for the future design of nanomotors. Follow up studies could further investigate the spin-orbit coupling in combination with other types of irregular nanoparticles. In particular, nanorods due to their high aspect ratio are promising candidates characterized by much higher spin rates under circular polarization [36], improving efficiency and rotation speeds of future systems.

METHODS

Experimental details

We consider a suspension of gold nanoparticles (radius $a = 75 \pm 9\,$nm, Sigma Aldrich) in a critical mixture of water and 2,6-lutidine at critical lutidine mass fraction $c_c = 0.286$ with a lower critical point at a temperature of $T_c \approx 34°C$ [25] (see Suppl. Fig. 2). As shown by their SEM image in Fig. 1a, these nanoparticles possess clear crystalline faces determining their non-sphericity. The suspension is confined in a sample chamber between a microscopic slide and a coverslip with an approximate height of $100\,\mu m$.

A schematic of the experimental setup is shown in Suppl. Fig. 1. The nanoparticle's translational motion is captured *via* digital video microscopy at $719\,$Hz, whereas its spin rotation under spherical polarization is recorded by a photomultiplier (by placing a linear polarizer in front of the photomultiplier, the intensity of the scattered light changes with the particle's orientation due to its non-sphericity). The corresponding scattering intensity autocorrelation reveals oscillations with spinning frequency Ω depending on the polarization of the beam as shown in Figs. 6d-f.

Fokker-Planck equation

In this section we develop the theory for the non-equilibrium behaviour observed for hot gold nanoparti-cles in an optical tweezers potential. We consider an active particle subject to the force $\mathbf{F} = -\nabla V$ deriving from the optical tweezers potential

$$V = -gV_0, \quad g = e^{-\frac{r^2}{2\sigma^2}} \qquad (9)$$

with the depth V_0, the Gaussian beam profile g and waist σ. Optical forces push the particle towards the solid boundary, strongly reducing the motion along the z-direction. Thus, we have discarded the vertical coordinate z, and treat the motion in the xy-plane only.

The equilibrium density of passive particles is determined from the steady-state condition, where motion induced by the optical tweezers force and gradient diffusion cancel each other,

$$-D\nabla\rho_{eq} + \gamma^{-1}\mathbf{F}\rho_{eq} = 0 \qquad (10)$$

where γ is Stokes' friction coefficient and $D = k_B T/\gamma$ the diffusion coefficient. With Eq. (9) this is readily integrated, resulting in the Boltzmann distribution

$$\rho_{eq} \propto e^{-V(r)/k_B T}. \qquad (11)$$

This result is independent of the details of the friction coefficient. Note that ρ_0 cannot be normalized, since the potential takes a finite value as $r \to \infty$: a trapped particle will eventually escape after a finite residence time. As an important feature, ρ_{eq} does not depend on the viscosity, since the friction factor γ is a common factor of both terms in the steady-state condition and thus disappears. In particular, the distribution remains valid close to a solid boundary where diffusion is slowed down by hydrodynamic interactions.

The motion of an active particle in a trap arises from the gradient diffusion, the optical tweezers force $\mathbf{F}$, and the self-propulsion velocity $\mathbf{u} = u\mathbf{n}$. The direction of the latter is given by the orientation of the particle axis $\mathbf{n}$. The probability current reads accordingly

$$\mathbf{J} = -D\nabla\Psi + \gamma^{-1}\mathbf{F}\Psi + \mathbf{u}\Psi. \qquad (12)$$

The probability distribution $\Psi(\mathbf{r}, \mathbf{n})$ depends on the particle position $\mathbf{r}$ and on the orientation of its axis $\mathbf{n}$, and satisfies the Fokker-Planck equation

$$\partial_t \Psi + \nabla \cdot \mathbf{J} + \mathcal{R} \cdot (\mathbf{\Omega} - D_r\mathcal{R})\Psi = 0, \qquad (13)$$

where the last term accounts for rotational diffusion about the particle axis, with the rate constant D_r and the operator $\mathcal{R} = \mathbf{n} \times \nabla_{\mathbf{n}}$, and for the angular velocity $\mathbf{\Omega} = \mathbf{T}/\gamma_R$ imposed by an applied torque $\mathbf{T}$. Following previous work on the dynamics of Janus particles, [33, 34] we resort to a moment expansion

$$\Psi(\mathbf{r}, \mathbf{n}) = \rho(\mathbf{r}) + \mathbf{n}\cdot\mathbf{p}(\mathbf{r}) + \mathbf{Q}:\left(\mathbf{nn} - \frac{1}{3}\right) + ... \quad (14)$$

with the probability density $\rho = \langle\Psi\rangle_{\mathbf{n}}$, the polarization density $\mathbf{p} = \langle\mathbf{n}\Psi\rangle_{\mathbf{n}}$, and the quadrupolar order parameter $\mathbf{Q} = \langle(\mathbf{nn} - \frac{1}{3})\Psi\rangle_{\mathbf{n}}$, where the orientational average is defined as $\langle...\rangle_{\mathbf{n}} = (4\pi)^{-1}\int d\mathbf{n}(...)$.

The continuity relation for the former is given by

$$\partial_t\rho + \nabla \cdot \mathbf{J} = 0, \qquad (15)$$

with the current

$$\mathbf{J} = -D\nabla\rho + \gamma^{-1}\mathbf{F}\rho + u\mathbf{p}. \qquad (16)$$

In order to close these equations for ρ, we need to evaluate higher moments and to truncate this hierarchy at some order. The polarisation density satisfies the continuity relation

$$\partial_t\mathbf{p} + \nabla \cdot \mathcal{J}_p + 2D_r\mathbf{p} - \mathbf{\Omega} \times \mathbf{p} = 0, \qquad (17)$$

with the second-rank tensor polarization current

$$\mathcal{J}_p = -D\nabla\mathbf{p} + u\mathbf{Q} + \frac{u\rho}{3} + \frac{1}{\gamma}\mathbf{F}\mathbf{p}. \qquad (18)$$

The quadrupolar order parameter $\mathbf{Q}$ is calculated for zero external torque. Putting $\Omega = 0$, we have

$$\partial_t\mathbf{Q} + \nabla \cdot \mathcal{J}_Q + 6D_r\mathbf{Q} = 0, \qquad (19)$$

with the corresponding third-rank tensor current

$$\mathcal{J}_Q = -D\nabla\mathbf{Q} + \frac{2}{3}u\mathbf{p} + \frac{1}{\gamma}\mathbf{F}\mathbf{Q} + ..., \qquad (20)$$

where we have discarded both the octupolar order parameter and the product $\mathbf{Qp}$.

Note that the advection term $u\rho$ in Eq. (18) generates the polarization density $\mathbf{p}$, and the advection $u\mathbf{p}$ in Eq. (20) generates the quadrupolar order parameter $\mathbf{Q}$. For small particles, rotational diffusion exceeds the derivatives of terms involving $\mathbf{p}$ and $\mathbf{Q}$.

Accordingly, we discard the current $\mathcal{J}_p$ except for the source term $u\rho$, and thus find

$$2D_r\mathbf{p} - \mathbf{\Omega} \times \mathbf{p} = -\frac{1}{3}\nabla(u\rho). \qquad (21)$$

Noting that $\nabla(u\rho)$ has a radial component only and that $\mathbf{\Omega}$ is perpendicular on the plane of motion (parameterized by $r, and\theta$), we obtain the polarization density

$$\mathbf{p} = -\frac{\partial_r(u\rho)}{6D_r}\frac{D_r\mathbf{e}_r + \Omega\mathbf{e}_\theta}{\sqrt{D_r^2 + \Omega^2}}. \qquad (22)$$

Thus, rotational diffusion favors polarization in radial direction, whereas an external spin frequency Ω turns the polarization vector in azimuthal direction. By the same token, we keep in $\mathcal{J}_Q$ the polarization advection $u\mathbf{p}$ only, and obtain

$$\mathbf{Q} = -\frac{\nabla(u\mathbf{p})}{9D_r}. \qquad (23)$$

The main approximation of the above hierarchy may be viewed as an expansion in inverse powers of the rotational diffusion coefficient. Because of its variation with particle size, $D_r \propto a^{-3}$, this is justified for small enough particles.

Non-equilibrium probability density

The formal expression of the probability density ρ is obtained from the steady-state condition for the radial component of the current, $J_r = 0$. Inserting p_r and regrouping the different terms, one finds

$$\nabla \ln \rho = \frac{\mathbf{F}/\gamma - u\nabla u/6\sqrt{D_r^2 + \Omega^2}}{D + u^2/6\sqrt{D_r^2 + \Omega^2}}. \quad (24)$$

For an explicit evaluation, we have to determine the velocity u as a function of the laser power. Active motion requires that the power at the particle position, $g(r)P$, exceeds the critical value P_c, corresponding to the lower critical temperature of water–2,6-lutidine. As the simplest relation, we take

$$u(r) = \begin{cases} C(gP - P_c) & \text{if } gP > P_c \\ 0 & \text{if } gP < P_c \end{cases}. \quad (25)$$

This describes the fact that active motion occurs only for powers above the critical value P_c. With the Gaussian beam profile $g = e^{-r^2/2\sigma^2}$, one readily finds that this condition is satisfied within a critical radius

$$r_c = \sigma\sqrt{2\ln(P/P_c)}. \quad (26)$$

Thus, the particle is active at distances $r < r_c$, its velocity $u(r)$ vanishes at the critical radius, and the particle is passive beyond r_c.

With this form, Eq. (24) is readily integrated, leading to the probability density in the active range $r < r_c$,

$$\rho(r) \propto \frac{1}{\sqrt{\mathscr{D}^2 + u(r)^2}} \exp\left(-\frac{V}{k_B T}\Phi(r)\right), \quad (27)$$

where we have defined $\mathscr{D} = \sqrt{6\sqrt{D_r^2 + \Omega^2}D}$ and

$$\Phi(r) = \frac{\mathscr{D}}{u_c + u}\arctan\frac{\mathscr{D}^2 - u_c u}{\mathscr{D}(u_c + u)}. \quad (28)$$

Beyond the critical radius r_c, the particle is passive ($u = 0$), and ρ is given by the Boltzmann distribution $\rho_{eq} \propto e^{-V/k_B T}$. Note that in the main text, ρ is discussed for $\Omega = 0$, that is, with $\mathscr{D} = \sqrt{6D_r D}$.

Orbital velocity

The probability and polarization densities $\rho(\mathbf{r})$ and $\mathbf{p}(\mathbf{r})$ depend on the radial coordinate only, as expected from the isotropic beam profile $g(r)$ and optical tweezers potential $V(r)$. Yet, an applied torque (for example due to angular momentum transfer from a polarized laser beam) [36, 44, 45] induces a spinning motion of the nanoparticle with angular velocity Ω. Then, the polarization density $\mathbf{p}$ no longer points along the radial direction but acquires an azimuthal component, as shown by Eq. (22).

A finite polarization density $\mathbf{p}$ implies a mean velocity $u(\mathbf{r})\mathbf{p}(\mathbf{r})$ at position $\mathbf{r}$. In the steady state, the radial component of the corresponding current up_r is compensated by the diffusion and the action of the optical tweezers force, resulting in $J_r = 0$. For the azimuthal component J_ϕ, however, there is no such compensation force. As a consequence, a finite p_ϕ describes a steady orbital motion of the nanoparticle around the center of the laser beam,

$$J_\theta = p_\theta u = -\frac{\Omega}{\sqrt{D_r^2 + \Omega^2}}\frac{\partial_r(u\rho)}{6D_r}u. \quad (29)$$

At small power, one has $\partial_r(u\rho) = -u(F/k_B T)\rho$ and $\Omega \ll D_r$, resulting in the velocity

$$v_\theta = -\frac{\Omega u^2}{6D_r\sqrt{D_r^2 + \Omega^2}}\frac{F}{k_B T}. \quad (30)$$

For $\Omega = 2.7\,\text{Hz}$ and $u_0 = 40\,\mu\text{m}\,\text{s}^{-1}$, the azimuthal velocity is of the order of microns per second. This is in good agreement with the experimental observations reported in Fig. 6a-c.

Acknowledgments

Authors Contribution

[1] C. Bechinger, R. Di Leonardo, H. Löwen, C. Reichhardt, G. Volpe, and G. Volpe, Rev. Mod. Phys. **88**, 045006 (2016).

[2] W. Tungittiplakorn, L. W. Lion, C. Cohen, and J.-Y. Kim, Environ. Sci. Technol. **38**, 1605 (2004).

[3] L. Soler, V. Magdanz, V. M. Fomin, S. Sanchez, and O. G. Schmidt, ACS Nano **7**, 9611 (2013).

[4] M. Safdar, J. Simmchen, and J. Jänis, Environ. Sci.: Nano **4**, 1602 (2017).

[5] A. Ghosh, W. Xu, N. Gupta, and D. H. Gracias, Nano Today **31**, 100836 (2020).

[6] W. Gao, B. E.-F. de Ávila, L. Zhang, and J. Wang, Adv. Drug Deliv. Rev. **125**, 94 (2018).

[7] M. Luo, Y. Feng, T. Wang, and J. Guan, Adv. Funct. Mater. **28**, 1706100 (2018).

[8] H. Wioland, F. G. Woodhouse, J. Dunkel, J. O. Kessler, and R. E. Goldstein, Phys. Rev. Lett. **110**, 268102 (2013).

[9] J. Simmchen, J. Katuri, W. E. Uspal, M. N. Popescu, M. Tasinkevych, and S. Sánchez, Nat. Commun. **7**, 10598 (2016).

[10] A. Pototsky and H. Stark, EPL **98**, 50004 (2012).

[11] O. Dauchot and V. Démery, Phys. Rev. Lett. **122**, 068002 (2019).

[12] S. C. Takatori, R. De Dier, J. Vermant, and J. F. Brady, Nat. Commun. **7**, 10694 (2016).

[13] C. Maggi, M. Paoluzzi, N. Pellicciotta, A. Lepore, L. Angelani, and R. Di Leonardo, Phys. Rev. Lett. **113**, 238303 (2014).

[14] A. Argun, A.-R. Moradi, E. Pinçe, G. B. Bagci, A. Imparato, and G. Volpe, Phys. Rev. E **94**, 062150 (2016).

[15] E. Pinçe, S. K. P. Velu, A. Callegari, P. Elahi, S. Gigan, G. Volpe, and G. Volpe, Nat. Commun. **7**, 10907 (2016).

[16] F. Schmidt, A. Magazzù, A. Callegari, L. Biancofiore, F. Cichos, and G. Volpe, Phys. Rev. Lett. **120**, 068004 (2018).

[17] F. Novotný, H. Wang, and M. Pumera, Chem. **6**, 867 (2020).

[18] P. Figliozzi, N. Sule, Z. Yan, Y. Bao, S. Burov, S. K. Gray, S. A. Rice, S. Vaikuntanathan, and N. F. Scherer, Phys. Rev. E **95**, 022604 (2017).

[19] Y. Yifat, D. Coursault, C. W. Peterson, J. Parker, Y. Bao, S. K. Gray, S. A. Rice, and N. F. Scherer, Light Sci. Appl. **7**, 105 (2018).

[20] M. Fernández-Medina, M. A. Ramos-Docampo, O. Hovorka, V. Salgueiriño, and B. Städler, Adv. Funct. Mater. **30**, 1908283 (2020).

[21] H. Šípová-Jungová, D. Andrén, S. Jones, and M. Käll, Chem. Rev. **120**, 269 (2020).

[22] D. Rings, R. Schachoff, M. Selmke, F. Cichos, and K. Kroy, Phys. Rev. Lett. **105**, 090604 (2010).

[23] D. Andrén, N. Odebo Länk, H. Šípová-Jungová, S. Jones, P. Johansson, and M. Käll, J. Phys. Chem. C **123**, 16406 (2019).

[24] P. H. Jones, O. M. Maragò, and G. Volpe, *Optical tweezers: Principles and applications*, 1st ed. (Cambridge University Press, Cambridge, UK, 2015).

[25] C. A. Grattoni, R. A. Dawe, C. Y. Seah, and J. D. Gray, J. Chem. Eng. Data **38**, 516 (1993).

[26] "Supplementary information,".

[27] I. Buttinoni, G. Volpe, F. Kümmel, G. Volpe, and C. Bechinger, J. Phys. Condens. Matter **24**, 284129 (2012).

[28] C. Lozano, B. ten Hagen, H. Löwen, and C. Bechinger, Nat. Commun. **7**, 12828 (2016).

[29] A. Würger, Phys. Rev. Lett. **115**, 188304 (2015).

[30] S. Samin and R. Van Roij, Phys. Rev. Lett. **115**, 188305 (2015).

[31] A. Würger, Phys. Rev. Lett. **107**, 164502 (2011).

[32] S. Michelin, E. Lauga, and D. Bartolo, Phys. Fluids **25**, 061701 (2013).

[33] R. Golestanian, Phys. Rev. Lett. **108**, 038803 (2012).

[34] T. Bickel, G. Zecua, and A. Würger, Phys. Rev. E **89**, 050303 (R) (2014).

[35] H. Brenner, Chem. Eng. Sci. **16**, 242 (1961).

[36] L. Shao, Z.-J. Yang, D. Andrén, P. Johansson, and M. Käll, ACS Nano **9**, 12542 (2015).

[37] Y. Zhao, J. S. Edgar, G. D. M. Jeffries, D. McGloin, and D. T. Chiu, Phys. Rev. Lett. **99**, 073901 (2007).

[38] L. Pérez García, J. Donlucas Pérez, G. Volpe, A. V. Arzola, and G. Volpe, Nat. Commun. **9**, 5166 (2018).

[39] A. V. Arzola, L. Chvátal, P. Jákl, and P. Zemánek, Sci. Rep. **9**, 4127 (2019).

[40] L. Shao and M. Käll, Adv. Funct. Mater. **28**, 1706272 (2018).

[41] J. R. Howse, R. A. L. Jones, A. J. Ryan, T. Gough, R. Vafabakhsh, and R. Golestanian, Phys. Rev. Lett. **99**, 048102 (2007).

[42] S. C. Takatori, W. Yan, and J. F. Brady, Phys. Rev. Lett. **113**, 028103 (2014).

[43] S. Shklyaev, J. F. Brady, and U. M. Córdova-Figueroa, J. Fluid Mech. **748**, 488 (2014).

[44] M. E. J. Friese, T. A. Nieminen, N. R. Heckenberg, and H. Rubinsztein-Dunlop, Nature **394**, 348 (1998).

[45] K. D. Bonin, B. Kourmanov, and T. G. Walker, Optics Express **10**, 984 (2002).

Non-equilibrium Properties of an Active Nanoparticle in a Harmonic Potential
(Supplementary Information)

Falko Schmidt,[1, *] Hana Šípová-Jungová,[2] Mikael Käll,[2] Alois Würger,[3, †] and Giovanni Volpe[1]

[1] *Department of Physics, University of Gothenburg, SE-41296 Gothenburg, Sweden*
[2] *Department of Physics, Chalmers University of Technology, SE-41296 Gothenburg, Sweden*
[3] *Laboratoire Ondes et Matière d'Aquitaine, Université de Bordeaux & CNRS, F-33405 Talence, France*

Here we provide supplementary information on experimental aspects and on the self-propulsion mechanism of our near-spherical nanoparticles.

SELF-PROPULSION MECHANISMS

For laser-heated gold nanoparticles in near-critical water-lutidine we have identified two mechanisms for self-generated motion: thermophoresis is expected to be dominant for temperatures below the lower critical solution point, and diffusiophoresis for temperatures above the lower critical solute point due to varying composition of water-lutidine [1–3]. Other possible mechanisms such as a non-spherical particle shape, non-uniform intensity of the laser beam over the particle surface, and spontaneous symmetry breaking due to a large molecular Péclet number are discussed in detail below.

In summary, we find that a comparison with our experimental observations provides strong arguments for the non-sphericity mechanism, as our estimate for the propulsion velocity u is of the right order and magnitude, and accounts for the rapid motion of the particle in the center of the trap, inward and outwards as well as in the azimuthal direction.

Self-thermophoresis of near-spherical particles

We start from the expression for the velocity of a particle in a temperature gradient,

$$u = \frac{1}{\eta} \int_0^\infty dz\, z h(z) \frac{\langle \nabla_\parallel T \rangle}{T} \tag{1}$$

where $\langle ... \rangle$ is the surface mean, h the excess enthalpy density of the liquid phase due to interactions with the particle, and $\nabla_\parallel T$ the gradient along the surface, which is due to laser heating.

We consider an axisymmetric particle whose surface is parameterized by the cosine $c = \cos\theta$ of the polar angle θ:

$$R(c) = a(1 + \chi), \quad \chi = \sum_{n \geq 2} \alpha_n P_n(c), \tag{2}$$

where P_n are Legendre polynomials. The origin is chosen such that $\alpha_1 = 0$.

The temperature field in the liquid satisfies Laplace's equation, $\nabla^2 T = 0$ and thus can be written as a series

$$T = T_0 + \Delta T \frac{a}{r} \left(1 + \sum_{n \geq 1} t_n P_n(c) \frac{a^n}{r^n} \right), \tag{3}$$

where ΔT is the excess temperature with respect to the bulk liquid. For a spherical particle, the coefficients t_n are zero. Here, we determine the temperature field of a non-spherical particle with isothermal surface because the high thermal conductivity of gold imposes a constant surface temperature

$$T(R(c), c) = T_0 + \Delta T. \tag{4}$$

The coefficients t_n are readily obtained by expanding the factors R^{-n} in powers of χ and then projecting the condition (4) on P_n. To leading order in α_n, the first coefficient is quadratic in the surface perturbation,

$$t_1 = \sum_{n=2}^\infty \frac{3n+2}{2n+3} \alpha_n \alpha_{n+1} \equiv \alpha^2, \tag{5}$$

whereas the remainder of the series contains linear terms,

$$t_n = \alpha_n + O(\alpha^2) \quad (n \geq 2). \tag{6}$$

The temperature at the particle surface is constant as imposed by the isothermal condition (4), yet at a distance z the temperature is modulated according to the Fourier series (3). Thus $\nabla_\parallel T$ vanishes at $z = 0$ but is finite for $z > 0$. In linear order in χ, only the first Fourier coefficient t_1 contributes to the surface average in (1),

$$\nabla_\parallel T = \mathbf{e}_\theta \frac{2z t_1 \Delta T}{(a+z)^2} \sin\theta + ... \tag{7}$$

Because of the z-dependence of the gradient, the analysis differs from the usual description of self-propulsion.

* falko.schmidt@physics.gu.se
† alois.wurger@u-bordeaux.fr

The excess enthalpy is expressed through the van der Waals energy density,

$$h(z) = -\frac{H}{z^3}, \tag{8}$$

with the Hamaker constants H and where a lower cut-off distance is provided by the molecular size ϵ. Projecting the temperature gradient on the particle axis, averaging over the surface, and performing the integral over z, we find the particle velocity

$$u = -\frac{4\alpha^2 H}{3\eta a^2}\frac{\Delta T}{T}\ln\frac{a}{\epsilon}. \tag{9}$$

There is another contribution which results from the coupling of the higher temperature multipoles t_n to the shape-induced perturbation of the hydrodynamic velocity field. Following Happel and Brenner [6], the rather intricate boundary conditions at a non-spherical particle are implemented in terms of the stream function

$$\frac{\psi}{ua^2} = \left(r_a^2 + \frac{B_2}{r_a}\right)\mathscr{I}_2 + \sum_{n\geq 3}\left(\frac{B_n}{r_a^{n-1}} + \frac{D_n}{r_a^{n-3}}\right)\mathscr{I}_n, \tag{10}$$

with a velocity scale u, the reduced coordinate $r_a = r/a$ and the Gegenbauer functions $\mathscr{I}_n(\cos\theta)$. The resulting velocity corrections are proportional to $\alpha_n\alpha_{n+1}$, like t_1, and of similar order of magnitude.

Self-diffusiophoresis of near-spherical particles

We start from the expression for the particle velocity derived in previous work on carbon-capped Janus particles [1],

$$u = -\frac{k_B T}{\bar{v}\eta}\int_0^\infty dz\, z\left\langle\frac{e^{-\psi_w} - e^{-\psi_l}}{\phi e^{-\psi_w} + (1-\phi)e^{-\psi_l}}\nabla_\parallel\phi\right\rangle, \tag{11}$$

where $k_B T\psi_{w,l}$ are excess interaction potentials of water and lutidine, $\bar{v}^{-1}$ is the mean inverse molecule, and z the distance from the surface. Angular brackets indicate the surface average.

Far from the hot particle, the mixture is at the critical value for the water content ϕ_c. Above the critical temperature T_c, the local equilibrium composition $\phi(T(\mathbf{r}))$ is given by the spinodal line of the phase diagram and thus depends on the local temperature $T(\mathbf{r})$, which in turn is solution of the heat diffusion equation around the hot particle. Hydrophilic surfaces attract water, resulting within the critical droplet in a water content larger than the critical value, $\phi > \phi_c$.

Active motion requires a perturbation with respect to ϕ. In the above expression (11), the interaction potentials $\psi_{w/l}$ of the particle with nearby water and lutidine molecules result in an out-of-equilibrium composition within an interaction layer. For hydrophilic surfaces, ψ_w is more negative than ψ_l, resulting in an enhancement of the water content beyond ϕ. This non-uniform excess water content along the surface, provides the thermodynamic force which drives the particle. The relation to the temperature gradient is given by

$$\nabla\phi = \phi_T\frac{\nabla T}{T}. \tag{12}$$

The remaining analysis is analogous to the case of thermophoresis treated above. The rather intricate phase behavior of the critical mixture is condensed in the parameter ϕ_T [1], which will be taken as a constant in the following.

The interaction potentials of water and lutidine with the particle surface is described by dispersion forces

$$\psi_{w/l} = -\frac{H_{w/l}}{k_B T}\frac{\bar{v}}{z^3}, \tag{13}$$

with effective Hamaker constants $H_{w/l}$. Linearizing the exponentials in (11), and integrating as above, we find

$$u = \alpha^2\frac{H_w - H_l}{\eta a^2}\frac{\Delta T_c}{T}\phi_T\ln\frac{a}{\epsilon} \tag{14}$$

with $\Delta T_c = T_S - T_c$. (The particle is active only at temperatures above T_c.) The velocity is similar to that for thermophoresis, with an additional factor ϕ_T. Given the small temperature differences in the experiments, diffusiophoresis is much faster compared to thermophoresis [2, 4]; thus we use in the following the value $\phi_T = 5$.

The particle's excess temperature with respect to the critical point of water-lutidine arises from the absorption of laser light, and reads explicitly

$$T(r) - T_c = \frac{a^2\beta}{3\kappa}\left(Pg(r) - P_c\right), \tag{15}$$

with the beam profile $g = e^{-\frac{r^2}{2\sigma^2}}$, the absorption coefficient β, the heat conductivity of the liquid κ, the laser power P, and the critical value P_c where T_c is attained. For further convenience we rewrite the self-propulsion velocity as

$$u(r) = \begin{cases} C(Pg - P_c) & \text{for } r < r_c, \\ 0 & \text{for } r > r_c, \end{cases} \tag{16}$$

where the various parameters are subsumed in

$$C = \alpha^2\frac{H_w - H_l}{\eta}\phi_T\frac{\beta}{3\kappa T}\ln\frac{a}{\epsilon}. \tag{17}$$

For a numerical estimate we put $H_w - H_l \approx k_B T$, $a = 75$ nm, $\eta \approx 2$ mPa.s, $\ln(a/d_0) \sim 5$, $\Delta T \sim 50$ K. With the Fourier component $\alpha_n = 0.1$, we find that each single mode n contributes the velocity

$$u_n \sim 40\,\mu\text{m/s}. \tag{18}$$

Assuming several modes to be relevant, this estimate accounts for the highest velocities measured. Like for thermophoresis, there is an additional contribution from hydrodynamic corrections, which merely enhance the numerical prefactor, but do not modify the overall features and functional dependencies of the above velocity.

Phoresis in a non-uniform laser beam

Here we calculate the self-propulsion velocity of a spherical particle due to the intensity profile $P(\mathbf{r})$ of the laser beam. The heat absorption rate in the particle is given by $q = \beta P(\mathbf{r} + \hat{\mathbf{r}})$, with the position $\mathbf{r}$ of the particle center and $\hat{\mathbf{r}}$ the distance with respect to the center. Linearizing in terms of $\hat{\mathbf{r}}$ we find

$$q = \beta\left[P(\mathbf{r}) + \hat{\mathbf{r}}\cdot\nabla P(\mathbf{r}) + ...\right], \tag{19}$$

where higher-order terms carry additional powers of the ratio of the particle radius and the beam waist, a/σ. The stationary temperature field T is determined by Fourier's law

$$\kappa\nabla^2 T + q = 0, \tag{20}$$

with the thermal conductivity κ and where $q = 0$ outside the particle. The boundary conditions at the interface require continuity for both the temperature T and the heat current $-\kappa\mathbf{n}\cdot\nabla T$ in normal direction. We readily obtain the excess temperature inside the particle,

$$T_p - T_0 = \frac{\beta P}{3\kappa_s}\left(1 + \epsilon\frac{a^2 - \hat{r}^2}{2a^2}\right) + \frac{\beta\hat{\mathbf{r}}\cdot\nabla P}{10\kappa_p}\left(\frac{3+2\epsilon}{1+2\epsilon} - \frac{\hat{r}^2}{a^2}\right), \tag{21}$$

and in the outside liquid

$$T_s - T_0 = \frac{\beta P}{3\kappa_s}\frac{a^2}{\hat{r}^2} + \frac{\beta\hat{\mathbf{r}}\cdot\nabla P}{5\kappa_p}\frac{1}{1+2\epsilon}\frac{a^3}{\hat{r}^3}, \tag{22}$$

where we use the thermal conductivity contrast between solvent κ_s and particle κ_p, $\epsilon = \kappa_s/\kappa_p$. The conductivity of gold being about thousand times larger than that of water and oil, we put $\epsilon = 0$ in the following.

Phoresis is driven by the component of the temperature gradient that is parallel to the particle surface,

$$\nabla_\parallel T = \frac{\beta(1 - \mathbf{nn})\cdot\nabla P(\mathbf{r})}{5\kappa_p}. \tag{23}$$

Proceeding as above, we readily obtain the diffusiophoretic self-propulsion velocity

$$u_{\text{grad}} = \frac{\kappa_s}{\kappa_p}\frac{H_w - H_l}{\eta a}\frac{\Delta T}{T}\phi_T\frac{r}{\sigma^2}e^{-r^2/2\sigma^2}. \tag{24}$$

With the above numbers and the heat conductivity ratio of water and gold, $\kappa_{\mathrm{s}}/\kappa_{\mathrm{p}} \approx 10^{-3}$, we find a velocity much smaller than one micron per second.

Moreover, u_{grad} vanishes at center of the beam, where the experiments show the highest velocities. Finally, u_{grad} is always aligned on the radial direction, whereas the observations show equally fast motion in polar direction. We conclude that the contribution proportional to the intensity gradient does not provide a major contribution to the active motion of our particles.

Spontaneous symmetry breaking

Michelin et al. [5] have shown that active motion of spherical particles may occur due to spontaneous symmetry breaking of the molecular composition of the surrounding solution.. This nonlinear mechanism sets as soon as the molecular Péclet number $\mathrm{Pe}_{\mathrm{m}} = au/D_{\mathrm{m}}$ exceeds a critical value of 4; in other words, the lowest velocity expected is of the order of $u_{\mathrm{min}} = 4D_{\mathrm{m}}/a$, which is larger than 1 mm/s. Yet our experiments show active motion with $u_0 \sim 25\mu$m/s, thus ruling out spontaneous symmetry breaking.

More importantly, the nonlinear driving mechanism works only if the excess molecular species is repelled from the particle surface. (In the language of Ref. [5], "activity" and "mobility" need to carry the same sign.) This is, however, never the case for particles in near-critical water-lutidine, since the excess molecular species is the one being attracted by the surface. As a consequence, non-linear effects at high Péclet number are not expected to result in self-propulsion.

[1] Würger, A. Self-diffusiophoresis of Janus particles in near-critical mixtures. *Phys. Rev. Lett.* **115**, 188304 (2015).
[2] Buttinoni, I., Volpe, G., Kümmel, F., Volpe, G. & Bechinger, Clemens Active Brownian motion tunable by light. *J. Phys.: Condens. Matter* **24**, 284129 (2012).
[3] Samin, S & Van Roij, R. Self-propulsion mechanism of active Janus particles in near-critical binary mixtures. *Phys. Rev. Lett.* **115**, 188305 (2015).
[4] Jiang, Hong-Ren, Yoshinaga, Natsuhiko, & Sano, Masaki Active motion of a Janus particle by self-thermophoresis in a defocused laser beam. *Phys. Rev. Lett.* **105**, 268302 (2010).
[5] Michelin, S, Lauga, E. & Bartolo, D. Spontaneous autophoretic motion of isotropic particles. *Phys. Fluids* **25**, 061701 (2013).
[6] J. Happel, H. Brenner. *Low Reynolds number hydrodynamics.* Martinus Nijhoff, Massachusetts, 1963.
[7] Grattoni, C. A., Dawe, R. A., Seah, C. Y. & Gray, J. D. Lower critical solution coexistence curve and physical properties (density, viscosity, surface tension, and interfacial tension) of 2,6-lutidine + water. *J. Chem. Eng. Data* **38**, 516 (1993).
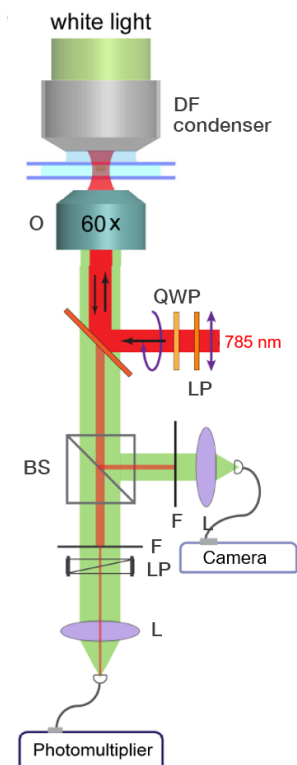
Supplementary Figure 1. Schematic of the experimental setup. A laser beam ($\lambda = 785$ nm) passes through a linear polarizer (LP) and quarter wave plate (QWP) for control over polarization turning linearly polarized light into right or left-handed spherical polarization, before being reflected onto a 60x high NA objective (O), through which the laser is being focused from below onto the sample chamber. From above white light illuminates the sample through a dark field (DF) condenser. Only the scattered light of the particle passes and is then split into to paths via a beam splitter (BS). In reflection the particle's translational motion is recorded as the scattered light is focused by a lens (L) into an optical fibre connected to a CMOS camera. Here, the laser light is filtered out before (F). In transmission, the particle's spinning motion is being recorded where the scattered light passes through a linear polarizer (LP) before being collected through a lens (L) by a photomultiplier.

5.3 Paper III: Light-controlled assembly of active colloidal molecules

Attached below is the full paper as published in the Journal of Chemical Physics and its accompanying Supplementary Information with figures on the binary critical mixture, the experimental setup and the model used for the forces acting inside a colloidal molecule.

7
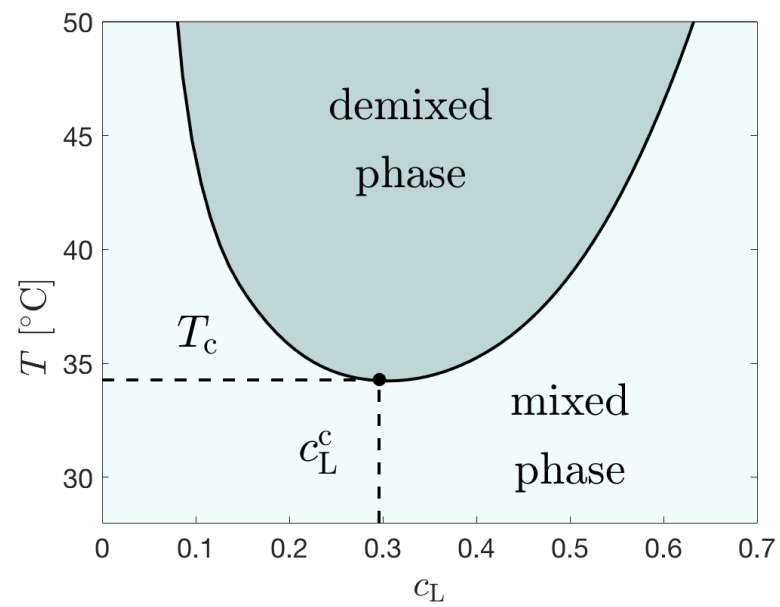
Supplementary Figure 2. Phase diagram of the water–2,6-lutidine mixture. The water–2,6-lutidine mixture is characterized by its spinoidal line (solid line) separating mixed phase from demixed phase. The mixture is prepared at the critical lutidine mass fraction $c_c = 0.286$ and at a temperature $T_0 = 3°C$ far away from the critical temperature $T_c \approx 34°C$. The data are obtained from Ref. [7].

Light-controlled assembly of active colloidal molecules

Falko Schmidt,[1,a] [ID] Benno Liebchen,[2,a] [ID] Hartmut Löwen,[2,b] [ID] and Giovanni Volpe[1,c] [ID]

AFFILIATIONS

[1] Department of Physics, University of Gothenburg, SE-41296 Gothenburg, Sweden
[2] Institut für Theoretische Physik II: Weiche Materie, Heinrich-Heine-Universität Düsseldorf, D-40225 Düsseldorf, Germany

Note: This article is part of the Special Topic "Chemical Physics of Active Matter" in J. Chem. Phys.
a) **Contributions:** F. Schmidt and B. Liebchen contributed equally to this work.
b) **Electronic mail:** hlowen@hhu.de
c) **Electronic mail:** giovanni.volpe@physics.gu.se

ABSTRACT

Thanks to a constant energy input, active matter can self-assemble into phases with complex architectures and functionalities such as living clusters that dynamically form, reshape, and break-up, which are forbidden in equilibrium materials by the entropy maximization (or free energy minimization) principle. The challenge to control this active self-assembly has evoked widespread efforts typically hinging on engineering of the properties of individual motile constituents. Here, we provide a different route, where activity occurs as an emergent phenomenon only when individual building blocks bind together in a way that we control by laser light. Using experiments and simulations of two species of immotile microspheres, we exemplify this route by creating active molecules featuring a complex array of behaviors, becoming migrators, spinners, and rotators. The possibility to control the dynamics of active self-assembly via light-controllable nonreciprocal interactions will inspire new approaches to understand living matter and to design active materials.

Published under license by AIP Publishing. https://doi.org/10.1063/1.5079861

I. INTRODUCTION

One promising approach to create functional materials as required by 21st century's technologies is self-assembly. Here, a basic starting point is to explore and control the binding of particles in a molecule, which works in principle on all scales, from atoms to colloids. As compared to their atomistic counterparts, the formation of colloidal molecules[1-6] offers an enhanced control, based on the possibility to design their shapes and coatings on demand, as illustrated, e.g., by the admirable achievements on "patchy colloids."[1-4]

While many studies exploring the self-assembly of molecules focus on equilibrium systems, active particles can then locally inject energy into a material open promising new horizons for self-assembly. These active particles are intrinsically away from thermal equilibrium,[7-10] which allows them to conquer a new level of complexity. This new complexity

finds its perhaps most spectacular expression in the hierarchical self-organization of biological matter, often leading to functionalities such as clustering,[11] navigation,[12] self-healing,[13] or reproduction.[14] It has been recently theoretically suggested[15-17] that activity can also be exploited to form active molecules where the nonequilibrium settings allow the spontaneous emergence of new physical properties: the nonequilibrium chemical interaction between two immotile particles of different species will be generally nonreciprocal,[15] resulting in the formation of colloidal molecules that may spontaneously acquire motility.[16,17] This differs conceptually from active molecules involving components that are individually motile[18-23] and also from molecules that are first prepared with an irreversible bonding and then acquire motility as an independent additional effect in electric ac-fields.[24,25]

Here, we experimentally demonstrate the formation of light-controllable active colloidal molecules from a suspension

of light-absorbing and non-absorbing immotile microspheres immersed in a subcritical liquid mixture. When illuminated, the liquid surrounding the light-absorbing microparticles warms up. This temperature increase is isotropic and, therefore, does not lead to self-propulsion of the light-absorbing particles, different from previous work on light-activated colloids;[26] however, it induces attraction among nearby colloids, which come together because of phoretic interactions at intermediate interparticle distances[26-28] (probably thermophoresis) and stick together because of short range attractions (probably van der Waals and perhaps critical Casimir forces).[29-31] For example, a Janus dimer is formed when this light-induced attraction holds a non-absorbing microsphere and an absorbing one together. This dimer experiences a temperature gradient and moves phoretically.[32-38] When more microspheres come together, they form more complex molecules including stators, migrators, spinners, and rotators. Importantly, we remark that the emergence of directed motion of two binding immotile particles is not an obvious consequence of symmetry breaking—rather, it is forbidden in equilibrium on the relevant scales and crucially exploits the presence of a nonequilibrium environment. The striking new feature of the present approach is that motility occurs as an emergent nonequilibrium phenomenon from particle interactions that are controllable by light. This establishes a generic route to control nonreciprocal interactions among colloids by light, which is based on the laser-stimulated production

of a phoretic field (e.g., chemicals, temperature, ions) by one species that attracts another species without causing a counteraction. This route offers control of the dynamics of active molecule formation, which can be switched on, off, paused or resumed on demand, and can be used to statistically control the composition of the system, e.g., with respect to the ratio of linear and chiral swimmers, as we demonstrate below. Remarkably, also the concept of emergent motility itself may inspire new collective phenomena beyond those featured by individually motile particles.[26,39-44]

## II. RESULTS

A. Experiments

We consider a mixture of light-absorbing and non-absorbing colloidal particles (radius $R \approx 0.49 \ \mu m$) made of silica with and without iron-oxide inclusions in a near-critical water-lutidine mixture in a quasi two-dimensional sample chamber (see Appendix A for details). Both species of particles settle down above the bottom wall of the sample at approximately the same distance because their specific density and electrostatic interactions are similar; when compared with the same particles in the bulk of the solution, this increases the viscous drag acting on the particles by a constant factor,[45] but does not otherwise qualitatively alter their dynamics. Without illumination, both species show Brownian diffusion
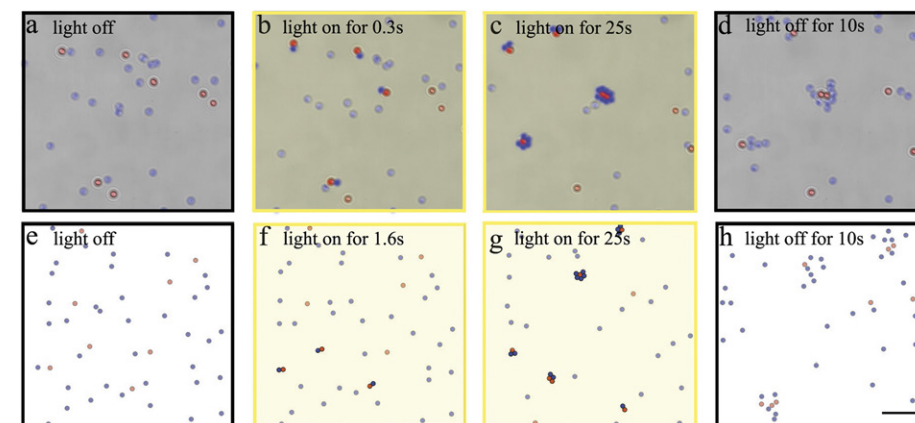

FIG. 1. **Spontaneous assembly of active colloidal molecules from immotile building blocks.** Series of snapshots from an experiment (top) and a simulation (bottom) [(a) and (e)]. Initially, there are building blocks of two non-interacting species: light-absorbing [red, Fig. 2(a)] and non-absorbing [blue, Fig. 2(b)] spherical colloidal particles, which perform standard Brownian motion. [(b) and (f)] When the sample is illuminated, the absorbing particles warm their surroundings, and when they randomly meet a non-absorbing particle, they stick together forming a self-propelling Janus dimer [Fig. 2(c)]. [(c) and (g)] As time passes, the dimers collect additional particles and more complex structures emerge, which feature more complex behaviors, such as *migrators* [Figs. 2(c)–2(e)], *stators* [Fig. 2(f)], *spinners* [Fig. 2(g)], and *rotators* [Fig. 2(h)]. [(d) and (h)] When the illumination is switched off, the active molecules disassemble and their component particles diffuse away. The simulations use 1 μm and 1 s as length and time units, respectively, and values of the particle radii, diffusion constants, and pair-molecule velocities as in the experiments (see Appendix B for a detailed discussion). The scale bar is 10 μm, and the laser intensity is $I = 80 \ \mu W \ \mu m^{-2}$. Multimedia view: https://doi.org/10.1063/1.5079861.1

[Fig. 1(a) (Multimedia view)], as can also be seen from their trajectories [Figs. 2(a) and 2(b)]. However, when illuminated, the fluid heats up only in the vicinity of the light-absorbing particles so that the fluid locally demixes and induces attractive interactions with other particles in the vicinity. The strength of the attractive interactions increases when enhancing the laser power, while control experiments in water show that no molecules form. When an absorbing microsphere comes close to a non-absorbing one, we observe the formation of a heterogeneous dimer [Fig. 1(b) (Multimedia view)], which, unlike the colloidal building blocks it consists of, starts to move ballistically. This ballistic motion is forbidden in equilibrium and is therefore not a simple consequence of symmetry breaking, but is also involves nonequilibrium fluctuations. In analogy to self-propelled Janus colloids, we call the emerging dimer a *Janus dimer*. Janus dimers represent the simplest active molecules. Their speed and rotational diffusion amounts to $v_2 = 2.0 \pm 0.4\ \mu\text{m s}^{-1}$ and $D_r = 0.11 \pm 0.05\ \text{s}^{-1}$. In the course of our experiments, the size of the molecules

keeps on growing as time passes and clusters coalesce: the dimers move around and collect additional particles so that more complex structures emerge, which feature more complex behaviors, as shown in Fig. 1(c) (Multimedia view). These behaviors are intimately linked to the symmetry properties of the resulting active molecules. There are axis-symmetric molecules that behave as *migrators* performing linear active Brownian motion, such as dimers [Fig. 2(c)], trimers [Fig. 2(d)], as well as larger structures [Fig. 2(e)], which move with the absorbing microsphere in front.[34–38] More symmetric shapes perform standard Brownian motion, behaving as *stators* [i.e., passive colloidal molecules, Fig. 2(f)]. Finally, chiral shapes behave as either *spinners* [Fig. 2(g)] or *rotators* [Fig. 2(h)], featuring different forms of chiral active Brownian motion. Importantly, the assembly mechanism of these active molecules is fully reversible and they melt by thermal diffusion when the light is switched off [Fig. 1(d) (Multimedia view)]. The speed and rotation frequency of these molecules depend on the details
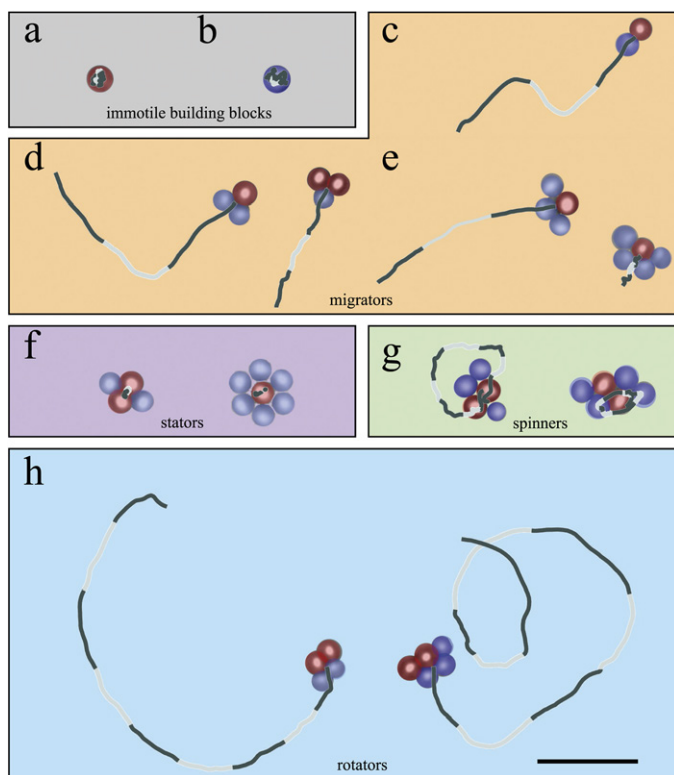
FIG. 2. **The zoological garden of active molecules.** While the constituting building blocks are immotile symmetric spherical (a) light-absorbing and (b) non-absorbing particles, the emerging active molecules present more and more complex shapes and behaviors as time evolves. We observe (c) dimers, (d) trimers, and (e) more complex axis-symmetric active molecules, which perform linear active Brownian motion (*migrators*); (f) highly symmetric molecules that do not show activity (*stators*); (g) rotationally symmetric chiral active molecules which rotate almost without translating (*spinners*); and (h) asymmetric chiral active molecules which swim in circles (*rotators*). In all cases, lines represent particle trajectories; grey and black segments correspond to 1-s stretches. The scale bar is 5 μm.
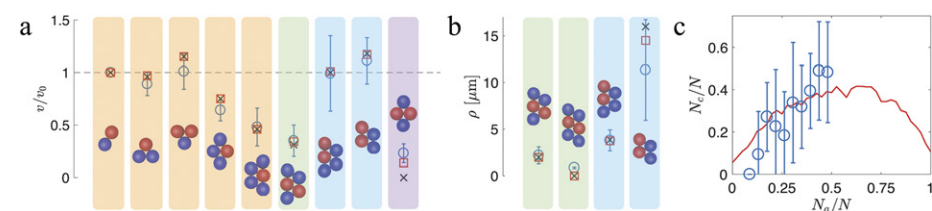
FIG. 3. **Quantitative agreement between experiments, simulations, and analytical predictions.** (a) The speed v (normalized by the speed of the dimer v_0) and (b) swimming radius ρ of active molecules obtained experimentally from the measured trajectories (blue circles and relative error bars representing a standard deviation), numerically from the simulated trajectories (red squares), and analytically for $D = 0$ from Eqs. (B7) and (B8) (black crosses) are all in good agreement. The molecules are given colored backgrounds depending on their classification reported in Fig. 2. (c) Chirality control: The fraction of chiral active molecules (N_c/N) can be controlled by the fraction of absorbing particles (N_a/N) in the initial suspension. The blue circles and relative error bars representing a standard deviation are the experimental data, and the red solid line represents the simulation results. Simulation parameters in Appendix B.

of their structure and composition, as shown in Figs. 3(a) and 3(b). However, for very large molecules ($N \to \infty$), where the phoretic drift contributions of the absorbing–non-absorbing pairs are distributed randomly within a molecule, for statistical reasons, they scale with $N^{-1/2}$, where N is the number of monomers in the molecule. All molecules generally attract each other. For the laser power used in Fig. 1 (Multimedia view), these interactions are strong enough to bind colliding molecules together. However, for appropriate weaker attractions (at a lower laser power of only $I = 13\ \mu\text{W}\ \mu\text{m}^{-2}$), dimers do not grow towards larger molecules allowing to generate a gas containing only monomers and dimers.

B. Theoretical model

To identify the key ingredients determining the emergence and dynamics of the colloidal molecules, we develop a phenomenological model based on the interplay of attractive (Lennard-Jones) interactions and particle diffusion inducing molecule formation, and the presence of nonreciprocal phoretic interactions creating self-propulsion of the molecules (see Appendix B for equations). The model describes a mixture of light-absorbing and non-absorbing overdamped Brownian (slightly soft) disks with radii R = 0.49 μm following overdamped Langevin dynamics including Gaussian white noise, which represents monomer diffusion and will automatically determine translational and rotational diffusion of the emerging molecules. We define the interactions among the individual colloids based on the following physical picture. Light-absorbing particles act as sources of phoretic fields (mainly temperature) in the near-critical binary liquid.[37,38,40] The gradients of these fields create a stress in the interfacial layer of all other colloids, which drives a solvent slip over their surfaces, leading to directed motion (phoresis) towards the absorbing particles.[27] Thus, light-absorbing particles attract each other reciprocally and non-reciprocally attract non-absorbing particles. In particular, when a non-absorbing particle closely approaches an absorbing one (distance 2R), it still experiences a gradient and pushes the absorbing particle forward, leading to directed motion of the

absorbing–non-absorbing pair. (In addition, the non-absorbing particle displaces the relevant phoretic fields so that the absorbing particle itself experiences a phoretic gradient leading to phoretic motion; this can support its directed motion.) When several non-absorbing particles attach to an absorbing one, they collectively push it forward, i.e., the nonreciprocal "forces" in a corresponding molecule essentially superimpose in competition with the overall drag force, the molecule's speed. Here, the involved phoretic fields might be effectively screened, e.g., due to heat-absorption processes or bulk-reactions[27] (unscreened phoretic attractions decaying quadratically with distance would provoke a rapid collapse of the system), so that their typical range extends over a few particle diameters. These interactions are supported by short-ranged attractions (van der Waals and perhaps critical Casimir interactions), which bind the particles in a molecule almost rigidly together. We phenomenologically model this using Lennard-Jones interactions, supplemented by nonreciprocal one-way attractions of non-absorbing particles by absorbing ones.

1. Speed and rotation rates

Here, we fix the strength of the nonreciprocal one-way attractions at contact distance (2R) by matching the dimer speed in our model (given by the non-reciprocal force at contact distance over Stokes drag force of the dimer) with experiments. The only remaining parameter to predict speed and rotation rates of all other molecules emerges from the fact that non-absorbing particles attaching to a molecule already containing non-absorbing particles (see a displaced phoretic field); thus, non-absorbing particles attaching adjacently to an absorbing one mutually reduce their contributions to the molecules' propulsion speed slightly. This reduction factor is fixed phenomenologically, as discussed in Appendix B. No further parameters are needed to predict the speed and the rotation rate of a given molecule, which can be done analytically in the absence of noise, based on force and torque balance equations (see Appendix B and the supplementary material). This allows us to predict the speed and rotation rates of all molecules in Fig. 3(a), quantitatively reproducing experiments.

### 2. Dynamics of molecule formation

To explore also the dynamics of molecule formation, we next perform Brownian dynamics simulations of our model. Here, we additionally account for the fact that nonabsorbing particles weakly attract each other in our experiments, if an absorbing particle is nearby. (In particular, they stay close to each other within a molecule rather than moving along the rim of an absorbing particle.) This weak attraction among nonabsorbing particles might result from a temperature dependence of the viscosity of the binary fluid, but could also involve, e.g., critical Casimir interactions activated by the absorbing colloids in the near-critical solvent. In our model, we account for these weak attractions by replacing excluded volume repulsions among nonabsorbing colloids with Lennard-Jones interactions with a small coefficient, if an absorbing particle is closer than a critical radius. (The choice of the coefficient and critical radius does not significantly influence the model's phenomenology.) Now simulating this model (see Appendix B for equations and details) using Brownian dynamics simulations, we observe the formation of active molecules as in the experiments, as shown by Figs. 1(e)–1(h) (Multimedia view): from a primordial broth of immotile single particles [Fig. 1(e) (Multimedia view)], first dimers form [Fig. 1(f) (Multimedia view)] and later grow into more complex active molecules [Fig. 1(g) (Multimedia view)]. Switching off the attractive interactions (corresponding to switching off the illumination in the experiment), the active molecules disassemble and their constituent particles diffuse away from each other [Fig. 1(h) (Multimedia view)]. Besides this qualitative agreement, our simulations allow us to extract the speed and rotation rates of the emerging molecules in the presence of Brownian noise (diffusion coefficient matched to experiments). Discretizing the simulated trajectory at 0.1 s (10 Hz), as in experiments, and then using finite differences to calculate speeds and swimming radii (i.e., speed over rotation frequency) allows for a quantitative comparison with experiments and our previous analytical calculations in the noise-free case. The blue circles in Fig. 3(a) represent experimentally measured speeds of various active molecules relative to the dimer speed, whereas red squares and black crosses show speed values found in analytical calculations and simulations, which are in quantitative agreement with the experimental results [Note that diffusion causes a finite speed even in perfectly symmetric molecules as can be seen in Fig. 3(a), right]. Blue circles in Fig. 3(b) represent the experimentally measured swimming radii ρ of various chiral active molecules ($\rho = \infty$ for achiral molecules), whereas the red squares represent the corresponding swimming radii obtained from the simulations, which also agree broadly with the experimental results.

Our model applies to rather small molecules (up to about 10 monomers) and also to large molecules containing a low fraction of absorbing particles; for a high density of absorbing particles, in the experiments, the solvent heats up over an extended spatial region leading to a breakdown of the short-range attractions and to the emergence of repulsive forces between the absorbing and the non-absorbing particles.

C. Controlling the clusters' behavior and functionality

The emergent behavior and functionality of this system can be controlled through a wealth of parameters. For example, in Fig. 3(c) we show that it is possible to change the fraction of achiral [e.g., Figs. 2(c)–2(e)] versus chiral [e.g., Figs. 2(g) and 2(h)] active molecules by changing the relative abundance of absorbing versus non-absorbing particles present in the initial suspension. The relative abundance of chiral active molecules increases with increasing deviation of the absorbing particle fraction from both 0 and 1. We can understand this result considering that only molecules featuring a common symmetry axis of composition and shape [Figs. 2(c)–2(e)] swim linearly, while molecules not featuring such a symmetry [Figs. 2(f) and 2(g)] are generally chiral (exceptions are molecules where rotational torques balance unsystematically); while such a symmetry is generally present for molecules consisting of only two or three individual colloids, all active molecules that break it involve at least two absorbing and two non-absorbing spheres. This latter requirement for being chiral is fulfilled for more molecules when the ratio of absorbing and non-absorbing colloids in the initial ensemble approaches 1/2. Also in this case, we find a good agreement between our experimental results [blue symbols in Fig. 3(c)] and the results of the simulations (red solid line). In fact, the simulations permit us to go beyond what can be realized experimentally as in experiments large assemblies including many absorbing colloids increase the temperature well beyond the critical point, inducing strong demixing around the colloids that prevents the formation of stable molecules involving attractive interactions. Also in this case, our simulations confirm the expectation described above, that the fraction of chiral to non-chiral molecules increases with increasing deviation of the fraction of absorbing to non-absorbing colloids from 1.

We can control the formation and growth of the molecules by tuning the light illumination. For example, it is possible to inhibit the formation of molecules larger than dimers by reducing the illumination to the minimum value ($I = 13 \, \mu W \, \mu m^{-2}$) where attraction between absorbing and non-absorbing monomers still occurs: Monomers can easily bind to each other but not to dimers; when occasionally trimers emerge, they typically decay on timescales of a few seconds. For higher levels of illumination ($I > 20 \, \mu W \, \mu m^{-2}$), the active molecules keep on growing in size indefinitely, if the illumination is constantly switched on. Despite this fact, we can control their size, shape, and functionality by subjecting them to periodic illumination. This is interesting because many natural phenomena are subject to periodic excitation (e.g., circadian rhythms, molecular clocks) and can be exploited to engineer artificial systems (e.g., autonomous nanorobots). For example, we can consider a periodic pattern of illumination where the illumination is alternatively switched on and off. Figure 4(a) (Multimedia view) shows that the active molecules that assemble when the light is periodically on for 5 s and off for 60 s are predominantly dimers and trimers, with few larger active molecules; this is in good agreement with simulations [Fig. 4(b) (Multimedia view)]. As the illumination time increases, the
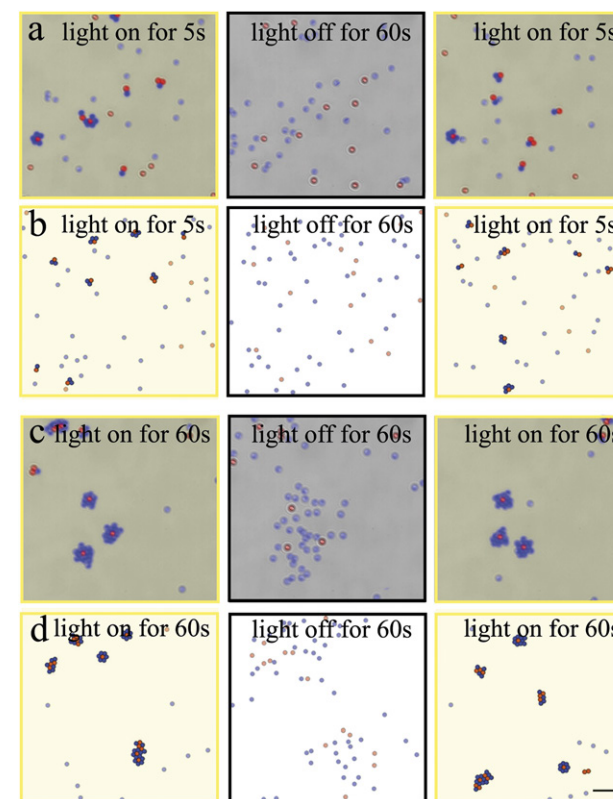
FIG. 4. **Controlling the assembly of active molecules by periodic illumination.** By subjecting the system to periodic illumination such that the light is periodically on for [(a) and (b)] 5 s and [(c) and (d)] 60 s and off always for 60 s, it is possible to assemble metastable active colloidal molecules with a controllable size, shape, and functionality, as their characteristic size increases with the light-on period. Each row features a series of three [(a) and (c)] experimental and [(b) and (d)] simulation snapshots taken at the end of a series of light-on, light-off, and light-on periods. Simulation parameters as in Fig. 1 (Multimedia view) and provided in Appendix B. The scale bar is 10 μm. Multimedia view: https://doi.org/10.1063/1.5079861.2

active molecules that form become larger and more complex and eventually will stop growing when the molecule has formed a large ring of non-absorbing particles around itself as shown in Fig. 4(c) (Multimedia view). Here, the light is periodically on for 60 s and off for 60 s, which is also in agreement with simulations [Fig. 4(d) (Multimedia view)].

III. DISCUSSION

We have demonstrated the light-controlled assembly of active colloidal molecules starting from a mixture of different species of immotile building blocks. These molecules spontaneously acquire motility through non-reciprocal interactions of their immotile components and represent a new route to create active matter. Our proof-of-principle setup serves as a construction kit to assemble modular linear swimmers, migrators, spinners, and rotators with light-controllable

shape, size, speed, and chirality. The table of the emerging active molecules and their characteristic properties can be quantitatively predicted by an effective model, which can be used in the future to design molecules and to predict their response to external fields, their large-scale collective behavior, and the properties of large molecules; the model may also be extended towards a more microscopic description[37,38] and to account for phoretic[46–49] and hydrodynamic interactions.[9,50] It will also be interesting to further explore the microscopic processes underlying the structure formation, explaining further how the structures are formed, how they can be controlled externally (e.g., by using spatiotemporal light modulators), and how individual molecules interact with each other. The exemplified route to create activity from immotile building blocks serves as a new design principle for active self-assembly. This might be useful both from a material perspective and to explore and design functionality in highly

controllable synthetic systems, which is so far often restricted to uncontrollable biological environments.

SUPPLEMENTARY MATERIAL

See supplementary material for a figure of the phase diagram of the water-2,6-lutidine mixture, a schematic of the experimental setup, and further details on the model of the forces employed in the simulations as well as experimental and simulated videos of the snapshots provided in Figs. 1 (Multimedia view) and 4 (Multimedia view).

ACKNOWLEDGMENTS

APPENDIX A: EXPERIMENTAL SETUP

We consider a suspension of colloidal particles in a critical mixture of water and 2,6-lutidine at the critical lutidine mass fraction $c_c = 0.286$ with a lower critical point at the temperature $T_c \approx 34\,^\circ C$[51] (see Fig. S1 of the supplementary material). The light-absorbing species consists of silica microspheres with absorbing iron-oxide inclusions (Microparticles GmbH), while the non-absorbing species consists of equally sized plain silica microspheres (Microparticles GmbH). Both particle species have the same radius ($R = 0.49 \pm 0.03\,\mu m$) and similar density ($\rho \approx 2\ g\ cm^{-3}$). The suspension is confined in a quasi-two-dimensional sample chamber realized between a microscope slide and a coverslip, where the particles sediment due to gravity.

A schematic of the setup is shown in Fig. S2 of the supplementary material. The motion of the particles is captured by digital video microscopy at 20 fps. Using a two-stage feedback temperature controller,[30,52] the temperature of the sample is adjusted to $T_0 = 31\,^\circ C$, which is below T_c so that water and 2,6-lutidine are homogeneously mixed. In these conditions, the microspheres of both species behave as independent immotile Brownian particles and undergo standard diffusion [Fig. 1(a) (Multimedia view)]. To illuminate the sample, we use a laser with a wavelength $\lambda = 532$ nm at an intensity $I = 80\ \mu W\ \mu m^{-2}$. The increase of temperature in the vicinity of the light-absorbing particles is rather small ($\Delta T \approx 4\,^\circ C$) so that they still diffuse as normal (non-active) Brownian particles. This is reflected also by the trajectories for the light-absorbing and non-absorbing particles in Figs. 2(a) and 2(b).

APPENDIX B: DETAILS OF THE MODEL

Following the physical picture discussed in the main text, (thermo-)phoretic interactions cause (i) mutual attractions among light-absorbing particles, (ii) nonreciprocal attractions of nonabsorbing particles towards absorbing particles (pushing them forward at close contact), and (iii) an additional phoretic drift of the absorbing particles when at close distance to a nonabsorbing particle, due to a displacement of the phoretic field by the latter, producing a gradient for the former. These phoretic effects are supported by short-range attractions among absorbing particles and particles in their vicinity (e.g., van der Waals and perhaps critical Casimir attractions in a near-critical solvent). Here, for simplicity, we phenomenologically model these effects as attractions between absorbing particles and all other particles, supplemented by a drift (nonreciprocal effective force) of absorbing-nonabsorbing pairs when in close distance (we assign these nonreciprocal forces to the absorbing particles; assigning them to the non-absorbing ones would equally work).

We now specifically define the model. To describe the dynamics of non-absorbing particles, we employ the following overdamped Langevin equation:[53]

$$\dot{\mathbf{r}}_i = -\frac{1}{\gamma}\sum_{j=1}^{N_a}\nabla_{\mathbf{r}_i}V_1(\mathbf{r}_i) - \frac{1}{\gamma}\sum_{j=1;j\neq i}^{N_p}\nabla_{\mathbf{r}_i}V_2(\mathbf{r}_i) + \sqrt{2D}\boldsymbol{\eta}_i(t), \quad (B1)$$

where the left sum extends over all N_a absorbing particles and the right one over all N_p non-absorbing particles (excluding particle i), γ is the Stokes drag coefficient (assumed to be independent from the distance to other particles), D is the Brownian diffusion coefficient, and $\boldsymbol{\eta}_i$ represents Gaussian white noise with zero mean and unit variance.

The pair-interaction potential V_1 represents Lennard-Jones interactions acting between the absorbing and non-absorbing particles representing van der Waals and other attractions

$$V_1(\mathbf{r}_{ij}) = 4\epsilon\left[\left(\frac{\sigma}{r_{ij}}\right)^{12} - \left(\frac{\sigma}{r_{ij}}\right)^6\right], \quad (B2)$$

where we have used $r_{ij} = |\mathbf{r}_{ij}|$, $\mathbf{r}_{ij} = \mathbf{r}_i - \mathbf{r}_j$, and ϵ is the depth of the potential which crosses zero at $r = \sigma = 2R/\epsilon^{1/6}$. Note that the precise form of the interactions does not affect the set of emerging molecules or their speeds and rotation rates; attractive Yukawa interactions in combination with Weeks-Chandler Anderson repulsions basically lead to the same results. In our simulations, we choose a cutoff distance of 8R for the Lennard-Jones interactions; also this choice does not affect the molecules and their speeds and hardly affects the kinetics of molecule formation.

Conversely to interactions among pairs involving an absorbing particle, interactions among non-absorbing particles are purely repulsive. However, when an absorbing particle is in the vicinity of one of the non-absorbing particles (we phenomenologically choose a critical distance of $r_c = 8R$), it heats up the solvent locally, leading to relatively weak attractions among the colloids. We therefore model the interactions among the non-absorbing particles as

$$\nabla_{\mathbf{r}_i}V_2(\mathbf{r}_{ij}) = \begin{cases} \nabla_{\mathbf{r}_i}V_1(\mathbf{r}_{ij}) & r_{ij} \leq 2R \\ \alpha\nabla_{\mathbf{r}_i}V_1(\mathbf{r}_{ij}) & r_{ij} > 2R \text{ and} \\ & \sum_{k=1}^{N_a}\theta(r_c - \max(r_{ik}, r_{jk})) > 0 \\ 0 & \text{otherwise,} \end{cases} \quad (B3)$$

where $\alpha \ll 1$ determines the relative interaction strength among non-absorbing particles compared to the interaction strength among absorbing particles. The key effect of the attractions among non-absorbing colloids in the vicinity of an absorbing one is that they tend to stay next to each other within a molecule, rather than moving almost freely along the rim of an absorbing particle.

When the laser is switched off, all particles are non-absorbing; however, when the laser is switched on, we describe the dynamics of absorbing particles by the following Langevin equation:

$$\dot{\mathbf{r}}_i = -\frac{1}{\gamma}\sum_{j=1;j\neq i}^{N}\nabla_{\mathbf{r}_i}V_1(\mathbf{r}_i) + \sum_{j=1}^{N_p}\mathbf{v}_{ij} + \sqrt{2D}\boldsymbol{\eta}_i(t), \quad (B4)$$

where we have introduced the phoretic drift velocity $\mathbf{v}_{ij} = \nu_{ij}\theta(r_p - r_{ij})\mathbf{r}_{ij}/r_{ij}^3$ describing the directed motion of non-absorbing particle i due to absorbing particle j. These drift terms represent the nonreciprocal contribution to the interaction of absorbing and nonabsorbing particles, and $\mathbf{F}_i = \gamma\sum_{j=1}^{N_p}\mathbf{v}_{ij}$ is the corresponding nonreciprocal force acting on particle i. Here, the values of ν_{ij} at contact distance 2R (see below) determine the speed and rotation rates of the molecules; the $1/r^2$-scaling and the cutoff at $r_p = 2.8R$ are arbitrary choices leading to a smooth onset of directed motion. Physically, such a directed motion occurs because gradients in the phoretic fields produce induce a stress in the interfacial layers of the non-absorbing particles leading to a localized solvent flow across their surface; this flow induces a directed motion of the non-absorbing particles towards the absorbing ones. When in close contact, the non-absorbing particles push the absorbing particles forward; at the same time, they displace the phoretic fields produced by the absorbing particles, which induces a phoretic motion of the absorbing particles themselves. Both effects lead to a directed motion of the absorbing–non-absorbing pairs.

Finally, we use the following expression for the coefficient of the phoretic velocity:

$$\nu_{ij} = \nu_0\left[1 - \frac{1}{6}\sum_{k=1,k\neq j}^{N_p}\theta(r_c - r_{jk})\right], \quad (B5)$$

where ν_0 determines the propulsion speed of an isolated absorbing–non-absorbing pair as $\nu_0/(8R^2)$. The term in square brackets accounts for the fact that adjacent non-absorbing particles attached to an absorbing one do not contribute fully independently to the propulsion-speed but mutually suppress their contributions slightly. This is partly caused by the fact that each non-absorbing particle displaces the phoretic field produced by an absorbing particle so that each additional non-absorbing particle attaching to an absorbing one sees a different phoretic field. This may be viewed as a mutual shielding of a part of the absorbing colloid's surface. Here, we phenomenologically assume that each non-absorbing particle covers an angle of $\theta = \pi/2$ (2D projection) of the surface of the absorbing colloids [see Fig. 3(a) of the supplementary material]. Thus, when two non-absorbing colloids adjacently attach to an absorbing colloid, the areas they cover overlap by an angle of $\theta_0 = \pi/6$ [see Fig. 3(b) of the supplementary material], reducing $\nu_0 \to 5\nu_0/6$. Analogously, the contribution of a non-absorbing colloid in between two other ones is reduced by a factor of 1/3. This is represented by the sum in Eq. (B5), where r_c is an arbitrary value which must be chosen slightly larger than 2R (here $r_c = 2.3R$).

1. Choice of parameters

Here, we provide the parameters we used in the implementation of the simulations. As discussed in the main text, the speed and the rotation rate can be predicted based on two parameters, the dimer speed (or ν_0) and the "shielding" angle θ (set to $\pi/2$ above) alone. Other parameters, most of which can be extracted from experiments, are relevant only to understand the dynamics of molecule formation. To allow for a straightforward comparison with experiments, we use $1\,\mu m$ and 1 s as length and time units in all the simulations. For Figs. 1 (Multimedia view) and 4 (Multimedia view), we have used $R = 0.49\,\mu m$ and $D = 0.1\,\mu m^2\ s^{-1}$. We have further chosen $\epsilon/\gamma = 10$, i.e., $\epsilon/(kT) = 100$, so that the molecules, once formed, are robust against thermal fluctuations, as in the experiments. We use $\nu_0 = 24R^2$ yielding a dimer speed of ≈ 3, or $3\,\mu m/s$, similar as in experiments. Finally, choosing $\alpha = 1/20$ yields a comparatively weak mutual attraction among non-absorbing particles [strength $\epsilon/(kT) = 5$], if an absorbing one is close by. In Fig. 3, which shows the molecule speed normalized by the pair speed, the absolute value of the propulsion speed is unimportant; here, we have chosen $\nu_0 = 80R^2$ for efficiency of the simulations. We have further used $R = 0.49\,\mu m$, $\epsilon/\gamma = 500$, and $\alpha = 1$ to strongly avoid fluctuations of the molecule shapes in the course of a simulation. Finally, we have used a somewhat stronger diffusion $D = 0.41\,\mu m^2\ s^{-1}$ [Figs. 3(a) and 3(b)] and $D = 0.195\,\mu m^2\ s^{-1}$ [Fig. 3(c)] to accelerate convergence of ensemble averages and the corresponding convergence of ensemble averages; here, noise is largely negligible (for the used sampling rate) as can be seen from the comparisons with the noise-free analytical calculations of the relative speed and rotation rates of the molecules which are practically identical to the simulated ones [Figs. 3(a) and 3(c)].

2. Analytical predictions of speed and rotation frequency of molecules

The speed, rotation radius, and reorientation frequency of a given molecule can be calculated analytically in the zero-noise limit by assuming hexagonal close packing within the molecule. Consider the molecule as a rigid body and the following balance conditions for the effective nonreciprocal forces $\mathbf{F}_i := \gamma\sum_{j=1}^{N_p}\mathbf{v}_{ij}$, evaluated at contact distance 2R ($\mathbf{F}_i = 0$ for non-absorbing particles), and the associated effective torques

$$\sum_{i=1}^{N}\mathbf{F}_i - \gamma\dot{\mathbf{r}}_i = 0, \quad \sum_{i=1}^{N}(\mathbf{r}_i - \mathbf{R})\times(\mathbf{F}_i - \gamma\dot{\mathbf{r}}_i) = 0, \quad (B6)$$

where we sum over all N particles in a molecule and choose $\mathbf{R}$ as the centre of mass of the molecule. From here, using polar coordinates, we readily find the considered molecule's velocity and rotation frequency as

$$\mathbf{v} = \dot{\mathbf{R}} = \frac{1}{N\gamma} \sum_{i=1}^{N} \mathbf{F}_i \qquad (B7)$$

and

$$\omega = \frac{1}{\gamma} \left| \frac{\sum_{i=1}^{N} \mathbf{x}_i \times \mathbf{F}_i}{\sum_{i=1}^{N} \mathbf{x}_i^2} \right|, \qquad (B8)$$

where $\mathbf{x}_i$ is the relative coordinate of sphere i with respect to the centre of mass of the active molecule. From Eq. (B8), the gyration radius ρ follows as $\rho = \frac{|\mathbf{v}|}{\omega}$. In Fig. 3(c) of the supplementary material, we exemplarily illustrate the analytical calculation of the swimming speed and swimming radius for a molecule consisting of 5 particles (2 absorbing and 3 non-absorbing).

REFERENCES

[1] V. N. Manoharan, M. T. Elsesser, and D. J. Pine, "Dense packing and symmetry in small clusters of microspheres," Science **301**, 483–487 (2003).

[2] E. Bianchi, J. Largo, P. Tartaglia, E. Zaccarelli, and F. Sciortino, "Phase diagram of patchy colloids: Towards empty liquids," Phys. Rev. Lett. **97**, 168301 (2006).

[3] Y. Wang, Y. Wang, D. R. Breed, V. N. Manoharan, L. Feng, A. D. Hollingsworth, M. Weck, and D. J. Pine, "Colloids with valence and specific directional bonding," Nature **491**, 51–55 (2012).

[4] T. A. Nguyen, A. Newton, D. J. Kraft, P. G. Bolhuis, and P. Schall, "Tuning patchy bonds induced by critical Casimir forces," Materials **10**, 1265 (2017).

[5] R. Niu, T. Palberg, and T. Speck, "Self-assembly of colloidal molecules due to self-generated flow," Phys. Rev. Lett. **119**, 028001 (2017).

[6] R. Niu, D. Botin, J. Weber, A. Reinmüller, and T. Palberg, "Assembly and speed in ion-exchange-based modular phoretic microswimmers," Langmuir **33**, 3450–3457 (2017).

[7] S. Ramaswamy, "The mechanics and statistics of active matter," Annu. Rev. Condens. Matter Phys. **1**, 323–345 (2010).

[8] A. M. Menzel, "Tuned, driven, and active soft matter," Phys. Rep. **554**, 1–45 (2015).

[9] A. Zöttl and H. Stark, "Emergent behavior in active colloids," J. Phys.: Condens. Matter **28**, 253001 (2016).

[10] C. Bechinger, R. Di Leonardo, H. Löwen, C. Reichhardt, G. Volpe, and G. Volpe, "Active particles in complex and crowded environments," Rev. Mod. Phys. **88**, 045006 (2016).

[11] F. Peruani, A. Deutsch, and M. Bär, "Nonequilibrium clustering of self-propelled rods," Phys. Rev. E **74**, 030904 (2006).

[12] D. B. Dusenbery, *Living at Micro Scale: The Unexpected Physics of Being Small* (Harvard University Press, 2009).

[13] R. Trask, H. Williams, and I. Bond, "Self-healing polymer composites: Mimicking nature to enhance performance," Bioinspiration Biomimetics **2**, P1 (2007).

[14] H. P. Narra and H. Ochman, "Of what use is sex to bacteria?," Curr. Biol. **16**, R705–R710 (2006).

[15] A. Ivlev, J. Bartnick, M. Heinen, C.-R. Du, V. Nosenko, and H. Löwen, "Statistical mechanics where Newton's third law is broken," Phys. Rev. X **5**, 011035 (2015).

[16] R. Soto and R. Golestanian, "Self-assembly of catalytically active colloidal molecules: Tailoring activity through surface chemistry," Phys. Rev. Lett. **112**, 068301 (2014).

[17] R. Soto and R. Golestanian, "Self-assembly of active colloidal molecules with dynamic function," Phys. Rev. E **91**, 052304 (2015).

[18] M. Popescu, M. Tasinkevych, and S. Dietrich, "Pulling and pushing a cargo with a catalytically active carrier," Europhys. Lett. **95**, 28004 (2011).

[19] L. Baraban, M. Tasinkevych, M. N. Popescu, S. Sanchez, S. Dietrich, and O. Schmidt, "Transport of cargo by catalytic Janus micro-motors," Soft Matter **8**, 48–52 (2012).

[20] J. Zhang, J. Yan, and S. Granick, "Directed self-assembly pathways of active colloidal clusters," Angew. Chem., Int. Ed. **55**, 5166 (2016).

[21] D. P. Singh, U. Choudhury, P. Fischer, and A. G. Mark, "Non-equilibrium assembly of light-activated colloidal mixtures," Adv. Mater. **29**, 1701328 (2017).

[22] S. Ilday, G. Makey, G. B. Akguc, Ö. Yavuz, O. Tokel, I. Pavlov, O. Gülseren, and F. Ö. Ilday, "Rich complex behaviour of self-assembled nanoparticles far from equilibrium," Nat. Commun. **8**, 14942 (2017).

[23] H. Löwen, "Active colloidal molecules," Europhys. Lett. **121**, 58001 (2018).

[24] F. Ma, S. Wang, D. T. Wu, and N. Wu, "Electric-field–induced assembly and propulsion of chiral colloidal clusters," Proc. Natl. Acad. Sci. U. S. A. **112**, 6307 (2015).

[25] F. Ma, X. Yang, H. Zhao, and N. Wu, "Inducing propulsion of colloidal dimers by breaking the symmetry in electrohydrodynamic flow," Phys. Rev. Lett. **115**, 208302 (2015).

[26] J. Palacci, S. Sacanna, A. P. Steinberg, D. J. Pine, and P. M. Chaikin, "Living crystals of light-activated colloidal surfers," Science **339**, 936 (2013).

[27] B. Liebchen and H. Löwen, "Which interactions dominate in active colloids?," preprint arxiv:1808.07389 (2018).

[28] T. Yu, P. Chuphal, S. Thakur, S. Y. Reigh, D. P. Singh, and P. Fischer, "Chemical micromotors self-assemble and self-propel by spontaneous symmetry breaking," Chem. Commun. **54**, 11933 (2018).

[29] C. Hertlein, L. Helden, A. Gambassi, S. Dietrich, and C. Bechinger, "Direct measurement of critical Casimir forces," Nature **451**, 172 (2008).

[30] S. Paladugu, A. Callegari, Y. Tuna, L. Barth, S. Dietrich, A. Gambassi, and G. Volpe, "Nonadditivity of critical Casimir forces," Nat. Commun. **7**, 11403 (2016).

[31] V. Nguyen, M. Dang, T. Nguyen, and P. Schall, "Critical Casimir forces for colloidal assembly," J. Phys.: Condens. Matter **28**, 043001 (2016).

[32] J. L. Anderson, "Colloid transport by interfacial forces," Annu. Rev. Fluid Mech. **21**, 61–99 (1989).

[33] R. Golestanian, T. B. Liverpool, and A. Ajdari, "Propulsion of a molecular machine by asymmetric distribution of reaction products," Phys. Rev. Lett. **94**, 220801 (2005).

[34] G. Volpe, I. Buttinoni, D. Vogt, H.-J. Kümmerer, and C. Bechinger, "Microswimmers in patterned environments," Soft Matter **7**, 8810 (2011).

[35] I. Buttinoni, G. Volpe, F. Kümmel, G. Volpe, and C. Bechinger, "Active Brownian motion tunable by light," J. Phys.: Condens. Matter **24**, 284129 (2012).

[36] F. Kümmel, B. ten Hagen, R. Wittkowski, I. Buttinoni, R. Eichhorn, G. Volpe, H. Löwen, and C. Bechinger, "Circular motion of asymmetric self-propelling particles," Phys. Rev. Lett. **110**, 198302 (2013).

[37] A. Würger, "Self-diffusiophoresis of Janus particles in near-critical mixtures," Phys. Rev. Lett. **115**, 188304 (2015).

[38] S. Samin and R. Van Roij, "Self-propulsion mechanism of active Janus particles in near-critical binary mixtures," Phys. Rev. Lett. **115**, 188305 (2015).

[39] I. Theurkauff, C. Cottin-Bizonne, J. Palacci, C. Ybert, and L. Bocquet, "Dynamic clustering in active colloidal suspensions with chemical signaling," Phys. Rev. Lett. **108**, 268303 (2012).

[40] I. Buttinoni, J. Bialké, F. Kümmel, H. Löwen, C. Bechinger, and T. Speck, "Dynamical clustering and phase separation in suspensions of self-propelled colloidal particles," Phys. Rev. Lett. **110**, 238301 (2013).

[41] P. H. Colberg and R. Kapral, "Nanoconfined catalytic Angström-size motors," J. Chem. Phys. **143**, 184904 (2015).

[42] S. H. Klapp, "Collective dynamics of dipolar and multipolar colloids: From passive to active systems," Curr. Opin. Colloid Interface Sci. **21**, 76–85 (2016).

[43] S. Ebbens, "Active colloids: Progress and challenges towards realising autonomous applications," Curr. Opin. Colloid Interface Sci. **21**, 14–23 (2016).

[44] M. C. Marchetti, Y. Fily, S. Henkes, A. Patch, and D. Yllanes, "Minimal model of active colloids highlights the role of mechanical interactions in controlling the emergent behavior of active matter," Curr. Opin. Colloid Interface Sci. **21**, 34–43 (2016).

[45] J. Happel and H. Brenner, *Low Reynolds Number Hydrodynamics* (Springer Science & Business Media, 2012), Vol. 1.

[46] S. Saha, R. Golestanian, and S. Ramaswamy, "Clusters, asters, and collective oscillations in chemotactic colloids," Phys. Rev. E **89**, 062316 (2014).

[47] O. Pohl and H. Stark, "Dynamic clustering and chemotactic collapse of self-phoretic active particles," Phys. Rev. Lett. **112**, 238303 (2014).

[48] B. Liebchen, D. Marenduzzo, I. Pagonabarraga, and M. Cates, "Clustering and pattern formation in chemorepulsive active colloids," Phys. Rev. Lett. **115** (2015).

[49] B. Liebchen, D. Marenduzzo, and M. E. Cates, "Phoretic interactions generically induce dynamic clusters and wave patterns in active colloids," Phys. Rev. Lett. **118**, 268001 (2017).

[50] S. C. Takatori and J. F. Brady, "Forces, stresses and the (thermo?) dynamics of active matter," Curr. Opin. Colloid Interface Sci. **21**, 24–33 (2016).

[51] C. A. Grattoni, R. A. Dawe, C. Y. Seah, and J. D. Gray, "Lower critical solution coexistence curve and physical properties (density, viscosity, surface tension, and interfacial tension) of 2,6-lutidine + water," J. Chem. Eng. Data **38**, 516 (1993).

[52] F. Schmidt, A. Magazzù, A. Callegari, L. Biancofiore, F. Cichos, and G. Volpe, "Microscopic engine powered by critical demixing," Phys. Rev. Lett. **120**, 068004 (2018).

[53] G. Volpe, S. Gigan, and G. Volpe, "Simulation of the active Brownian motion of a microswimmer," Am. J. Phys. **82**, 659–664 (2014).
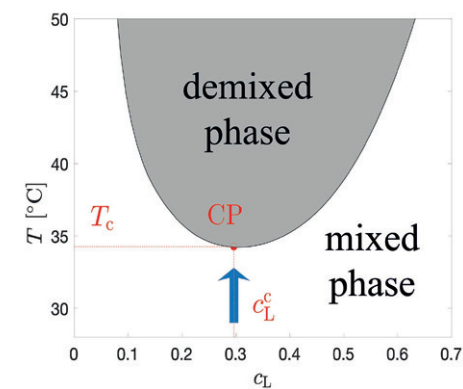
Light-controlled assembly of active colloidal molecules

Supplemental Materials

Falko Schmidt,[1, *] Benno Liebchen,[2, *] Hartmut Löwen,[2, †] and Giovanni Volpe[1, ‡]

[1] *Department of Physics, University of Gothenburg, SE-41296 Gothenburg, Sweden*

[2] *Institut für Theoretische Physik II: Weiche Materie,*

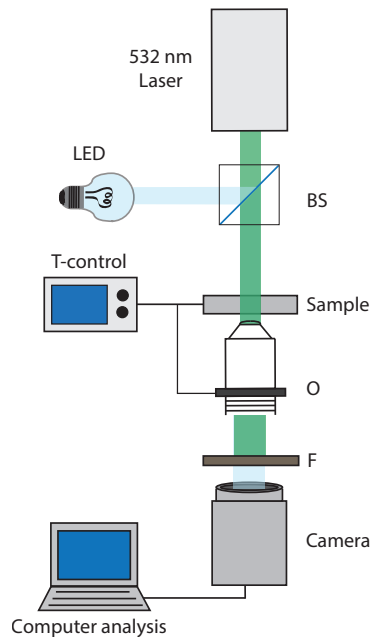*Heinrich-Heine-Universität Düsseldorf, D-40225 Düsseldorf, Germany*

1

Supplementary Figure 1. Phase diagram of the water-2,6-lutidine mixture The water-2,6-lutidine mixture features a lower critical point (CP) at the bottom of the coexistence line (solid line). The system is prepared at the critical lutidine mass fraction $c_c = 0.286$ and at a temperature $T_0 = 31°C$ significantly below the critical temperature $T_c \approx 34°C$ (arrow). The data are obtained from Ref. [1].

---

[*] FS and BL contributed equally

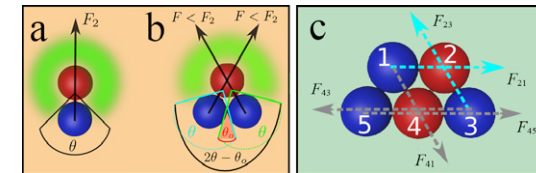[†] hlowen@hhu.de

[‡] giovanni.volpe@physics.gu.se

Supplementary Figure 3. Model for the forces. (a) The model assumes that each non-absorbing (blue) particle effectively shields part of the absorbing (red) particle surface, which can be characterized by an angle θ. (b) The shielding effect of adjacent blue particles may partly cancel their contributions to self-propulsion and lead to an overlap angle θ_{o} (red shaded area), reducing the overall adsorption angle to $2\theta - \theta_{\mathrm{o}}$. (c) Forces occurring for a five-sphere swimmer. Red and blue spheres represent absorbing and non-absorbing colloids respectively.

We now exemplarily illustrate the analytical calculation of the swimming speed and swimming radius for the molecule shown in (c) where red and blue spheres represent absorbing and non-absorbing colloids respectively. In the reference system of the centre of mass of the shown molecule, the coordinate vectors of the five hexagonally close-packed spheres read

$$\mathbf{x}_1 = R\left(-1, 3\sqrt{3}/5\right),$$
$$\mathbf{x}_2 = R\left(1, 3\sqrt{3}/5\right),$$
$$\mathbf{x}_3 = R\left(2, -2\sqrt{3}/5\right),$$
$$\mathbf{x}_4 = R\left(0, -2\sqrt{3}/5\right),$$
$$\mathbf{x}_5 = R\left(-2, -2\sqrt{3}/5\right).$$

The effective nonreciprocal forces produced by pairs of red and blue particles which act at the locations of the red spheres (spheres 2 and 4) read

$$\mathbf{F}_2 = \mathbf{F}_{23} + \mathbf{F}_{21} = F_2\left(\frac{\mathbf{x}_2 - \mathbf{x}_3}{|\mathbf{x}_2 - \mathbf{x}_3|} + \frac{\mathbf{x}_2 - \mathbf{x}_1}{|\mathbf{x}_2 - \mathbf{x}_1|}\right),$$
$$\mathbf{F}_4 = \mathbf{F}_{41} + \mathbf{F}_{43} + \mathbf{F}_{45}$$
$$= F_2\left(\frac{5}{6}\frac{\mathbf{x}_4 - \mathbf{x}_1}{|\mathbf{x}_4 - \mathbf{x}_1|} + \frac{\mathbf{x}_4 - \mathbf{x}_3}{|\mathbf{x}_4 - \mathbf{x}_3|} + \frac{5}{6}\frac{\mathbf{x}_4 - \mathbf{x}_5}{|\mathbf{x}_4 - \mathbf{x}_5|}\right),$$

where F_2 is the magnitude of the effective force occurring for a linear 2-sphere swimmer. The 5/6-coefficients represent shielding overlaps as illustrated in (b) and discussed in the definition of the model in the Methods. From here, we can readily determine the speed of the swimmer as

$$|\mathbf{v}| = \frac{|\mathbf{F}_2 + \mathbf{F}_4|}{5\gamma} = \frac{1}{5}\sqrt{\frac{7}{2}}v_2 \approx 0.31v_2, \tag{1}$$

where we have employed the relation $2\gamma v_2 = F_2$ holding true for the 2-sphere-swimmer (γ is the Stokes drag coefficient for a single colloid). The rotation rate follows as:

$$\omega = \frac{1}{\gamma}\left|\frac{\sum_{i=1}^{N}\mathbf{x}_i \times \mathbf{F}_i}{\sum_{i=1}^{N}\mathbf{x}_i^2}\right| = \frac{3\sqrt{3}F_2}{136R\gamma} = \frac{6\sqrt{3}v_2}{136R}, \tag{2}$$

where ω and the associated cycle period $T = 2\pi/\omega$, depend on the explicit value of the pair velocity v_2. However, the swimming radius, which can be determined as $\rho = |\mathbf{v}|/\omega$ is independent of v_2 and reads $\rho \approx 1.96\,\mu$m for a particle radius of $R = 0.49\,\mu$m. This value can be easily compared with the experiment, even without requiring any information of the absolute speed of the pair swimmer.

2

Supplementary Figure 2. Schematic of the experimental setup. The setup consists of a homemade inverted microscope. The two-dimensional sample chamber is prepared using a microscopic slide and sealed with a cover glass separated by spacer particles (radius $R = 0.85 \pm 0.02\,\mu$m, Microparticles GmbH). The whole sample is illuminated using a LED lamp, reflected by a 50:50 beamsplitter (BS), collected by an objective (O, 100×, NA= 1.30), filtered by a filter (F) to eliminate the laser light, and projected onto a camera. The laser ($\lambda = 532\,$nm) inducing the attractions between the colloids illuminates the whole sample homogeneously. The sample is temperature-stabilized using a copper-plate heat exchanger coupled to a circulating water heat bath (T100, Grant Instruments) with ±50 mK temperature stability; the temperature is then fine-tuned (±3 mK) by two Peltier elements (TEC3-6, Thorlabs) attached to the microscope objective O using a feedback controller (TED4015, Thorlabs).

5.4 Paper IV: Measurement of anomalous diffusion using recurrent neural networks

Attached below is the full paper as published in Physical Review E as well as its accompanying Supplementary Information, providing more details on the two sets of experimental setups involved and the experimental data acquired. In addition, we provide details on the training and structure of the recurrent neural network.

4

[1] Grattoni, C. A., Dawe, R. A., Seah, C. Y. & Gray, J. D. Lower critical solution coexistence curve and physical properties (density, viscosity, surface tension, and interfacial tension) of 2,6-lutidine + water. J. Chem. Eng. Data **38**, 516 (1993).

Measurement of anomalous diffusion using recurrent neural networks

Stefano Bo,[1,*] Falko Schmidt,[2] Ralf Eichhorn,[1] and Giovanni Volpe[2]

[1]*Nordita, Royal Institute of Technology and Stockholm University, Roslagstullsbacken 23, SE-106 91 Stockholm, Sweden*
[2]*Department of Physics, University of Gothenburg, SE-412 96 Gothenburg, Sweden*

Anomalous diffusion occurs in many physical and biological phenomena, when the growth of the mean squared displacement (MSD) with time has an exponent different from one. We show that recurrent neural networks (RNNs) can efficiently characterize anomalous diffusion by determining the exponent from a single short trajectory, outperforming the standard estimation based on the MSD when the available data points are limited, as is often the case in experiments. Furthermore, the RNNs can handle more complex tasks where there are no standard approaches, such as determining the anomalous diffusion exponent from a trajectory sampled at irregular times, and estimating the switching time and anomalous diffusion exponents of an intermittent system that switches between different kinds of anomalous diffusion. We validate our method on experimental data obtained from subdiffusive colloids trapped in speckle light fields and superdiffusive microswimmers.

Anomalous diffusion underlies various physical and biological systems, such as the motion of microscopic particles in a crowded subcellular environment and the active dynamics of biomolecules in the cytoplasm [1–3]. While normal diffusion is characterized by a linear growth of the mean squared displacement (MSD) with time, anomalous diffusion features a nonlinear, power-law growth. If we consider a microscopic particle whose position is $X(t)$, its MSD is, in the stationary case,

$$E[(X(t+\tau) - X(t))^2] = K_\alpha \tau^\alpha, \qquad (1)$$

where α is the exponent characterizing the anomalous diffusion and K_α is a generalized diffusion coefficient with dimension [length^2 time$^{-\alpha}$]. The exponent α contains crucial information regarding the nature of these systems distinguishing standard diffusion ($\alpha = 1$) from anomalous diffusion ($\alpha < 1$ for subdiffusion and $\alpha > 1$ for superdiffusion). Therefore, it is crucial to be able to determine its value from experimental data. When large datasets are available, the exponent can be straightforwardly fitted from the empirical MSD [4–8], or using alternative techniques [9–15]. Most of these methods work under the assumption that the exponent does not change abruptly over the duration of the measurement, and require the particles' trajectory to be sufficiently long and to be sampled at regular time intervals (unless several trajectories are available for each case).

However, especially in single-molecule studies and in nonequilibrium experiments, the dynamic and unsteady character of the process under study and the variability of the environment restrict the possibility to collect large amounts of data under the exact same conditions [16]. Therefore, often one has only access to trajectories that are short (e.g., limited

measurement time [11,15,17]), that are sampled at irregular times (e.g., due to fluorophore blinking [17]), or whose diffusion properties change over time (e.g., intermittent anomalous diffusion [18–20]). In these cases, the standard approaches based on the MSD cannot be straightforwardly employed. Instead, suitable approaches need to be developed on a case-by-case basis—a process that is often time-consuming and subject to user bias.

Recently, data-driven approaches have emerged as an alternative paradigm to analyze experimental data in several branches of physics and biology [21,22]. While standard algorithms require the user to explicitly give rules to process the input data in order to obtain the sought-after result, data-driven algorithms are trained through a large series of input data and the corresponding desired outputs from which they autonomously determine the rules for recognizing patterns. In this way, data-driven approaches can make very efficient use of all the information contained in the available data. Neural networks are one of the most successful data-driven approaches in estimation and regression tasks due to their great ability to automatically learn from data [23,24]. This feature has been successfully employed in a number of tasks ranging from handwritten digits and image recognition to natural language translation [25]. Therefore, neural networks ideally complement standard techniques to perform inference in cases for which no standard algorithmic procedures are available. In fact, some seminal works have already applied machine-learning techniques to determine the properties of anomalous diffusion with a focus on identifying its underlying mechanisms [26–28]. We remark that, similarly to other advanced machine-learning techniques, neural networks often operate as black boxes and therefore should be applied carefully to new experimental data and situations, always testing and benchmarking their performance against established techniques.

In this Rapid Communication, we show that recurrent neural networks (RNNs) can successfully be employed to

characterize anomalous diffusion. While RNNs perform equally well as MSD approaches when characterizing the anomalous diffusion from sufficiently long, regularly sampled and stationary time series, RNNs marginally outperform MSD approaches when the available data points are limited, as is often the case in experiments. More importantly, RNNs can also straightforwardly deal with more complex cases for which there are no standard approaches: when trajectories are sampled at irregular sampling times, and when the system features an intermittent behavior. We validate the use of RNNs on experimental data obtained from colloids subdiffusing in a speckle light field [29,30] and microswimmers superdiffusing when illuminated [31].

Figures 1(a)–1(c) show some examples of experimental trajectories (128 measurement points each; see Supplemental Material [32]) corresponding to a colloidal microsphere (SiO_2, radius $R = 2.5\ \mu$m) undergoing subdiffusion in a speckle light field [29] [Fig. 1(a)], the same colloid without the speckle light field normally diffusing [Fig. 1(b)], and a microswimmer (SiO_2 microsphere with iron-oxide inclusions, $R = 0.49\ \mu$m) that superdiffuses in a critical mixture when illuminated by light [31] [Fig. 1(c)]. The time-averaged MSD is calculated from each of these trajectories as

$$\text{MSD}(\tau) = \frac{1}{T/\delta t - j + 1} \sum_{i=0}^{T/\delta t - j} (X_{i+j} - X_i)^2, \qquad (2)$$

where the discrete measurements $X_i = X(i\delta t)$ are taken at intervals δt, and the time lag is given by $\tau = j\delta t$. The corresponding MSDs are plotted by colored lines in log-log scale in Figs. 1(d)–1(f) and the value of the exponent is obtained from linear interpolation. Clearly, for these short trajectories a precise estimation of the exponent is challenging [16]: there is some arbitrariness in what segments of the trajectories or of the MSD plots to use for the fitting; and the choice depends on the specific α, on the measurement noise, and on the length of the trajectory, so that additional *a priori* knowledge about the system is required [33–35].

We propose a method based on RNNs to determine α directly from the single trajectories. RNNs are ideal to deal with time sequences because they process the input data sequence iteratively and, therefore, explicitly model the sequentiality of the input data [24,36]. In fact, differently from other neural network architectures that process the input data at once (e.g., dense and convolutional neural networks), RNNs loop over the input data sequence, keeping an internal model of the information they are processing, built from past information and constantly updated as new information arrives [24,36]. Thanks to their recurrent nature, RNNs typically require fewer layers to perform a given task than alternative neural network architectures; for example, the neural network that currently powers the Google Translate algorithm is a stack of just seven large "long short-term memory" (LSTM) layers [25]. We employ a RNN constituted of two LSTM layers with states of dimension 64 and 16, respectively, and a densely connected output layer, which provides the estimate of the exponent $\hat\alpha$ [32]. We have implemented this neural network using the Python-based Keras library [37] with a TensorFlow backend [38] because of their broad adoption in research and industry;
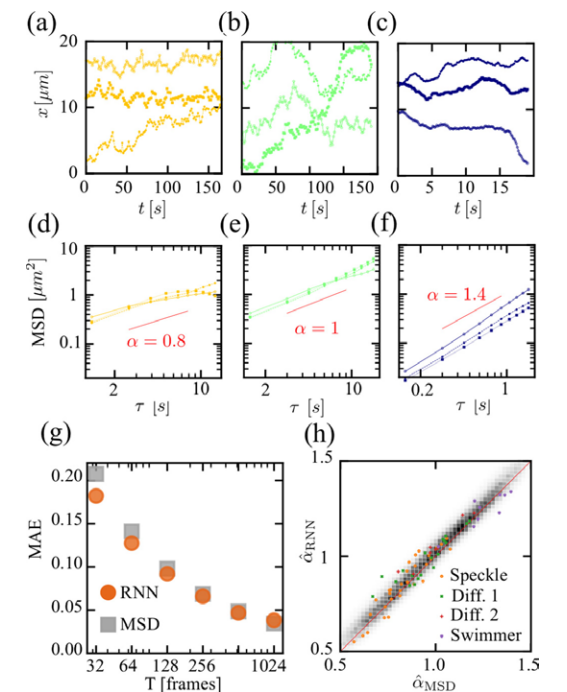

FIG. 1. Measurement of anomalous diffusion with recurrent neural networks (RNNs). (a)–(c) Experimental trajectories of a particle undergoing (a) subdiffusion (motion in a speckle light field), (b) normal diffusion, and (c) superdiffusion (light-activated microswimmer). (d)–(f) Corresponding MSDs. (g) Mean absolute error (MAE) of the exponent inferred using the standard time-averaged MSD (gray squares) and the RNNs (orange circles) as a function of the trajectory length. The performances are tested on 185 000 simulated trajectories undergoing fractional Brownian motion with α uniformly sampled between [0.5, 1.5]. (h) Exponents estimated by the RNNs vs those estimated by the MSD. The gray background represents a density plot of exponents obtained from simulated trajectories and the colored points represent exponents obtained from experimental data: orange circles for the subdiffusive colloids in a speckle light field, green "x" symbols for the same colloids freely diffusing, purple triangles for the superdiffusive microswimmers, and red plus symbols for the inactive microswimmers that diffuse normally.

nevertheless, we remark that the approach we propose is independent of the framework used for its implementation.

Once the network architecture is defined, we need to train it on a set of single trajectories for which we know the ground-truth values of α. For each trajectory containing T measurement points, the input data to the network is a $2 \times T$-dimensional array containing position and time for each measurement point $[(x_1, t_1), (x_2, t_2), \ldots, (x_T, t_T)]$ (suitably normalized so that the position's average and standard deviation of a trajectory are, respectively, 0 and 1 and the rescaled measurement times are between 0 and 1, as discussed in the Supplemental Material [32]). In each training step,

*Present address: Max Planck Institute for the Physics of Complex Systems, Nöthnitzer Str. 38, DE-01187 Dresden, Germany; stefabo@pks.mpg.de

the neural network is tasked with predicting the exponent corresponding to each trajectory from a batch of the training set; its predictions are then compared to the ground-truth values of the exponents; and the prediction errors are finally used to adjust the trainable parameters of the neural network using a back-propagation algorithm [24,36]. The training of a neural network is notoriously data intensive, requiring in our case several hundreds of thousand to millions of trajectories. In order to have enough trajectories and to accurately know the ground-truth values of the corresponding exponents, we simulate the trajectories. There are several models and mechanisms that can give rise to anomalous diffusion dynamics [3] and several methods to identify such models from data (e.g., [11,28,39–41]). We choose to train using fractional Brownian motion (fBm) [42], which is defined as a continuous-time Gaussian process $[B_\alpha(t)]$ with zero mean and correlated increments that give rise to the covariance function

$$E[B_\alpha(t)B_\alpha(s)] = \tfrac{1}{2}(|t|^\alpha + |s|^\alpha - |t - s|^\alpha), \qquad (3)$$

where α is the exponent with which the mean squared displacement grows [Eq. (3)]. We simulate the trajectories using the Davies-Harte and the Hosking algorithm [43] implemented in a Python library [44].

To assess the performance of the RNN, we test it on independently simulated trajectories with α uniformly sampled in [0.5, 1.5] against the MSD, because this is the most widespread and easy-to-use method in soft-matter and biophysics experiments. We linearly fit the time-averaged MSD for $\tau = 1, \ldots, 5$, which delivers a good performance for fractional Brownian motion in cases without measurement noise. In the case of the RNN, we train a different network for each of the different trajectories' lengths we consider. Figure 1(g) shows the mean absolute error (MAE) for the two methods as a function of the trajectory's length. For long trajectories, both methods perform similarly well with MAE for RNNs (MSD) 0.038 (0.035), 0.047 (0.049), and 0.066 (0.069) for trajectories with 1024, 512, and 256 samples, respectively. For shorter trajectories, which are known to be problematic for MSD-based methods [7,34], the RNN performs slightly better, achieving MAE 0.092 (vs 0.098 for the MSD), 0.127 (vs 0.141), and 0.182 (vs 0.207) for 128, 64, and 32 samples, respectively. This demonstrates that the RNN is able to extract information from the trajectories that is not used by the MSD. We remark that there is some variability in the performance of the networks across different trainings and that, focusing on a specific trajectory length, it is possible to further improve the predictions by fine-tuning the training and by pooling the predictions of different networks. In any case, the predictions made with the RNN and the MSD are strongly correlated, as can be seen in Fig. 1(h) where the estimations made using the RNN are plotted against the ones for the MSD for simulated trajectories of length 128. Importantly, even though the RNN is trained on a specific model for anomalous diffusion (fBM), it is able to generalize and to correctly analyze also experimental data for which we do not know the precise mechanism underlying the anomalous diffusion behavior. The colored points in Fig. 1(g) represent the estimations made using the RNN plotted against the ones for the MSD for the experimental data corresponding to
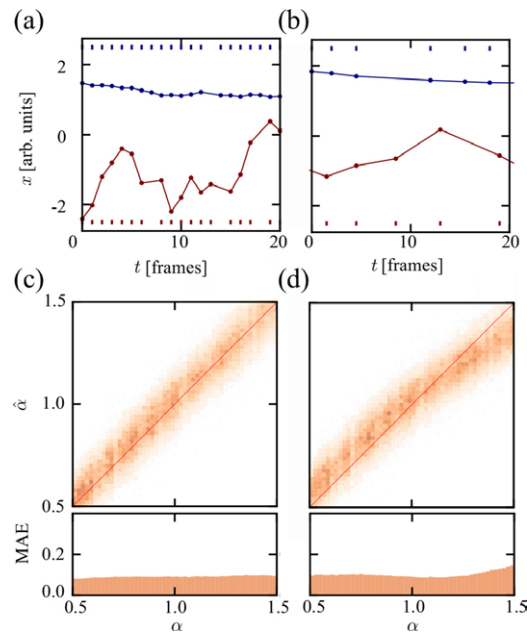

FIG. 2. Measurement of anomalous diffusion in irregularly sampled trajectories. Often a trajectory is sampled irregularly, either (a) because some data points are missing ("missing data," here 12.5% data points are missing), or (b) because data points are sampled at random times ("uneven data," here according to a geometric distribution). For each case, two trajectories with different α are shown. (c),(d) Estimated exponent $\hat{\alpha}$ as a function of the actual exponent α for the two cases using simulated trajectories with 128 frames. The lower panels show the MAE as a function of α. The MAE averaged over all α is 0.091 in (c) and 0.101 in (d). There exists a systematic bias in the more challenging "uneven data" case, visible in (d) for large α.

subdiffusive particles moving in a speckle light field (orange circles), to diffusive Brownian particles (green "x" and red "+" symbols), and to superdiffusive microswimmers (purple triangles). The RNN and MSD estimations are correlated in a similar way as for the data generated from simulations using a fBM model, providing strong evidence for the experimental reliability of the RNN method even when the underlying microscopic dynamics for the anomalous diffusion are other than fBM.

In the next step, we show that RNNs can be used to determine α in two cases where a straightforward computation of the MSD becomes challenging: trajectories are sampled at irregular times, and a system featuring an intermittent behavior.

The first situation is motivated by the fact that, in several experimental settings, it is not possible to record the trajectories at equally spaced time intervals. For example, the fluorescent biomarkers commonly employed for tracking biomolecules are subject to blinking so that some portion of a trajectory might be missing [17]. In general, tracking

algorithms might miss some frames, especially in noisy and challenging experimental conditions, leading to trajectories with missing data points. No standard technique exists to deal with these cases for single trajectories. Here, we test the RNNs, trained in Fig. 1 on trajectories sampled at regular times, on trajectories sampled at irregular times. We consider two scenarios: (a) a fraction of the regularly recorded data is missing ["missing data" scenario, Fig. 2(a)]; (b) the data points are sampled at random times ["uneven data" scenario, Fig. 2(b)]. As shown in Figs. 2(c) and 2(d), the RNN is in fact able to generalize to these cases. In particular, for the "missing data" scenario with 12.5% data points randomly missing, the performance of the network is unaffected as long as the same number of data points as in the training set (in this case 128) is fed into the RNN [Fig. 2(c)]. For case (b), with measurement times geometrically distributed so that on average one frame every eight contains a signal, the RNN provides reasonable predictions, which however are slightly biased and tend to underestimate large exponents [Fig. 2(d)]. For more accurate predictions, one can retrain the RNN on irregularly sampled simulated data and significantly improve its performance [32].

As the second situation, we consider systems featuring intermittent behavior, where the particle diffusion switches between different behaviors characterized by different α. Such behavior occurs, for instance, when particles are transiently trapped such as in sodium channels [18] or when self-propulsion is switched on and off [31]. Relying on traditional MSD measurements, one would first need to detect the change in behavior (e.g., using change-point analysis techniques [45]) and successively to estimate the exponents of the two subtrajectories. This is a challenging procedure, which has been attempted only recently for trajectories switching
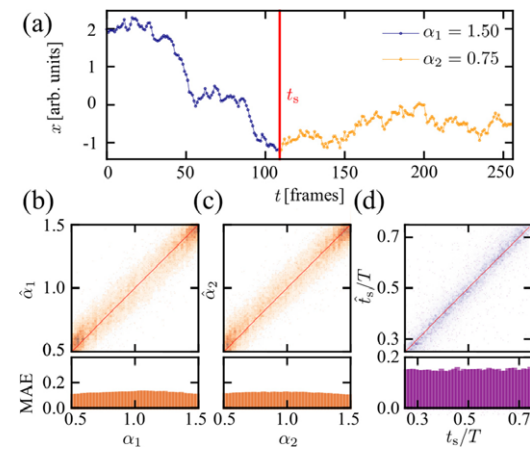

FIG. 3. Measurement of the switch between two anomalous diffusion behaviors. (a) Simulated trajectory of a particle whose exponent switches from $\alpha_1 = 1.50$ to $\alpha_2 = 0.75$ at time $t_s = 108$. Estimation by a RNN of (b) $\hat{\alpha}_1$, (c) $\hat{\alpha}_2$, and (d) $\hat{t}_s/T$ as a function of the respective ground-truth values, for a test data set where $|\Delta\alpha| > 0.25$, $t_s \in [0.25T, 0.75T]$, and $T = 256$.

between subdiffusive and superdiffusive dynamics [19,46]. We employ a modified version of the RNN discussed above to determine simultaneously the exponent before switching $\hat{\alpha}_1$, the exponent after switching $\hat{\alpha}_2$, and the switching time $\hat{t}_s$ from the acquired trajectory. Specifically, we use a network with the same architecture as before but with five output neurons that estimate $\hat{\alpha}_1$, $\hat{\alpha}_2$, $\Delta\hat{\alpha} = \hat{\alpha}_2 - \hat{\alpha}_1$, $\sin(2\pi\hat{t}_s/T)$, and $\cos(2\pi\hat{t}_s/T)$ (see [32]). We train this RNN on a set of 1.6-million simulated trajectories where a change in exponent occurs randomly with a uniform distribution at time t_s (see [32]). Figures 3(b)–3(d) show the performance of the estimations of $\hat{\alpha}_1$ [Fig. 3(b)], $\hat{\alpha}_2$ [Fig. 3(c)], and $\hat{t}_s$ [Fig. 3(d)], when the change in α is not too small ($|\Delta\alpha| > 0.25$) and the switch occurs around the middle of the trajectory ($t_s \in [0.25T, 0.75T] = [64, 192]$). Under these conditions, the performance in estimating $\hat{\alpha}_1$ [Fig. 3(b)], MAE 0.116] and $\hat{\alpha}_2$ [Fig. 3(c), MAE 0.112] is comparable to the case of constant α reported in Fig. 1. The switching-time estimation can be challenging when the change of the exponent is small or occurs very early or late. For $\hat{t}_s/T$ we have a MAE 0.148 as illustrated in Fig. 3(d).

In Fig. 4, we illustrate the power of the neural-network approach using an experimental trajectory. We consider a
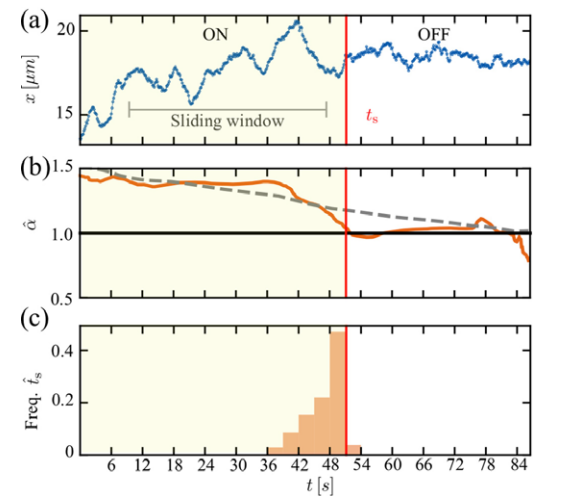

FIG. 4. Determination of anomalous diffusion exponents and switching time in an experimental time series by sliding a window containing 256 measurement points ($T = 38.3$ s). (a) Trajectory of a microswimmer activated by light ($\alpha \simeq 1.4$); at $t = 51.3$ s the light is switched off and the microswimmer becomes a passive Brownian particle ($\alpha = 1.0$). (b) Orange solid curve: exponent $\hat{\alpha}$ estimated by averaging the predictions of the RNN for each sliding window. For reference, the gray dashed curve reports the exponent $\hat{\alpha}$ estimated by averaging the predictions of the MSD for the same sliding windows. (c) Histogram of the switching times $\hat{t}_s$ estimated by the RNN. Each prediction is obtained from a different starting point of the sliding window and the histogram is built from reliable windows where $|\Delta\hat{\alpha}| > 0.25$ and the estimated change point is far from the boundaries of the window $\hat{t}_s \in [0.25T, 0.75T]$.

microswimmer, which undergoes superdiffusion ($\alpha \simeq 1.4$) when illuminated by light [31], and becomes diffusive when the light is turned off ($\alpha = 1.0$). Figure 4(a) shows the corresponding trajectory with a switching time at $t = 51.3$ s. We measure this switch using the RNN with a sliding window containing 256 measurement points (38.3 s). The estimated exponent (averaged over the various sliding windows) is shown in Fig. 4(b), where one can see that there is a clear shift from $\hat{\alpha} \simeq 1.4$ to $\hat{\alpha} = 1.0$ around $t = 50$ s. As a reference, we show the prediction from the MSD [gray curve in Fig. 4(b)] obtained by averaging the exponents inferred by a sliding window. One can see that, in this case, the transition between the high and low exponent is smoothed out and takes place in a longer time interval. One could try to alleviate the issue by choosing shorter window sizes but this would come at the cost of a noisier estimation. The histogram of the switching times predicted by the RNN in the different windows is shown in Fig. 4(c), where it can be seen that the network correctly determines the switching time.

In conclusion, we introduced an alternative method for the estimation of the exponent from single trajectories in anomalous diffusion systems based on RNNs. We have shown that it can be straightforwardly applied to more complex situations, where standard approaches are lacking. Our method then emerges as a promising tool for the analysis of single trajectories with irregular measurements and intermittent behaviors. We remark that our analysis has been limited to the case in which the observed time series can be described by a single exponent on the observation timescales (or a distinct switch between two exponents). In several systems, the MSD smoothly interpolates between different linear (in the log-log plot) regimes on different timescales (see, e.g., [5,7]). The approach we propose here should not be directly applied to

analyze such time series on timescales where the transition between different diffusive regimes occurs, but has to be separately applied to the different linear regimes. In general, when dealing with completely unseen data, before proceeding to a deeper analysis, it is advisable to benchmark the preliminary predictions of the RNN against the ones of the MSD. As future work, it will be interesting to test the inference of the RNN method trained on fBM simulated data on data obtained from different anomalous diffusion models, such as, for instance, continuous-time random walks. It would also be possible to train the RNN using simulated data not generated from fBM. Along these lines, it would be interesting to consider higher-order moments, which are sensitive to the specific kind of anomalous diffusion model; however, this will likely require a more extensive training. Another interesting extension would be to train a network on data of the type mentioned above which is characterized by different exponents on different timescales to infer the whole profile of the MSD as a function of time instead of separately considering its distinct diffusive regimes. This extension may not be completely trivial since one would have to learn more parameters that can be used to parametrize more general curves.

[1] E. Barkai, Y. Garini, and R. Metzler, Phys. Today **65**(8), 29 (2012).

[2] F. Höfling and T. Franosch, Rep. Prog. Phys. **76**, 046602 (2013).

[3] R. Metzler, J. H. Jeon, A. G. Cherstvy, and E. Barkai, Phys. Chem. Chem. Phys. **16**, 24128 (2014).

[4] I. Golding and E. C. Cox, Phys. Rev. Lett. **96**, 098102 (2006).

[5] I. Bronstein, Y. Israel, E. Kepten, S. Mai, Y. Shav-Tal, E. Barkai, and Y. Garini, Phys. Rev. Lett. **103**, 018102 (2009).

[6] S. C. Weber, A. J. Spakowitz, and J. A. Theriot, Phys. Rev. Lett. **104**, 238102 (2010).

[7] J. H. Jeon, N. Leijnse, L. B. Oddershede, and R. Metzler, New J. Phys. **15**, 045011 (2013).

[8] A. Caspi, R. Granek, and M. Elbaum, Phys. Rev. Lett. **85**, 5655 (2000).

[9] V. Tejedor, O. Bénichou, R. Voituriez, R. Jungmann, F. Simmel, C. Selhuber-Unkel, L. B. Oddershede, and R. Metzler, Biophys. J. **98**, 1364 (2010).

[10] K. Burnecki, E. Kepten, Y. Garini, G. Sikora, and A. Weron, Sci. Rep. **5**, 11306 (2015).

[11] Y. Meroz and I. M. Sokolov, Phys. Rep. **573**, 1 (2015).

[12] N. Makarava, S. Benmehdi, and M. Holschneider, Phys. Rev. E **84**, 021109 (2011).

[13] K. Hinsen and G. R. Kneller, J. Chem. Phys. **145**, 151101 (2016).

[14] D. Krapf, N. Lukat, E. Marinari, R. Metzler, G. Oshanin, C. Selhuber-Unkel, A. Squarcini, L. Stadler, M. Weiss, and X. Xu, Phys. Rev. X **9**, 011019 (2019).

[15] A. Weron, J. Janczura, E. Boryczka, T. Sungkaworn, and D. Calebiro, Phys. Rev. E **99**, 042149 (2019).

[16] J. H. Jeon and R. Metzler, J. Phys. A: Math. Theor. **43**, 252001 (2010).

[17] J. Elf and I. Barkefors, Annu. Rev. Biochem. **88**, 635 (2019).

[18] E. J. Akin, L. Solé, B. Johnson, M. E. Beheiry, J. B. Masson, D. Krapf, and M. M. Tamkun, Biophys. J. **111**, 1235 (2016).

[19] G. Sikora, A. Wyłomańska, J. Gajda, L. Solé, E. J. Akin, M. M. Tamkun, and D. Krapf, Phys. Rev. E **96**, 062404 (2017).

[20] A. Weron, K. Burnecki, E. J. Akin, L. Solé, M. Balcerek, M. M. Tamkun, and D. Krapf, Sci. Rep. **7**, 5404 (2017).

[21] L. Zdeborová, Nat. Phys. **13**, 420 (2017).

[22] S. Helgadottir, A. Argun, and G. Volpe, Optica **6**, 506 (2019).

[23] M. A. Nielsen, *Neural Networks and Deep Learning* (Determination Press, 2015).

[24] Z. C. Lipton, J. Berkowitz, and C. Elkan, arXiv:1506.00019.

[25] Y. Wu *et al.*, arXiv:1609.08144.

[26] T. Wagner, A. Kroll, C. R. Haramagatti, H.-G. Lipinski, and M. Wiemann, PLoS One **12**, e0170165 (2017).

[27] G. Muñoz-Gil, M. A. Garcia-March, C. Manzo, J. D. Martín-Guerrero, and M. Lewenstein, arXiv:1903.02850.

[28] N. Granik, L. E. Weiss, E. Nehme, M. Levin, M. Chein, E. Perlson, Y. Roichman, and Y. Shechtman, Biophys. J. (2019), doi:10.1016/j.bpj.2019.06.015.

[29] G. Volpe, G. Volpe, and S. Gigan, Sci. Rep. **4**, 3936 (2014).

[30] G. Volpe, L. Kurz, A. Callegari, G. Volpe, and S. Gigan, Opt. Express **22**, 18159 (2014).

[31] F. Schmidt, B. Liebchen, H. Löwen, and G. Volpe, J. Chem. Phys. **150**, 094905 (2019).

[32] See Supplemental Material at http://link.aps.org/supplemental/10.1103/PhysRevE.100.010102, including Refs. [47–49], for the description of the experimental setup and information on the neural network architecture and training.

[33] E. Kepten, I. Bronshtein, and Y. Garini, Phys. Rev. E **87**, 052713 (2013).

[34] E. Kepten, A. Weron, G. Sikora, K. Burnecki, and Y. Garini, PLoS One **10**, e0117722 (2015).

[35] Y. Lanoiselée, G. Sikora, A. Grzesiek, D. S. Grebenkov, and A. Wyłomańska, Phys. Rev. E **98**, 062139 (2018).

[36] S. Hochreiter and J. Schmidhuber, Neural Comput. **9**, 1735 (1997).

[37] F. Chollet and others, Keras, https://keras.io (2015).

[38] M. Abadi *et al.*, arXiv:1603.04467.

[39] M. Magdziarz, A. Weron, K. Burnecki, and J. Klafter, Phys. Rev. Lett. **103**, 180602 (2009).

[40] S. Thapa, M. Lomholt, J. Krog, A. G. Cherstvy, and R. Metzler, Phys. Chem. Chem. Phys. **20**, 29018 (2018).

[41] K. Burnecki, E. Kepten, J. Janczura, I. Bronshtein, Y. Garini, and A. Weron, Biophys. J. **103**, 1839 (2012).

[42] B. B. Mandelbrot and J. W. Van Ness, SIAM Rev. **10**, 422 (1968).

[43] T. Dieker, Simulation of Fractional Brownian Motion, MSc theses, University of Twente, Amsterdam, 2004.

[44] C. Flynn, Exact methods for simulating fractional Brownian motion and fractional Gaussian noise in python, https://github.com/crflynn/fbm.

[45] D. Montiel, H. Cang, and H. Yang, J. Phys. Chem. B **110**, 19763 (2006).

[46] G. Sikora, A. Wyłomańska, and D. Krapf, Comput. Stat. Data Anal. **128**, 380 (2018).

[47] I. Buttinoni, G. Volpe, F. Kümmel, G. Volpe, and C. Bechinger, J. Phys.: Condens. Matter **24**, 284129 (2012).

[48] F. Schmidt, A. Magazzù, A. Callegari, L. Biancofiore, F. Cichos, and G. Volpe, Phys. Rev. Lett. **120**, 068004 (2018).

[49] S. L. Smith, P.-J. Kindermans, C. Ying, and Q. V. Le, arXiv:1711.00489.

Measurement of Anomalous Diffusion
Using Recurrent Neural Networks
Supplemental Material

Stefano Bo,[1] Falko Schmidt,[2] Ralf Eichhorn,[1] and Giovanni Volpe[2]

[1]*Nordita, Royal Institute of Technology and Stockholm University,*
*Roslagstullsbacken 23, SE-106 91 Stockholm, Sweden*

[2]*Department of Physics, University of Gothenburg, SE-412 96 Gothenburg, Sweden*

(Dated: July 2, 2019)

EXPERIMENTAL DATA

Subdiffusion experiments

We use experiments with sub-diffusive particles to validate our recurrent neural network (RNN) approach for the determination of the exponent α of the mean square displacement (MSD). The sub-diffusive particles are colloids in speckle light fields [1, 2]. Speckle light fields occur due to the interference of light beams with different phases and generate random
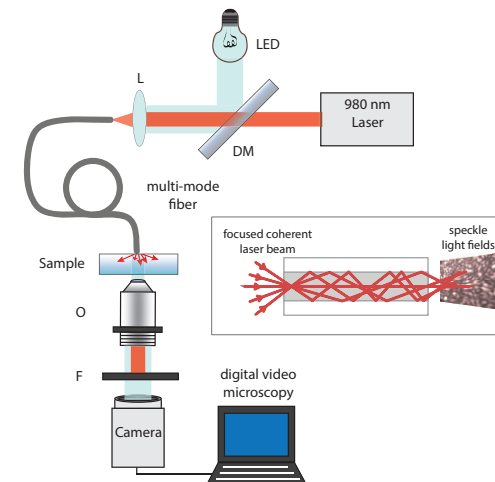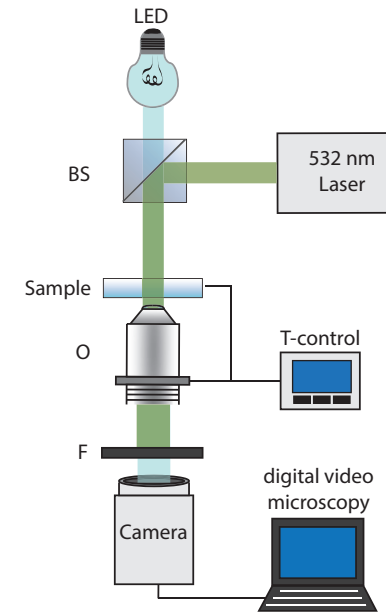

SUPPL. FIG. 1. Setup for the measurement of sub-diffusion in a speckle light field. The setup is a homemade version of an inverted microscope. The sample is confined in a quasi-two-dimensional space between a microscopic slide and a coverslip separated by spacer particles (radius $R = 3.50 \pm 0.15\mu$m, microParticles GmbH). A laser ($\lambda = 980\,\text{nm}$) passes through a dichroic mirror (DM) and is then focused by a lens (L) into a multimode fiber (step index, core diameter $d = 105\,\mu\text{m}$). Due to phase interference inside the fiber, speckles are generated at the exit of the fiber, which is in direct contact with the sample. The complete sample is illuminated by a white LED lamp, reflected on the dichroic mirror (DM), collected by an objective (O, 100×, NA=1.30), passing through a filter (F) eliminating the laser light, and projected onto a camera. Inset: When a coherent laser beam is focused into a multimode fiber, modes with different phases propagate through the fiber and interfere at the exit, creating a speckle pattern.

optical potentials. For example, when a beam passes through a multi-mode fiber, phase interference occurs if the inner core diameter is large enough to allow for multiple phase propagation. When exiting the fiber, the phase front of the beam is randomized so that bright and dark spots of different sizes are observed (see inset Suppl. Fig. 1). The bright intensity spots can trap particles and, if the laser power is adjusted appropriately, they metastably trap particles and lead to sub-diffusive behaviors [1]. In Suppl. Fig. 3(a), we plot the MSD for the x coordinate for three long trajectories (containing 10100 data points measured for about $\simeq 880\,$s, see inset in Suppl. Fig. 3(a)). On a time scale from a second to hundreds of seconds, a clear sub-diffusive behavior can be seen, characterized by an exponent $\alpha \simeq 0.8$. In the main text, when speaking about the sub-diffusive experimental trajectories we refer to segments of these trajectories sampled every $\simeq 1.3\,$s. On shorter time scales the particles undergo normal diffusion, as shown in Suppl. Fig. 4(a). The same kind of colloids, without the speckles undergo normal diffusion, as shown in Suppl. Fig. 3(b).
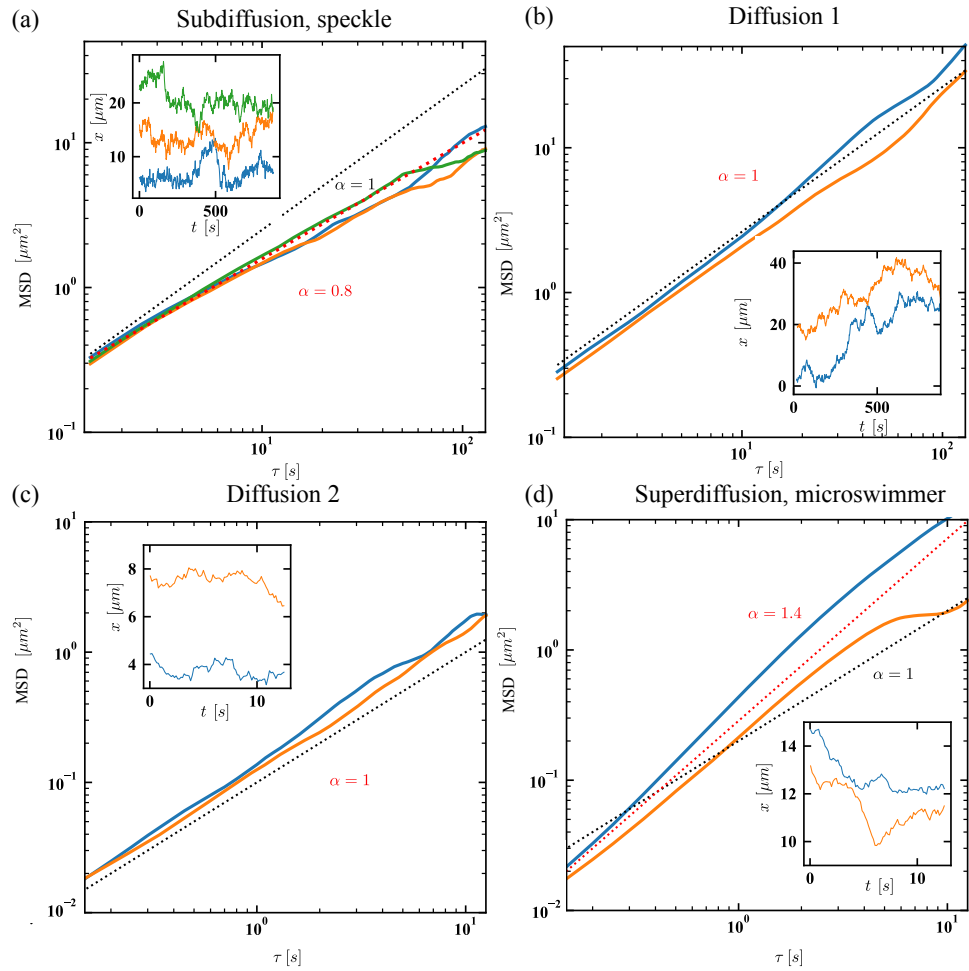
Superdiffusion experiments

Under homogeneous light illumination Janus particles self-propel inside a critical binary mixture [3]. Here we employ a very similar system but replace Janus particles with commercially available magnetic beads (Microparticles GmbH) composed of Silica in which iron-oxide nanoparticles have been incorporated [4]. The random distribution of nanoparticles on the surface produces an inhomogeneous absorption profile that, similarly to the two sides of a Janus particle, creates a demixing profile responsible for the ensuing diffusiophoretic motion [5]. Using video microscopy and the setup illustrated in Suppl. Fig. 2 we find this motion to be super-diffusive on time scales from the order of a tenth of a second to a few seconds. As shown by the two trajectories reported in Suppl. Fig. 3(d), one can identify an exponent of $\alpha \simeq 1.4$. The irregular behavior for large τ is due to the finite length of the acquired trajectory ($T \simeq 50\,$s and $T \simeq 75\,$s for the blue and orange curve, respectively). In the main text, when speaking about the super-diffusive experiments we refer to segments of these two trajectories sampled every $\simeq 0.15$s. On longer time scales the system recovers a normal diffusion behavior as shown in Suppl. Fig. 4(b).

When the light is switched off the colloids diffuse normally as shown in Suppl. Fig. 3(c).

SUPPL. FIG. 2. Setup for the measurement of the super-diffusion of microswimmers. The setup is a homemade version of an inverted microscope. The sample is confined in a quasi-two-dimensional space between a microscopic slide and coverslip separated by spacer particles (radius $R = 0.85 \pm 0.02\,\mu$m, microParticles GmbH). The complete sample is illuminated by a white LED lamp, passing through a 50:50 beamsplitter (BS) and collected by an objective (O, 100×, NA=1.30), passing through a filter (F) eliminating the laser light, and finally imaged onto a camera. A broadened laser beam ($\lambda = 532\,$nm) that illuminates the whole sample heats up the absorbing magnetic colloids inside the critical mixture and causes self-propulsion. The complete sample is temperature-stabilized using a two-stage controller system consisting of a copper-plate for heat exchange with a water bath (T100, Grant Instruments) with $\pm50\,$mK temperature stability, and of two Peltier elements attached to the objective (O) in feedback with a temperature controller (TED45, Thorlabs), reaching a temperature stability of $\pm3\,$mK.

SUPPL. FIG. 3. Experimental trajectories and mean squared displacement (MSD) corresponding to (a) sub-diffusion, (b,c) normal diffusion, and (d) super-diffusion. (a) Sub-diffusive MSDs for three trajectories of colloids in a speckle light field. (b) Diffusive MSDs for two trajectories with same kind of colloids as in (a) but without the external light field. (c) Diffusive MSDs for two trajectories of absorbing magnetic beads without an external light field. (d) Super-diffusive MSDs for two trajectories using the same colloids as in (c) but activated under light illumination. In all panels, the inset show the trajectories.
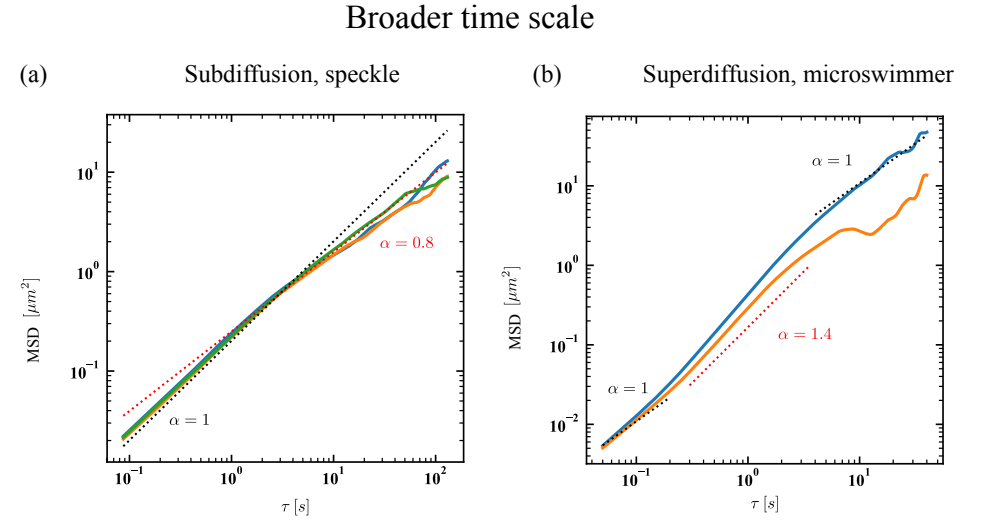
SUPPL. FIG. 4. Broader view of the mean squared displacement (MSD). (a) MSDs for three trajectories of colloids in a speckle light field, same as reported in Suppl. Fig. 3(a) but including shorter time scales. One can observe a normal diffusive behavior on short time scales and a sub-diffusive one on longer time scales. (b) MSDs for two trajectories of absorbing magnetic beads activated under light illumination, same as reported in Suppl. Fig. 3(d) but including both shorter and longer time scales. On intermediate time scales the system shows super-diffusion and on larger timescales normal diffusion is recovered.

RECURRENT NEURAL NETWORK (RNN): ARCHITECTURE AND TRAINING

Our task is to infer the anomalous diffusion exponent α from a (short) single trajectory using a neural network. The input to the neural network is then the single trajectory itself and its output the estimated exponent $\hat{\alpha}$. More precisely, for a trajectory containing T measurement points, the input data is a $2 \times T$-dimensional array, which contains position and time for each measurement point $[(x_1, t_1), (x_2, t_2), \dots (x_T, t_T)]$. Before being presented to the network, the trajectories are normalized such that the average of the measured positions is 0 and their variance is 1. The measurement time is also normalized to be (roughly) between 0 and 1. To process the input we employ two layers of Long Short Term Memory (LSTM) Recurrent Neural Networks (RNN) [6, 7] as sketched in Suppl. Fig. 5. This architecture consists of a sequence of repeated LSTM modules, one for each measurement point in the input trajectory i for a total length of T. Each module i of the LSTM is characterized by a hidden cell state $\boldsymbol{s}_i$, which is used to produce the hidden output $\boldsymbol{h}_i$ and is also passed to the module at the consecutive time $i + 1$. For the first layer, each module i receives input from the current data point (x_i, t_i) and from the hidden output at the previous time $\boldsymbol{h}_{i-1}^1$. This input is multiplied by a weight matrix, added a bias and passed through a tanh activation
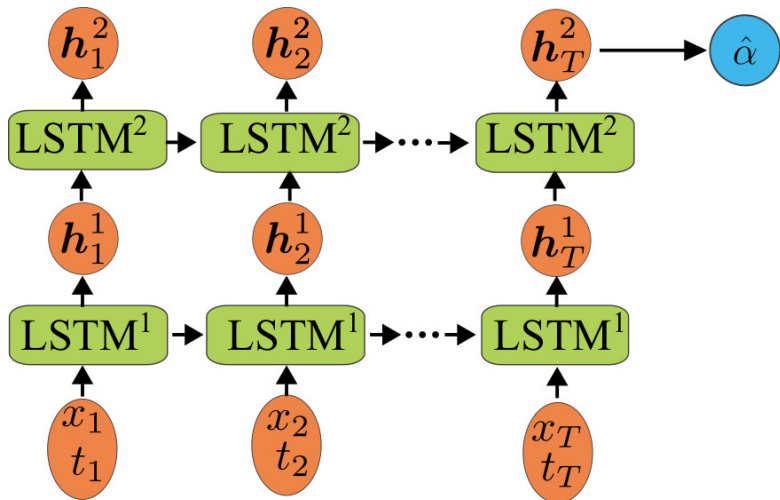
SUPPL. FIG. 5. Sketch of the neural network architecture for the case in which α is constant throughout the trajectory.

function to give the input node. What part of the input node will be used to modify the cell state and what part of the previous cell state $\boldsymbol{s}_{i-1}$ should be "remembered" are determined by the input and forget gates (which themselves depend on the incoming input). What part of the updated cell state should be given as the a hidden output $\boldsymbol{h}_i^1$ is set by the output gate, which itself depends on incoming input.

The input node and each of the three gates involve one weight matrix and a bias vector so that we have four weight matrices and four bias vectors. These are kept equal for each of the T LSTM modules. We choose the first layer to be of dimension 64, meaning that for each module i the cell state $\boldsymbol{s}_i^1$ and the hidden output $\boldsymbol{h}_i^1$ are 64-dimensional vectors. At each time step the 2-dimensional input and the 64-dimensional hidden output (from the previous time step) has to be mapped into a 64-dimensional hidden output. A similar procedure is involved in the update of the 64-dimensional cell state. We therefore have four weight matrices of dimension 66×64 and four 64-dimensional bias vectors, resulting in $17152 = (66 \times 64 + 64) \times 4$ parameters for the first layer. We choose the second layer to be of dimension 16. Each module i of the second LSTM layer receives a $(16 + 64)$-dimensional vector, which is given by the 64-dimensional hidden output of the first layer $\boldsymbol{h}_i^1$ and by the 16-dimensional hidden output of the previous module $\boldsymbol{h}_{i-1}^2$. We then have four 80×16 weight matrices and four 16-dimensional bias vectors giving $5184 = (80 \times 16 + 16) \times 4$ parameters for the second layer. To generate the final output we do not use the whole sequence of hidden outputs of the second layer but just the last one $\boldsymbol{h}_T^2$. This 16-dimensional hidden output is densely connected to the final output neuron with a linear activation function, which provides the estimate of the exponent $\hat{\alpha}$. Including the weights and bias of this fully connected last layer, we have a total of 22353 trainable parameters. Notice that the number of the parameters does not depend on the trajectory length T since each of the T LSTM modules of layer 1 (2) has the same weights and biases.

For the training, we use the mean square error (MSE) as a loss function and optimize via a RMSProp (root mean squared prop) optimizer with constant learning rate 0.001 and a moving average parameter $\rho = 0.9$ (see Ref. [8] and references therein). For the two LSTM, we adopt a hyperbolic tangent (tanh) activation function and a hard sigmoid activation function for the recurrent steps (input, forget and output gates). We use the bias vector (initialized to 0, with the bias of the forget unit initialized to 1) and initialize the weights used for the linear transformation of the inputs with a Glorot uniform initializer, also called

Xavier uniform initializer, and the ones for the recurrent transformation by an orthogonal random matrix [8]. We do not use any regularizer nor constrain the weight matrices. No dropout or recurrent dropout is used.

Training and testing for constant α

To train the networks we have used 330000 simulated trajectories with an exponent α uniformly sampled between $[0.02, 1.98]$. We have considered trajectories of different lengths, ranging from 32 measurement points to 1024 (as shown in Fig. 1(g) in the main text) and trained a specific network for each of the different lengths. The simulations are performed using the Davies-Harte and the Hosking algorithm [9] implemented in a Python library [10]. We choose a unit time step, such that the typical magnitude of the increments remains the same for simulations with different α. Furthermore, we choose a constant generalized diffusion coefficient set to 1 in adimensional units.

In each training step, the neural network is tasked with predicting the exponents corresponding to each trajectory from a portion of the training set (batch); its predictions are then compared to the ground-truth values of the exponents; and the prediction errors are finally used to adjust the trainable parameters of the neural network using a back-propagation algorithm. The various batches in which the training set has been split are successively used in the training. Once all the batches have been used, an epoch of the training is completed. During the training procedure we do not vary the learning rate in different epochs but increase the batch size [11] from an initial size of 32 to 128. For trajectories of length $T = 32, 64, 128$ we train for 10 epochs for each of the two batch sizes. For trajectories of length $T = 256, 512$ we train for 7 epochs with batches of size 32 and for 5 epochs with batches containing 128 trajectories. For trajectories of length $T = 1024$ we train for 4 epochs with batches of size 32 and for 5 epochs with batches of size 128. The trained networks are tested on 187500 trajectories with α uniformly sampled between $[0.5, 1.5]$ and produce the results reported in Fig. 1 in the main text.
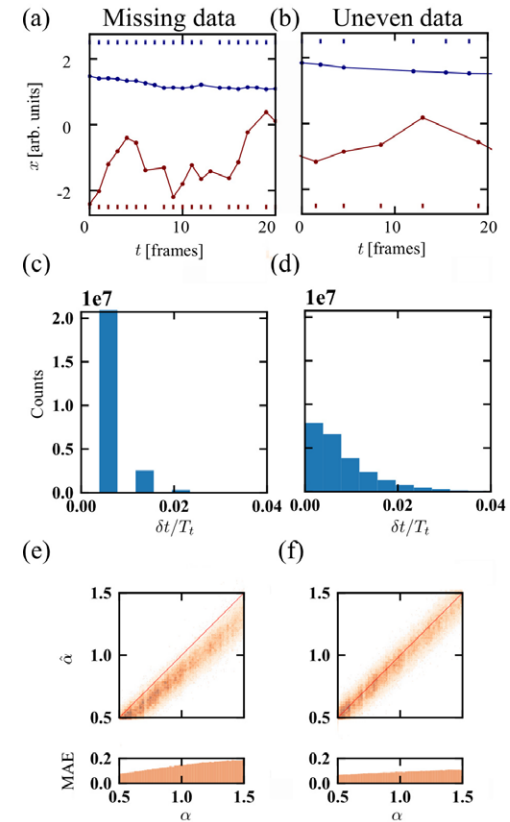
SUPPL. FIG. 6. Measurement of anomalous diffusion in irregularly sampled trajectories with a RNN trained specifically on uneven data. Often a trajectory is sampled irregularly, either (a) because some data points are missing ("missing data", here 12.5% data points are missing), or (b) because data points are sampled at random times ("uneven data", here according to a geometric distribution). (c-d) Histograms of the time difference between consecutive frames δt normalized by the total length of a reference trajectory, containing approximately 128 measurement points: T_t. (e-f) Estimated exponent $\hat{\alpha}$ as a function of the actual exponent α for the two cases using simulated trajectories with 128 frames. The MAE is (e) 0.142 for the "missing data" case and (f) 0.092 for the "uneven data" case. Also, note the presence of a systematic bias in the for the case of "missing data".

Missing and uneven data

As discussed in the main text, we considered two scenarios in which the data points are not acquired at equally spaced times. For case (a) dubbed "missing data" scenario (Suppl. Fig. 6(a)), we start from an equally spaced time series and randomly remove frames (on average 1 every 8). As shown in Suppl. Fig. 6(c) the time interval between two measurement points is mostly constant (in about 87.5% of the times) and equal to one time step of the original equally spaced time series; a few data points are distant 2 time steps; and a very small number are farther apart. For case (b) dubbed "uneven data" scenario (Suppl. Fig. 6(b)), we start again from an equally spaced time series but now randomly keep frames at times following a geometric distribution (on average 1 every 8). As shown in Suppl. Fig. 6(d), the histogram of the time interval between two measurement points is now much broader (it samples a geometric distribution). The results presented in Fig. 2 in the main text are obtained by applying the neural network trained on equally spaced data on 185000 trajectories to unequally sampled measurements.

We can also train a network with the same architecture as in Suppl. Fig. 5, on this uneven data for trajectories containing 128 measurement points (frames) for 10 epochs for the two batch sizes. By doing this, we obtain better performances on the uneven test data with a MAE of 0.092 (Suppl. Fig. 6(f)). However, one starts performing significantly worse on the missing data scenario (in which most frames contain signal) with a MAE of 0.142 and a significant bias, as shown in Suppl. Fig. 6(e).

Intermittent behavior

Neural networks can be used to address more challenging cases, in which the system switches (at time t_s) between behaviors characterized by different exponents (α_1 before the switch and α_2 after the switch). We use a network with the architecture shown in Suppl. Fig. 7, which is a slight modification of the one used for the case of constant α with 5 output neurons instead of 1. This network has 22421 trainable parameters. The output neurons estimate $\hat{\alpha}_1$, $\hat{\alpha}_2$, $\Delta\hat{\alpha}$, $\sin\left(2\pi\hat{t}_\mathrm{s}/T\right)$, and $\cos\left(2\pi\hat{t}_\mathrm{s}/T\right)$. The choice of estimating the sine and the cosine of the normalized switching time is motivated by the fact that a trajectory with an early exponent switch is similar to one with a switch occurring late since, in both cases, most of the trajectory has the same exponent. In this respect, an early switch time $t_\mathrm{s} \simeq 0$ and a late one $t_\mathrm{s} \simeq T$ correspond to very similar trajectories. To make this explicit, we choose to represent time in a periodic way so that $t_\mathrm{s} \simeq 0$ is "close" to $t_\mathrm{s} \simeq T$. We train this RNN on a set of 1.6-million simulated trajectories containing 256 frames where a change in exponent occurs randomly with a uniform distribution at time $t_\mathrm{s} \in [0, T)$ and where the exponent before (after) the jump α_1 (α_2) is drawn from a uniform distribution between 0.02 and 1.98. Note that this implies that the difference between the exponents $\Delta\alpha$ is not
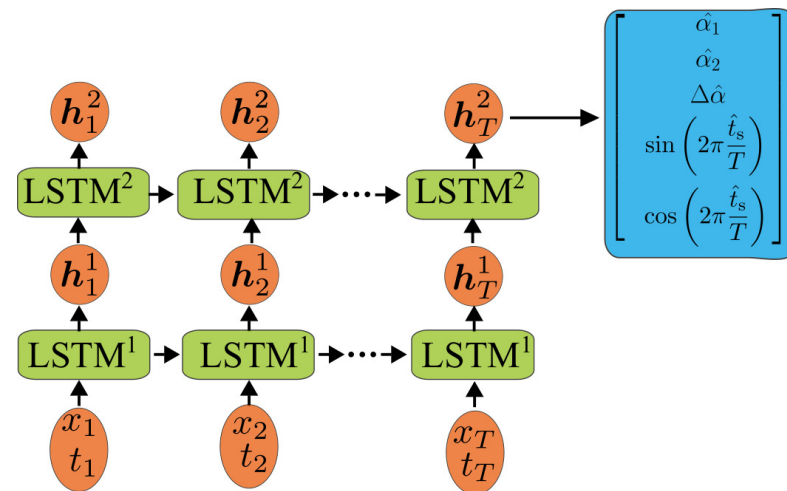
SUPPL. FIG. 7. Sketch of the neural network architecture for the intermittent case in which the exponent switches between two different values, from α_1 to α_2 at time t_s.

uniformly distributed, but has a "triangular shape" with a maximum at $\Delta\alpha = 0$. We test the predictions of the RNN on 375000 simulated trajectories where a change in exponent occurs randomly with a uniform dsicrete distribution at time $t_s \in [0, T)$ and where α_1 and α_2 are drawn from a uniform distribution between 0.5 and 1.5. The results shown in Fig. 3 in the main text refer to the 105701 trajectories from this set in which the switch takes place around the middle of the trajectory ($t_s \in [0.25T, 0.75T] = [64, 192]$) and the change in α is not too small ($|\Delta\alpha| > 0.25$).

Intermittent behavior — experiment

The network trained on trajectories containing 256 measurement points and displaying a switch can be used to study trajectories of arbitrary length with potentially multiple changes in the exponent. The idea is to slide a window of length 256 along the trajectory and estimate the exponent of the first and the second part of the sub-trajectory contained in the window (respectively $\hat{\alpha}_1$ and $\hat{\alpha}_2$) their change $\Delta\hat{\alpha}$ and the time when the switch occurred $\hat{t}_s$. If the exponent does not change in the observed window, $\Delta\hat{\alpha}$ will be small and $\hat{t}_s$ not very meaningful. In Fig. 4 in the main text we studied the behavior of an experimental intermittent trajectory obtained by first illuminating an absorbing magnetic colloid (inducing super-diffusion as described in Suppl. Fig. 2 and 3) and then rapidly switching off the illumination (thereby recovering a passive colloid that normally diffuses). By sliding the window over the trajectory, normalizing the data and feeding it to the RNN we can estimate the exponent when the light is on, when the light is off and the time when the switch occurred. In practice, the prediction is made in the following way: each window i is fed data from frame i to $i + 255$ and predicts $\hat{\alpha}_1^i$, $\hat{\alpha}_2^i$ and a switching time $\hat{t}_s^i$. This means that, for the i-th window, the network predicts that from time i to time $i + \hat{t}_s^i - 1$ the exponent is $\hat{\alpha}_1^i$ and from time $i + \hat{t}_s^i$ to time $i + 255$ the exponent is $\hat{\alpha}_2^i$ and that the switch took place at time $i + \hat{t}_s^i$. Then i is increased from the initial time of the trajectory t_0 until the end of the last window covers the last available data point $i_f = t_f - 255$. In Fig. 4(b) in the main text we plot what value of α is predicted at a specific time t. This is obtained by averaging the predictions made by all the windows that contained time t. Each window predicts also a switching time. Some of these windows do not contain data featuring an actual switch in the exponent so that it is preferable to consider only the "reliable" predictions that predicted a

non-negligible change in the exponent $|\Delta\hat{\alpha}| > 0.25$ and for which the estimated change point is far from the boundaries of the window $\hat{t}_s \in [0.25T, 0.75T]$. To locate the actual switching time t_s we build a histogram of the predictions for the switching time $\hat{t}_s = i + \hat{t}_s^i$ made by each reliable window. Such histogram represents the empiric probability of the switch occurring in a certain time interval. In case of ideal predictions, the histogram should be concentrated on the actual switching point with about 128 counts.

————————

[1] G. Volpe, G. Volpe, and S. Gigan, Sci. Rep. **4**, 3936 (2014).

[2] G. Volpe, L. Kurz, A. Callegari, G. Volpe, and S. Gigan, Opt. Express **22**, 18159 (2014).

[3] I. Buttinoni, G. Volpe, F. Kümmel, G. Volpe, and C. Bechinger, J. Phys.: Condens. Matter **24**, 284129 (2012).

[4] F. Schmidt, B. Liebchen, H. Löwen, and G. Volpe, J. Chem. Phys. **150**, 094905 (2019).

[5] F. Schmidt, A. Magazzù, A. Callegari, L. Biancofiore, F. Cichos, and G. Volpe, Physical review letters **120**, 068004 (2018).

[6] S. Hochreiter and J. Schmidhuber, Neural Computation **9**, 1735 (1997).

[7] Z. C. Lipton, J. Berkowitz, and C. Elkan, (2015), arXiv:1506.00019.

[8] F. Chollet and Others, "Keras," https://keras.io (2015).

[9] T. Dieker, Simulation of fractional Brownian motion (MSc theses, University of Twente, Amsterdam, 2004).

[10] C. Flynn, "Exact methods for simulating fractional Brownian motion and fractional Gaussian noise in python," https://github.com/crflynn/fbm.

[11] S. L. Smith, P.-J. Kindermans, C. Ying, and Q. V. Le, (2017), 10.1016/S0169-7161(05)80045-8, arXiv:1711.00489.

5.5 Paper V: Responsive environments induce hierarchical self-organization in active particles

Attached below is the manuscript in preparation for submission including all experimental results and the corresponding simulations, as well as further analysis of the droplet's growth dynamics.

Responsive environments induce hierarchical self-organization in active droploids

E-mail:

preliminary list of authors in alphabetical order: Jens Grauer, Benno Liebchen, Hartmut Löwen, Falko Schmidt, and Giovanni Volpe

Abstract

The coupling of an active system of colloidal particles and a binary liquid mixture can lead to a versatile feedback loop allowing for the emergence of self-organized structures and dynamical patterns. Here, we study the behavior of light-absorbing microspheres, initiating droplet formation in a water–2,6-lutidine mixture that is kept away from thermodynamic equilibrium by an external supply of energy. Combining experiments and simulations based on a modified Cahn-Hilliard equation, we find the formation of active colloidal molecules and *active droploids*, i.e. colloids immersed inside a liquid droplet, driven by its interior molecules, and whose dynamics can be controlled by light intensity. Moreover, for large energy inputs, the environment can actively respond to the colloids by generating pronounced interfaces around the droplet's surface that can serve to concentrate the colloids. These findings shine light on the interplay between the motion of active molecules and the bulk motion response of their environment, and may thus be relevant for spatial organization in living cells and models for the origin of life.

1

Introduction

In equilibrium systems the environment essentially is a passive bath, in which matter is constrained by entropy maximization (or free energy minimization). In nonequilibrium systems, however, the environment acts as a persistent free energy source which emancipates matter from those fundamental constraints and induces a rich phenomenology which is fundamentally beyond equilibrium physics. For example, nonequilibrium environments allow the conversion of fluctuations into mechanical work. This has been realized for a wide variety of ratchet-setups from individual cold atoms in AC-driven light-fields to vortices in superconducting arrays[1] and living organisms in 3D printed superstructures[2] Here, the environment typically comprises external AC-fields (or a source for chemical energy) allowing the system to bypass the second law of thermodynamics resulting in the spontaneous emergence of a directed particle current in an *unbiased* fluctuating environments – which is of course forbidden in all equilibrium systems, where the environment is a passive bath.[3,4] Nonequilibrium environments also allow for the spontaneous emergence of spatiotemporal patterns, illustrating the remarkable fact that driving systems far away from equilibrium often creates structure, not chaos. This is central for the existence of life itself, which hinges on maintaining hierarchically ordered structures through metabolism, which would immediately collapse in equilibrium.[5–7] The phenomenology which can arise from nonequilibrium environments is further enriched by recent studies in active matter, where nonequilibrium arises at the level of individual particles. In active colloids for example, reactions are catalyzed on part of the surface of the particles, resulting in self-propulsion and collective self-organization,[8–13] similar to biological microswimmers like bacteria, algae or sperm cells.[14–16]

While leading to a spectacular phenomenology beyond equilibrium physics, in all these examples (and, more generally, in most studies of nonequilibrium systems in the physics literature), the environment unidirectionally feeds energy into the system of interest and is hardly affected by the behaviour of the latter. There are remarkable counterexamples to this in the macroscopic world, illustrating the possibility of a more active response of the environment. The melting of icebergs as induced by global heating for example results in a reduced overall heat-absorption. This acts back onto the environment and accelerates global warming, therefore acting as a much discussed tipping element of the climate on earth.[17] More sophisticated feedback loops between nonequilibrium systems and their environments occur e.g. in childbirth, involving a remarkable two-fold coupling between the baby (system) and its environment (mother).[18] These examples illustrate the possibility of a "responsive environment" which influences and is influenced by the system under consideration.

In this work, we demonstrate the possibility to implement a comparable two-way coupling between a nonequilibrium system and its environment in a simple and controllable setup. To achieve this, we experimentally realize and theoretically model an active system which shapes and is shaped by its "responsive environment". We use a mixture of colloidal particles, some of which absorb heat under laser-light irradiation and expose them to a near-critical bath. We then observe that the light-absorbing particles heat up and initiate phase separation in their local environment. This leads to the formation of active colloidal molecules composed of absorbing and non-absorbing particle, which self-propel under light illumination. Upon further heating, local phase separations increase and liquid droplets start emerging, in which the colloids are immersed. This new type of active matter, called *active droploids* is an example for, how a phase separating environment acts back onto the colloids by providing a rich landscape of interfaces. Those droploids mainly attract the non-absorbing colloids and induce local phase-separation of the colloids. In appropriate parameter regimes, this two-way coupling between the environment and the system of colloids can continue: the colloids can for example form motile clusters within the droplets which can continuously deform the boundaries of the droplets or can induce self-propulsion of the latter, leading to an enhanced merging of droplets, and accelerating phase separation in the environment. Overall, we have realized a two-way coupling between an active colloidal system and a responsive environment, resulting in a hierarchical self-organization where the system and its environment mutually influence each other at multiple levels.

We provide a minimal model system highlighting the importance of feedback mechanisms towards understanding the compartmentalization processes inside the cell's cytoplasm.
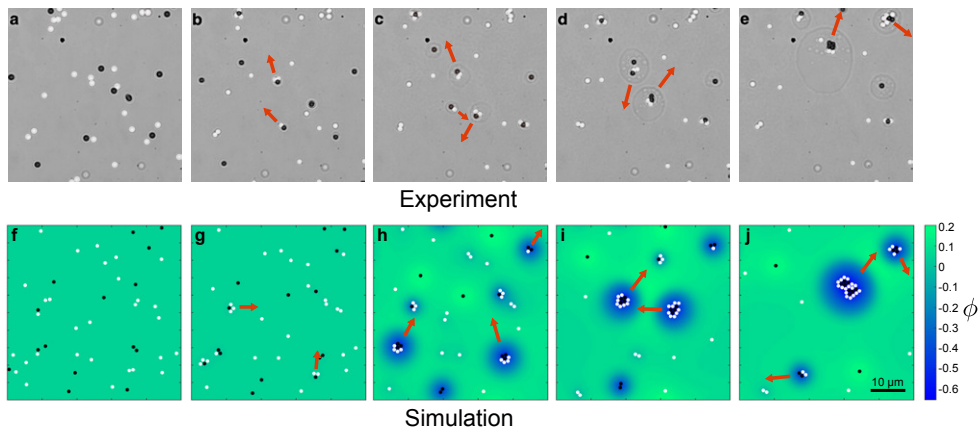
Experimental observations of active droploids

Figure 1: **Snapshots of active droploid formation and growth over time. a,f** Single particles of two species, absorbing (black) and non-absorbing (white), are immersed in a near-critical mixture and behave as passive particles in a standard liquid. **b,g** Upon illumination, the two species of particles come together and form small motile molecules until eventually, **c,h** local phase separations lead to water-rich droplets surrounding absorbing particles and molecules. **d,i** Over time droplets move together with the active molecules, grow in size, and **e,j** eventually coalesce together to form even larger droplets. The box length is $L_{box} = 50\,\mu m$ with $N_a = 15$ absorbing and $N_{na} = 25$ non-absorbing particles under light irradiation with $I = 150\,\mu W/\mu m^2$ ($k_0 = 60 \times 10^3\,K\mu m^2 s^{-1}$), composition $\phi = 0.05$ and initial temperature $T_0 = 32.5\,°C$ (see Appendix B for other parameter values). Videos of experiment V1 and simulation V2 are provided in SI. The scale bar is $10\,\mu m$.

In order to study a system where there is a feedback cycle between particles and environment, we consider a system of colloidal particles ($R = 0.49\,\mu m$) immersed in a near-critical water–2,6-lutidine mixture with a critical composition $c_c = 28.4\%$ and critical temperature $T_c = 34.1°C$, where we use an off-critical composition (a slightly higher lutidine concentration will push water into minority, thus induce water-rich droplets later on). We fix the temperature of the sample at $T = 32.5°C$ using a water-heat bath and temperature controller

(see experimental setup in SI Fig. S1). The particles are quasi two-dimensionally confined between two glass slides separated by a distance smaller than two particle diameters. We use two species of hydrophilic particles; light-absorbing and non-absorbing particles. Without illumination both species behave passively characterized by their Brownian motion (diffusion coefficient $D = 0.0454 \pm 0.003\,\mu m^2 s^{-1}$) and are homogeneously distributed (Fig. 1a,f in experiments and simulations, respectively). Under illumination, absorbing particles induce local temperature gradients that eventually heat up the surrounding fluid close to the critical temperature ($T \approx T_c$). By demixing their surrounding fluid colloids alter their local environment. That is, the light-absorbing particles induce local field gradients (temperature field, composition field) which phoretically attract all other particles in the system.[19–22] In particular, this leads to a unidirectional, i.e. non-reciprocal, effective attraction of the non-absorbing particles by the absorbing ones leading to ballistically moving active molecules (Fig. 1b,g); Janus-dimers being the simplest example.[22] At sufficiently large intensities, the system of active colloids induces temperatures that exceed the critical point ($T > T_c$, Fig. 1c,h) causing a strong response of the environment; phase separation around the molecules leads to the formation of water-rich droplets in a lutidine-rich background. These droplets can spontaneously acquire mobility through their inner active molecules, which exhibit a phoretic motion and shift the self-generated temperature field with their movement. The immersed molecules are thus in constant feedback with their environment causing the droplets to follow the molecules' motion, and characterizing the state of *active droploids*. These active droploids collide and merge with each other and consequently grow over time (Fig. 1d,i), until they eventually all coalesce into a large droplet (Fig. 1e,j).

Model and simulations

We develop a minimalistic model which describes the combined dynamics of the water–2,6-lutidine mixture and the dynamics of the colloids, helping us to identify the key ingredients

determining the observations made in experiments. The model describes a mixture of over-damped Brownian particles at position $\mathbf{r}_i^s(t)$ following Langevin dynamics including Gaussian white noise ($i = 1, \ldots, N$, $s \in \{a,na\}$ for absorbing and non-absorbing particles, respectively)

$$\gamma \partial_t \mathbf{r}_i^s(t) = \beta_s \nabla \phi + \alpha_s \nabla (\nabla \phi)^2 - \nabla_{\mathbf{r}_i} V + \sqrt{2D} \gamma \boldsymbol{\eta}_i^s \,, \tag{1}$$

where D is the translational diffusion coefficient of the particles, γ is the Stokes drag coefficient (assumed to be the same for both equally-sized species), $\boldsymbol{\eta}_i^s(t)$ represents unit-variance Gaussian white noise with zero mean and V accounts for steric repulsions among the colloids, represented by Weeks-Chandler-Anderson (WCA) repulsions here. The dynamics of the particles is coupled to the water-lutidine-composition field $\phi(\mathbf{r}, t)$ (environment), described by the first two terms on the RHS of Eq. 1. Here, the first term with $\beta_s < 0$ leads to attraction into water-rich regions, caused by the particles hydrophilicity. In the second term, $(\nabla \phi)^2$ is large at interfaces and $\nabla (\nabla \phi)^2$ induces motion towards (or away from) interfaces, depending on the sign of the coefficient, i.e. $\alpha_s > 0$ describes the tendency of the particles to attach themselves to the water-lutidine interface, and $\alpha_s < 0$ as the preference to remain inside the water-rich droplet. The state of the mixture is defined by an order parameter ϕ of the composition of the two fluids describing the relative concentration difference to the critical point. This variable ϕ is introduced to describe the concentration of the two components A and B (here water and lutidine, respectively), with $\phi = 0$ over regions where A and B are homogeneously mixed and $\phi = \pm 1$ in pure A and B regions, respectively. To model the phase separation dynamics we use the Cahn-Hilliard equation taking into account an inhomogeneous temperature distribution $T(\mathbf{r}, t)$, caused by the light-absorbing particles

$$\partial_t \phi(\mathbf{r}, t) = M \nabla^2 \left(a(T - T_c)\phi + b\phi^3 - \kappa \nabla^2 \phi + A_s \sum_{s \in \{a,na\}} \delta(\mathbf{r} - \mathbf{r}_i) \right) \,, \tag{2}$$

where M is the inter-diffusion constant of the mixture, and T_c is the critical temperature, with constant $a < 0$ and $b, \kappa > 0$ such that the fluid demixes, where $T > T_c$. We describe the impact of the hydrophilicity of the light-absorbing and non-absorbing particles on the dynamics of the fluid with an additional term including a δ-function at the particle positions, whose strength is given by A_a and A_{na}, respectively. The two-way coupling between the nonequilibrium system of particles and its environment is mainly controlled by the concentration of the mixture and the energy supplied to the system by irradiating the absorbing colloids, which is regulated by the light intensity I and the density of absorbing particles ρ_a. In our simulation model we describe the light intensity $I(\mathbf{r})$ that corresponds to the local illumination of an absorbing particle by a suitable source term for the absorbed power per unit volume with the Dirac delta function $\frac{\alpha'}{\rho c_p} I(\mathbf{r}) = k_0 \delta(\mathbf{r} - \mathbf{r}_i)$, where α' is the optical absorption coefficient, ρ the density of the mixture, c_p the specific heat at constant pressure, and k_0 is the strength of the light source at the particle position $\mathbf{r}_i$.[23] The inhomogeneous temperature field is then to be calculated from the heat equation

$$\partial_t T(\mathbf{r}, t) = D_T \Delta T + k_0 \sum_{\text{absorb.}} \delta(\mathbf{r} - \mathbf{r}_i) - k_d T \tag{3}$$

with diffusion constant D_T. Here, the decay rate k_d describes the coupling of the sample to an external water heat bath stabilizing the temperature (see Appendix and SI for a detailed description of the experimental setup and the equations of motion.) In simulations we can replicate the experimental states, i.e. passive disperse particles, ballistically moving *active droploids* that form around active particles and into which other molecules can enter.

Phase diagram

It is interesting to consider exploring the full nonequilibrium state-diagram of both species of particles in a water–2,6-lutidine mixture in Fig. 2 as a function of the concentration difference to the critical point ϕ, describing the composition of the mixture (see also phase diagram SI
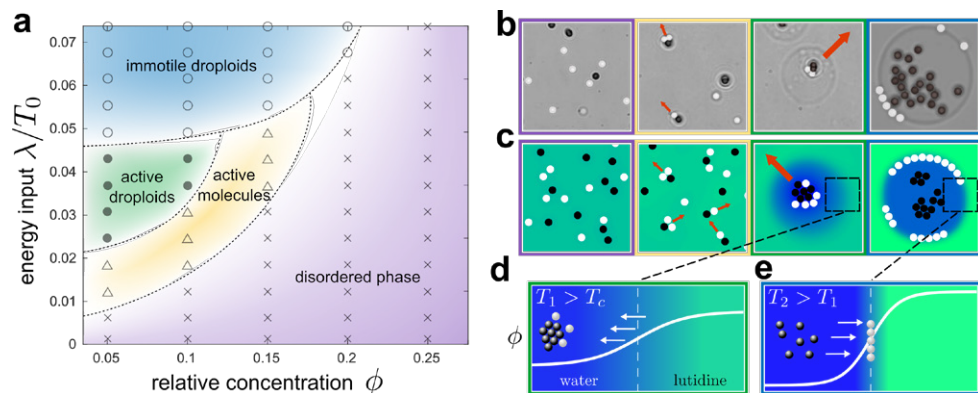
Figure 2: **Nonequilibrium phase diagram of molecule and droplet states. a** State diagram as a function of the energy input $\lambda = \frac{\rho_a k_0}{k_d}$ and the relative concentration difference from the critical point ϕ. We increase the energy input λ by increasing the number of absorbing particles (between $N_a = 10$ and 240 absorbing and at fixed $N_{na} = 50$ non-absorbing particles in a simulation box of length $L_{box} = 100\,\mu m$). Other simulation parameters in Appendix B. The evaluated state points are indicated by empty circles (blue - droplets with particles at the interface), filled circles (green - active droploids), triangles (yellow - active molecules) and crosses (purple - disordered phase). Dashed lines indicate approximate boundaries between phases and serve as a guide to the eye. The different phases were identified by visual inspection of each individual simulation trajectory. **b,c** Typical snapshots from the experiment and the simulations of the different phases indicated in the state diagram. **d,e** exemplarily show the concentration profile of the composition, where the gradient at the interface gets steeper as temperature locally increases from $T_1 > T_c$ (active droploids) to $T_2 > T_1$ (immotile droploids) causing non-absorbing particles to accumulate there.

Fig. S1), and the expression $\lambda = \frac{\rho_a k_0}{k_d}$, serving as a measure of energy input into the system. We identify four different states depending on their activity (or their lack thereof) and the presence of droplets. The *disordered phase* (purple region in Fig. 2a), characterized by randomly dispersed Brownian particles (Fig. 2b,c purple frame), is found at very low energy input and at concentrations far away from the critical composition ($\phi > 0$). The *active molecular state* (yellow region in Fig. 2a), represented by motile molecules (Fig. 2b,c yellow frame), situates slightly above and expands to higher energy inputs when the relative concentration ϕ increases. The remaining two phases of our state diagram are located at even higher energy inputs at which temperatures around absorbing particles and active molecules have exceeded the critical temperature ($T > T_c$). The so induced phase separations result

into the formation of water-rich droplets in which particles and molecules are immersed. Nearby colloids are absorbed into the droplet due to their own hydrophilicity, which allows the immersed molecules to grow in size over time. This procedure permits a good observation of the influence of colloids on their environment, which deform the interface when entering the droplet or while moving alongside it (see Fig. 4a,b, SI Video V...). These droplets follow the motion of their immersed active molecules (Fig. 2b,c green frame), thus becoming active themselves characterizing the state of *active droploids* in our phase diagram (green region in Fig. 2a). In this way, an active molecule inside the droplet acts as an internal motor whose speed determines the speed of its droplet. Over time, these active droploids can collect other molecules and droplets, thereby growing further and possibly altering their speed and direction of movement (see Supplementary Video V...). Moreover, the speed and growth process of the droplets can be controlled by light intensity, i.e. droplets can be accelerated with increasing laser power and the growth process can be arrested by a periodic illumination of the sample (More details on these processes given below.). At even larger energy inputs, either due to an increase in light intensity or due to a higher density of absorbing particles, the stronger increase in temperature far beyond the critical temperature ($T \gg T_c$) results into a large phoretic gradient close to the interface of the droplet (Fig. 2e) compared to active droploids where the gradient is more moderate (Fig. 2d). Because the dynamics of the particles are mainly controlled by the interaction of their surface with the local composition of the mixture, non-absorbing particles, which are less hydrophilic than their absorbing counterpart, move towards the droplet's interface (Fig. 2b,c blue frame). This results from the fact that the only weakly hydrophilic non-absorbing particles, similar to completely amphiphilic particles, prefer both phases rather equally and therefore accumulate at the droplet's surface to reduce the total interfacial area of the system. Consequently, existing molecular structures break up with absorbing particles remaining at the center of the droplet and non-absorbing particles decorating its interface. The loss of motility therefore characterizes this state as *immotile droploids* (blue region in Fig. 2a). This shows that
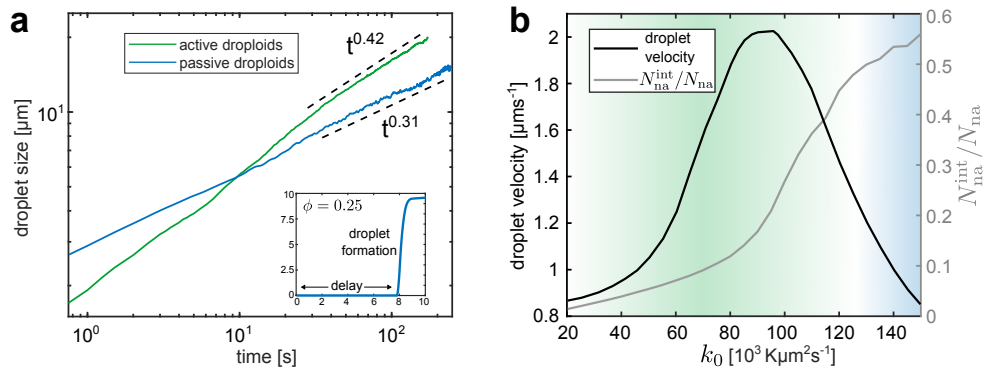
Figure 3: **Droplet velocity and growth over time. a** Average droplet size of active droploids (green) and immotile non-moving droplets (blue) over time calculated from the simulations. The inset shows the size of a droplet during the initial formation at early times. **b** Simulated mean velocity of active droploids (solid curve) and fraction of non-absorbing particles located at the interface of the droplets $N_{\text{n}}^{\text{int}}/N_{\text{n}}$ (grey curve) as a function of the illumination strength k_0. $\phi = 0.05$, other simulation parameters in Appendix B.

absorbing particles continously alter their local environment, whose feedback can induce assembly and disassembly of molecules and therefore determine the activity of the whole system of colloids and droplets.

Characterization and control of droplet dynamics and growth

Having an external source of energy along with the concentration of the mixture allows us to control the degree of interaction between active colloids and their local environment, which determines the overall state of the system (Fig. 2). Moreover, by fine tuning system parameters we can not only determine its spatial organization but allows us to have temporal control over the system, too.

We start by characterizing the overall growth of our system. At early times, the system is characterized by nucleation and formation of droplets initiated by light-absorbing particles. In this initial process, the droplets slowly grow over time as droplet-forming molecules diffuse inside from the bulk phase. The dominant growth process is therefore diffusion-limited and a droplet diameter $R \sim t^{\frac{1}{2}}$ is expected.[7] Using a mixture composition far away from the
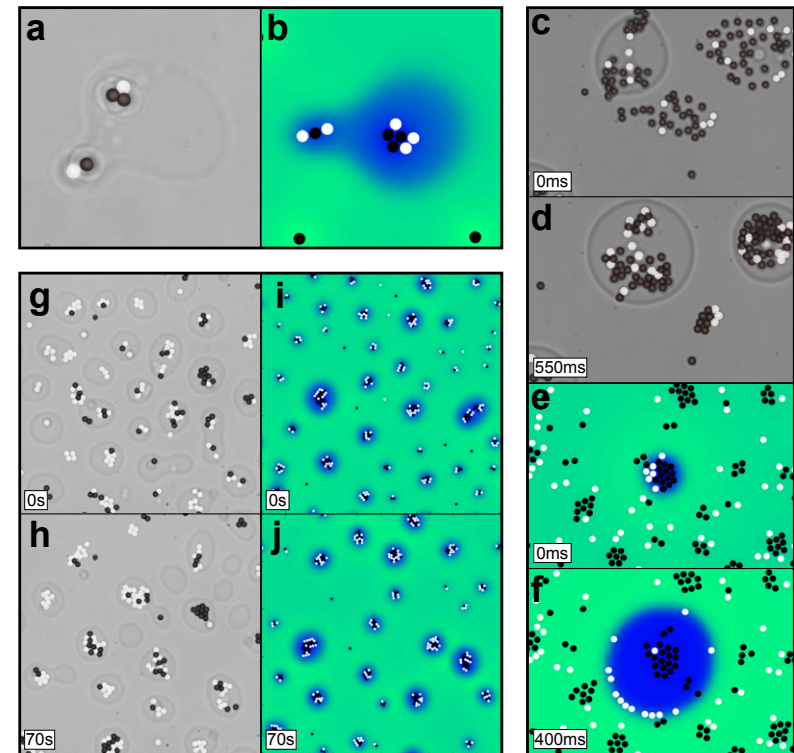

Figure 4: **Sequence of snapshots showing droplet behavior.** Experimental snapshots in grayscale and simulated snapshots in color (background displays the relative concentration ϕ.) **a,b** show clusters of colloids deforming the boundary of the droplet. **c,d** and **e,f** show accumulation of absorbing particles in a very off-critical supersaturated background phase ($\phi = 0.2$ in experiments, $\phi = 0.25$ in simulations) leading to an explosive formation of droplets within very short time. **g,h** and **i,j** show the formation of droplets around absorbing particles with a periodic light illumination such that the light is periodically on and off for $10\,\text{s}$. The average size of the droplets does not change within a period of $70\,\text{s}$ between (g,i) and (h,j). Simulation parameters in Appendix B.

critical concentration (here at much larger lutidine concentrations with $\phi > 0.2$), we find that the emergence and growth of droplets is significantly altered during this initial process. For off-critical compositions the bulk phase is already supersaturated and a considerable (free-energy) barrier emerges, separating the mixed phase from complete phase separation (see Supplementary Fig. S1b). Consequently, a large accumulation of absorbing particles

is required to provide sufficient local energy to overcome this barrier and cause nucleation, resulting in a ballistic formation of a droplet. This means that droplets do not form immediately, but with a slight time delay, and grow rapidly in size. The size of such an droplet is shown in the inset of Fig. 3, where it takes 8s after the critical temperature has already been exceeded to allow the formation of a droplet. A typical procedure of such an "explosive" droplet formation is shown both in experiments (Fig. 4c,d and SI Video V...) and in simulations (Fig. 4e,f and SI Video V...). Droplet nucleation can be further delayed if other nearby absorbing particles also form clusters or even droplets, which then "compete" with each other as the concentration of the droplet's phase (here water) is locally decreased inside the bulk mixture.

Once the droplets have formed and the initially supersaturated bulk phase is depleted, a transition from growth to coarsening can be observed. Such a late-time coarsening regime is expected, determined by either diffusion-limited coarsening (DLC or Ostwald ripening) and/or Brownian motion coalescence (BMC) of droplets. In BMC, small droplets collide with each other and fuse to form larger droplets, reducing the overall interface. For DLC, the dominant growth process is given by the transport of droplet-forming molecules from small droplets into large droplets growing by diffusion from the bulk phase. For both DLC and BMC, $R \sim t^{\frac{1}{3}}$ is expected,[7,24–29] which we can also find in our simulations by measuring the average size of non-moving droplets over time ((blue) curve in Fig. 3a), and that are passive because, either the number of non-absorbing particles is small, or these particles are concentrated at the droplet's interface.

The picture is different if the droplets themselves show ballistic movement due to internal active molecules. The self-propulsion of *active droploids* can accelerate the growth process described above. This results in a velocity of a droploid that is determined by the number and composition of contained molecules[22] and which can additionally be controlled by light intensity. In the parameter regime in which active droploids can be found ($60 < k_0[10^3 \,\mathrm{K}\mu\mathrm{m}^2\mathrm{s}^{-1}] < 120$) an increase in light intensity leads to an increase in droplet speed (see Fig. 3b). For increasing intensities, however, the velocity reduces as the resulting temperature in the sample increases and non-absorbing particles accumulate at the water-lutidine interface (transition from green to blue in the state diagram in Fig. 2a). Consequently, molecules inside the droplet slowly dissolve. We can characterize this transition counting the number of non-absorbing particles located at the interface $N_{\mathrm{na}}^{\mathrm{int}}$ as a fraction of the total number of non-absorbing particles N_{na} (see grey line in Fig. 3b). Between $k_0 = 90$ and $110 \times 10^3 \,\mathrm{K}\mu\mathrm{m}^2\mathrm{s}^{-1}$ the fraction of non-absorbing particles at the interface significantly increases from $N_{\mathrm{na}}^{\mathrm{int}}/N_{\mathrm{na}} = 0.15$ to 0.35 whereas the growth in the droplet's velocity is slowly reduced until the droplet reaches its maximum velocity of $v = 2\,\mu\mathrm{ms}^{-1}$ at $k_0 = 90 \times 10^3 \,\mathrm{K}\mu\mathrm{m}^2\mathrm{s}^{-1}$. For larger values of k_0, the number of non-absorbing particles at the interface is sufficiently large to rapidly decrease the droplet's velocity and finally reach a value similar to that of immotile droplets ($v = 0.85\,\mu\mathrm{ms}^{-1}$).

Because of the higher velocities of active droploids, we can find a much larger exponent, $R \sim t^{0.42}$, which is close to the expected exponent of $1/2$ for ballistic aggregation.[30,31] This results from the fact that active droplets move ballistically, collide and fuse together more quickly. This enhanced growth process is depicted by the average size of the droplet domain in Fig. 3a (green curve). We suspect that this deviation originates from the varying velocities of droplets at late times. For statistical reasons, the velocity decreases with increasing molecule size, as the symmetry in the particle composition of the molecules increases.[22] Furthermore, the temperature locally increases with molecule size, which changes the degree of demixing. As a consequence, the droplets loose speed at late times.

As the growth of droplets can be accelerated by increasing the laser intensity, so can the growth process be arrested by periodic light illumination. Employing periodic illumination where the light is alternately switched on and off for durations of 10 s (0.1 Hz) we show that the growth of droplets can be slowed down and even arrested (Fig. 4g,h), which is in good agreement with simulations (Fig. 4i,j).

Conclusion

We have investigated a two-way coupling of a non-equilibrium system with a responsive environment, by applying an active system of colloidal light-absorbing particles that shapes its environment by initiating phase separation and the formation of droplets in a critical water–2,6-lutidine mixture. The droplets interact with their environment in a variety of ways, for example resulting in the generation of active droplets that spontaneously acquire mobility driven by non-reciprocal interactions of their inner active molecules. The speed and size of the droplets can be controlled by light intensity, allowing the growth process to be significantly accelerated ($R \sim t^{0.42}$) compared to the classical growth in liquid-liquid phase separations ($R \sim t^{\frac{1}{3}}$). Furthermore, at high laser intensities, the environment can actively respond to the colloids by driving the internal non-absorbing particles to the water-lutidine interface of the droplet, thus strongly reducing the speed of the active droplets. The characteristics of the emerging phases can be quantitatively predicted with a simple model describing the dynamics of the critical water-2,6-lutidine mixture coupled to the dynamics of the particles. The approach presented constitutes a new route for generating droplets in a liquid-liquid mixture equipped with mobility that can be easily controlled externally. It provides a minimal model system of the cell cytoplasm for understanding intrinsic and extrinsic forces driving compartmentalisation as an important step towards understanding biological regulation associated with neurodegenerative diseases such as Alzheimers and Parkinson.[32,33]

Supporting Information Available

See supplementary information for experimental and simulated videos of the snapshots provided in Fig. 1, a figure of the water–2,6-lutidine phase diagram, a schematic of the experimental setup, and further details on control experiments.

Appendix A: Experimental setup

We consider a suspension of colloidal particles in a critical mixture of water and 2,6-lutidine at the critical lutidine mass fraction $c_c^{\mathrm{L}} = 0.286$ with a critical temperature at $T_c \approx 34°\mathrm{C}$ [51] (see Supplementary Fig. S1). The light-absorbing particles consists of silica microspheres with absorbing iron-oxide inclusions (Microparticles GmbH), while the non-absorbing particles consists of equally-sized plain silica microspheres (Microparticles GmbH). Both particle species possess the same radius ($R = 0.49 \pm 0.03\,\mu\mathrm{m}$) and have similar density ($\rho \approx 2\,\mathrm{gcm}^{-3}$). The suspension is confined in a sample chamber quasi-two-dimensional between a microscope slide and a coverslip, where the particles are sedimenting to due to gravity. We use spacer particles (silica microspheres, Microparticles GmbH) with a radius $R = 0.85\,\mu\mathrm{m}$ for constant separation. We have treated our glass surface prior with NaOH solution ($c = 1\,\mathrm{mol}$) creating a smooth hydrophilic layer on top. Surprisingly, we found that a particle solution prepared at c_c^{L} in such a sample chamber behaved off-critical (i.e. nucleation of droplets). By adding about 2% more water to the mixture critical behaviour returned (i.e. spinoidal demixing). We expect that the hydrophilic surfaces of the sample chamber reduced the bulk concentration of water for which we have compensated.

A schematic of the setup is shown in Supplementary Fig. S2. The motion of the particles is captured by digital video microscopy at $20\,\mathrm{fps}$. Using a two-stage feedback temperature controller,[34,35] the sample's temperature is kept near-critical at $T_0 = 32.5°\mathrm{C}$, where water and 2,6-lutidine are homogeneously mixed. In these conditions, the microspheres of both species are passive immotile Brownian particles performing standard diffusion (Fig. 1a,f). For illumination of the sample from the top we use a defocused laser of wavelength $\lambda = 1070\,\mathrm{nm}$ at varying intensities. The increase of temperature surrounding the light-absorbing particles is rather small ($\Delta T \approx 2°\mathrm{C}$) such that they still behave as non-active Brownian particles.

Appendix B: Details on the simulation model

To model our experimental findings, we consider an ensemble of N overdamped spheroidal colloids at position $\mathbf{r}_i$ immersed in a near-critical water-lutidine mixture, described by the Cahn-Hilliard equation, which can be derived from the total free energy functional

$$\mathcal{F}[\phi] = \int d\mathbf{r} \left(\frac{a}{2}(T - T_c)\phi^2 + \frac{b}{4}\phi^4 + \frac{\kappa}{2}(\nabla\phi)^2 + \sum_{i=1}^{N} \phi V_{co}^s \right) \tag{4}$$

where T_c is the critical temperature of the composition, with constant $a < 0$ and $b, \kappa > 0$ such that the fluid demixes, where $T > T_c$. Here we describe the coupling of the hydrophilic particles to the concentration of the mixture with an external potential which we approximate with $V_{co}^s(|\mathbf{r} - \mathbf{r}_i|) \approx A_s \delta(\mathbf{r} - \mathbf{r}_i)$, where $s \in \{a, na\}$ for absorbing and non-absorbing particles, respectively. The evolution of the conserved order parameter ϕ (composition of the two components) is than given by the Cahn-Hilliard equation

$$\partial_t \phi = M\Delta \frac{\delta \mathcal{F}[\phi]}{\delta \phi} \tag{5}$$

$$\partial_t \phi = M\nabla^2 \left(a(T - T_c)\phi + b\phi^3 - \kappa\nabla^2\phi + A_a \sum_{\text{absorb.}} \delta(\mathbf{r} - \mathbf{r}_i) + A_{na} \sum_{\text{non-abs.}} \delta(\mathbf{r} - \mathbf{r}_i) \right) \tag{6}$$

where M is the inter-diffusion constant of the mixture. We describe the impact of the hydrophilicity of the light-absorbing and non-absorbing particles on the dynamics of the fluid with an additional term including a δ-function at the particle positions, whose strength is given by A_a and A_{na}, respectively. The inhomogeneous temperature field produced by the light-absorbing particles with rate k_0 is to be calculated from the heat equation

$$\partial_t T(\mathbf{r}, t) = D_T \Delta T + k_0 \sum_{\text{absorb.}} \delta(\mathbf{r} - \mathbf{r}_i) - k_d T \tag{7}$$

with decay rate k_d and diffusion constant D_T. We can then phenomenologically describe the motion of the light-absorbing and non-absorbing particles $\mathbf{r}_i^s(t)$ ($i = 1, \ldots, N$, $s \in \{a, na\}$)

$$\gamma \partial_t \mathbf{r}_i^s(t) = \beta_s \nabla\phi + \alpha_s \nabla(\nabla\phi)^2 - \nabla_{\mathbf{r}_i} V + \sqrt{2D}\gamma \boldsymbol{\eta}_i^s \tag{8}$$

where D is the translational diffusion coefficient of the particles, γ is the Stokes drag coefficient (assumed to be the same for both species) and $\boldsymbol{\eta}_i^s(t)$ represents unit-variance Gaussian white noise with zero mean. Here, the first term describes the attraction into water-rich regions, caused by the particles hydrophilicity, where the second term describes the tendency of the particles to attach themselves to the interface of the two components. In addition, V accounts for excluded volume interactions among the particles which all have the same radius R and which we model using the Weeks-Chandler-Anderson potential $V = \frac{1}{2}\sum_{i, j \neq i} V_{ij}$ where the sums run over all particles and where $V_{ij} = 4\epsilon \left[\left(\frac{\sigma}{r_{ij}}\right)^{12} - \left(\frac{\sigma}{r_{ij}}\right)^6 \right] + \epsilon$ if $r_{ij} \leq 2^{1/6}\sigma$ and zero else. Here ϵ determines the strength of the potential, r_{ij} denotes the distance between particles i and j, $r_c = 2^{1/6}\sigma$ indicates a cutoff radius beyond which the potential energy is zero and $\sigma = 2R$ is the particle diameter.

Simulation Parameters

In the simulation model we measure the distance in units of $1\,\mu$m and the time in units of $1\,$s and match the parameters such as diffusion constants, particle radius and typical velocity of the particles with the experiment. In all our simulations we use for the Cahn-Hilliard equation $M = 10^2\,\mu\text{m}^2\text{s}^{-1}$, $a = -2.5\,\text{K}^{-1}$, $b = 50$, $\kappa = -5\,\mu\text{m}^2$, $A_a = 2.5\,\mu\text{m}^2$, $A_{na} = 1.5\,\mu\text{m}^2$, for the dynamics of the heat equation $k_0 = 60 \times 10^3\,\text{K}\mu\text{m}^2\text{s}^{-1}$, $k_d = 0.5 \times 10^3\,\text{s}^{-1}$, $D_T = 10^4\,\mu\text{m}^2\text{s}^{-1}$, and for the Langevin equation of the particles $\beta_a/\gamma = -0.5 \times 10^3\,\mu\text{m}^2\text{s}^{-1}$, $\beta_{na}/\gamma = -0.2 \times 10^3\,\mu\text{m}^2\text{s}^{-1}$, $\alpha_a/\gamma = 0$, $\alpha_{na}/\gamma = 1.5 \times 10^3\,\mu\text{m}^4\text{s}^{-1}$, $D = 0.1\,\mu\text{m}^2\text{s}^{-1}$, and $\epsilon/\gamma = 100\,\mu\text{m}^2\text{s}^{-1}$. Additionally we used in Fig. 1 $N_a = 15$, $N_{na} = 25$, $L_{box} = 50\,\mu$m, $\phi = 0.05$, $T_0 = 32.5\,°$C and in Fig. 3 we have $T_0 = 32.5\,°$C, $L_{box} = 200\,\mu$m, $N_{na} = 160$, and

$k_0 = 80 \times 10^3 \, \text{K} \mu \text{m}^2 \text{s}^{-1}$, $N_\text{a} = 200$ (active droploids) and $k_0 = 50 \times 10^3 \, \text{K} \mu \text{m}^2 \text{s}^{-1}$, $N_\text{a} = 800$ (immotile droplets)

References

(1) Schiavoni, M.; Sanchez-Palencia, L.; Renzoni, F.; Grynberg, G. Phase control of directed diffusion in a symmetric optical lattice. *Phys. Rev. Lett.* **2003**, *90*, 094101.

(2) Peskin, C. S.; Odell, G. M.; Oster, G. F. Cellular motions and thermal fluctuations: The Brownian ratchet. *Biophys. J.* **1993**, *65*, 316–324.

(3) Evans, D. J.; Cohen, E. G. D.; Morriss, G. P. Probability of second law violations in shearing steady states. *Phys. Rev. Lett.* **1993**, *71*, 2401.

(4) Wang, G.; Sevick, E. M.; Mittag, E.; Searles, D. J.; Evans, D. J. Experimental demonstration of violations of the second law of thermodynamics for small systems and short time scales. *Phys. Rev. Lett.* **2002**, *89*, 050601.

(5) Hyman, A. A.; Weber, C. A.; Jülicher, F. Liquid-liquid phase separation in biology. *Annu. Rev. Cell Dev. Biol.* **2014**, *30*, 39–58.

(6) Zwicker, D.; Seyboldt, R.; Weber, C. A.; Hyman, A. A.; Jülicher, F. Growth and division of active droplets provides a model for protocells. *Nat. Phys.* **2017**, *13*, 408–413.

(7) Berry, J.; Brangwynne, C. P.; Haataja, M. Physical principles of intracellular organization via active and passive phase transitions. *Reports on Progress in Physics* **2018**, *81*, 046601.

(8) Heckel, S.; Grauer, J.; Semmler, M.; Gemming, T.; Löwen, H.; Liebchen, B.; Simmchen, J. Active Assembly of Spheroidal Photocatalytic BiVO4 Microswimmers. *Langmuir* **2020**,

(9) Paxton, W. F.; Kistler, K. C.; Olmeda, C. C.; Sen, A.; St. Angelo, S. K.; Cao, Y.; Mallouk, T. E.; Lammert, P. E.; Crespi, V. H. Catalytic nanomotors: Autonomous movement of striped nanorods. *J. Am. Chem. Soc.* **2004**, *126*, 13424–13431.

(10) Dey, K. K.; Zhao, X.; Tansi, B. M.; Méndez-Ortiz, W. J.; Córdova-Figueroa, U. M.; Golestanian, R.; Sen, A. Micromotors powered by enzyme catalysis. *Nano Lett.* **2015**, *15*, 8311–8315.

(11) Ebbens, S. J.; Gregory, D. A. Catalytic Janus colloids: Controlling trajectories of chemical microswimmers. *Acc. Chem. Res.* **2018**, *51*, 1931–1939.

(12) Palacci, J.; Sacanna, S.; Steinberg, A. P.; Pine, D. J.; Chaikin, P. M. Living crystals of light-activated colloidal surfers. *Science* **2013**, *339*, 936–940.

(13) Soto, R.; Golestanian, R. Self-assembly of catalytically active colloidal molecules: Tailoring activity through surface chemistry. *Phys. Rev. Lett.* **2014**, *112*, 068301.

(14) Nakamura, S.; Minamino, T. Flagella-driven motility of bacteria. *Biomolecules* **2019**, *9*, 279.

(15) Qin, B.; Gopinath, A.; Yang, J.; Gollub, J. P.; Arratia, P. E. Flagellar kinematics and swimming of algal cells in viscoelastic fluids. *Sci. Rep.* **2015**, *5*, 9190.

(16) Gaffney, E. A.; Gadêlha, H.; Smith, D. J.; Blake, J. R.; Kirkman-Brown, J. C. Mammalian sperm motility: Observation and theory. *Annu. Rev. Fluid Mech.* **2011**, *43*, 501–528.

(17) Schloesser, F.; Friedrich, T.; Timmermann, A.; DeConto, R. M.; Pollard, D. Antarctic iceberg impacts on future Southern Hemisphere climate. *Nat. Clim. Chang.* **2019**, *9*, 672–677.

(18) Ferguson, J. A study of the motility of the intact uterus at term. *Surg Gynecol Obstet* **1941**, *73*, 359–366.

(19) Varma, A.; Montenegro-Johnson, T. D.; Michelin, S. Clustering-induced self-propulsion of isotropic autophoretic particles. *Soft Matter* **2018**, *14*, 7155–7173.

(20) Bregulla, A. P.; Cichos, F. Flow fields around pinned self-thermophoretic microswimmers under confinement. *J. Chem. Phys.* **2019**, *151*, 044706.

(21) Chuphal, P.; Venugopal, I.; Thakur, S. Formation of self-propelling clusters starting from randomly dispersed Brownian particles. *Bull. Mater. Sci.* **2020**, *43*, 183.

(22) Schmidt, F.; Liebchen, B.; Löwen, H.; Volpe, G. Light-controlled assembly of active colloidal molecules. *J. Chem. Phys.* **2019**, *150*, 094905.

(23) Voit, A.; Krekhov, A.; Enge, W.; Kramer, L.; Köhler, W. Thermal Patterning of a Critical Polymer Blend. *Phys. Rev. Lett.* **2005**, *94*, 214501.

(24) Lifshitz, I.; Slyozov, V. The kinetics of precipitation from supersaturated solid solutions. *J. Phys. Chem. Solids* **1961**, *19*, 35 – 50.

(25) Bray, A. J. Theory of phase-ordering kinetics. *Adv. Phys.* **2002**, *51*, 481–587.

(26) Gonnella, G.; Marenduzzo, D.; Suma, A.; Tiribocchi, A. Motility-induced phase separation and coarsening in active matter. *C. R. Phys.* **2015**, *16*, 316 – 331.

(27) Laradji, M.; Sunil Kumar, P. B. Domain growth, budding, and fission in phase-separating self-assembled fluid bilayers. *J. Chem. Phys.* **2005**, *123*, 224902.

(28) Camley, B. A.; Brown, F. L. H. Dynamic scaling in phase separation kinetics for quasi-two-dimensional membranes. *J. Chem. Phys.* **2011**, *135*, 225106.

(29) Stanich, C. A.; Honerkamp-Smith, A. R.; Putzel, G. G.; Warth, C. S.; Lamprecht, A. K.; Mandal, P.; Mann, E.; Hua, T.-A. D.; Keller, S. L. Coarsening Dynamics of Domains in Lipid Membranes. *Biophys. J.* **2013**, *105*, 444 – 454.

(30) Grauer, J.; Löwen, H.; Be'er, A.; Liebchen, B. Swarm Hunting and Cluster Ejections in Chemically Communicating Active Mixtures. *Scientific Reports* **2020**, *10*, 5594.

(31) Cremer, P.; Löwen, H. Scaling of cluster growth for coagulating active particles. *Phys. Rev. E* **2014**, *89*, 022307.

(32) Shulman, J. M.; De Jager, P. L.; Feany, M. B. Parkinson's disease: Genetics and pathogenesis. *Annu. Rev. Pathol.* **2011**, *6*, 193–222.

(33) Brundin, P.; Melki, R.; Kopito, R. Prion-like transmission of protein aggregates in neurodegenerative diseases. *Nat. Rev. Mol. Cell Biol.* **2010**, *11*, 301–307.

(34) Paladugu, S.; Callegari, A.; Tuna, Y.; Barth, L.; Dietrich, S.; Gambassi, A.; Volpe, G. Nonadditivity of critical Casimir forces. *Nature Communications* **2016**, *7*, 11403.

(35) Schmidt, F.; Magazzù, A.; Callegari, A.; Biancofiore, L.; Cichos, F.; Volpe, G. Microscopic Engine Powered by Critical Demixing. *Phys. Rev. Lett.* **2018**, *120*, 068004.

5.6 Paper VI: QED Casimir forces vs. critical Casimir forces: trapping and releasing of flat metallic particles

Attached below is a preliminary draft containing the figures of the experiments, the analysis of the particle's height due to diffusion, the calculation of the QED Casimir force on the particle, as well as the experimental evidence for the release of a trapped particle due to repulsive critical Casimir forces.

Casimir forces vs. Critical Casimir forces: Trapping and releasing of flat metallic particles

preliminary list of authors in alphabetical order: Agnese Callegari, Abdallah Daddi-Moussa-Ider, Mikael Käll, Hartmut Löwen, Battulga Munkhbat, Falko Schmidt, Timur Shegai, Ruggero Verre, and Giovanni Volpe

In microelectromechanical system (MEMS) devices, surface forces such as the Casimir force can lead to undesired stiction of two metallic surface causing device failure. Here, we propose a mechanism for restoration of collapsed structures using critical Casimir forces (CCF). Conceptually very similar to the Casimir force, the CCF results from density fluctuations in a critical binary mixture and whose strength and direction we can precisely control using temperature and self-assembled monolayers (SAMs). We show in a simple proof-of-principle device that we can reverse the reduced diffusion of a flat metallic particle trapped over a metallic surface, by adjusting the temperature close to the mixture's critical point. This results into reversible transitions of particles from metal to dielectric surfaces, which were previously impeded by Casimir forces. Using hydrodynamic simulations we reconstruct the particle's height above surface and the resulting forces from its diffusion constant alone and provide experimental evidence that repulsive CCFs are large enough to overcome attractive Casimir forces. As critical binary mixtures possess universal quantities and thus can be interchanged, the application range of our system can be expanded far beyond our current realization for restoring stiction in MEMS devices caused by sources other than Casimir forces.
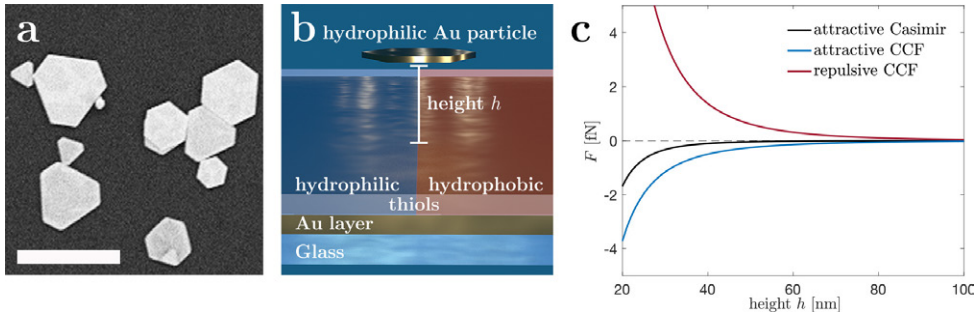
Figure 1. Diffusion of a Gold flake over a metallic surface. a SEM images of thin Au flakes of various sizes. **b** Schematic of a hydrophilic Au flake hovering at height h above a glass surface coated with a 30 nm Au layer and treated with thiols that change the surface's wetting properties. **c** The presence of two metallic surfaces, i.e. the Au particle and Au layer, induces an attractive Casimir force depending on h. The hydrophilic (hydrophobic) wetting layer induces in the presence of a near-critical binary mixture of water and 2,6-lutidine an attractive (repulsive) critical Casimir forces (CCF) depending on h. Scale bar is $5\,\mu$m.
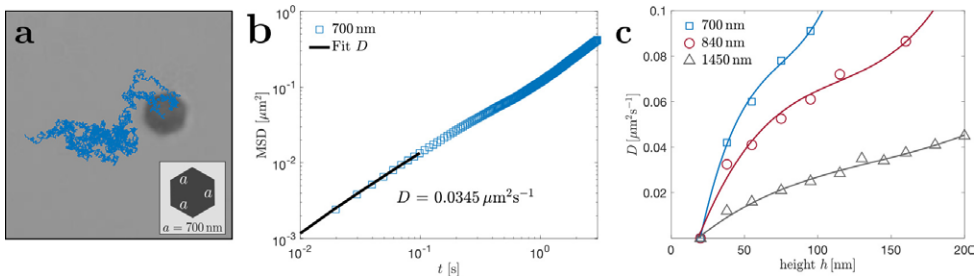
Figure 2. Experimental analysis and hydrodynamic calculations of a flake above a hydrophilic Au surface. a Microscope image and trajectory of a diffusing flake shaped as a convex equilateral hexagon with side length a (inset). **b** Mean squared displacement analysis of its trajectory with linear fit of its diffusion constant D. **c** From D the height h above surface can be reconstructed using hydrodynamic simulations. Here, the diffusion constant of three particles of different size $a = 700, 840, 1450$ nm are calculated at specific heights h (markers), and then fitted with theory (lines).

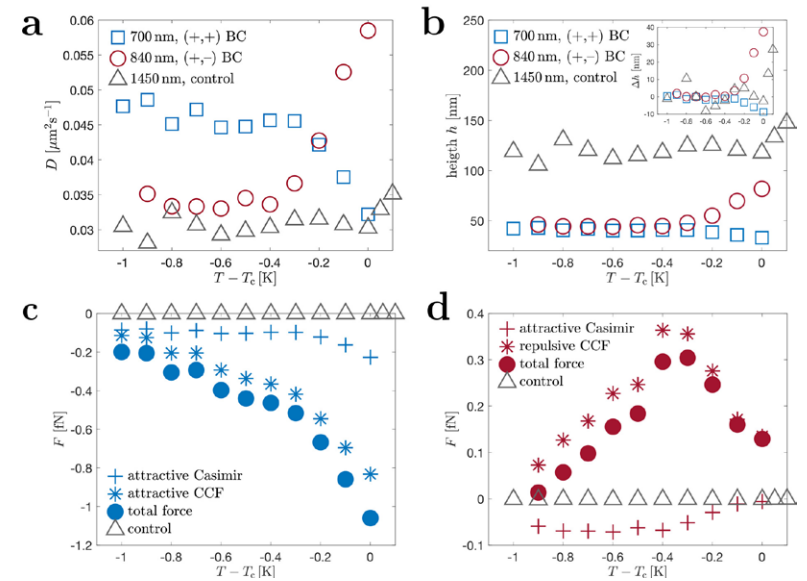**Figure 3. Effects of different surface boundary conditions (BC) on the particle's motion. a** D depending on temperature difference to the critical temperature $T - T_\mathrm{c}$ for three particles and cases; hydrophilic particle and surface, i.e. $(+,+)$ BC, lead to an decrease in D when approaching T_c (blue squares); whereas for hydrophilic particle and hydrophobic surface, i.e. $(+,-)$ BC, D increases close to T_c (red circles); compared to a weakly hydrophilic, dielectric surface, where D remains approximately constant (grey triangles). **b** Corresponding height h, calculated using Fig. 2c, shows that in the presence of a metal surface h is small (blue square and red circles), compared to the control with a dielectric surface (grey triangles). Close to T_c, depending on the BC, h increases or decreases as clearly seen by the difference in height Δh (inset). **c** Calculations of the QED Casimir force, attractive CCF and total force depending on h for a flake with $a = 700$ nm and $(+,+)$ BC, and **d** repulsive CCF for a flake with $a = 840$ nm and $(+,-)$ BC. This confirms that a reduction (increase) in D is a result of attractive (repulsive) CCF close to T_c and the smaller absolute height for metal surfaces due to the presence of Casimir attraction.
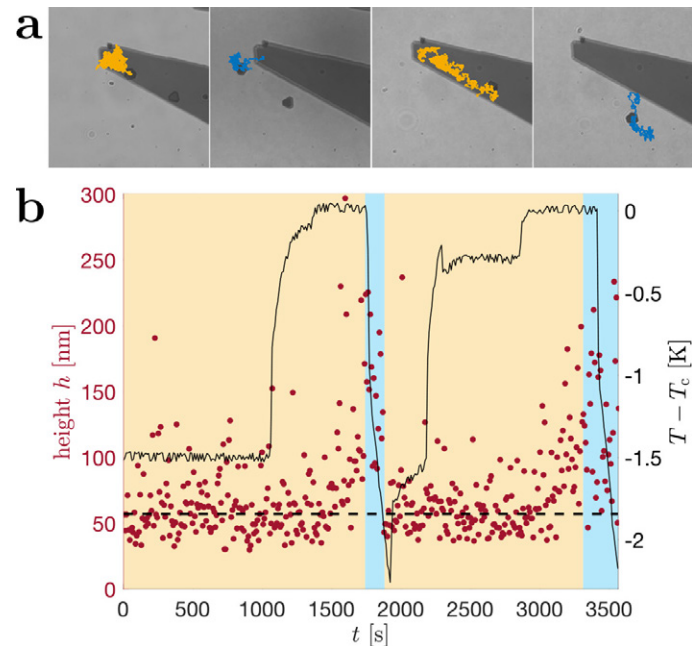
Figure 4. **Trapping and release of an Au flake from a metallic surface.** **a** Snapshots of diffusing Au particles and corresponding trajectories when trapped on an Au surface (dark background, yellow trajectories), and when released and freely diffusing over a dielectric surface (bright background, blue trajectories). **b** Transitions of a particle trapped over a metallic surface (yellow background) and its release towards a dielectric surface (blue background) can be induced and reversed by tuning the temperature of the system far away $(T - T_c \ll 0)$ and close to the critical point $(T - T_c \approx 0)$, respectively. Over a metal surface, attractive Casimir forces keep the particle confined and reduce its overall height to $h \approx 54\,\mathrm{nm}$ (black dotted line). Under $(+,-)$ BC, increasing the temperature of the system close to its critical point lifts the particle far enough from the metallic surface $(\Delta h > 50\,\mathrm{nm})$ due to repulsive critical Casimir forces such that it freely diffuses and eventually transits towards the dielectric surface. Upon decrease of temperature, Casimir forces become predominant and attract nearby particles again. This process can be repeated continuously.

Bibliography

[1] Irma Richter. Codex atl. *Notebooks/IrmaRichter*, page 381v/1051v, 1999.

[2] Paris Ms. E, 45v; Richard O. Prum. "Leonardo and the science of bird flight". in: Grody (publ.) Leonardo Da Vinci. *Drawings from the Biblioteca Reale in Turin*; Capra, *Learning*, p. 266.

[3] Danielis Bernoulli. *Hydrodynamica, sive de viribus et motibus fluidorum commentarii : opus academicum ab auctore, dum Petropoli ageret, congestum.* Johannis Reinholdi Dulseckeri, 1783.

[4] Robert Brown. XXVII. A brief account of microscopical observations made in the months of June, July and August 1827, on the particles contained in the pollen of plants; and on the general existence of active molecules in organic and inorganic bodies. *Philos. Mag.*, 4(21):161–173, 1828.

[5] Shuichi Nakamura and Tohru Minamino. Flagella-driven motility of bacteria. *Biomolecules*, 9(7):279, 2019.

[6] Boyang Qin, Arvind Gopinath, Jing Yang, Jerry P. Gollub, and Paulo E. Arratia. Flagellar kinematics and swimming of algal cells in viscoelastic fluids. *Sci. Rep.*, 5:9190, 2015.

[7] Jalal Mosayebi, Mehdi Kiyasatfar, and Sophie Laurent. Synthesis, functionalization, and design of magnetic nanoparticles for theranostic applications. *Adv. Healthc. Mater.*, 6(23):1700306, 2017.

[8] Berta Esteban-Fernández de Ávila, Pavimol Angsantikul, Jinxing Li, Miguel Angel Lopez-Ramirez, Doris E. Ramírez-Herrera, Soracha Thamphiwatana, Chuanrui Chen, Jorge Delezuk, Richard Samakapiruk, Valentin Ramez, Marygorret Obonyo, Liangfang Zhang, and Joseph Wang. Micromotor-enabled active drug delivery for in vivo treatment of stomach infection. *Nat. Commun.*, 8(1):272, 2017.

[9] Wen Sun, Jiangli Fan, Suzhen Wang, Yao Kang, Jianjun Du, and Xiaojun Peng. Biodegradable drug-loaded hydroxyapatite nanotherapeutic agent for targeted drug release in tumors. *ACS Appl. Mater. Interfaces*, 10(9):7832–7840, 2018.

[10] Stefanie Wohlfart, Svetlana Gelperina, and Jörg Kreuter. Transport of drugs across the blood–brain barrier by nanoparticles. *J. Control Release*, 161(2):264 – 273, 2012.

[11] Jesper Tranekjær Jørgensen, Kamilla Norregaard, Pengfei Tian, Poul Martin Bendix, Andreas Kjaer, and Lene B. Oddershede. Single particle and PET-based platform for identifying optimal plasmonic nano-heaters for photothermal cancer therapy. *Sci. Rep.*, 6(1):30076, 2016.

[12] Arthur Ashkin. Acceleration and trapping of particles by radiation pressure. *Phys. Rev. Lett.*, 24:156–159, 1970.

[13] Arthur Ashkin, Joseph M. Dziedzic, John E. Bjorkholm, and Steven Chu. Observation of a single-beam gradient force optical trap for dielectric particles. *Opt. Lett.*, 11(5):288–290, 1986.

[14] Marlies E. J. Friese, Timo A. Nieminen, Norman R. Heckenberg, and Halina Rubinsztein-Dunlop. Optical alignment and spinning of laser-trapped microscopic particles. *Nature*, 394(6691):348–350, 1998.

[15] Péter Galajda and Pál Ormos. Complex micromachines produced and driven by light. *Appl. Phys. Lett.*, 78(2):249–251, 2001.

[16] Hana Šípová-Jungová, Daniel Andrén, Steven Jones, and Mikael Käll. Nanoscale inorganic motors driven by light: Principles, realizations, and opportunities. *Chem. Rev.*, 120(1):269–287, 2020.

[17] Jie Zhang, Jing Yan, and Steve Granick. Directed self-assembly pathways of active colloidal clusters. *Angew. Chem.*, 128(17):5252–5255, 2016.

[18] Unyong Jeong, Xiaowei Teng, Yong Wang, Hong Yang, and Younan Xia. Superparamagnetic colloids: Controlled synthesis and niche applications. *Adv. Mater.*, 19(1):33–60, 2007.

[19] Stephanus Büttgenbach. Electromagnetic micromotors—design, fabrication and applications. *Micromachines*, 5(4):929–942, 2014.

[20] René Nyffenegger, Christian Quellet, and Jaroslav Ricka. Synthesis of fluorescent, monodisperse, colloidal silica particles. *J. Colloid Interface Sci.*, 159(1):150–157, 1993.

[21] Wei Gao and Joseph Wang. Synthetic micro/nanomotors in drug delivery. *Nanoscale*, 6(18):10486–10494, 2014.

[22] Jan K. G. Dhont. *An introduction to dynamics of colloids*. Elsevier, 1996.

[23] Johannes Lyklema. *Fundamentals of interface and colloid science: Soft colloids*, volume 5. Elsevier, 2005.

[24] Günter Schmid. *Clusters and colloids: From theory to applications*. John Wiley & Sons, 2008.

[25] Monzer Fanun. *Colloids in biotechnology*, volume 152. CRC Press, 2010.

[26] Anthony A. Hyman, Christoph A. Weber, and Frank Jülicher. Liquid-liquid phase separation in biology. *Annu. Rev. Cell Dev. Biol.*, 30(1):39–58, 2014.

[27] David Zwicker, Rabea Seyboldt, Christoph A. Weber, Anthony A. Hyman, and Frank Jülicher. Growth and division of active droplets provides a model for protocells. *Nat. Phys.*, 13(4):408–413, 2017.

[28] Carsten Donau, Fabian Späth, Marilyne Sosson, Brigitte Kriebisch, Fabian Schnitter, Marta Tena-Solsona, Hyun-Seo Kang, Elia Salibi, Michael Sattler, Hannes Mutschler, and Job Boekhoven. Active coacervate droplets as a model for membraneless organelles and a platform towards synthetic life. *ChemRxiv*, page 11648598, 2020.

[29] Martin Blume, Victor J. Emery, and Robert B. Griffiths. Ising model for the λ transition and phase separation in He3-He4 mixtures. *Phys. Rev. A*, 4(3):1071, 1971.

[30] Carlos. A. Grattoni, Richard A. Dawe, C. Yen. Seah, and Jane D. Gray. Lower critical solution coexistence curve and physical properties (density, viscosity, surface tension, and interfacial tension) of 2,6-lutidine + water. *J. Chem. Eng. Data*, 38:516, 1993.

[31] Ivo Buttinoni, Giovanni Volpe, Felix Kümmel, Giorgio Volpe, and Clemens Bechinger. Active Brownian motion tunable by light. *J. Condens. Matter Phys.*, 24(28):284129, 2012.

[32] Felix Kümmel, Borge ten Hagen, Raphael Wittkowski, Ivo Buttinoni, Ralf Eichhorn, Giovanni Volpe, Hartmut Löwen, and Clemens Bechinger. Circular motion of asymmetric self-propelling particles. *Phys. Rev. Lett.*, 110(19):198302, 2013.

[33] Hiroo Totsuji and Taro Kihara. The correlation function for the distribution of galaxies. *Publ. Astron. Soc. Jpn.*, 21:221, 1969.

[34] Claude J. Allegre, Jean L. Le Mouël, and Ariel Provost. Scaling rules in rock fracture and possible implications for earthquake prediction. *Nature*, 297(5861):47–49, 1982.

[35] Zhengyu Ma, Gina G. Turrigiano, Ralf Wessel, and Keith B. Hengen. Cortical circuit dynamics are homeostatically tuned to criticality in vivo. *Neuron*, 104(4):655–664.e4, 2019.

[36] Clifford P. Brangwynne, Christian R. Eckmann, David S. Courson, Agata Rybarska, Carsten Hoege, Jöbin Gharakhani, Frank Jülicher, and Anthony A. Hyman. Germline P granules are liquid droplets that localize by controlled dissolution/condensation. *Science*, 324(5935):1729–1732, 2009.

[37] Joel Berry, Clifford P. Brangwynne, and Mikko Haataja. Physical principles of intracellular organization via active and passive phase transitions. *Rep. Prog. Phys.*, 81(4):046601, 2018.

[38] Dante R. Chialvo. Emergent complex neural dynamics. *Nat. Phys.*, 6(10):744–750, 2010.

[39] Per Bak, Chao Tang, and Kurt Wiesenfeld. Self-organized criticality: An explanation of the 1/f noise. *Phys. Rev. Lett.*, 59(4):381, 1987.

[40] John M. Beggs and Dietmar Plenz. Neuronal avalanches in neocortical circuits. *J. Neurosci.*, 23(35):11167–11177, 2003.

[41] Janina Hesse and Thilo Gross. Self-organized criticality as a fundamental property of neural systems. *Front. Syst. Neurosci.*, 8:166, 2014.

[42] John M. Beggs and Nicholas Timme. Being critical of criticality in the brain. *Front. Physiol.*, 3:163, 2012.

[43] Barbara Drossel and Franz Schwabl. Self-organized criticality in a forest-fire model. *Physica A*, 191(1):47 – 50, 1992.

[44] Gunnar Pruessner. *Self-organised criticality: Theory, models and characterisation.* Cambridge University Press, 2012.

[45] Florian Soyka, Olga Zvyagolskaya, Christopher Hertlein, Laurent Helden, and Clemens Bechinger. Critical Casimir forces in colloidal suspensions on chemically patterned surfaces. *Phys. Rev. Lett.*, 101(20):208301, 2008.

[46] Dennis V. Nguyen, Minh T. Dang, Tuan A. Nguyen, and Peter Schall. Critical Casimir forces for colloidal assembly. *J. Condens. Matter Phys.*, 28(4):043001, 2016.

[47] Shoji Maruo and Hiroyuki Inoue. Optically driven micropump produced by three-dimensional two-photon microfabrication. *Appl. Phys. Lett.*, 89(14):144101, 2006.

[48] Simon J. Parkin, Gregor Knöner, Timo A. Nieminen, Norman R. Heckenberg, and Halina Rubinsztein-Dunlop. Picoliter viscometry using optically rotated particles. *Phys. Rev. E*, 76(4):041507, 2007.

[49] Valentin Blickle and Clemens Bechinger. Realization of a micrometre-sized stochastic heat engine. *Nat. Phys.*, 8(2):143–146, 2012.

[50] Ignacio A. Martínez, Édgar Roldán, Luis Dinis, Dmitri Petrov, Juan M. R. Parrondo, and Raúl A. Rica. Brownian Carnot engine. *Nat. Phys.*, 12(1):67–70, 2016.

[51] Pedro A. Quinto-Su. A microscopic steam engine implemented in an optical tweezer. *Nat. Commun.*, 5(1):5889, 2014.

[52] Shahed Behzadi, Vahid Serpooshan, Wei Tao, Majd A. Hamaly, Mahmoud Y. Alkawareek, Erik C. Dreaden, Dennis Brown, Alaaldin M. Alkilany, Omid C. Farokhzad, and Morteza Mahmoudi. Cellular uptake of nanoparticles: Journey inside the cell. *Chem. Soc. Rev.*, 46:4218–4244, 2017.

[53] Oleg V. Salata. Applications of nanoparticles in biology and medicine. *J. Nanobiotechnology*, 2(1):3, 2004.

[54] Walter F. Paxton, Kevin C. Kistler, Christine C. Olmeda, Ayusman Sen, Sarah K. St. Angelo, Yanyan Cao, Thomas E. Mallouk, Paul E. Lammert, and Vincent H. Crespi. Catalytic nanomotors: Autonomous movement of striped nanorods. *J. Am. Chem. Soc.*, 126(41):13424–13431, 2004.

[55] Yang Wang, Rose M. Hernandez, David J. Bartlett, Julia M. Bingham, Timothy R. Kline, Ayusman Sen, and Thomas E. Mallouk. Bipolar electrochemical mechanism for the propulsion of catalytic nanomotors in hydrogen peroxide solutions. *Langmuir*, 22(25):10451–10456, 2006.

[56] Lei Shao, Zhong-Jian Yang, Daniel Andrén, Peter Johansson, and Mikael Käll. Gold nanorod rotary motors driven by resonant light scattering. *ACS Nano*, 9(12):12542–12551, 2015.

[57] Daniele Zanaga, Folkert Bleichrodt, Thomas Altantzis, Naomi Winckelmans, Willem Jan Palenstijn, Jan Sijbers, Bart de Nijs, Marijn A. van Huis, Ana Sánchez-Iglesias, Luis M. Liz-Marzán, Alfons van Blaaderen, K. Joost Batenburg, Sara Bals, and Gustaaf Van Tendeloo. Quantitative 3D analysis of huge nanoparticle assemblies. *Nanoscale*, 8:292–299, 2016.

[58] Patrick Figliozzi, Nishant Sule, Zijie Yan, Ying Bao, Stanislav Burov, Stephen K. Gray, Stuart A. Rice, Suriyanarayanan Vaikuntanathan, and Norbert F. Scherer. Driven optical matter: Dynamics of electrodynamically coupled nanoparticles in an optical ring vortex. *Phys. Rev. E*, 95:022604, 2017.

[59] Serim Ilday, Ghaith Makey, Gursoy B. Akguc, Özgün Yavuz, Onur Tokel, Ihor Pavlov, Oguz Gülseren, and F. Ömer Ilday. Rich complex behaviour of self-assembled nanoparticles far from equilibrium. *Nat. Commun.*, 8(1):14942, 2017.

[60] Yuval Yifat, Delphine Coursault, Curtis W. Peterson, John Parker, Ying Bao, Stephen K. Gray, Stuart A. Rice, and Norbert F. Scherer. Reactive optical matter: Light-induced motility in electrodynamically asymmetric nanoscale scatterers. *Light Sci. Appl.*, 7(1):105, 2018.

[61] Marina Fernández-Medina, Miguel A. Ramos-Docampo, Ondrej Hovorka, Verónica Salgueiriño, and Brigitte Städler. Recent advances in nano- and micromotors. *Adv. Funct. Mater.*, 30(12):1908283, 2020.

[62] Rémi Dreyfus, Jean Baudry, Marcus L. Roper, Marc Fermigier, Howard A. Stone, and Jérôme Bibette. Microscopic artificial swimmers. *Nature*, 437(7060):862–865, 2005.

[63] Brandon H. McNaughton, Karen A. Kehbein, Jeffrey N. Anker, and Raoul Kopelman. Sudden breakdown in linear response of a rotationally driven magnetic microparticle and application to physical and chemical microsensing. *J. Phys. Chem. B*, 110(38):18958–18964, 2006.

[64] Jérémie Palacci, Stefano Sacanna, Asher Preska Steinberg, David J. Pine, and Paul M. Chaikin. Living crystals of light-activated colloidal surfers. *Science*, 339(6122):936–940, 2013.

[65] Terrell L. Hill. *An introduction to statistical thermodynamics*. Courier Corporation, 1986.

[66] Eric S. Harper, Greg van Anders, and Sharon C. Glotzer. The entropic bond in colloidal crystals. *Proc. Natl. Acad. Sci. U. S. A.*, 116(34):16703–16710, 2019.

[67] Brunno C. Rocha, Sanjib Paul, and Harish Vashisth. Role of entropy in colloidal self-assembly. *Entropy*, 22(8), 2020.

[68] Marek Grzelczak, Jan Vermant, Eric M. Furst, and Luis M. Liz-Marzán. Directed self-assembly of nanoparticles. *ACS Nano*, 4(7):3591–3605, 2010.

[69] Yufeng Wang, Yu Wang, Dana R. Breed, Vinothan N. Manoharan, Lang Feng, Andrew D. Hollingsworth, Marcus Weck, and David J. Pine. Colloids with valence and specific directional bonding. *Nature*, 491(7422):51–55, 2012.

[70] Evan Pretti, Hasan Zerze, Minseok Song, Yajun Ding, Nathan A. Mahynski, Harold W. Hatch, Vincent K. Shen, and Jeetain Mittal. Assembly of three-dimensional binary superlattices from multi-flavored particles. *Soft Matter*, 14(30):6303–6312, 2018.

[71] Minseok Song, Yajun Ding, Hasan Zerze, Mark A. Snyder, and Jeetain Mittal. Binary superlattice design by controlling DNA-mediated interactions. *Langmuir*, 34(3):991–998, 2018.

[72] Andreas Walther and Axel H. E. Müller. Janus particles. *Soft Matter*, 4(4):663–668, 2008.

[73] Hong-Ren Jiang, Natsuhiko Yoshinaga, and Masaki Sano. Active motion of a Janus particle by self-thermophoresis in a defocused laser beam. *Phys. Rev. Lett.*, 105:268302, 2010.

[74] Rodrigo Soto and Ramin Golestanian. Self-assembly of catalytically active colloidal molecules: Tailoring activity through surface chemistry. *Phys. Rev. Lett.*, 112(6):068301, 2014.

[75] Ran Niu, Thomas Palberg, and Thomas Speck. Self-assembly of colloidal molecules due to self-generated flow. *Phys. Rev. Lett.*, 119(2):028001, 2017.

[76] Mark Goulian and Sanford M. Simon. Tracking single proteins within cells. *Biophys. J.*, 79(4):2188 – 2198, 2000.

[77] Giorgio Volpe, Giovanni Volpe, and Sylvain Gigan. Brownian motion in a speckle light field: Tunable anomalous diffusion and selective optical manipulation. *Sci. Rep.*, 4:3936, 2014.

[78] Ido Golding and Edward C. Cox. Physical nature of bacterial cytoplasm. *Phys. Rev. Lett.*, 96(9):098102, 2006.

[79] Irena Bronstein, Y. Israel, Eldad Kepten, Sabine Mai, Yaron Shav-Tal, E. Barkai, and Yuval Garini. Transient anomalous diffusion of telomeres in the nucleus of mammalian cells. *Phys. Rev. Lett.*, 103(1):018102, 2009.

[80] Vincent Tejedor, Olivier Bénichou, Raphael Voituriez, Ralf Jungmann, Friedrich Simmel, Christine Selhuber-Unkel, Lene B. Oddershede, and Ralf Metzler. Quantitative analysis of single particle trajectories: Mean maximal excursion method. *Biophys. J.*, 98(7):1364–1372, 2010.

[81] Krzysztof Burnecki, Eldad Kepten, Yuval Garini, Grzegorz Sikora, and Aleksander Weron. Estimating the anomalous diffusion exponent for single particle tracking data with measurement errors - An alternative approach. *Sci. Rep.*, 5(1):1–11, 2015.

[82] Yasmine Meroz and Igor M. Sokolov. A toolbox for determining subdiffusive mechanisms. *Phys. Rep.*, 573:1–29, 2015.

[83] Thorsten Wagner, Alexandra Kroll, Chandrashekara R. Haramagatti, Hans-Gerd Lipinski, and Martin Wiemann. Classification and segmentation of nanoparticle diffusion trajectories in cellular micro environments. *PloS one*, 12(1):e0170165, 2017.

[84] Naor Granik, Lucien E. Weiss, Elias Nehme, Maayan Levin, Michael Chein, Eran Perlson, Yael Roichman, and Yoav Shechtman. Single-particle diffusion characterization by deep learning. *Biophys. J.*, 117(2):185–192, 2019.

[85] Gorka Muñoz-Gil, Miguel Angel Garcia-March, Carlo Manzo, José D. Martín-Guerrero, and Maciej Lewenstein. Single trajectory characterization via machine learning. *New J. Phys.*, 22(1):013010, 2020.

[86] Michele Schiavoni, Laurent Sanchez-Palencia, Ferruccio Renzoni, and Gilbert Grynberg. Phase control of directed diffusion in a symmetric optical lattice. *Phys. Rev. Lett.*, 90(9):094101, 2003.

[87] Charles S. Peskin, Garrett M. Odell, and George F. Oster. Cellular motions and thermal fluctuations: The Brownian ratchet. *Biophys. J.*, 65(1):316–324, 1993.

[88] Fabian Schloesser, Tobias Friedrich, Axel Timmermann, Robert M. DeConto, and David Pollard. Antarctic iceberg impacts on future Southern Hemisphere climate. *Nat. Clim. Chang.*, 9(9):672–677, 2019.

[89] James K. W. Ferguson. A study of the motility of the intact uterus at term. *Surg Gynecol Obstet*, 73:359–366, 1941.

[90] Stefano Palagi, Andrew G. Mark, Shang Yik Reigh, Kai Melde, Tian Qiu, Hao Zeng, Camilla Parmeggiani, Daniele Martella, Alberto Sanchez-Castillo, Nadia Kapernaum, Frank Giesselmann, Diederik S. Wiersma, Eric Lauga, and Peer Fischer. Structured light enables biomimetic swimming and versatile locomotion of photoresponsive soft microrobots. *Nat. Mater.*, 15(6):647–653, 2016.

[91] Aykut Argun, Ali-Reza Moradi, Ercag Pince, Gokhan Baris Bagci, Alberto Imparato, and Giovanni Volpe. Non-boltzmann stationary distributions and nonequilibrium relations in active baths. *Phys. Rev. E*, 94(6):062150, 2016.

[92] Ambarish Ghosh and Peer Fischer. Controlled propulsion of artificial magnetic nanostructured propellers. *Nano Lett.*, 9(6):2243–2245, 2009.

[93] Paul Mestres, Ignacio A. Martinez, Antonio Ortiz-Ambriz, Raul A. Rica, and Edgar Roldan. Realization of nonequilibrium thermodynamic processes using external colored noise. *Phys. Rev. E*, 90(3):032116, 2014.

[94] Clemens Bechinger, Roberto Di Leonardo, Hartmut Löwen, Charles Reichhardt, Giorgio Volpe, and Giovanni Volpe. Active particles in complex and crowded environments. *Rev. Mod. Phys.*, 88(4):045006, 2016.

[95] Nadim Maluf and Kirt Williams. *Introduction to microelectromechanical systems engineering*. Artech House, 2004.

[96] John H. Lau, Cheng Kuo Lee, Chirayarikathuveedu S. Premachandran, and Aibin Yu. *Advanced MEMS packaging*. Citeseer, 2010.

[97] Mohamed Gad-el Hak. *MEMS: Design and fabrication*. CRC press, 2005.

[98] Hendrik B. G. Casimir and Dirk Polder. The influence of retardation on the London-van der Waals forces. *Phys. Rev.*, 73:360–372, 1948.

[99] Michael F. Serry, Dirk Walliser, and Jordan G. Maclay. The role of the Casimir effect in the static deflection and stiction of membrane strips in microelectromechanical systems (MEMS). *J. Appl. Phys.*, 84(5):2501–2506, 1998.

[100] Merlijn W. Van Spengen, Robert Puers, and Ingrid De Wolf. The prediction of stiction failures in MEMS. *IEEE transactions on device and materials reliability*, 3(4):167–172, 2003.

[101] G. T. Mulhernm. Supercritical carbon dioxide drying of microstructures. In *Tech. Digest 7th Int. Conf. Solid-State Sensors and Actuators, Yokohama, Japan*, volume 296, 1993.

[102] Henry Guckel, Jeffrey J. Sniegowski, Todd R. Christenson, and Farshid Raissi. The application of fine-grained, tensile polysilicon to mechanicaly resonant transducers. *Sens. Actuator A Phys.*, 21(1-3):346–351, 1990.

[103] Jong Hyun Lee, Hoi Hwan Chung, Seung Youl Kang, Jong Tae Baek, and Hyung Joun Yoo. Fabrication of surface micromachined polysilicon actuators using dry release process of HF gas-phase etching. In *Int. Electron Devices Meeting. Tech. Digest*, pages 761–764. IEEE, 1996.

[104] José Anguita and Fernando Briones. HF/H2O vapor etching of SiO2 sacrificial layer for large-area surface-micromachined membranes. *Sens. Actuator A Phys.*, 64(3):247–251, 1998.

[105] Roya Maboudian, Robert W. Ashurst, and Carlo Carraro. Tribological challenges in micromechanical systems. *Tribol. Lett.*, 12(2):95–100, 2002.

[106] Rodney L. Alley. Surface roughness modification of interfacial contacts in polysilicon microstructures. In *7th Int. Conf. Sensors and Actuators, Yokohama, Japan*, volume 291, 1993.

[107] Uthara Srinivasan, Micheal R. Houston, R. T. Rowe, and Roya Maboudian. Self-assembled fluorocarbon films for enhanced stiction reduction. In *Proceedings of Int. Solid State Sensors and Actuators Conference (Transducers' 97)*, volume 2, pages 1399–1402. IEEE, 1997.

[108] Uthara Srinivasan, Michael R. Houston, Roger T. Howe, and Roya Maboudian. Alkyltrichlorosilane-based self-assembled monolayer films for stiction reduction in silicon micromachines. *J. Microelectromech. Syst.*, 7(2):252–260, 1998.

[109] Keren Deng, Rochael J. Collins, Mehran Mehregany, and Chaim N. Sukenik. Performance impact of monolayer coating of polysilicon micromotors. *J. Elektrochem. Soc.*, 142(4):1278, 1995.

[110] Wyatt C. Shields and Orlin D. Velev. The evolution of active particles: Toward externally powered self-propelling and self-reconfiguring particle systems. *Chem*, 3(4):539 – 559, 2017.

[111] Samuel Sánchez, Lluís Soler, and Jaideep Katuri. Chemically powered micro-and nanomotors. *Angew. Chem.*, 54(5):1414–1444, 2015.

[112] Alexander M. Maier, Cornelius Weig, Peter Oswald, Erwin Frey, Peer Fischer, and Tim Liedl. Magnetic propulsion of microswimmers with DNA-based flagellar bundles. *Nano Lett.*, 16(2):906–910, 02 2016.

[113] Alexandre Douplik, Guennadi Saiko, Irina Schelkanova, and Valery V. Tuchin. 3 - The response of tissue to laser light. In Helena Jelínková, editor, *Lasers for medical applications*, Woodhead Publishing Series in Electronic and Optical Materials, pages 47–109. Woodhead Publishing, 2013.

[114] Jérémie Palacci, Stefano Sacanna, Sean-Hay Kim, Gi-Ra Yi, David J. Pine, and Paul M. Chaikin. Light-activated self-propelled colloids. *Philos. T. R. Soc. A.*, 372(2029):20130372, 2014.

[115] Dhruv P. Singh, Udit Choudhury, Peer Fischer, and Andrew G. Mark. Non-equilibrium assembly of light-activated colloidal mixtures. *Adv. Mater.*, 29(32):1701328, 2017.

[116] Muhammad Safdar, Juliane Simmchen, and Janne Jänis. Light-driven micro- and nanomotors for environmental remediation. *Environ. Sci.: Nano*, 4:1602–1616, 2017.

[117] LinLin Wang, Mihail N. Popescu, Fernando Stavale, Astrid Ali, Thomas Gemming, and Juliane Simmchen. Cu@TiO2 Janus microswimmers with a versatile motion mechanism. *Soft Matter*, 14:6969–6973, 2018.

[118] Walter F. Paxton, Paul T. Baker, Timothy R. Kline, Yang Wang, Thomas E. Mallouk, and Ayusman Sen. Catalytically induced electrokinetics for motors and micropumps. *J. Am. Chem. Soc.*, 128(46):14881–14888, 2006.

[119] Wei Gao, Xiaomiao Feng, Allen Pei, Yonge Gu, Jinxing Li, and Joseph Wang. Seawater-driven magnesium based Janus micromotors for environmental remediation. *Nanoscale*, 5(11):4696–4700, 2013.

[120] Claudio Maggi, Filippo Saglimbeni, Michele Dipalo, Francesco De Angelis, and Roberto Di Leonardo. Micromotors with asymmetric shape that efficiently convert light into work by thermocapillary effects. *Nat. Commun.*, 6:7855, 2015.

[121] Matthieu Martin, Alexandre Barzyk, Eric Bertin, Philippe Peyla, and Salima Rafai. Photofocusing: Light and flow of phototactic microswimmer suspension. *Phys. Rev. E*, 93(5):051101, 2016.

[122] Laurene Aoun, Alexander Farutin, Nicolas Garcia-Seyda, Paulin Nègre, Mohd Suhail Rizvi, Sham Tlili, Solene Song, Xuan Luo, Martine Biarnes-Pelicot, and Rémi Galland. Amoeboid swimming is propelled by molecular paddling in lymphocytes. *Biophys. J.*, 119(6):1157–1177, 2020.

[123] Eamonn A. Gaffney, Hermes Gadêlha, David. J. Smith, J. R. Blake, and Jackson C. Kirkman-Brown. Mammalian sperm motility: Observation and theory. *Annu. Rev. Fluid Mech.*, 43:501–528, 2011.

[124] Tom G. Bean, Alistair B. A. Boxall, Julie Lane, Katherine A. Herborn, Stéphane Pietravalle, and Kathryn E. Arnold. Behavioural and physiological responses of birds to environmentally relevant concentrations of an antidepressant. *Philos. T. R. Soc. B.*, 369(1656):20130575, 2014.

[125] Karen A. Kidd, Michael J. Paterson, Michael D. Rennie, Cheryl L. Podemski, Dave L. Findlay, Paul J. Blanchfield, and Karsten Liber. Direct and indirect responses of a freshwater food web to a potent synthetic oestrogen. *Philos. T. R. Soc. B.*, 369(1656):20130578, 2014.

[126] Warapong Tungittiplakorn, Leonard W. Lion, Claude Cohen, and Ju-Young Kim. Engineered polymeric nanoparticles for soil remediation. *Environ. Sci. Technol.*, 38(5):1605–1610, 2004.

[127] Lluis Soler, Veronika Magdanz, Vladimir M. Fomin, Samuel Sanchez, and Oliver G. Schmidt. Self-propelled micromotors for cleaning polluted water. *ACS nano*, 7(11):9611–9620, 2013.

[128] Manuele Brambilla, Eliseo Ferrante, Mauro Birattari, and Marco Dorigo. Swarm robotics: A review from the swarm engineering perspective. *Swarm Intell.*, 7(1):1–41, 2013.

[129] Sangwoo Shin. Diffusiophoretic separation of colloids in microfluidic flows. *Phys. Fluids*, 32(10):101302, 2020.

[130] Alexei V. Ivlev, Jörg Bartnick, Marco Heinen, Chengran Du, Vladimir Nosenko, and Hartmut Löwen. Statistical mechanics where Newton's third law is broken. *Phys. Rev. X*, 5(1):011035, 2015.

[131] Daniel Rings, Romy Schachoff, Markus Selmke, Frank Cichos, and Klaus Kroy. Hot Brownian motion. *Phys. Rev. Lett.*, 105(9):090604, 2010.

[132] Daniel Rings, Markus Selmke, Frank Cichos, and Klaus Kroy. Theory of Hot Brownian motion. *Soft Matter*, 7:3441–3452, 2011.

[133] Roberto Piazza and Alberto Parola. Thermophoresis in colloidal suspensions. *J. Phys. Condens. Matter*, 20(15):153102, 2008.

[134] Takeaki Araki and Anna Maciołek. Illumination-induced motion of a Janus nanoparticle in binary solvents. *Soft matter*, 15(26):5243–5254, 2019.

[135] Alois Würger. Self-diffusiophoresis of Janus particles in near-critical mixtures. *Phys. Rev. Lett.*, 115(18):188304, 2015.

[136] Juliane Simmchen, Jaideep Katuri, William E. Uspal, Mihail N. Popescu, Mykola Tasinkevych, and Samuel Sánchez. Topographical pathways guide chemical microswimmers. *Nat. Commun.*, 7:10598, 2016.

[137] Stephen J. Ebbens and David A. Gregory. Catalytic Janus colloids: Controlling trajectories of chemical microswimmers. *Acc. Chem. Res.*, 51(9):1931–1939, 2018.

[138] Daiki Nishiguchi and Masaki Sano. Mesoscopic turbulence and local order in Janus particles self-propelling under an ac electric field. *Phys. Rev. E*, 92(5):052309, 2015.

[139] Claudio Maggi, Juliane Simmchen, Filippo Saglimbeni, Jaideep Katuri, Michele Dipalo, Francesco De Angelis, Samuel Sanchez, and Roberto Di Leonardo. Self-assembly of micromachining systems powered by Janus micromotors. *Small*, 12(4):446–451, 2016.

[140] Antoine Aubret, Mena Youssef, Stefano Sacanna, and Jérémie Palacci. Targeted assembly and synchronization of self-spinning microgears. *Nat. Phys.*, 14(11):1114–1118, 2018.

[141] Felix C. Keber, Etienne Loiseau, Tim Sanchez, Stephen J. DeCamp, Luca Giomi, Mark J. Bowick, M. Cristina Marchetti, Zvonimir Dogic, and Andreas R. Bausch. Topology and dynamics of active nematic vesicles. *Science*, 345(6201):1135–1139, 2014.

[142] Andrea Ranzoni, Xander J. A. Janssen, Mikhail Ovsyanko, Leo J. van Ijzendoorn, and Menno W. J. Prins. Magnetically controlled rotation and torque of uniaxial microactuators for lab-on-a-chip applications. *Lab Chip*, 10:179–188, 2010.

[143] George J. Besseris and Donovan B. Yeates. Rotating magnetic particle microrheometry in biopolymer fluid dynamics: Mucus microrheology. *J. Chem. Phys.*, 127(10):09B610, 2007.

[144] Unè G. Būtaitė, Graham M. Gibson, Ying-Lung D. Ho, Mike Taverne, Jonathan M. Taylor, and David B. Phillips. Indirect optical trapping using light driven micro-rotors for reconfigurable hydrodynamic manipulation. *Nat. Commun.*, 10(1):1–10, 2019.

[145] Michelle D. Wang, Hong Yin, Robert Landick, Jeff Gelles, and Steven M. Block. Stretching DNA with optical tweezers. *Biophys. J.*, 72(3):1335, 1997.

[146] Kirstine Berg-Sørensen and Henrik Flyvbjerg. Power spectrum analysis for optical tweezers. *Rev. Sci.*, 75(3):594–612, 2004.

[147] Yonggun Jun, Momčilo Gavrilov, and John Bechhoefer. High-precision test of Landauer's principle in a feedback trap. *Phys. Rev. Lett.*, 113(19):190601, 2014.

[148] Eric Lutz and Sergio Ciliberto. From Maxwell's demon to Landauer's eraser. *Phys. Today*, 68(9):30, 2015.

[149] Philip H. Jones, Onofrio M. Maragò, and Giovanni Volpe. *Optical tweezers: Principles and applications.* Cambridge University Press, 1st edition, 2015.

[150] George M. Whitesides and Bartosz Grzybowski. Self-assembly at all scales. *Science*, 295(5564):2418–2421, 2002.

[151] David A. Giljohann, Dwight S. Seferos, Weston L. Daniel, Matthew D. Massich, Pinal C. Patel, and Chad A. Mirkin. Gold nanoparticles for biology and medicine. *Angew. Chem.*, 49(19):3280–3294, 2010.

[152] Rachel R. Collino, Tyler R. Ray, Rachel C. Fleming, Camille H. Sasaki, Hossein Haj-Hariri, and Matthew R. Begley. Acoustic field controlled patterning and assembly of anisotropic particles. *Extreme Mech. Lett.*, 5:37–46, 2015.

[153] Vinothan N. Manoharan, Mark T. Elsesser, and David J. Pine. Dense packing and symmetry in small clusters of microspheres. *Science*, 301(5632):483–487, 2003.

[154] Andreas P. Bregulla and Frank Cichos. Flow fields around pinned self-thermophoretic microswimmers under confinement. *J. Chem. Phys.*, 151(4):044706, 2019.

[155] Benno Liebchen and Hartmut Löwen. Which interactions dominate in active colloids? *J. Chem. Phys.*, 150(6):061102, 2019.

[156] Qian Chen, Jonathan K. Whitmer, Shan Jiang, Sung Chul Bae, Erik Luijten, and Steve Granick. Supracolloidal reaction kinetics of Janus spheres. *Science*, 331(6014):199–202, 2011.

[157] Fuduo Ma, Xingfu Yang, Hui Zhao, and Ning Wu. Inducing propulsion of colloidal dimers by breaking the symmetry in electrohydrodynamic flow. *Phys. Rev. Lett.*, 115(20):208302, 2015.

[158] Hartmut Löwen. Active colloidal molecules. *EPL*, 121(5):58001, 2018.

[159] Ran Niu, Andreas Fischer, Thomas Palberg, and Thomas Speck. Dynamics of binary active clusters driven by ion-exchange particles. *ACS Nano*, 12(11):10932–10938, 2018.

[160] Dan Bracha, Mackenzie T. Walls, and Clifford P. Brangwynne. Probing and engineering liquid-phase organelles. *Nat. Biotechnol.*, 37(12):1435–1445, 2019.

[161] Pierre Curie. Quelques remarques relatives á l'équation réduite de Van der Waals. *Archives des sciences physiques et naturelles, 3e période*, 26:13, 1891.

[162] Fabio Giavazzi, Alessandro Fornasieri, Alberto Vailati, and Roberto Cerbino. Equilibrium and non-equilibrium concentration fluctuations in a critical binary mixture. *EPJ E*, 39(10):103, 2016.

[163] John M. G. Cowie and Valeria Arrighi. *Polymers: Chemistry and physics of modern materials.* CRC press, 2007.

[164] John M. Kincaid and Ezechiel G. D. Cohen. Phase diagrams of liquid helium mixtures and metamagnets: Experiment and mean field theory. *Phys. Rep.*, 22(2):57–143, 1975.

[165] Sela Samin and René van Roij. Self-propulsion mechanism of active Janus particles in near-critical binary mixtures. *Phys. Rev. Lett.*, 115(18):188305, 2015.

[166] Sow Hsin Chen and Raj Rajagopalan. *Micellar solutions and microemulsions: Structure, dynamics, and statistical thermodynamics.* Springer Verlag, 2012.

[167] Yang Yang, JianCheng Wang, Xuan Zhang, WangLiang Lu, and Qiang Zhang. A novel mixed micelle gel with thermo-sensitive property for the local delivery of docetaxel. *J. Control Release*, 135(2):175 – 182, 2009.

[168] Omar Adame-Arana, Christoph A. Weber, Vasily Zaburdaev, Jacques Prost, and Frank Jülicher. Liquid phase separation controlled by pH. *Biophys. J.*, 2020.

[169] Wilton T. Snead and Amy S. Gladfelter. The control centers of biomolecular phase separation: How membrane surfaces, PTMs, and active processes regulate condensation. *Mol. Cell*, 76(2):295 – 305, 2019.

[170] Christine D. Keating. Aqueous phase separation as a possible route to compartmentalization of biological molecules. *Acc. Chem. Res.*, 45(12):2114–2124, 2012.

[171] Yongdae Shin, Joel Berry, Nicole Pannucci, Mikko P. Haataja, Jared E. Toettcher, and Clifford P. Brangwynne. Spatiotemporal control of intracellular phase transitions using light-activated optoDroplets. *Cell*, 168(1):159 – 171.e14, 2017.

[172] Michael E. Fisher and Pierre G. D. Gennes. Wall phenomena in a critical binary mixture. *C. r. hebd. séances Acad. sci.*, 287(8):207–209, 1978.

[173] Giacomo Bressi, Giovanni Carugno, Roberto Onofrio, and Giuseppe Ruoso. Measurement of the Casimir force between parallel metallic surfaces. *Phys. Rev. Lett.*, 88:041804, 2002.

[174] Daniel Garcia-Sanchez, King Yan Fong, Harish Bhaskaran, Steve Lamoreaux, and Hong X. Tang. Casimir force and in situ surface potential measurements on nanomembranes. *Phys. Rev. Lett.*, 109:027202, 2012.

[175] Sathyanarayana Paladugu, Agnese Callegari, Yazgan Tuna, Lukas Barth, Siegfried Dietrich, Andrea Gambassi, and Giovanni Volpe. Nonadditivity of critical Casimir forces. *Nat. Commun.*, 7(1):11403, 2016.

[176] Andrea Gambassi, Ania Maciołek, Clemens Hertlein, Ursula Nellen, Laurent Helden, Clemens Bechinger, and Siegfried Dietrich. Critical Casimir effect in classical binary liquid mixtures. *Phys. Rev. E*, 80:061143, 2009.

[177] Salima Rafaï, Daniel Bonn, and Jacques Meunier. Repulsive and attractive critical casimir forces. *Physica A*, 386(1):31–35, 2007.

[178] Ursula Nellen, Laurent Helden, and Clemens Bechinger. Tunability of critical Casimir interactions by boundary conditions. *EPL*, 88(2):26001, 2009.

[179] Clemens Hertlein, Laurent Helden, Andrea Gambassi, Siegfried Dietrich, and Clemens Bechinger. Direct measurement of critical Casimir forces. *Nature*, 451(7175):172–175, 2008.

[180] Andrea Gambassi and Siegfried Dietrich. Critical Casimir forces steered by patterned substrates. *Soft Matter*, 7(4):1247–1253, 2011.

[181] Anna Maciołek and Siegfried Dietrich. Collective behavior of colloids due to critical casimir interactions. *Rev. Mod. Phys.*, 90(4):045001, 2018.

[182] Emanuele Marino, Thomas E. Kodger, Jan Bart ten Hove, Aldrik H. Velders, and Peter Schall. Assembling quantum dots via critical Casimir forces. *Sol. Energy Mater Sol.*, 158:154–159, 2016.

[183] Daniel Bonn, Jakub Otwinowski, Stefano Sacanna, Hua Guo, Gerard Wegdam, and Peter Schall. Direct observation of colloidal aggregation by critical Casimir forces. *Phys. Rev. Lett.*, 103(15):156101, 2009.

[184] Truc A. Nguyen, Arthur Newton, Daniela J. Kraft, Peter G. Bolhuis, and Peter Schall. Tuning patchy bonds induced by critical Casimir forces. *Materials*, 10(11):1265, 2017.

[185] Hakan Ceylan, Immihan Ceren Yasa, Oncay Yasa, Ahmet Fatih Tabak, Joshua Giltinan, and Metin Sitti. 3D-printed biodegradable microswimmer for theranostic cargo delivery and release. *ACS nano*, 13(3):3353–3362, 2019.

[186] Per Artursson, Erik Arro, Peter Edman, Jan L. E. Ericsson, and Ingvar Sjöholm. Biodegradable microspheres V: Stimulation of macrophages with microparticles made of various polysaccharides. *J. Pharm. Sci.*, 76(2):127–133, 1987.

[187] Armando Maestro, Nicolas Bruot, Jurij Kotar, Nariya Uchida, Ramin Golestanian, and Pietro Cicuta. Control of synchronization in models of hydrodynamically coupled motile cilia. *Commun. Phys.*, 1(1):1–8, 2018.

[188] Chao Zhou, Nobuhiko Jessis Suematsu, Yixin Peng, Qizhang Wang, Xi Chen, Yongxiang Gao, and Wei Wang. Coordinating an ensemble of chemical micromotors via spontaneous synchronization. *ACS Nano*, 14(5):5360–5370, 2020.

[189] John P. S. Peterson, Tiago B. Batalhão, Marcela Herrera, Alexandre M. Souza, Roberto S. Sarthour, Ivan S. Oliveira, and Roberto M. Serra. Experimental characterization of a spin quantum heat engine. *Phys. Rev. Lett.*, 123(24):240601, 2019.

[190] Adam W. Hauser, Subramanian Sundaram, and Ryan C. Hayward. Photothermocapillary oscillators. *Phys. Rev. Lett.*, 121:158001, 2018.

[191] Yuzhi Shi, Tongtong Zhu, Kim Truc Nguyen, Yi Zhang, Sha Xiong, Peng Huat Yap, Wee Ser, Shubo Wang, Cheng-Wei Qiu, C. T. Chan, and Ai Qun Liu. Optofluidic microengine in a dynamic flow environment via self-induced back-action. *ACS Photonics*, 7(6):1500–1507, 2020.

[192] Songbo Ni, Jessica Leemann, Ivo Buttinoni, Lucio Isa, and Heiko Wolf. Programmable colloidal molecules from sequential capillarity-assisted particle assembly. *Sci. Adv.*, 2(4):e1501779, 2016.

[193] Andrey Pototsky and Holger Stark. Active Brownian particles in two-dimensional traps. *EPL*, 98(5):50004, 2012.

[194] Olivier Dauchot and Vincent Démery. Dynamics of a self-propelled particle in a harmonic trap. *Phys. Rev. Lett.*, 122(6):068002, 2019.

[195] Sho C. Takatori, Raf De Dier, Jan Vermant, and John F. Brady. Acoustic trapping of active matter. *Nat. Commun.*, 7(1):1–7, 2016.

[196] Falko Schmidt, Alessandro Magazzù, Agnese Callegari, Luca Biancofiore, Frank Cichos, and Giovanni Volpe. Microscopic engine powered by critical demixing. *Phys. Rev. Lett.*, 120(6):068004, 2018.

[197] Ruggero Verre, Lei Shao, Nils Odebo Länk, Pawel Karpinski, Andrew B. Yankovich, Tomasz J. Antosiewicz, Eva Olsson, and Mikael Käll. Metasurfaces and colloidal suspensions composed of 3D chiral Si nanoresonators. *Adv. Mater.*, 29(29):1701352, 2017.

[198] Akhil Varma, Thomas D. Montenegro-Johnson, and Sébastien Michelin. Clustering-induced self-propulsion of isotropic autophoretic particles. *Soft Matter*, 14:7155–7173, 2018.

[199] Tingting Yu, Prabha Chuphal, Snigdha Thakur, Shang Yik Reigh, Dhruv P Singh, and Peer Fischer. Chemical micromotors self-assemble and self-propel by spontaneous symmetry breaking. *ChemComm*, 54(84):11933–11936, 2018.

[200] Zaiyi Shen, Alois Würger, and Juho S Lintuvuori. Hydrodynamic self-assembly of active colloids: Chiral spinners and dynamic crystals. *Soft Matter*, 15(7):1508–1521, 2019.

[201] Prabha Chuphal, Ishwar Venugopal, and Snigdha Thakur. Formation of self-propelling clusters starting from randomly dispersed Brownian particles. *Bull. Mater. Sci.*, 43(1):183, 2020.

[202] Jens Grauer, Hartmut Löwen, Avraham Be'er, and Benno Liebchen. Swarm hunting and cluster ejections in chemically communicating active mixtures. *Sci. Rep.*, 10(1):5594, 2020.

[203] Gorka Muñoz-Gil, Giovanni Volpe, Miguel Angel Garcia-March, Ralf Metzler, Maciej Lewenstein, and Carlo Manzo. AnDi: The anomalous diffusion challenge. *arXiv preprint arXiv:2003.12036*, 2020.

[204] Frank Cichos, Kristian Gustavsson, Bernhard Mehlig, and Giovanni Volpe. Machine learning for active matter. *Nat. Mach. Intell.*, 2(2):94–103, 2020.

[205] Luca Biferale, Fabio Bonaccorso, Michele Buzzicotti, Patricio Clark Di Leoni, and Kristian Gustavsson. Zermelo's problem: Optimal point-to-point navigation in 2D turbulent flows using reinforcement learning. *Chaos*, 29(10):103138, 2019.

[206] Soon Hoe Lim, Ludovico Theo Giorgini, Woosok Moon, and John S. Wettlaufer. Predicting rare events in multiscale dynamical systems using machine learning. *arXiv preprint arXiv:1908.03771*, 2019.

[207] Joanna Janczura, Patrycja Kowalek, Hanna Loch-Olszewska, Janusz Szwabiński, and Aleksander Weron. Machine learning classification of particle trajectories in living cells: Machine learning versus statistical testing hypothesis. *arXiv preprint arXiv:2005.06239*, 2020.

[208] Walter B. Cannon. Organization for physiological homeostasis. *Physiol. Rev.*, 9(3):399–431, 1929.

[209] Onn Brandman and Tobias Meyer. Feedback loops shape cellular signals in space and time. *Science*, 322(5900):390–395, 10 2008.

[210] Patrik Brundin, Ronald Melki, and Ron Kopito. Prion-like transmission of protein aggregates in neurodegenerative diseases. *Nat. Rev. Mol. Cell Biol.*, 11(4):301–307, 2010.

[211] Joshua M. Shulman, Philip L. De Jager, and Mel B. Feany. Parkinson's disease: Genetics and pathogenesis. *Annu. Rev. Pathol.*, 6:193–222, 2011.

[212] Igor E. Dzyaloshinskii, Efrat M. Lifshitz, and Lev P. Pitaevskii. The general theory of van der Waals forces. *Adv. Phys.*, 10(38):165–209, 1961.

[213] Timothy H. Boyer. Van der Waals forces and zero-point energy for dielectric and permeable materials. *Phys. Rev. A*, 9(5):2078, 1974.

[214] Ulf Leonhardt and Thomas G. Philbin. Quantum levitation by left-handed metamaterials. *New J. Phys.*, 9(8):254, 2007.

[215] Eyal Buks and Michael L. Roukes. Casimir force changes sign. *Nature*, 419(6903):119–120, 2002.

[216] Norio Inui. Diamagnetic effect on the Casimir force. *Phys. Rev. A*, 83(3):032513, 2011.

[217] Kimball A. Milton, E. K. Abalo, Prachi Parashar, Nima Pourtolami, Iver Brevik, and Simen Å. Ellingsen. Repulsive Casimir and Casimir–Polder forces. *J. Phys. A Math. Theor.*, 45(37):374006, 2012.

[218] Venkatesh K. Pappakrishnan, Pattabhiraju C. Mundru, and Dentcho A. Genov. Repulsive Casimir force in magnetodielectric plate configurations. *Phys. Rev. B*, 89(4):045430, 2014.

[219] Rongkuo Zhao, Lin Li, Sui Yang, Wei Bao, Yang Xia, Paul Ashby, Yuan Wang, and Xiang Zhang. Stable Casimir equilibria and quantum trapping. *Science*, 364(6444):984–987, 2019.

[220] Battulga Munkhbat, Adriana Canales, Betul Kucukoz, Denis G. Baranov, and Timur Shegai. Casimir microcavities for tunable self-assembled polaritons. *arXiv preprint arXiv:2010.08634*, 2020.

[221] Gaszton Vizsnyiczai, Giacomo Frangipane, Claudio Maggi, Filippo Saglimbeni, Silvio Bianchi, and Roberto Di Leonardo. Light controlled 3D micromotors powered by bacteria. *Nat. Commun.*, 8(1):1–7, 2017.

[222] Rachel P. Doherty, Thijs Varkevisser, Margot Teunisse, Jonas Hoecht, Stefania Ketzetzi, Samia Ouhajji, and Daniela J. Kraft. Catalytically propelled 3D printed colloidal microswimmers. *Soft Matter*, 2020.

[223] Naoto Shiraishi, Keiji Saito, and Hal Tasaki. Universal trade-off relation between power and efficiency for heat engines. *Phys. Rev. Lett.*, 117(19):190601, 2016.

[224] Patrick Pietzonka and Udo Seifert. Universal trade-off between power, efficiency, and constancy in steady-state heat engines. *Phys. Rev. Lett.*, 120(19):190602, 2018.

[225] Jae Sung Lee and Hyunggyu Park. Stochastic thermodynamics and hierarchy of fluctuation theorems with multiple reservoirs. *New J. Phys.*, 20(8):083010, 2018.

[226] Darwin Palima and Jesper Glückstad. Gearing up for optical microrobotics: Micromanipulation and actuation of synthetic microstructures by optical forces. *Laser Photonics Rev.*, 7(4):478–494, 2013.

[227] Saga Helgadottir, Aykut Argun, and Giovanni Volpe. Digital video microscopy enhanced by deep learning. *Optica*, 6(4):506–513, 2019.

[228] Aykut Argun, Tobias Thalheim, Stefano Bo, Frank Cichos, and Giovanni Volpe. Enhanced force-field calibration via machine learning. *arXiv preprint arXiv:2006.08963*, 2020.

Acknowledgements